

Western Australian School of Mines: Minerals, Energy and
Chemical Engineering

Fundamental evaluation of
Electrochemically Mediated Amine
Regeneration: Application to Natural Gas
Sweetening

Michael Edward Lev Massen-Hane

This thesis is presented for the Degree of
Doctor of Philosophy
of
Curtin University

November 2020

Declaration

To the best of my knowledge and belief this thesis contains no material previously published by any other person except where due acknowledgment has been made.

This thesis contains no material which has been accepted for the award of any other degree or diploma in any university.

Signature:

Date: *4 November 2020*

Abstract

The removal of carbon dioxide from flue gas, natural gas and that generated during steel, cement and ammonia production is predominantly performed by absorption with aqueous amines. The amine solution, once loaded with carbon dioxide must be regenerated before it can be reused - this is typically performed at elevated temperatures which requires significant thermal energy and causes amine degradation. This research examines an alternative electrochemical method for regeneration of amines, specifically the Electrochemically Mediated Amine Regeneration (EMAR) cycle. The EMAR cycle was initially intended for post combustion carbon capture systems, where operating conditions and gas compositions are considerably different to those in natural gas treating. EMAR specifically relies on the use of ethylenediamine and aqueous copper(II) to moderate the aqueous solution capacity for CO₂. Since aqueous ethylenediamine is non-standard in natural gas treating, the absorption reactions between ethylenediamine and common natural gas contaminants: CO₂, COS, CS₂, H₂S and CH₃SH, were evaluated with quantum chemical methods. Furthermore, the desorption reactions that result when aqueous copper(II) is introduced were evaluated with similar techniques. The electrochemical response of the electrolyte was examined experimentally via exposure to high pressure hydrocarbons and sulfide contaminants. Lastly, a process model was built to determine the total energy requirement of an EMAR based system to compare with existing thermal systems. Ethylenediamine will absorb all contaminants listed, though species that generate aqueous sulfides must be removed or the cyclic capacity of the EMAR process will be compromised. Quantum chemical results suggest that the dissociation of sulfur containing ethylenediamine carbamates will occur in the presence of copper(II), which extends the applicability of the EMAR cycle to handling COS and CS₂. Experimental results demonstrate that high pressure hydrocarbons present no significant obstacle to the EMAR process, and that the electrolyte system and cell operating conditions can be modified to improve reaction kinetics and the quality of the electrodeposited copper formed on the cathode. The results of the detailed EMAR process model indicate that at low applied overpotentials (0.1 V) and high ethylenediamine concentration (4 molal), the EMAR process becomes competitive with state of the art thermal amine systems, at 75 kJ/mole CO₂ captured.

Acknowledgments

Professor Vishnu Pareek

Thank you Professor for the opportunity to complete a PhD under your supervision, and for all the support you have provided. Our discussions of the 'big picture' and the interplay between government, academia and industry have helped me to see the forrest, when I had a penchant for the trees.

Professor Julian Gale

Thank you for adopting this engineer into your almost exclusively computational chemistry family. Your technical knowledge, guidance and patience over the years has been invaluable to my success. You have inspired me to become more of a critical thinker, and perhaps to the dismay of my engineering supervisors, more of a chemist.

Dr. Luke McElroy

From formal research updates and quantitative coffee appreciation meetings (with former colleagues) to the less formal online meetings made in isolation, you have always been supportive and a joy to be around. Thank you for remarkably specific and thorough feedback over the years. I will be glad to be named your first PhD completion, and will miss the sarcastic, sardonic and sometimes silly encounters we have shared over the years.

I would also like to thank: Curtin University for providing my stipend in the form of the Australian Postgraduate Award, the Pawsey Computing Centre and the National Computing Infrastructure facilities for providing computational time and support, and to Randall Ng, Lemlem Seloman, Evelyn Wong and Avryl Pusey for aiding in all matters logistical and financial.

The Hatton Group

I am thankful for all the members of The Hatton Group, especially to Professor Hatton himself. Thank you for making me feel at home in Boston and for all your guidance, in and out of the lab. In particular I appreciate the help and support provided by my project lab mates: Miao Wang, Subrahmaniam Hariharan, Mohammad Rahimi, and Sahag Voskian. It was a pleasure working with you all and a fantastic exchange experience.

My Friends and Family

Thank you mother, for tolerating the ridiculous working hours - your support was immensely helpful. Thank you father, for constantly expanding my scope of interest and knowledge. I owe much of the way I think about the world to you. And thank you, friends, for the comic relief and emotional support over these last few years. Special mention to: Tristan - for the numerous fitness challenges, Radoman - for the long philosophical discussions, and Sahag - for being a great teacher and friend in a foreign place.

Common Abbreviations

AGRU	Acid Gas Removal Unit.
AMP	2-amino-2-methyl-1-propanol.
AP	2-amino-1-propanol.
BCM	Billion Cubic Metres.
CC	Coupled Cluster.
CI	Configuration Interaction.
CPE	Constant Phase Element.
CV	Cyclic Voltammogram.
DEA	Diethanolamine.
DFT	Density Functional Theory.
DGA	Diglycolamine.
ECP	Effective Core Potential.
EDA	Ethylenediamine.
EDTA	Ethylenediaminetetraacetic Acid.
EIS	Electrochemical Impedance Spectroscopy.
EMAR	Electrochemically Mediated Amine Regeneration.
EMCCS	Electrochemically-Mediated Competitive Complexation Separation.
EMCS	Electrochemically-Mediated Complexation Separation.
EoS	Equation Of State.
ESV	EMAR Separation Vessel.
GGA	Generalised Gradient Approximation.
GTO	Gaussian-type Orbital.
HAO	Hydrogenic Atomic Orbital.
HF	Hartree-Fock.
HiPACT	High Pressure Acid Gas Capture Technology.
IFT	Intermediate Flash Tank.
IHB	Intramolecular Hydrogen Bond.
KS	Kohn-Sham.
LNG	Liquefied Natural Gas.
LP	Low Pressure.
LSDA	Local Spin Density Approximation.

MDEA	N-methyldiethanolamine.
MEA	Monoethanolamine.
MGGA	Meta-GGA.
MO	Molecular Orbital.
NBS	National Bureau Of Standards.
NG	Natural Gas.
OCV	Open Circuit Voltage.
ORC	Organic Rankine Cycle.
PCCC	Post-Combustion Carbon Capture.
PD	Piperadine.
PES	Potential Energy Surface.
PEX	Proton Exchange.
PR	Peng-Robinson.
PZ	Piperazine.
QM	Quantum Mechanical.
RHF	Restricted Hartree-Fock.
SAS	Solvent Accessible Surface.
SCF	Self-consistent Field.
SCRf	Self-consistent Reaction Field.
STO	Slater-type Orbital.
TRIS	Trishydroxymethyl-aminomethane.
TS	Transition State.
UHF	Unrestricted Hartree-Fock.

Contents

Abstract	i
Acknowledgments	iii
Common Abbreviations	v
1 Introduction	1
1.1 LNG production	2
1.2 Electrochemical separation methods	7
1.3 Thesis structure	10
2 Quantum chemistry: an introduction	15
2.1 Schrödinger equation	16
2.2 <i>Ab initio</i> theories	17
2.2.1 Hartree-Fock approach	18
2.2.2 Coupled cluster theory	21
2.3 Density functional theory	23
2.4 Basis sets	26
2.5 Solvation models	27
3 Ethylenediamine with Natural Gas Contaminants	31
3.1 Methods	32
3.2 Results and Discussion	35
3.2.1 Preliminary gas phase results	35
3.2.2 Aqueous phase results	37
3.2.3 Interaction of product derivatives	48

3.2.4	Effect of explicit solvent on CO ₂ zwitterion energetics . . .	55
3.3	Summary	60
4	Solvation and complexation of copper(II)	63
4.1	Methods	64
4.2	Results and Discussion	67
4.2.1	The copper(II) ethylenediamine complex in EMAR	67
4.2.2	Modelling copper(II) EDA complexation	68
4.2.3	Ethylenediamine carbamate dissociation	90
4.3	Summary	93
5	Electrochemistry of EMAR with natural gas	95
5.1	Electrochemistry of EMAR	96
5.2	Methods	97
5.3	Results and Discussion	99
5.3.1	Electrolyte effect	99
5.3.2	The EMAR stack	105
5.3.3	Application to natural gas treating	109
5.3.4	Effect of cell pressure	115
5.4	Summary	128
6	Process model	131
6.1	EMAR process model	132
6.1.1	Model development	132
6.1.2	Liquid and vapour phase treatment	133
6.1.3	Process unit operations	141
6.2	Thermal amine model	157
6.2.1	Process optimisation	159
6.3	EMAR: Sensitivity to process variables	160
6.3.1	EDA concentration	161
6.3.2	Copper loading shift	163
6.3.3	Desorption pressure	166
6.3.4	Desorber temperature	173
6.3.5	Surface and transport overpotential	174

6.3.6	Absorber pressure and inlet CO ₂ concentration	176
6.3.7	Outlet CO ₂ target concentration	178
6.4	Powering EMAR	180
6.5	Summary	181
7	Conclusions and Recommendations	183
7.1	Summary	183
7.2	Directions for future research	186
	References	189
	Appendix A Copyright agreements	211

Chapter 1

Introduction

Liquefied natural gas (LNG) has long been a reliable source of energy and will be used in the transition to renewable sources as power stations fuelled by more polluting traditional fossil fuels are decommissioned. Natural gas generates 33% less carbon emissions than coal per unit heat supplied and 50% less than coal per unit electricity generated.¹ Under current governmental policies, world natural gas demand is set to increase to 5,891 billion cubic metres (BCM) by 2040, a 50% increase on 2018 demand of 3,952 BCM.¹ The majority of consumption projected is in Asian markets, primarily China, which over the 2017-2018 period increased its gas consumption by 33%.¹ Australia's LNG exports primarily supply the Asian market with 94% of exports in the 2018-2019 year destined for that region.² As a result, Australia is looking to further increase its export capacity, and as of 2019 Australia became the worlds largest exporter of LNG.³ The increase in Australia's export capacity of natural gas over the last 6 years is shown in Figure 1-1.

To ensure global carbon emissions are not further increased as production meets demand, new production facilities are performing sequestration of CO₂ captured during LNG production. Additionally, improvements in the efficiency of each section of the LNG production facility are being investigated. A brief description of a typical LNG production facility follows.

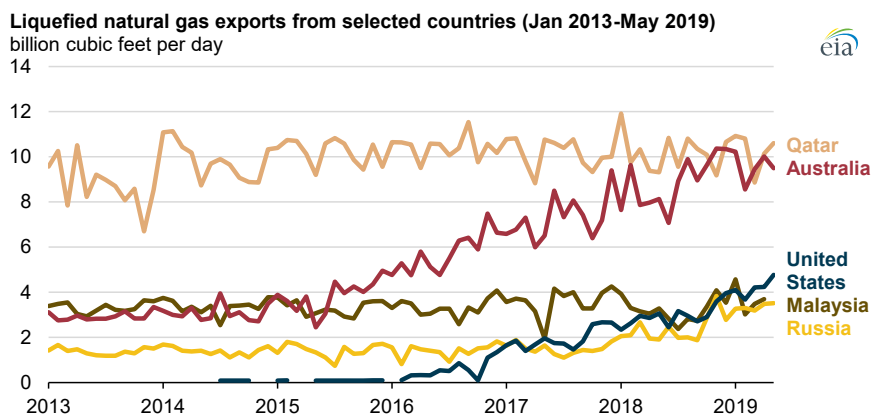


Figure 1-1: LNG exports from selected countries between 2013 and 2019 expressed in billion cubic feet per day (1 cubic foot is 0.028 m^3).^{5*}

1.1 LNG production

Specifics of the LNG production process depend on the well gas composition and operating conditions, though the generic steps presented in the block flow diagram in Figure 1-2 are typically present to remove contaminants and generate marketable products. Removal of contaminants is necessary for reasons of operational safety, corrosion management, product specifications, preventing freeze-out at low temperatures, reducing compression costs, preventing poisoning of catalysts in downstream equipment and meeting various environmental regulations.⁴

The three phase well fluid, containing a mixture of hydrocarbons, acid gases (CO_2 and H_2S), various species (N_2 and He), water and additional miscellaneous components are received at the facility. The Inlet Receival stage ensures reasonable phase separation between gas, water and oil phases. Oils are sent to Condensate Stabilisation where lighter components are recovered to the gas processing section of the plant and heavier components are marketed as lubricants. Separated well water is sent to water treatment, while the sour gas leaving Inlet Receival, that which contains CO_2 and H_2S , is forwarded to Acid Gas Removal (AGRU).

Acid gas contaminants, mainly CO_2 and H_2S (though additionally carbon disulfide, carbonyl sulide and thiols if sufficient H_2S is present) cause a number of

^{5*} Figure reproduced from *Today in Energy* with attribution, no permission required.⁶

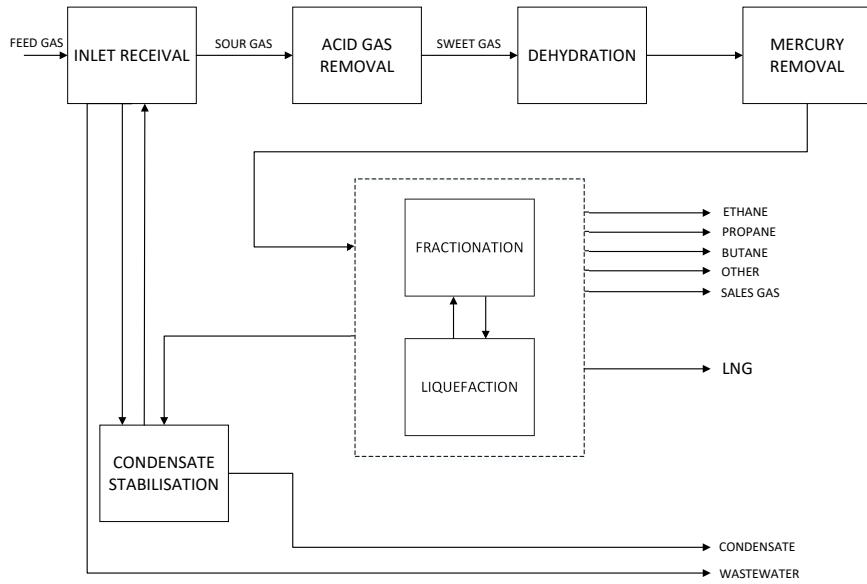


Figure 1-2: Block flow diagram of the LNG production process

the aforementioned issues if not removed.⁷ Namely they dissolve to form acidic solutions (exacerbating corrosion), freeze in the cryogenic fractionation and liquefaction section of the plant (causing erosion and damage to equipment), and reduce the heating value of the LNG or sales gas product. Depending on the age and operation of the facility, separated acid gases are vented to atmosphere or compressed and sequestered into nearby empty wells. The sweet gas, devoid of acidic components, is dehydrated, mercury is removed, and the treated gas is sent to fractionation and liquefaction. The majority of facilities operate to produce LNG and various other marketable products such as propane, butane and lubricants. Depending on government regulations, LNG facilities may also be required to supply sales gas for the domestic market.

Within LNG production the acid gas removal unit (AGRU) and liquefaction stages are the most energy intensive and the subject of extensive investigation. One cause of the high energy requirement of acid gas capture is the strict outlet target of 50 ppm CO₂ and 0.1 ppm H₂S for the treated gas, which is necessary to avoid downstream issues.⁷ Several techniques are available to remove acid gases, including solvent absorption (chemical, physical or hybrid), solid ad-

sorption, membrane separation, direct conversion and cryogenic fractionation.⁷ Parrish and Kidnay⁷ provide a removal technology selection guide based on the outlet conditions required, summarised in Figure 1-4.

Due to the stringent CO₂ outlet target and variability of well gas, chemical absorption with aqueous amines is favoured because it is the only technology that can reduce acid gas concentrations to ppm levels when acid gas partial pressure in the feed is low.⁷ Absorption and release of acid gases with an aqueous amine is achieved by the thermal swing process shown in Figure 1-3. In the absorber, lean aqueous amine contacts the sour gas (at high pressure 50 - 120 bar absolute, bara) and the amine leaves rich with CO₂ and H₂S. This rich stream is flashed down to a moderate pressure (8 bara) where light hydrocarbons are recovered to a low pressure (LP) fuel gas system and heavier hydrocarbons, which form a separate liquid phase, are skimmed off and recovered. The resulting aqueous solution of rich amine is pre-heated before entering the regeneration column. The regeneration column operates at elevated temperatures (typically 120 °C) and low pressures (2 bara), where acid gases are driven off. Condensables leaving the top of the column are refluxed and the desorbed acid gases are sent to a thermal oxidiser* and vented to atmosphere or sent to compression for sequestration. The now lean amine leaving the reboiler pre-heats the rich amine entering the regenerator column and is then cooled to near the absorber temperature.

The regenerator reboiler accounts for 70-80 % of the AGRU system operating cost,⁸ and 80 % of the heat load of the entire LNG plant.⁹ The regeneration energy has three components: the heat change of the rich amine solution; the heat of vaporisation of stripping steam generated; and the heat of absorption of CO₂ into the aqueous amine solution.¹⁰ The heat change and amount of stripping steam generated depends on system operating conditions, while the heat of absorption is dependent on the size, shape and constituents of the amine molecule.¹¹⁻¹³ To reduce the energy required for regeneration, studies have been performed aimed at either increasing the loading capacity of amines or reducing the heat of CO₂ absorption, both of which reduce the circulation rate and the regenerator reboiler duty. This has been achieved by varying degrees through modifying the structure

*This will depend on the concentrations of H₂S and volatile organic compounds and the local environmental regulations.

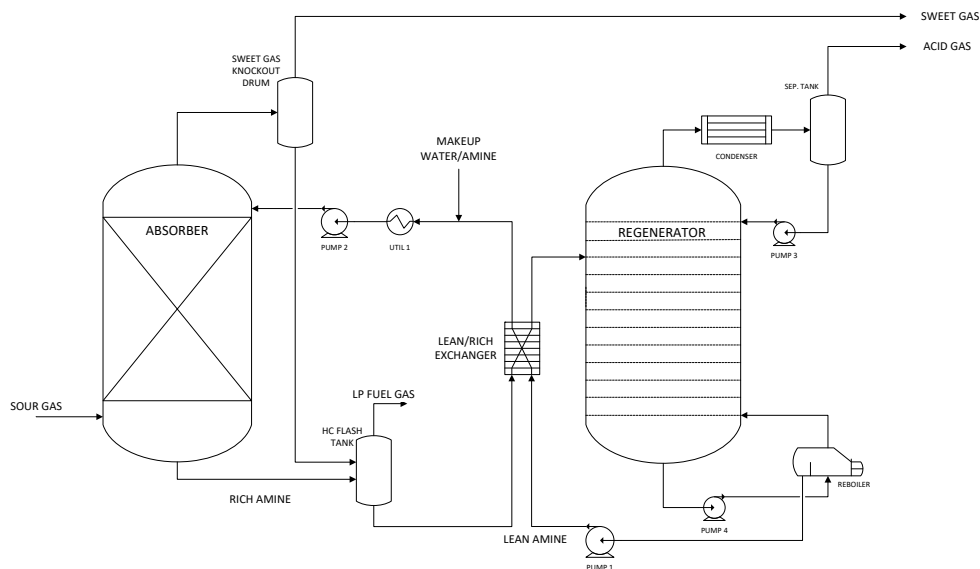


Figure 1-3: Process flow diagram of a thermal amine system for acid gas capture

of the amine molecule, using sterically hindered amines,^{14–18} or using blends of different amines.^{19–21} Primary and secondary amines, such as Monoethanolamine (MEA) and Diethanolamine (DEA), are used less now due to their comparatively high heat of absorption and corrosion rates. Additionally, primary and secondary amines are more prone to forming heat stable salts, which require further processing to sufficiently regenerate.⁷ N-methyldiethanolamine (MDEA) has become the amine of choice in natural gas sweetening applications due to its selective removal of H_2S in the presence of CO_2 ,⁷ and low heat of absorption (45–60 kJ/mol CO_2 depending on solution concentration^{22–24}). When blended with a suitable activator, such as Piperazine (PZ), the absorption rate of CO_2 is increased, and the cyclic capacity and degradation resistance improves.^{25,26} This MDEA/PZ blend has become the standard for acid gas removal in LNG production applications. Absorption into this blend occurs by the two pathways shown in Figure 1-5. MDEA facilitates CO_2 absorption by base catalysed hydration and does not directly react with CO_2 , while the secondary amines in PZ directly react with CO_2 forming zwitterion intermediates which deprotonate to a nearby base (e.g. MDEA), leaving carbamate products. At high CO_2 loadings, the dicarbamate PZ product dominates the total PZ concentration.²⁷ Both reactions are driven to the

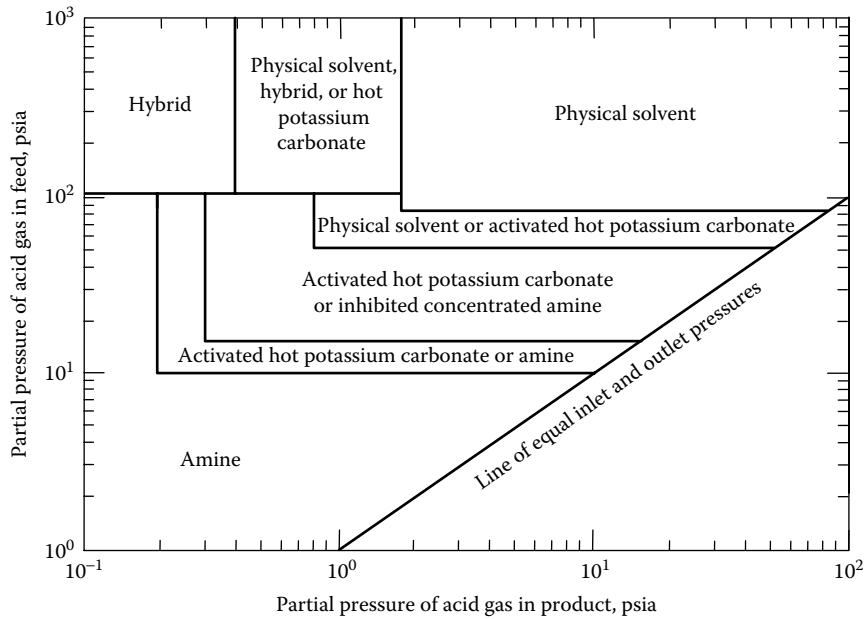


Figure 1-4: Selection guide for liquid absorbent acid gas removal technology based on inlet and outlet acid gas partial pressures.^{7*} 1 psia is 6.895 kPa.

right at high partial pressures of CO₂ and low temperatures (absorber column conditions), and are reversed at the regeneration column.

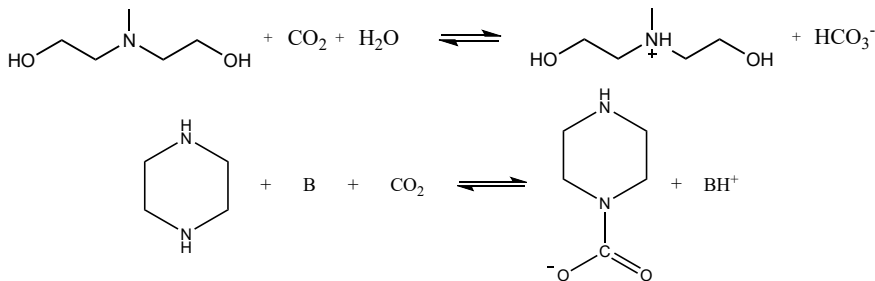


Figure 1-5: MDEA reaction with CO₂ to form bicarbonate HCO₃⁻ (top) and PZ absorption of CO₂ forming carbamate (bottom).

Due to the large reboiler duty requirement and low pressure operation of the regenerator (necessitating high pump work for solvent return and high compressor work if CO₂ sequestration is required), alternative solvents and processes

*Reprinted from Fundamentals of Natural Gas Processing, 2006, Kidnay, Arthur J. with permission from Taylor & Francis Group LLC - Books. Copyright license in Appendix A.

are being investigated. The proprietary solution provided by JGC Corporation and BASF SE, high pressure acid gas capture technology (HiPACT), has been demonstrated to require lower regenerator duties (10-20%) and circulation rates (20-27%) when applied to natural gas treating and Post-Combustion Carbon Capture (PCCC) facilities.^{28-30*} Additionally, the HiPACT regeneration column is operated at approximately 5 bara resulting in lower capital and operating costs of downstream compressors. Significant work has been performed by the Rochelle Group[†] to assess the performance of aqueous and water lean solutions of PZ in an ‘advanced flash stripper’ configuration.^{31,32} In pilot scale demonstrations of this technology applied to PCCC plants,^{33,34} the regenerator operates at 5-8 bara corresponding to reboiler temperatures of 134-151°C. The regenerator pressure is limited by the reboiler temperature, which is set to avoid significant thermal degradation of the amine solvent - recommended to be no greater than 163 °C for PZ.^{35,36}

Though improving, current thermal processes suffer from the disadvantages of operating at elevated temperatures. High reboiler duties, amine degradation and the low pressure gas release of thermal amine systems have motivated research into alternative regeneration techniques. Newly developed electrochemical regeneration techniques (not present in the selection guide in Figure 1-4) have been proposed for use in carbon dioxide capture and are described herein.

1.2 Electrochemical separation methods

Electrochemical separations make use of redox active absorbents or blockers to transport chemical species, of which there are two schemes: Electrochemically-Mediated Complexation Separation (EMCS) and Electrochemically-Mediated Competitive Complexation Separation (EMCCS), both of which are represented in Figure 1-6.³⁷ In the context of CO₂ separation, an EMCS cycle activates a redox species at one electrode, facilitating CO₂ absorption, and is deactivated at the opposing polarity electrode resulting in CO₂ release. This cycle has been demonstrated with quinones,³⁸⁻⁴⁰ bipyridines,⁴¹ and tholates^{42,43} as absorbent re-

*Reboiler duty and circulation rate compared against standard MDEA/PZ blend.

†University of Texas at Austin, McKetta Dept. of Chemical Engineering

dox active species. An EMCCS cycle instead deactivates a blocker species at one electrode allowing the absorption of CO_2 , and at the opposing electrode activates the blocker species which preferentially binds the to absorbent, releasing CO_2 . This cycle has been demonstrated with CO_2 absorbents more familiar to natural gas sweetening, primary amines.⁴⁴⁻⁴⁶ The thermodynamics of these schemes in various system geometries has been examined by Shaw and Hatton⁴⁷, who showed that by coupling electrochemical and absorption or desorption processes the work of separation approaches the thermodynamic minimum.

Given the proven ability of amines to achieve the stringent CO_2 outlet target for LNG production applications, the latter EMCCS cycle is the focus moving forward. Electrochemical techniques used to regenerate amine absorbents propose the following benefits: limited solvent degradation due to moderate temperature operation, elevated pressure CO_2 desorption and lower energy requirements. Electrochemical separations also avoid inefficient generation of utility heat required for absorbent regeneration. Instead, they may utilise on-site power generation or renewable energy sources to facilitate CO_2 separation.

An EMCCS cycle with Ethylenediamine (EDA) as the absorbent and Cu^{2+} as the active blocker (entitled Electrochemically Mediated Amine Regeneration (EMAR)), is under development at The Hatton Group, MIT. Initial investigations were performed by Stern³⁷ and Eltayeb⁴⁸ with further thermodynamic and engineering development by Shaw⁴⁹. A lab scale version of the technology has shown promising performance, operating for 200 hours with an average energy consumption of 40-80 $\text{kJ}_e/\text{mol CO}_2$ of electrical work,*which is comparable to current thermal systems.⁵⁰ Of several metal (blocker) and amine (absorbent) combinations examined, ethylenediamine with copper was deemed the most suitable given that the stability of the metal amine complex exceeded that of the individual amine CO_2 complexes (see Eqn. 1.1), the metal complex was more stable than the hydroxide salt, the reduction potential of the complex limited copper oxidation, and the combination demonstrated the highest cyclic reversibility.³⁷ Amines commonly employed in acid gas treating (MDEA & PZ) were unsuited to the process because a limited release of CO_2 was observed due to the low

* kJ_e indicates electrical energy and kJ_{th} thermal energy.

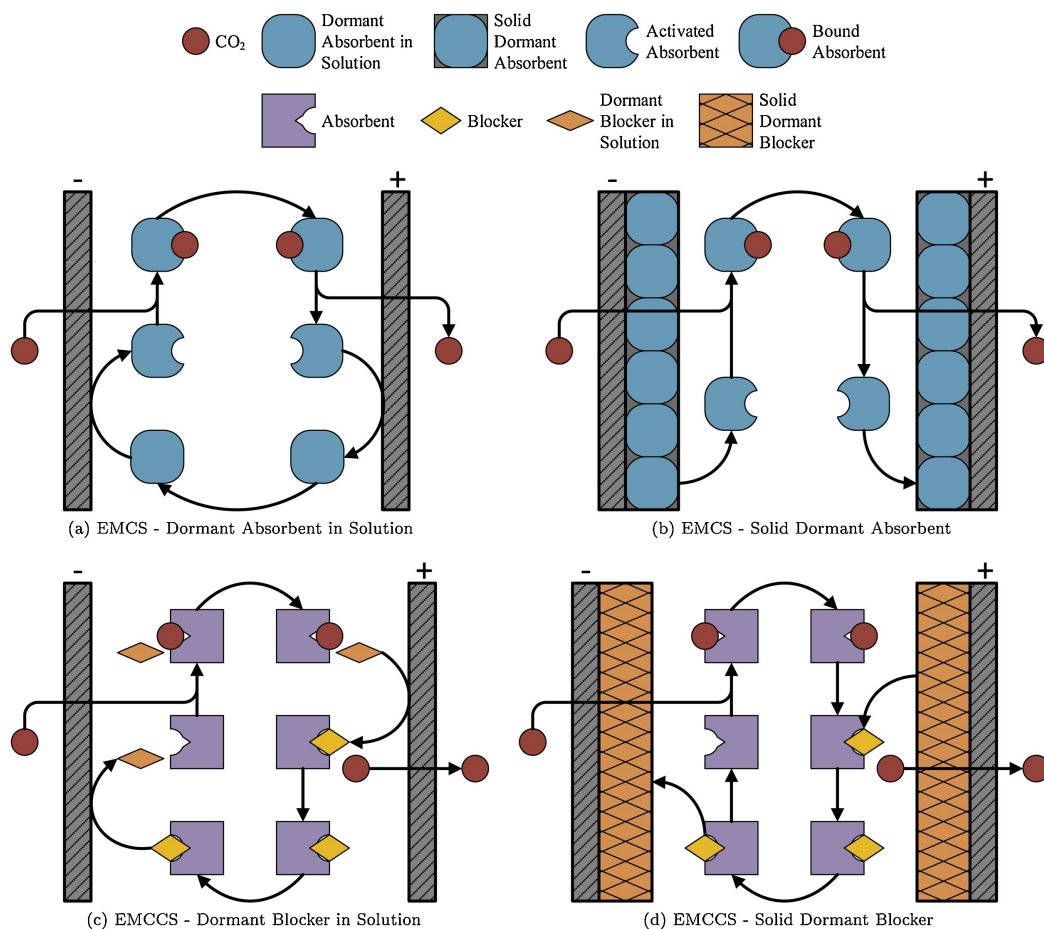


Figure 1-6: Two architectures of EMCS and EMCCS systems where the dormant species is in solution (a,c) and when only the active species is in solution (b,d). Figure reproduced from Shaw and Hatton⁴⁷ with permission.*

stability of the metal-amine complexes formed.

$$\log(\beta) > n_{ligand} \log K_{CO_2} \quad (1.1)$$

In Eqn. 1.1, β is the stability constant of the metal amine complex, n_{ligand} is the number of ligands per metal cation, and K_{CO_2} is the equilibrium constant between amine and CO_2 .

*Reprinted from International Journal of Greenhouse Gas Control, Volume 95, April 2020, 102878, Ryan A. Shaw, T. Alan Hatton, Electrochemical CO_2 capture thermodynamics, 1-10, Copyright (2020), with permission from Elsevier. Copyright license in Appendix A.

Ethylenediamine was rejected for use in thermal amine stripping early on due to its high heat of absorption (ca. 86 kJ/mol) though has been recently tested at the pilot plant scale in post-combustion carbon capture applications.⁵¹⁻⁵⁴ EDA demonstrates high capacity and fast kinetics with respect to CO₂ absorption, via the same mechanism as PZ, shown in Figure 1-7, through a zwitterion intermediate, and subsequently deprotonating to form a carbamate product.

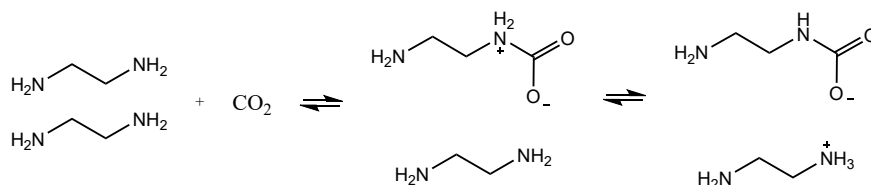


Figure 1-7: Absorption mechanism of CO₂ with EDA.

An electrochemical cycle using copper(II) ions and EDA for the separation of CO₂ is shown in Figure 1-8. The lean ethylenediamine contacts the sour gas in the absorber. The rich amine enters the anode where copper(II) ions are released into the aqueous solution. In forming the metal-amine complex, CO₂ is released and separated from the aqueous stream. The cathode reduces the copper-amine complex, removing the copper from solution, and returns lean ethylenediamine to the absorber where the cycle repeats. A process flow diagram of an EMAR cycle applied to natural gas treating is shown in Figure 1-9.

1.3 Thesis structure

This thesis aims to assess the applicability of an EMAR cycle to natural gas treating. Firstly the suitability of EDA to absorb the contaminants found in natural gas is examined computationally and compared to available experimental data. The degree to which the copper amine complexation reaction will reverse the formation of amine carbamate is also investigated computationally, using results from the previous section. The EMAR electrochemistry is evaluated at conditions under which a natural gas treating facility may operate and finally, a thermodynamic process model is presented for the scaled operation of the EMAR cycle. Due to the broad scope of this thesis, an introduction to each topic follows.

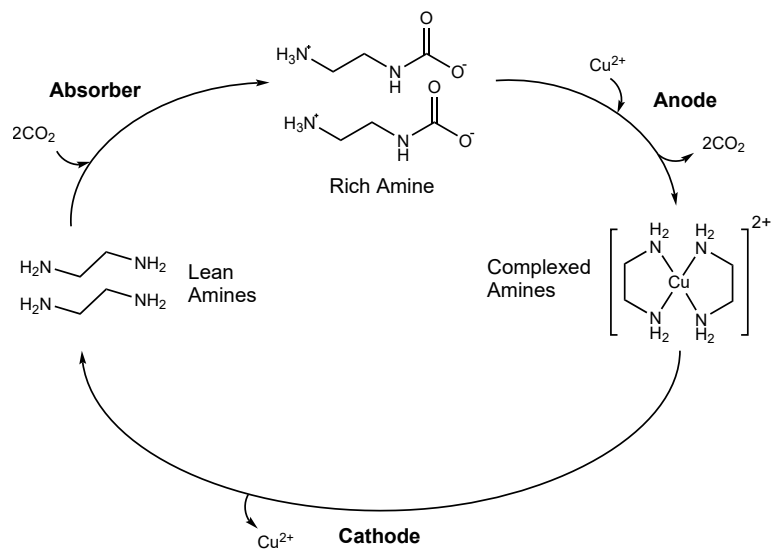


Figure 1-8: EMAR cycle based on copper and ethylenediamine.

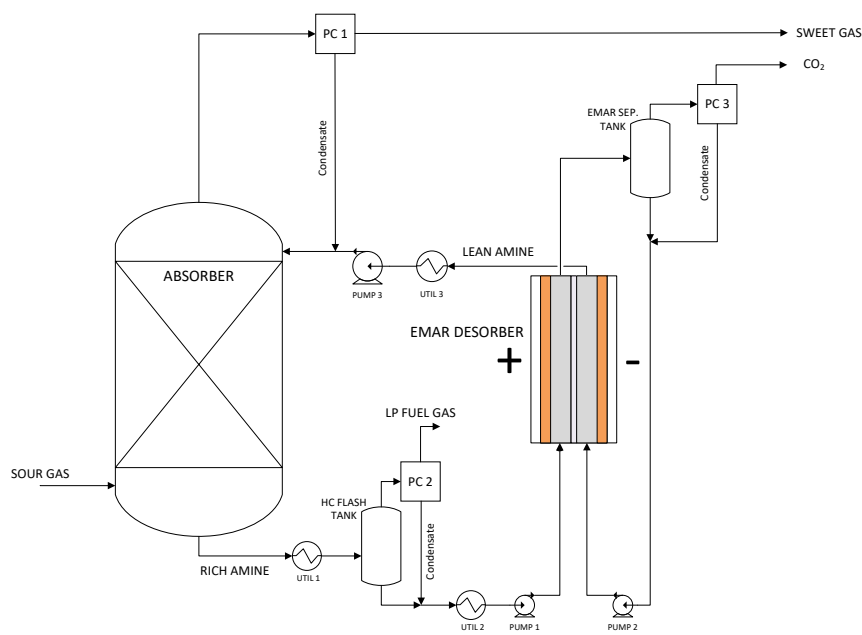


Figure 1-9: EMAR desorber in a natural gas treating application.

Computational modelling of EMAR reactions

Molecular modelling of reactions between amines and acid gases is becoming more prevalent since new methods are increasingly accurate and more compu-

tational resources are becoming available. Insight into specific interactions of amines already in use, those under trial or others of theoretical interest can be evaluated computationally, providing detail not available from experiment. Aspects such as the energy of interaction between amines and contaminants, activation energy barriers to forming intermediates and products, pK_a of the amine or derivatives, and relative energies of reactants and products can all be determined quantitatively to judge the suitability of certain amines to a gas treating process. As the above interactions pertain to bond forming and bond breaking processes, the use of quantum chemical simulation over classical molecular mechanics is more appropriate, with several examples in literature: investigation of activation energy barriers, structure of the transition state and relative energy of product and reactant species between CO_2 and amines MEA, DEA, MDEA, PZ, 2-amino-2-methyl-1-propanol (AMP), EDA;⁵⁵⁻⁶⁹ effect of substituent groups on interaction with CO_2 ;^{12,70,71} theoretical calculation of pK_a of MEA, trishydroxymethylaminomethane (TRIS), EDA, diglycolamine (DGA), 2-amino-1-propanol (AP), AMP, PZ, piperadine (PD);^{13,72-75} and surveys of carbamate formation of amino acids not yet applied in PCCC or natural gas treating.⁷⁶ Quantum chemistry is an increasingly useful tool to study the reactions of current amines in natural gas treating and as a means of screening new absorbents for future use. Chapter 3 uses quantum chemical techniques to determine reaction energetics of EDA with the common contaminants found in natural gas and the stability of products formed.

Quantum chemical simulation has also been widely applied to transition metal systems for catalyst development and mechanistic studies, examining bonding character and predicting electronic or nuclear spectra.^{77,78} Coordination complexes of Cu^{2+} have received a large amount of attention due to the d^9 electronic configuration of this metal, which often results in (Jahn-Teller) distortion of the complexes it forms.⁷⁹ A number of studies have used quantum chemical simulation to examine the structure and electronic spectra of copper(II) coordination compounds,⁸⁰⁻⁸² the redox behaviour,^{83,84} and surface interactions to understand and improve catalyst performance (eg. aqueous CO_2 reduction).⁸⁵⁻⁸⁷ Accurate evaluation of reaction pathways and thermodynamics requires a good computational technique, of which a myriad are available among Density Functional

Theory (DFT) and *ab initio* methods. Chapter 4 evaluates the thermodynamics of the metal-amine complex formation reaction necessary for the EMAR cycle to function. A number of methods are trialed to obtain the best description of the solvent environment around the copper ion, and once arrived at, reaction thermodynamics with the carbamates formed in the previous chapters are evaluated.

Electrochemistry of EMAR with gas contaminants

The electrochemistry of the copper-EDA system was previously characterised by Stern³⁷ in nitrate and chloride electrolytes. The degradation of nitrate salts on copper electrodes is evident in the literature⁸⁸⁻⁹⁰ and was proposed by Shaw⁴⁹ as a reason for the low efficiency of a prototype EMAR electrochemical cell. Characterisation of an alternative electrolyte for the EMAR system is performed in Chapter 5 by analysis of Cyclic Voltammogram (CV) data under inert, CO₂ and natural gas atmospheres. Natural gas with H₂S present affects the solubility of the blocker species (copper) in the EMAR cycle by forming solid metallic sulfides (though hindered in the presence of strong complexing agents^{91,92}) removing the blocker from circulation. This is investigated by examining the spectra and electrochemical behaviour of the electrolyte when a sulfide source is introduced. To minimise pumping losses in the EMAR cycle, the anode and cathode can be operated at elevated pressure, closer to the operating pressure of the absorption column. Limited examples of flow through electrochemical cells operating at elevated pressure exist due to challenges in mechanical design (with recent exceptions applied in high pressure CO₂ reduction^{93,94}), though high pressure batch studies have been performed on transition metal complexes to extract details of their reduction mechanism.⁹⁵ The effect of increasing pressure and presence of contaminants within a representative natural gas on the polarisation behaviour of the EMAR electrolyte is extracted with CVs in a high pressure cell. Additionally, the kinetic resistance of a sandwich electrode under elevated pressure and additives is probed with electrochemical impedance spectroscopy (EIS) and presented.

Process simulation of EMAR

A number of commercial process simulators are used to model natural gas treating, with Aspen Hysys, Aspen Plus and ProTreat the most common. The

models can be standalone or integrated into a larger model of an entire process facility to reflect a real plant. Aspen HYSYS is well suited to simulating thermal amine systems due to extensive data fitting of kinetic and equilibrium parameters for the most common solvents.⁹⁶⁻⁹⁸ Additional validation studies have been performed to improve the accuracy of process models in LNG service, so as to reflect real plant performance.^{99,100} As EDA is not used by the natural gas industry as a solvent, the kinetic and equilibrium parameters for EDA have not been included into commercial process simulators. Recently a rigorous speciation model was developed to evaluate the energy use of an EMAR cycle applied to PCCC.¹⁰¹ This model, built in MATLAB, is further developed in Chapter 6 to evaluate the performance of the EMAR applied to a natural gas treating facility. The sensitivity of an EMAR cycle to a number of process variables is evaluated and the total energy consumption is ultimately compared with the current state of the art MDEA/PZ simulated in Aspen Hysys V10.

Before the main content of the thesis is explored, the theoretical foundations of the quantum chemical simulations used in Chapter 3 and 4 are presented. Though quantum chemistry is becoming increasingly useful for chemical engineers, it is not commonly taught and so a brief introduction to the concepts and methods is presented in the following chapter.

Chapter 2

Quantum chemistry: an introduction

An introduction to the theoretical methods used in Chapters 3 and 4, which determine the thermodynamics of specific reactions in the EMAR cycle, are described herein. Quantum mechanical (QM) theories have been used to evaluate chemical reactivity and properties since their beginning in the early 20th century. The development of computers and improvements in methods since that time have enabled the wide-spread use of quantum chemistry on many chemical systems. Starting with the Schrödinger equation for a many-electron system, the foundation of some *ab initio* and DFT methods are described. The applications of such methods are generally limited to smaller systems (<1000 atoms) due to the computational expense of the necessary calculations. This chapter is not intended to be an exhaustive review of the methods available, rather just those that pertain to the work presented in this thesis, with recommendations for further reading in text.

2.1 Schrödinger equation

In 1926, Schrödinger published his wave-equation describing the behaviour of electrons, with the example of the hydrogen atom.¹⁰² For a general system, it can be written in terms of the Hamiltonian, \hat{H} , and the wavefunction, Ψ , in equation 2.1, where \hbar is modified Planck's constant ($\hbar = h/2\pi$).

$$\hat{H}\Psi(\vec{r}, t) = i\hbar\frac{\partial\Psi(\vec{r}, t)}{\partial t} \quad (2.1)$$

The Hamiltonian contains the sum of kinetic and potential energy contributions to the system, where the time-independent Hamiltonian for a many-electron, many atom system is expressed in Eqn 2.2, and the associated time-independent Schrödinger equation in Eqn 2.3. This Hamiltonian, includes the kinetic energy of the electrons and nuclei, the attraction between electrons and nuclei, the interelectronic repulsion (electron/electron) and internuclear repulsion (nuclei/nuclei).^{*} Here, i and j run over all electrons, k and l run over all nuclei, m_e is the mass of an electron, m_k the mass of the nucleus, e the charge on an electron, Z the nucleus atomic charge, and ∇^2 the Laplacian operator.

$$\hat{H} = -\sum_i \frac{\hbar^2}{2m_e} \nabla_i^2 - \sum_k \frac{\hbar^2}{2m_k} \nabla_k^2 - \sum_i \sum_k \frac{e^2 Z_k}{r_{ij}} + \sum_{i<j} \frac{e^2}{r_{ij}} + \sum_{k<l} \frac{e^2 Z_k Z_l}{r_{kl}} \quad (2.2)$$

$$\hat{H}\Psi(\vec{r}) = E\Psi(\vec{r}) \quad (2.3)$$

The Hamiltonian can be simplified by invoking the Born-Oppenheimer approximation,¹⁰³ which separates the motion of electrons and nuclei, by determining the wavefunction at fixed nuclei positions. An electronic Hamiltonian, \hat{H}_{el} , can then be written as the sum of the first, third and fourth terms of \hat{H} in Eqn 2.2, and a constant, V_N , due to the internuclear repulsion at the fixed nuclei positions. From this new Hamiltonian, electronic energies are determined for electron coordinates \mathbf{q}_i , and a fixed set of nuclei positions \mathbf{q}_k , as in the eigenvalue,

^{*}Neglecting any external electric or magnetic fields, spin-orbit coupling, or relativistic effects.

eigenfunction equation below:

$$(\hat{H}_{el} + V_N)\psi_{el}(\mathbf{q}_i; \mathbf{q}_k) = E_{el}\psi_{el} \quad (2.4)$$

The subscript el is omitted in the following sections.

In order to solve the above equation for the energies of an atomic system, we must define the nature of the wavefunction, used in *ab initio* theories, or analogously the density, derived from the wavefunction $\rho = |\psi_{el}|^2$, as in DFT, and the Hamiltonian for the many-electron system, as follows.

2.2 *Ab initio* theories

Ab initio, 'from the beginning', methods use various descriptions of the wavefunction and Hamiltonian to solve for the energies of the many-electron system. In general, these theories aim to solve the secular equation, which arises from the selection of a trial wavefunction as a solution to Eqn 2.3. For instance, a trial many-electron wavefunction, ϕ , may be defined as a linear combination of atomic orbital basis functions (e.g. the solutions to the one electron Schrödinger equation), as in Eqn 2.5.*

$$\phi = \sum_{i=1}^N a_i \varphi_i \quad (2.5)$$

From equation 2.3, the energy of the system can be determined as below, where ϕ^* is the complex conjugate of ϕ .

$$E = \frac{\int \phi^* \hat{H} \phi d\mathbf{r}}{\int \phi^* \phi d\mathbf{r}} \quad (2.6)$$

$$= \frac{\int (\sum a_i \varphi_i) \hat{H} (\sum a_j \varphi_j) d\mathbf{r}}{\int (\sum a_i \varphi_i) (\sum a_j \varphi_j) d\mathbf{r}} \quad (2.7)$$

$$= \frac{\sum a_i a_j \int \varphi_i \hat{H} \varphi_j d\mathbf{r}}{\sum a_i a_j \int \varphi_i \varphi_j d\mathbf{r}} \quad (2.8)$$

$$= \frac{\sum a_i a_j H_{ij}}{\sum a_i a_j S_{ij}} \quad (2.9)$$

*This is initially over-simplistic, and is refined in Section 2.2.1.

Here, H_{ij} can be further decomposed into a Coulomb integral and a resonance integral, α_i and β_{ij} , respectively*, and S_{ij} the overlap integral, as the atomic basis functions may not be orthogonal.

Through differentiation of the above, the basis function coefficients a_k that minimise the total energy can be found by solving the set of equations represented in Eqn 2.10, or as a determinant in Eqn 2.11.

$$\sum_{i=1}^N a_i (H_{ki} - ES_{ki}) = 0 \quad (2.10)$$

$$\begin{vmatrix} H_{11} - ES_{11} & H_{12} - ES_{12} & \cdots & H_{1N} - ES_{1N} \\ H_{21} - ES_{21} & H_{22} - ES_{22} & \cdots & H_{2N} - ES_{2N} \\ \vdots & \vdots & \ddots & \vdots \\ H_{N1} - ES_{N1} & H_{N2} - ES_{N2} & \cdots & H_{NN} - ES_{NN} \end{vmatrix} = 0 \quad (2.11)$$

The latter is defined as the secular equations, the solution of which has N roots (due to N basis functions employed) of E, which represent the energies of the molecular orbitals formed as linear combinations of atomic orbital basis functions. Unfortunately, the many-electron wavefunction cannot be accurately represented as a linear combination of one or two electron atomic basis functions. It is more accurately represented as a determinant, as is used in the Hartree-Fock (HF) approach.

2.2.1 Hartree-Fock approach

In the HF approach, a single electron operator is defined, h_i in Eqn 2.12, which is used to solve a set one electron Schrödinger equations. This one electron

*In bra-ket notation:

$$\alpha_i = \langle \varphi_i | \hat{H} | \varphi_i \rangle = \int \varphi_i (\hat{H} \varphi_i) d\mathbf{r}$$

$$\beta_{ij} = \langle \varphi_i | \hat{H} | \varphi_j \rangle = \int \varphi_i (\hat{H} \varphi_j) d\mathbf{r}$$

operator includes the electron kinetic energy, the nuclear attraction term and a potential $V_i\{j\}$, which accounts for the electron-electron repulsion, determined as an average due to all electrons present, in Eqn. 2.13.

$$h_i = -\frac{1}{2}\nabla_i^2 - \sum_{k=1}^M \frac{Z_k}{r_{ik}} + V_i\{j\} \quad (2.12)$$

$$V_i\{j\} = \sum_{j \neq i} \int \frac{\rho_j}{r_{ij}} d\mathbf{r} \quad (2.13)$$

To account for electron spin and the Pauli exclusion principle,* the wavefunction is approximated as a Slater determinant, represented in Eqn 2.14. Each element of the matrix is a one-electron spin orbital represented by χ , where electrons are of α or β spin (with angular momentum $\pm\hbar/2$). The prefactor in Eqn. 2.14 is the normalisation constant, necessary to ensure that $|\Psi_{SD}|^2 = 1$.

$$\Psi_{SD} = \frac{1}{\sqrt{N!}} \begin{vmatrix} \chi_1(1) & \chi_2(1) & \cdots & \chi_N(1) \\ \chi_1(2) & \chi_2(2) & \cdots & \chi_N(2) \\ \vdots & \vdots & \ddots & \vdots \\ \chi_1(N) & \chi_2(N) & \cdots & \chi_N(N) \end{vmatrix} \quad (2.14)$$

Hartree¹⁰⁴ defined a self-consistent field (SCF) procedure where the initial potential $V_i\{j\}$ was determined from a guess wavefunction, which was subsequently improved with each iteration as the density, ρ , and potential, $V_i\{j\}$, were refined until the difference between orbital energies of previous iterations were within some tolerance, and therefore self-consistent. While Hartree¹⁰⁴ applied the procedure to atoms, Roothaan¹⁰⁵ extended the procedure to molecules where molecular orbitals (MOs) are formed from a set of basis functions. In the simplest implementation, each pair of electrons occupy a two electron orbital, and are paired - this is know as restricted Hartree-Fock (RHF). Here a similar one electron Hamiltonian is defined in Eqn 2.15. When basis functions are incorporated (represented by Greek letters), the Fock operator is defined as in Eqn. 2.17.

*The wavefunction is antisymmetric - it must change sign when the coordinates of two electrons are exchanged.

This enters into the secular equation in Eqn 2.16 (defined previously in Eqn 2.11), with the same definition for orbital overlap, S_{ij} . The solution of this equation yields the energy of basis functions used in representing the wavefunction.

$$f_i = -\frac{1}{2}\nabla_i^2 - \sum_k^{nuclei} +V_i^{RHF}\{j\} \quad (2.15)$$

$$\begin{vmatrix} F_{11} - ES_{11} & F_{12} - ES_{12} & \cdots & F_{1N} - ES_{1N} \\ F_{21} - ES_{21} & F_{22} - ES_{22} & \cdots & F_{2N} - ES_{2N} \\ \vdots & \vdots & \ddots & \vdots \\ F_{N1} - ES_{N1} & F_{N2} - ES_{N2} & \cdots & F_{NN} - ES_{NN} \end{vmatrix} = 0 \quad (2.16)$$

$$F_{\mu\nu} = \left\langle \mu \left| -\frac{1}{2}\nabla^2 \right| \nu \right\rangle - \sum_k^{nuclei} Z_k \left\langle \mu \left| \frac{1}{r_k} \right| \nu \right\rangle + \sum_{\lambda\sigma} P_{\lambda\sigma} \left[(\mu\nu|\lambda\sigma) - \frac{1}{2}(\mu\lambda|\nu\sigma) \right] \quad (2.17)$$

$$P_{\lambda\sigma} = 2 \sum_i^{occupied} a_{\lambda i} a_{\sigma i} \quad (2.18)$$

All terms in equation Eqn 2.17 use the bra-ket compact notation.* The first two terms are the electron kinetic energy and nuclear repulsion energy. The last bracketed term captures the Coulomb and exchange (when electrons of the same spin switch orbitals) energy. The density matrix P , determines the significance of the basis functions in the many-electron wave function and the coefficients $a_{\zeta i}$ specify the contribution to the MO. A similar procedure is used when separate basis functions are defined for individual electron spin orbitals, known as unrestricted Hartree-Fock (UHF). In UHF, a separate density matrix, $P_{\lambda\sigma}$, exists for both α and β electron spins.

*

$$\begin{aligned} \langle \mu | g | \nu \rangle &= \int \phi_\mu (g \phi_\nu) d\mathbf{r} \\ (\mu\nu|\lambda\sigma) &= \iint \phi_\mu(1)\phi_\nu(1) \frac{1}{r_{12}} \phi_\lambda(2)\phi_\sigma(2) d\mathbf{r}(1)d\mathbf{r}(2) \end{aligned}$$

The maximum computational cost of HF approaches scales with N^4 due to the two electron integrals in the Fock operator. Since HF methods determine the interelectronic repulsion (Coulomb and exchange) as the sum of single electrons interacting with an average potential of the remaining $N - 1$ electrons, $V_i\{j\}$, their correlated behaviour is not captured and therefore accurate ground state energies cannot be obtained. The difference between the HF limit (in an infinite basis set) and the exact energy, is defined as the correlation energy, represented in Eqn 2.19.

$$E_{corr} = E - E_{HF} \quad (2.19)$$

Electron correlation can be captured by including additional configurations (as Slater determinants) in the description of the wavefunction. The exact energy can be attained through application of the full configuration interaction (CI) method, which defines the wavefunction as a linear combination of all possible excitations of a HF reference wavefunction, as in 2.20.

$$\Psi = a_0\Psi_{HF} + \sum_i^{occ.} \sum_r^{vir.} a_i^r \Psi_i^r + \sum_{i<j}^{occ.} \sum_{r<s}^{vir.} a_{ij}^{rs} \Psi_{ij}^{rs} + \dots \quad (2.20)$$

Here, i and j are the indexes of occupied MOs, and r and s indexes of virtual (or unoccupied) MOs, and a are coefficients that account for the normalisation and relative weighting of the state.

Full CI is rarely performed for all but the smallest molecules (or with a small number of basis functions) due to the extreme computational cost. To achieve reasonable accuracy at a lower computational cost, the above series (or one similar) is often truncated after the second or third term, which corresponds to the inclusion of all single excitations, and all double excitations, respectively. This is employed in the CCSD(T) method, described next, often called the ‘gold standard’ in quantum chemistry (at the extrapolated basis set limit).

2.2.2 Coupled cluster theory

The coupled cluster (CC) method, developed by Čížek¹⁰⁶, defines the wavefunction as a product of e^T , and a reference wavefunction (here Ψ_{HF}), shown in

Eqn 2.21. Here, \mathbf{T} is the excitation operator (Eqn 2.22) that promotes electrons from occupied to virtual MOs. Terms \mathbf{T}_1 and \mathbf{T}_2 are shown in Eqn 2.23 and are analogous to the prefactors in the second and third terms of Eqn 2.20.

$$\Psi = e^{\mathbf{T}}\Psi_{HF} \quad (2.21)$$

$$\mathbf{T} = \mathbf{T}_1 + \mathbf{T}_2 + \mathbf{T}_3 + \dots + \mathbf{T}_n \quad (2.22)$$

$$\mathbf{T}_1 = \sum_i^{\text{occ.}} \sum_a^{\text{vir.}} t_i^a \Psi_i^a \quad \mathbf{T}_2 = \sum_{i<j}^{\text{occ.}} \sum_{a<b}^{\text{vir.}} t_{ij}^{ab} \Psi_{ij}^{ab} \quad (2.23)$$

The exponential of \mathbf{T} is written as a Taylor series expansion, in 2.24, and expanded into individual operators \mathbf{T}_n in 2.25. The product of two excitation operators, $\mathbf{T}_2\mathbf{T}_1$ for example, yields a triple excitation of the reference wavefunction, and are called ‘disconnected’, where the \mathbf{T}_3 operator alone results in ‘connected’ triples excitations.

$$e^{\mathbf{T}} = 1 + \mathbf{T} + \frac{\mathbf{T}^2}{2!} + \frac{\mathbf{T}^3}{3!} + \dots = \sum_{k=0}^{\infty} \frac{\mathbf{T}^k}{k!} \quad (2.24)$$

$$e^{\mathbf{T}} = 1 + \mathbf{T}_1 + (\mathbf{T}_2 + \frac{1}{2}\mathbf{T}_1^2) + (\mathbf{T}_3 + \mathbf{T}_2\mathbf{T}_1 + \frac{1}{6}\mathbf{T}_1^3) + (\mathbf{T}_4 + \mathbf{T}_3\mathbf{T}_1 + \frac{1}{2}\mathbf{T}_2^2 + \frac{1}{2}\mathbf{T}_2\mathbf{T}_1^2 + \frac{1}{24}\mathbf{T}_1^4) + \dots \quad (2.25)$$

At an appropriate truncation of the series, the individual cluster amplitudes, $t_i^a, t_{ij}^{ab}, \dots$ are solved for via an iterative procedure. The series is often truncated to include partial (or linearised) triples, where Trucks et al.¹⁰⁷ defined the popular CCSD(T) method.* This method, often called the ‘gold standard’ in quantum chemistry, recovers 99.99% of the correlation energy against a CCSDTQ reference.¹⁰⁸ This accuracy comes at cost of increased computational requirements, with the CCSD method ($\mathbf{T} \approx \mathbf{T}_1 + \mathbf{T}_2$) scaling with N^6 and CCSD(T) with N^7 . The CCSD(T) method is used in this thesis to determine the relative energy of a number of molecular species, though the molecular structure that the CCSD(T) energy is calculated for is arrived at via DFT, covered next.

*Where the S in the method name indicates single excitation by \mathbf{T}_1 , D, doubles excitation by \mathbf{T}_2 , T, triples excitation by \mathbf{T}_3 and so on. T is in parenthesis due to the incomplete treatment of triples excitation.

2.3 Density functional theory

The foundation of DFT, put forth by Hohenberg and Kohn¹⁰⁹ and Kohn and Sham¹¹⁰, states that the ground state energy of a system is a unique functional of the electronic density, and it may be represented by a wavefunction that satisfies Eqn 2.26, where the electronic density of the system depends on the positions of all electrons and nuclei and is determined by the product of the wavefunction with its' complex conjugate, $\rho(\mathbf{r}) = |\Psi\Psi^*|$. The first three contributions to the total energy in Eqn 2.26, are the kinetic energy, nuclear attraction and electronic repulsion potentials for all electrons, where electronic repulsion is due to the interaction with the density. The last two terms are then the correction to the kinetic and electron-electron repulsion energy due to their interaction. Expanded in 2.27, the non-interacting electron kinetic and potential energy are summed, and the last two terms of Eqn 2.26 are combined into, E_{xc} , known as the electron-correlation energy.

$$E[\rho(\mathbf{r})] = T_{ni}[\rho(\mathbf{r})] + V_{ne}[\rho(\mathbf{r})] + V_{ee}[\rho(\mathbf{r})] + \Delta T[\rho(\mathbf{r})] + \Delta V_{ee}[\rho(\mathbf{r})] \quad (2.26)$$

$$E[\rho(\mathbf{r})] = \sum_i^N \left(\left\langle \chi_i \left| -\frac{1}{2}\nabla_i^2 \right| \chi_i \right\rangle - \left\langle \chi_i \left| \sum_k^{nuclei} \frac{Z_k}{|\mathbf{r}_i - \mathbf{r}_k|} \right| \chi_i \right\rangle \right) + \sum_i^N \left\langle \chi_i \left| \frac{1}{2} \int \frac{\rho(\mathbf{r}')}{|\mathbf{r} - \mathbf{r}'|} d\mathbf{r}' \right| \chi_i \right\rangle + E_{xc}[\rho(\mathbf{r})] \quad (2.27)$$

In Eqn 2.27, χ_i are electron orbitals which satisfy $h_i^{KS}\chi_i = \varepsilon_i\chi_i$, where h_i^{KS} is the one electron Kohn-Sham (KS) Hamiltonian defined in 2.28, and ε_i is the energy (eigenvalue) of the electron orbital.

$$h_i^{KS} = -\frac{1}{2}\nabla_i^2 - \sum_k^{nuclei} \frac{Z_k}{|\mathbf{r}_i - \mathbf{r}_k|} + \int \frac{\rho(\mathbf{r}')}{|\mathbf{r}_i - \mathbf{r}'|} d\mathbf{r}' + V_{xc} \quad (2.28)$$

$$V_{xc} = \frac{\delta E_{xc}}{\delta \rho} \quad (2.29)$$

If, as in the RHF formalism, electrons occupy orbitals which are a linear combination of basis functions (again denoted by Greek letters, which form KS

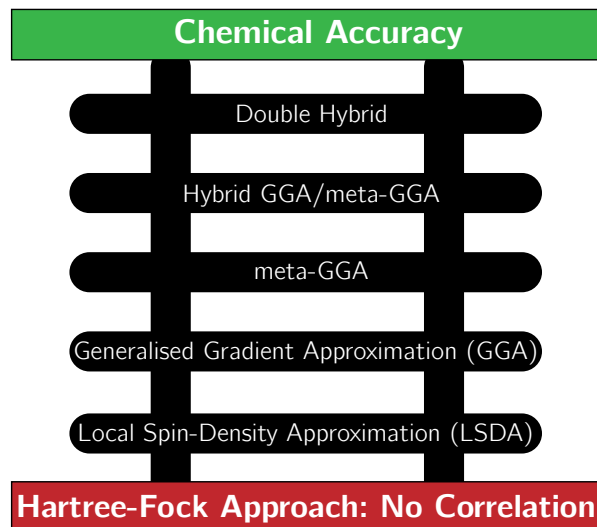


Figure 2-1: Jacob's ladder of functional accuracy,¹¹¹ where ascension progresses to chemical accuracy.

orbitals), then the KS operator (analogous to the Fock operator in Eqn 2.17) can be written as:

$$H_{\mu\nu}^{KS} = \left\langle \mu \left| -\frac{1}{2}\nabla^2 - \sum_k^{\text{nuclei}} \frac{Z_k}{|\mathbf{r} - \mathbf{r}_k|} + \int \frac{\rho(\mathbf{r}')}{|\mathbf{r} - \mathbf{r}'|} d\mathbf{r}' + V_{xc} \right| \nu \right\rangle \quad (2.30)$$

The issue, however, lies in the definition of the exchange-correlation energy (or potential), for which no exact functional form exists in general. A significant number of xc functionals have been developed since KS introduced the formalism, the development of which has loosely followed the 'Jacobs's ladder' towards chemical accuracy, outlined by Perdew and Schmidt¹¹¹, shown in Figure 2-1.

The lowest rung on the ladder is the situation described by HF methods, where no correlation is accounted for. Each rung up the ladder includes contributions to the xc functional that should theoretically improve its' accuracy, up to within 1 kcal/mol of experimental values, or 'chemical accuracy'. In rung one, the xc energy depends only on the local electron spin density (the local spin density approximation (LSDA)), derived from a uniform electron gas. This does not account for any inhomogeneities in the density and is often improved by con-

sidering the local gradient of the density, $\nabla\rho(\mathbf{r})$, which constitutes the second rung - generalised gradient approximation (GGA). In rung three, meta-GGAs (mGGAs) go further and include terms that depend on the Laplacian of the density, $\nabla^2\rho(\mathbf{r})$, and/or the kinetic energy density, $\tau = \sum_i |\nabla\chi_i|^2$. Functionals can be further improved by considering non-local effects by including a proportion of the HF exchange energy in their makeup, and are thus denoted ‘Hybrid’ functionals. The last rung on the ladder ‘Double Hybrid’ includes contributions of perturbation theory corrections to the Kohn-Sham energy. Mardirossian and Head-Gordon¹¹² provides a substantive review of functional development over the last 30 years, and Goerigk et al.¹¹³ and Chan et al.¹¹⁴ assess the performance of various functionals on the ladder.

One of the most ubiquitous functionals in the literature is the B3LYP x_c functional, that is, the Becke three parameter Lee-Yang-Parr functional.^{115–118} B3LYP, a Hybrid-GGA, appears on the fourth rung of the ladder; its’ individual contributions are represented in Eqn 2.31.

$$E_{xc}^{B3LYP} = (1 - a)E_x^{LSDA} + aE_x^{HF} + b\Delta E_x^B + (1 - c)E_c^{LSDA} + cE_c^{LYP} \quad (2.31)$$

Where $a = 0.20$, $b = 0.72$, and $c = 0.81$, E_x^{HF} is the exchange (fourth) term in the Fock operator (in Eqn. 2.17). The inclusion of E_x^{HF} arises from the adiabatic connection method, which states the exact solution for E_{xc} of a non-interacting KS system is E_x^{HF} , and the difference between the non-interacting and fully interacting system is given by E_{xc}^{DFT} , represented in Eqn 2.32. For the B3LYP functional, the exchange and correlation parts of E_{xc}^{DFT} have been separated.

$$E_{xc} = (1 - a)E_{xc}^{DFT} + aE_x^{HF} \quad (2.32)$$

Though B3LYP has been popular, it is not appropriate in all scenarios and, like most GGA and mGGAs, fails to account for long-range dynamical correlation (dispersion). This can, in part, be corrected for by including the dispersion contributions put forward by Grimme and co-workers,^{119–122} which take the form

of Eqn 2.33, and are added to the KS energy.

$$E_{disp}^{DFT-D\#} = - \sum_{A<B} \sum_{n=6,8,..} s_n \frac{C_n^{AB}}{R_{AB}^n} f_{damp,n}(R_{AB}) \quad (2.33)$$

The dispersion correction is a sum across all atoms, where the index n and damping function $f_{damp,n}$ depend on the specific DFT-D# method, and coefficients s_n depend on the functional used. The coefficients, C_n^{AB} , are determined from the van der Waals radii of the atoms present.

DFT methods formally scale with N^3 , though successive inclusion of the contributions within the rungs of ‘Jacobs ladder’, and non-local effects increase the computational cost. They are still, however, less costly than the ‘chemically accurate’ *ab initio* methods, such as CCSD(T). Therefore this thesis employs DFT methods to determine the geometry and energy of species under investigation, with more accurate methods used to re-evaluate the energy.

2.4 Basis sets

As mentioned above, MOs or KS orbitals (ϕ_i) are formed from a linear combination of basis functions, Φ_μ , as below (Eqn 2.34):

$$\phi_i = \sum_{\mu} c_{\mu} \Phi_{\mu} \quad (2.34)$$

These basis functions are (often) atom-centred and similar in nature to those obtained from the solution to the one-electron Schrödinger equation, that is, the hydrogenic atomic orbitals (HAOs). Slater-type orbitals (STOs), introduced by Slater¹²³ and Zener¹²⁴, were simpler than HAOs though retained the same characteristic radial decay, e^{-r} , and were intended for use in multi-electron atoms. The absence of an analytical solution to the four index integrals in the Fock operator (Eqn 2.17), however, presented an issue. Gaussian-type orbitals (GTOs) were introduced by Boys¹²⁵ to overcome this problem, by using Gaussian functions to describe the radial dependence of the atomic orbital i.e. $e^{-\alpha r^2}$. A linear series of GTOs (known as contracted Gaussians), with various weightings and exponential

coefficients, is necessary to achieve the radial decay of STOs. Though this increases the number of integrals, it reduces the complexity and permits analytical evaluation. A number of families of GTOs are available in literature, the most widely used are those of Pople and Dunning, both of which are used in this thesis. To improve the flexibility and chemical accuracy of the constructed MOs, basis sets will often define multiple 'shells' for the valence orbitals. This is referred to as 'split valence', where for instance the Pople type double zeta split valence basis set, 6-31G, employs six (6) Gaussians for core orbitals, three (3) Gaussians for the inner valence orbital 'shell' and one (1) Gaussian for the outer valence orbital 'shell'. This is then extended in triple and quadruple zeta (and so on) split valence basis sets to include three and four, respectively, shells in the valence orbitals. Additionally, polarisation (of higher angular momentum than the valence orbitals) and diffuse (low α values) functions provide additional flexibility and are often necessary to yield accurate ground state geometries.¹²⁶ To reduce the number of basis functions necessary at higher atomic numbers and account for core electron relativistic effects, effective core potentials (ECPs) are used which replace core electrons with a potential that represents the combined interaction between the nuclear-electronic core and the remaining electrons. In this work, the Los Alamos National Lab ECPs,¹²⁷⁻¹²⁹ are used for the core electrons of copper, to reduce the computational cost.

Though increasing the number of basis functions improves the description of the MOs or KS orbitals, it can significantly increase the computational cost. In this work, a balance of cost and accuracy is achieved using polarised and diffuse double and triple zeta split valence basis sets of Pople¹³⁰⁻¹³³, and Dunning¹³⁴.

2.5 Solvation models

Accurate determination of the free energy of solvation for a species is necessary to determine aqueous phase reaction energies and resulting equilibrium constants. The free energy of solvation, the change in free energy of a species A leaving the gas phase and entering a liquid or fluid phase, can be approximated computationally. The solvent can either be represented in the simulation explicitly (and treated with the same electronic structure method or a simpler classical method)

or it can be represented as a dielectric continuum. The former method requires consideration of the number of solvent molecules to include, in what configuration and whether they should be treated classically or otherwise. The latter (treatment by a continuum) is more attractive as there is no need to explicitly define the solvent molecules, and therefore no sampling of the configuration space is necessary. The continuum approach considers the solvent as a uniform polarisable medium with a constant dielectric constant, ϵ . Here, the free energy of solvation ΔG_{solv} , is equal to the sum of the free energy required to form the cavity for the solute, ΔG_{cavity} , the dispersion forces between the solute and solvent, ΔG_{disp} , and an electrostatic component, ΔG_{elec} . Cavitation and dispersion contributions are often (though depending on the specific continuum model) taken as proportional to the solvent accessible surface (SAS), inside which the cavity for the solute is formed. The SAS is usually formed from the overlapping van der Waals radii of the solute atoms (or a proportion thereof), and smoothed to avoid cusps and regions where the solvent cannot approach (again depending on the specifics of the continuum model). The electrostatic component of the free energy is determined as:

$$\Delta G_{elec} = \frac{1}{2} \int \rho(\mathbf{r})\phi(\mathbf{r})_{reac}d\mathbf{r} \quad (2.35)$$

Where $\rho(\mathbf{r})$ is the charge density inside the solute cavity (determined from *ab initio* or DFT methods) and $\phi(\mathbf{r})_{reac}$ is the reaction field, that is the difference between the electric field when the solute is present in the solvent or in vacuum, $\phi_{reac} = \phi_{solvent} - \phi_{vacuum}$.

As the solute polarises the solvent and vice-versa, a self-consistent procedure is used to determine the solute density and the reaction electric field. An additional term, ϕ_{σ} , is added to the Hamiltonian operator (of the electronic structure method used) which represents the surface charges at the solute cavity, and are determined from the Poisson-Boltzmann equation. This is called a self-consistent reaction field (SCRF) method, because the density of the solute is consistent with the electric field developed by the surrounding solvent. The solvation models used in this thesis are COSMO,¹³⁵ and SMD,¹³⁶ both of which employ the SCRF method to determine the electrostatic component of the free energy of solvation. The SMD model was trained against a large dataset to reproduce experimental

solvation free energies,¹³⁶ while COSMO uses empirical relations to determine the non-electrostatic components of the solvation free energy.¹³⁵

Chapter 3

Ethylenediamine with Natural Gas Contaminants

The compounds CO_2 , H_2S , CH_3SH , COS , CS_2 found in natural gas are often removed by contact and reaction with aqueous solutions of amines. The primary amine under investigation, EDA, is the most chemically suited to the electrochemical regeneration process which was first examined by Stern³⁷. This chapter examines the mechanism of reactive absorption of the aforementioned acid gas contaminants found in natural gas to ethylenediamine. The binding in gas phase is first estimated with extension to the aqueous phase by solvation calculations. The binding in the aqueous phase is examined in more depth and the transition states involved in the reactive absorption process identified. The activation energy barrier is determined for each of the contaminants, as well as the relative energies of products relative to the isolated reactants. The pK_a of a number reaction products is estimated to characterise their acidity and potential for further interaction with aqueous species present. Limited interactions of reaction products are examined and lastly the effect of explicitly including the solvent in estimating acid gas absorption is considered.

3.1 Methods

Initial conformers of isolated and interacting species were generated with the MMFF94 forcefield implemented in Avogadro.¹³⁷ NWChem was used for all quantum chemical calculations.¹³⁸ Gas phase interactions presented in Section 3.2.1 are generated via DFT with the reasonably accurate hybrid functional, B3LYP (Becke three parameter Lee Yang Parr) functional,^{113,115–118} DFT-D3 dispersion corrections,¹²¹ the aug-cc-pVDZ basis set,¹³⁴ and the SMD solvent model¹³⁶ for single point solvation calculations. The B3LYP-D3/aug-cc-pvdz combination has been shown to generate equilibrium structures of van der Waals complexes with small least root-mean-square displacements compared to the CCSD(T)/CBS reference method.¹³⁹

Barrier heights, relative energies of reactants, transition states and products were estimated in aqueous solution with geometries generated in the presence of the SMD SCRF solvation model at the B3LYP-D3/aug-cc-pvdz level of theory. Further electronic energies were calculated by the coupled cluster method with single, double and perturbative triple excitations,¹⁰⁷ at the same geometry and with the same basis set, i.e. CCSD(T)/aug-cc-pvdz, as B3LYP has been demonstrated to underestimate barrier heights,^{140,141} and overestimate the relative energy of reaction intermediates.¹⁴² Where multiple transition states were found, the lowest energy structure was used to estimate the barrier height. Ground state and transition state (TS) geometries were confirmed to be a local minimum or saddle point, respectively, on the potential energy surface (PES) by examining the Hessian eigenvalues, where all are positive or one is negative, again respectively. Thermal enthalpy corrections, entropic contributions and single point solvation calculations at optimised SMD/B3LYP-D3/aug-cc-pvdz geometries (where “SMD/” indicates the structure was optimised in the presence of the SMD SCRF solvent model) were combined with CCSD(T) electronic energies to determine the species or complex enthalpy (Eqn 3.1) and free energy (Eqn 3.2). Basis set superposition error was also corrected for with the counterpoise method at the relevant computational level.

Gas phase reaction enthalpy is given by Eqn 3.3, and aqueous phase free energy by Eqn 3.4. Calculation of the aqueous reaction free energy requires each

species to be at 1 mol/L, the same as the solvation free energy calculations, with the following correction $\Delta G^{\circ \rightarrow *}$, from 1 mol of an ideal gas at 1 atm (V_0) to 1 M (V^*) in solution (Eqn 3.5).¹⁴³

$$H = E_0^{CCSD(T)} + E_{BSSSE}^{CCSD(T)} + E_{ZPE} + E_{Therm} \quad (3.1)$$

$$G = E_0^{CCSD(T)} + E_{BSSSE}^{CCSD(T)} + E_{ZPE} + E_{Therm} + \Delta G_{solv}^* - T \times S_{vib,rot,trans} \quad (3.2)$$

$$\Delta H_{reaction} = \Sigma H_{products} - \Sigma H_{reactants} \quad (3.3)$$

$$\Delta G_{reaction} = \Sigma G_{products} - \Sigma G_{reactants} \quad (3.4)$$

$$\Delta G^{\circ \rightarrow *} = -T \Delta S^{\circ \rightarrow *} = RT \ln(V_0/V^*) = RT \ln(24.26) = 1.89 \text{ kcal/mol} \quad (3.5)$$

Unless otherwise stated, the reaction free energy and activation barrier is calculated with the free energy of the isolated species at the optimised conformer closest to that in the complex. Further interactions in Section 3.2.3 were obtained at the SMD/B3LYP/X, where X is either 6-31+G* or 6-31G*, where the former is used when anionic species are present. The explicit water structures in Section 3.2.4 were determined at the B3LYP/6-31G* level of theory with single point SMD solvation calculations and application of the thermodynamic cycle below (Figure 3-1) to determine the aqueous reaction free energy.

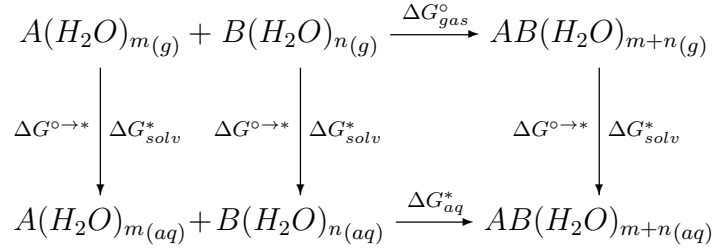


Figure 3-1: Thermodynamic cycle to determine the aqueous free energy of reaction between solvated species A and B , with m and n explicit water molecules, respectively, to form solvated complex AB with $(m + n)$ water molecules.

ΔG_{aq}^* is calculated in Eqn 3.8, where $G_{gas}^{\circ,i}$ is the standard gas phase free energy of species i (Eqn. 3.8, v_i is the stoichiometric coefficient, and $\Delta G_{solv}^{*,i}$ is the solvation free energy of that species at the gas phase geometry.

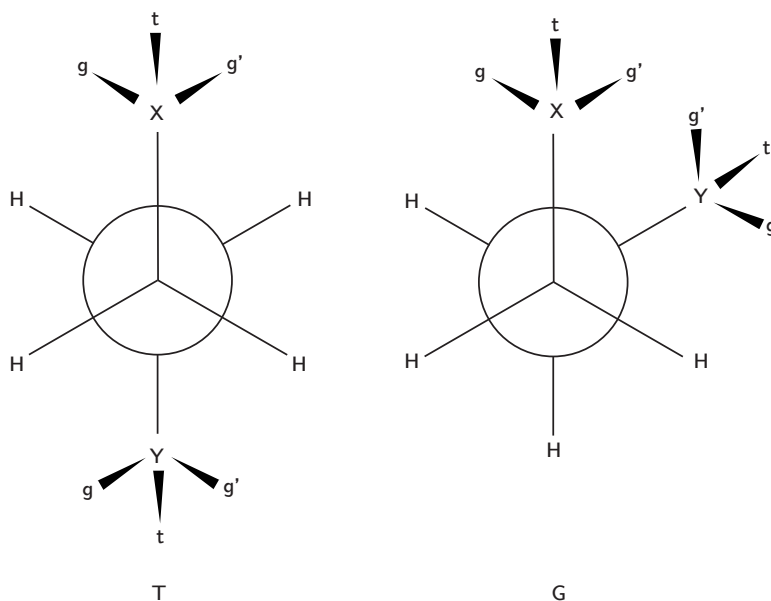


Figure 3-2: Ethylenediamine conformer notation. X and Y represent amino groups terminating the alkane chain. In the neutral form of EDA g, g' and t represent the possible positions of the lone pair of electrons on each nitrogen atom. Trans (T) structure on the left, gauche (G) on the right.

$$G_{gas}^{o,i} = E_0 + E_{BSSE} + E_{ZPE} + E_{Therm} - T \times S_{vib,rot,trans} \quad (3.6)$$

$$G_{aq}^{*,i} = G_{gas}^{o,i} - \Delta G^{o \rightarrow * } + \Delta G_{solv}^{*,i} \quad (3.7)$$

$$\Delta G_{aq}^* = \sum_i v_i G_{aq}^{*,i} \quad (3.8)$$

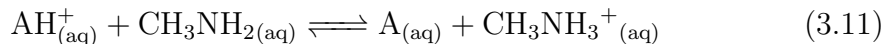
The notation for conformers of EDA and derivatives follows that of Radom et al.¹⁴⁴ presented in Figure 3-2 where the g, t and g' label refers to the position of the lone pair of electrons on the nitrogen atom at positions X and Y.

Species pK_a was estimated with the direct method Eqn. 3.9, where the free energy of $H_{(aq)}^+$ is taken as -6.28 kcal/mol,¹⁴⁵ and its solvation free energy as -265.9 kcal/mol,¹⁴⁶ where the pK_a is given by Eqn. 3.10; and the proton exchange (PEX) method with methylamine as a reference acid, Eqn. 3.11, and pK_a given by Eqn. 3.12. Methylamine was chosen for its simplicity and chemical similarity to EDA. All pK_a calculations were performed with CCSD(T)/aug-cc-pvdz energies

at SMD/B3LYP-D3/aug-cc-pvdz geometries.



$$pK_a = \frac{\Delta G_{aq}^*}{RT \ln(10)} \quad (3.10)$$



$$pK_a = \frac{\Delta G_{aq}^*}{RT \ln(10)} + pK_a(\text{CH}_3\text{NH}_3^+) \quad (3.12)$$

All images of molecular conformers were generated with Chemcraft,¹⁴⁷ using the Gaussview colour scheme: hydrogen - light grey; carbon - dark grey; nitrogen - blue; oxygen - red; sulfur - yellow.

3.2 Results and Discussion

3.2.1 Preliminary gas phase results

Interaction between EDA and acid gas contaminants was first examined with gas phase DFT. The lowest energy conformers of each interaction pair are shown in Figure 3-3 with reaction energies summarised in Table 3.1. In each complex, EDA prefers the gauche form, tGg' with H₂S and CH₃SH and gGg with COS, CO₂ and CS₂. In isolation EDA will preferentially form an intramolecular hydrogen bond (as tGg' or gGg') which is disrupted by the presence of the absorbate resulting in thermodynamically unfavourable complexes^{144,148-150}. The increasing trend in gas phase reaction free energy, H₂S < CO₂ < CH₃SH < COS < CS₂, follows that of weakening dipole moment and shielding of the partial positive charge on the carbon centre. In moving from H₂S to CH₃SH, the loss in dipole by substitution of a methyl group reduces the interaction energy and increases the distance between amino and SH groups from 2.041 Å to 2.399 Å.

Although the Mulliken partial charge on the central carbon increases moving through CO₂, COS, to CS₂ from +0.17, +0.44 to +1.60, it is shielded from the amine by the attached sulfur increasing the interaction distance from 2.857 Å to 3.124 Å to 3.429 Å, respectively, reducing the binding energy. Negligible difference in the binding energy is observed for COS when oxygen and sulfur exchange

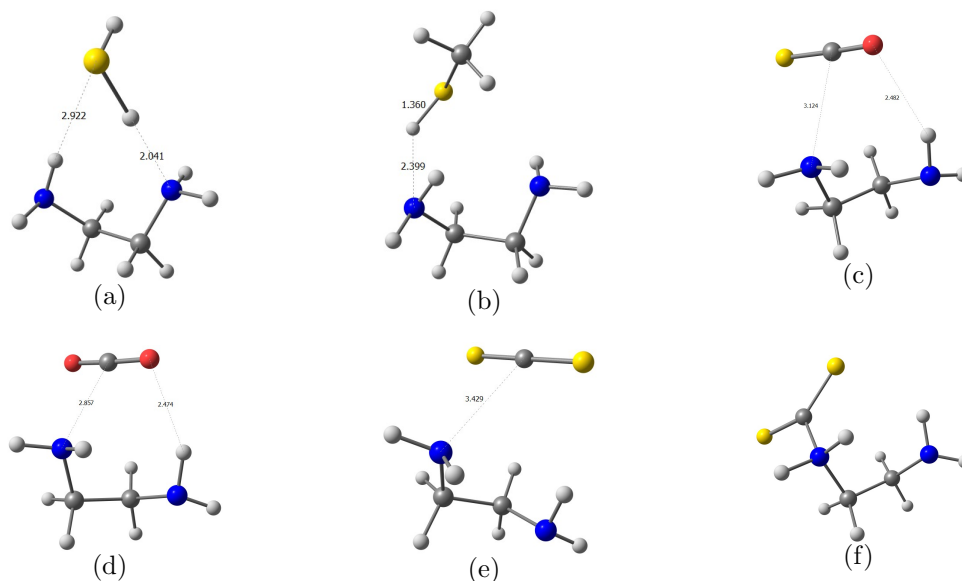


Figure 3-3: Structures of EDA with (a) H_2S (b) CH_3SH and (c) COS (d) CO_2 (e) CS_2 (f) CS_2 bound as a stable zwitterion. Distances show in Angstroms (\AA). See Section 3.1 for colour scheme.

positions as the majority of the binding energy is due to electrostatic interaction between the central carbon and the amino group lone pair. Additionally, initial geometries of gas phase zwitterions of CO_2 , COS and CS_2 were optimised, where only that of CS_2 was stable, see 3-3(f), as the positive quaternary amine is stabilised by through bond charge transfer of sulfur electron density. Those of CO_2 and COS dissociated into similar complexes to those presented previously.

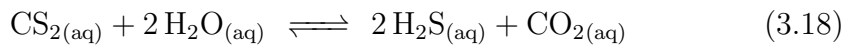
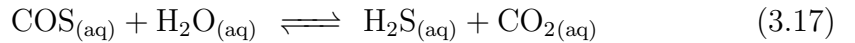
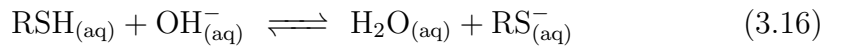
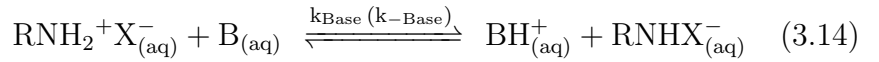
The reaction free energy of the complex formation displays a similar trend when solvation contributions are included, though formation of the CS_2 zwitterion is heavily stabilised by the solvent, only 1.3 kcal above the complex. Though interaction is generally unfavourable in gas phase (or at gas phase geometries with solvent contributions), the shapes of the potential energy surfaces shift upon solvation, stabilising reaction intermediates and permitting additional hydrolysis reactions that promote acid gas absorption, which are covered next.

Table 3.1: Reaction enthalpy and free energy of acid gas interaction with EDA (kcal/mol)

Absorbate	ΔH_{gas}	ΔG_{gas}	ΔG_{aq}
H ₂ S	-4.0	2.9	2.3
CH ₃ SH	-3.8	5.4	6.8
CS ₂	-1.4	5.8	5.4
COS	-2.3	5.5	5.3
CO ₂	-3.6	3.6	3.7
CS ₂ bound	7.9	18.9	6.7

3.2.2 Aqueous phase results

Absorption in aqueous solution occurs either by hydrolysis or direct interaction with EDA. H₂S and CH₃SH are absorbed via proton transfer to EDA or water (Eqn. 3.15, 3.16) while the electrophilic species (X) CO₂, COS and CS₂ will react directly with the amine to form a zwitterion (Eqn. 3.13) which is subsequently deprotonated to a nearby base (B) (Eqn. 3.14),^{151,152} or hydrolyse with water to produce CO₂ and H₂S (Eqn. 3.17, 3.18), carbonic acid, bicarbonate or carbonates depending on solution pH.



Using the steady state approximation, the zwitterion (RNH₂⁺X⁻) concentration can be approximated by Eqn 3.20 and the depletion of species X expressed by Eqn 3.21 and simplified in Eqn 3.22, where hydrolysis of X is not considered as

it does not significantly impact the reaction rate.

$$[zwitterion] = \frac{k_2[X][RNH_2]}{k_{-1}} + \sum k_{Base}[B] \quad (3.20)$$

$$-r_X = k_2[X][RNH_2] - k_{-1}[zwitterion] \quad (3.21)$$

$$-r_X = \frac{[X][RNH_2]}{1/k_3[B] + 1/k_2} \text{ where } k_3 = \frac{k_2 k_{Base}}{k_{-1}} \quad (3.22)$$

The rate constants for zwitterion formation of EDA with CO₂ and COS, and their deprotonation to amine or water have been experimentally determined by a conductimetric stopped flow technique.^{153,154} The activation energy for k_2 , in the Arrhenius relation Eqn 3.23, was estimated at $E_a = 12.08$ kcal/mol for the EDA-CO₂ system,¹⁵³ though is not available for sulfur-containing species COS and CS₂. For both COS and CO₂, formation of the zwitterion intermediate was found to be rate limiting, i.e. $k_2 \ll k_3[B]$.

$$k_2 = Ae^{-E_a/RT} \quad (3.23)$$

Here the activation free energies in forming zwitterions of CO₂, COS and CS₂ are calculated and compared to assess the reactivity trend when oxygen is replaced by sulfur. The Eyring Equation, Eqn 3.24,¹⁵⁵ is fitted against experimental data, where available, to directly compare against the computational result.

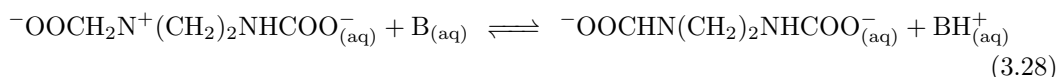
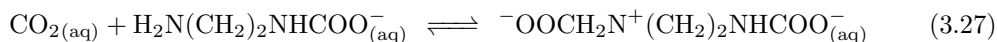
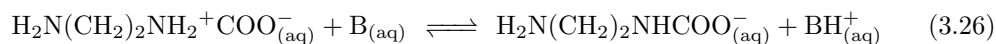
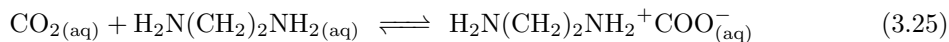
$$k = \kappa \frac{k_B T}{h} e^{-\Delta G^\ddagger/RT} \quad (3.24)$$

Additionally, since experimental evidence exists for EDA dicarbamate, which can make up between 20 and 37 % of carbamate present and is necessary to include to obtain accurate CO₂ absorption rate constants,^{153,156–158} its reaction energetics have been estimated. Lastly, for comparison the barriers to protonation of EDA by H₂S and CH₃SH are estimated.

3.2.2.1 Zwitterion formation energetics

Initial conformers of EDA for reaction with an electrophile were chosen on the basis of the active site and most stable conformers in aqueous solution. Previous gas electron diffraction studies show the gauche conformer to be predominant in gas phase,¹⁴⁹ and Radom et al.¹⁴⁴ calculate the most stable conformers to be tGg' and gGg', being within 0.26 kcal/mol of each other, where all trans conformers are at least 1 kcal/mol higher in energy. For CCSD(T)/aug-cc-pvdz energies at SMD/B3LYP-D3/aug-cc-pvdz geometries, the lowest two conformers found were gTt and g'Gt, where the trans conformer sits 0.21 kcal/mol below the gauche one. In the strong dielectric environment of water, the trans conformer is predicted to be more stable. Additionally, as the concentration of EDA increases, molecular dynamics studies suggest it further adopts a trans orientation.¹⁵⁹ In each gauche and trans conformer the N-lone pair is oriented away from the rest of the molecule, ideal for the addition of an electrophilic species (avoiding the crowding of the g' N lone pair in g'Gt EDA for example). The barrier to reaction can be an additional 3 kcal/mol higher where rotation of the amine to the reaction coordinate is necessary, as is the case between MEA and CO₂.⁶² The activation energy barriers between CO₂ and neutral g'Gt and gTt EDA are presented in Figures 3-4 and 3-5, respectively. Additionally, the barriers to forming the dicarbamate from the gauche and trans forms of the EDA carbamate are present in the same figures.

Formation of the dicarbamate may occur through a similar zwitterion mechanism into the monocarbamate anion (Eqn. 3.25 to 3.28),¹⁵⁸ where alternative reactants include carbamic acid, which is unlikely to be present due to its low pK_a, and a protonated (quaternary) amine, for which electrophilic addition is unfeasible.



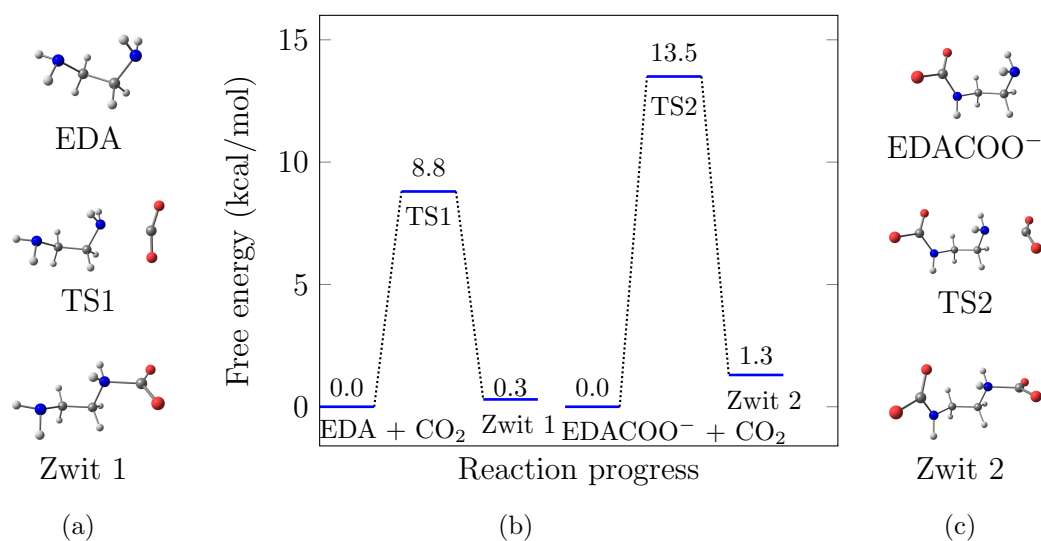


Figure 3-4: Structures of g'Gt EDA reactant, TS and product (a) reaction profile of EDA and EDACOO⁻ with CO₂ (b) and structures of EDACOO⁻ reactant, TS and product (c)

The transition state for CO₂ addition to the gauche conformer of EDA is 3 kcal/mol lower than its trans counterpart, though this is reversed on addition of a second CO₂ where formation of the dicarbamate zwitterion is more favourable in the trans conformer of EDACOO⁻ by 2 kcal/mol. Two transition states were found into neutral gauche EDA (the lowest is shown) with frequencies of -160.57 cm^{-1} and -248.7 cm^{-1} , where the latter is 2.9 kcal/mol higher in energy, representing a total barrier of 11.7 kcal/mol. The energy difference lies in the distance between the free g' nitrogen and the nearest H on the reacting amine. In the lower energy transition state the distance is reduced from its nominal value of 2.687 Å in isolated g'Gt EDA, to 2.685 Å in the lower transition state versus 2.765 Å in the higher TS, and down to 2.492 Å in the zwitterion product. The trans conformer by comparison has negligible internal structure change, experiencing predominately solvent stabilisation of the transition state and zwitterion without significant intramolecular (or through space) charge transfer. The barrier for addition to the trans form agrees well with that calculated by Davran-Candan⁶¹. The temperature-rate data from Li et al.¹⁵³ for k_2 was fitted against the Eyring Equation ($\kappa = 1$), Eqn 3.24 via non-linear regression,¹⁶⁰

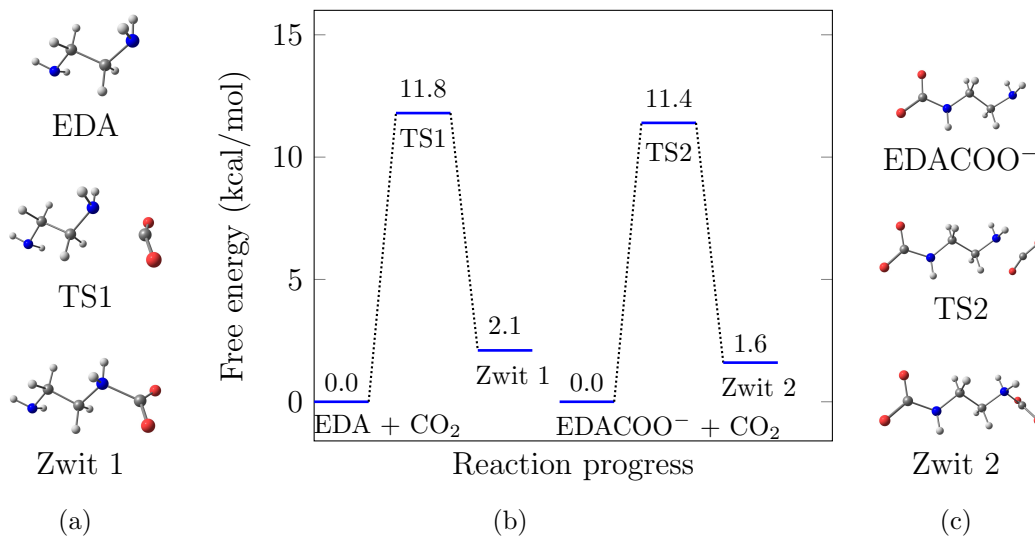


Figure 3-5: Structures of g'Tt EDA reactant, TS and product (a) reaction profile of EDA and EDACOO⁻ with CO₂ (b) and structures of EDACOO⁻ reactant, TS and product (c)

yielding $\Delta G^\ddagger = 11.9$ kcal/mol at 298 K in excellent agreement with the activation barrier for reaction with the trans conformer. The partitioning of gauche and trans conformers in aqueous solution has been estimated by molecular dynamics simulations,¹⁵⁹ where the trans form accounted for >66% of EDA at low solute concentrations, in qualitative agreement with the energy difference between g'Gt and gTt conformers calculated here, 0.21 kcal/mol, leading to a trans:gauche ratio of 58:42. The average activation energy barrier can be approximated as the weighted contribution of each conformer, yielding 10.5 kcal/mol, which is lower than that derived from experiment because fitting the reaction data lumps contributions from conformations and neglects solvent perturbations and barrier re-crossings (i.e. $\kappa = 1$).¹⁶¹ The formation of the dicarbamate, with a similar driving force to monocarbamate formation in both gauche and trans forms, suffers from a higher barrier than the gauche form due to repulsion between the negative carbamate and partial negative charge on the oxygens in CO₂, which is clear when in the trans conformer the barrier is reduced by 2 kcal/mol. The gauche form sits 0.92 kcal/mol below trans, and is likely the dominant conformer in solution with a ratio of gauche:trans at 83:17. This is in qualitative agreement with the low

amounts of dicarbamate in solution, as the ratio of theoretical maximum reaction rate for dicarbamate to carbamate formation is 0.012 (from Eqn. 3.24), with a rate law that is expected to be first order in both EDACOO⁻ and CO₂. The formation of dicarbamate is anticipated to be more favourable than direct CO₂ hydrolysis, which has an activation free energy of $\Delta G^\ddagger = 21.8$ kcal/mol.¹⁶²

The reaction energetics for formation of zwitterions of COS and CS₂ are shown in Figure 3-6. Given the similar structure of the transition state, the activation barriers for COS and CS₂ zwitterions are significantly higher than that of CO₂, at 16.4 and 17.6 kcal/mol, respectively. The separation distance between the reacting nitrogen and carbon centre follows the trend of the Mulliken partial charges (in parenthesis) on carbon i.e. 2.10 Å, 2.07 Å and 1.87 Å for CO₂ (+0.17) < COS (+0.43) < CS₂ (+1.60) while the activation energy follows the reverse trend, as the partial charges on oxygen and sulfur become increasingly negative: CO₂ -0.08, COS -0.15 and -0.28, CS₂ -0.8. The CS₂ zwitterion is the only thermodynamically favourable product, where optimisation in SMD SCRF provides additional stabilisation over that experienced by the gas phase product. Similar to the EDA CO₂ zwitterion, intramolecular charge transfer to the g' amino N lone pair is present in COS and CS₂ zwitterions where the N...H distance is reduced from 2.687 Å in neutral g'Gt EDA to 2.413 Å and 2.375 Å in COS and CS₂ zwitterions, respectively. Alper and Bouhamra¹⁵⁴ collected a single rate constant for EDA COS zwitterion formation at 298 K, which if fitted against the Eyring Eqn. (3.24) yields a free energy of activation of 15.5 kcal/mol, in reasonable agreement with that calculated here. Unfortunately reaction rate data for the EDA CS₂ zwitterion is unavailable, though Sharma¹⁶³ suggests the approximate relationship for the ratio of CO₂ and CS₂ zwitterion formation rates:

$$\log k_{Am-CO_2} \cong \log k_{Am-CS_2} - 5 \quad (3.29)$$

If the reduction in rate is entirely subsumed into the free energy of activation, that for CS₂ zwitterion formation would be 6.8 kcal/mol above CO₂, whereas the calculated result is 8.8 kcal/mol higher than that of the estimate for CO₂. The barrier for sulfur containing zwitterions is overestimated here, and without accounting for deviations from the Eyring Eqn. ($\kappa \neq 1$) - the likely cause of which

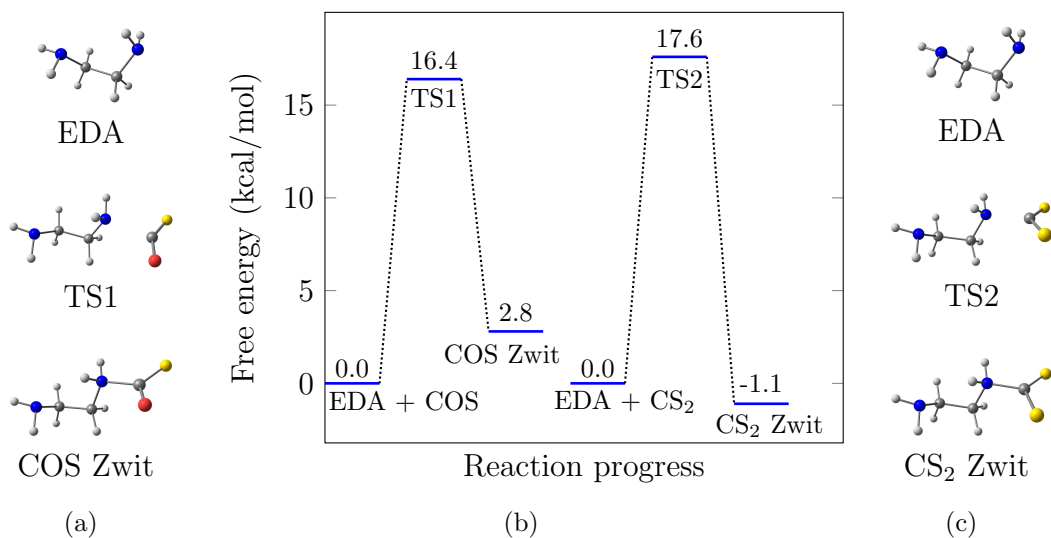


Figure 3-6: Structures of EDA-COS TS and product (a) reaction profile of EDA and with COS (b) and structures of EDA \cdots CS₂ TS and product (c)

is the poor treatment of sulfur species by the solvent model, SMD.¹³⁶ In each case, the reaction between EDA and COS and CS₂ is predicted to be more favourable than direct hydrolysis reactions Eqn. 3.17 and 3.18 at ca. 25 - 28 kcal/mol.^{164,165}

The zwitterion formation energetics of CO₂, COS and CS₂ for conformer g'Gt have been summarised in Table 3.2, where it is noted the energies from B3LYP-D3 provide the correct trend in activation free energy, though it overestimates and incorrectly identifies the trend in the relative energies of zwitterion products. These zwitterionic intermediates are generally short-lived, deprotonating to a nearby base (often a free amine) where the deprotonation rate does not limit zwitterion formation in the case of primary amines, determined experimentally,^{153,154} and examined computationally.⁶¹ The availability of free amine will be reduced, however, if simultaneous absorption of mercaptans, H₂S or CH₃SH, occurs - as covered in the next section.

3.2.2.2 Mercaptan absorption energetics

It is usually quoted that the protonation of primary amines by mercaptans is instantaneous,¹⁶⁶ and as such if significant quantities are present the formation

Table 3.2: Summary of activation free energy (ΔG^\ddagger) and relative zwitterion free energy (ΔG^{Zwit}) for CO₂, COS and CS₂ absorption with EDA, calculated at the B3LYP-D3 and CCSD(T) level of theory (kcal/mol).

Electrophile (X)	$\Delta G_{B3LYP-D3}^\ddagger$	$\Delta G_{CCSD(T)}^\ddagger$	$\Delta G_{B3LYP-D3}^{Zwit}$	$\Delta G_{CCSD(T)}^{Zwit}$
CO ₂	5.8	8.8	0.8	0.3
COS	11.5	16.4	6.0	2.8
CS ₂	13.6	17.6	5.2	-1.1

of primary amine carbamates is blocked, and the working capacity of the solution for CO₂ reduced. The activation barrier for protonation of g'Gt EDA by H₂S and CH₃SH with reactant, TS and product structures is presented in Figure 3-7.

From totally isolated EDA and mercaptan reactants to their respective TS there is a clear barrier to proton transfer. The formation of the EDA···H₂S complex in the tGg' conformer is the most significant contributor to the activation energy barrier (7.6 kcal/mol), where the transition state is only 0.9 kcal/mol above that. Not so for CH₃SH, where complex formation accounts for 8.6 kcal/mol and a further increase of 4.7 kcal/mol to the transition state, where the substitution of an alkyl group for a proton (as in H₂S) reduces the mercaptan acidity.¹⁶⁷ There is no explicit data on the activation energy for protonation of EDA or protonation of primary amines by mercaptans as absorption rates are often limited by mass transfer. Parrish and Kidnay⁷ state there is little difference in the rate of absorption of CO₂ and H₂S, which is seen explicitly for EDA based on the barriers estimated here. The energetics of mercaptan deprotonation by EDA are summarised in Table 3.3. It is again noted that B3LYP-D3 consistently underestimates the activation free energy and relative free energies of the products, and in the case of H₂S suggests barrierless protonation. Although the geometry of the TS for deprotonation of CH₃SH was confirmed on the B3LYP PES, energies calculated at CCSD(T) with SMD single point corrections yield a barrier less than the relative energy of the products.

Although the formation of CO₂, COS, and CS₂ zwitterions with EDA is more thermodynamically favourable than the formation of a EDAH⁺-SH⁻ pair, the barriers are higher. It is then possible CO₂ will interact with products of protonated EDA (by H₂S) and in turn H₂S with the products and derivatives of CO₂

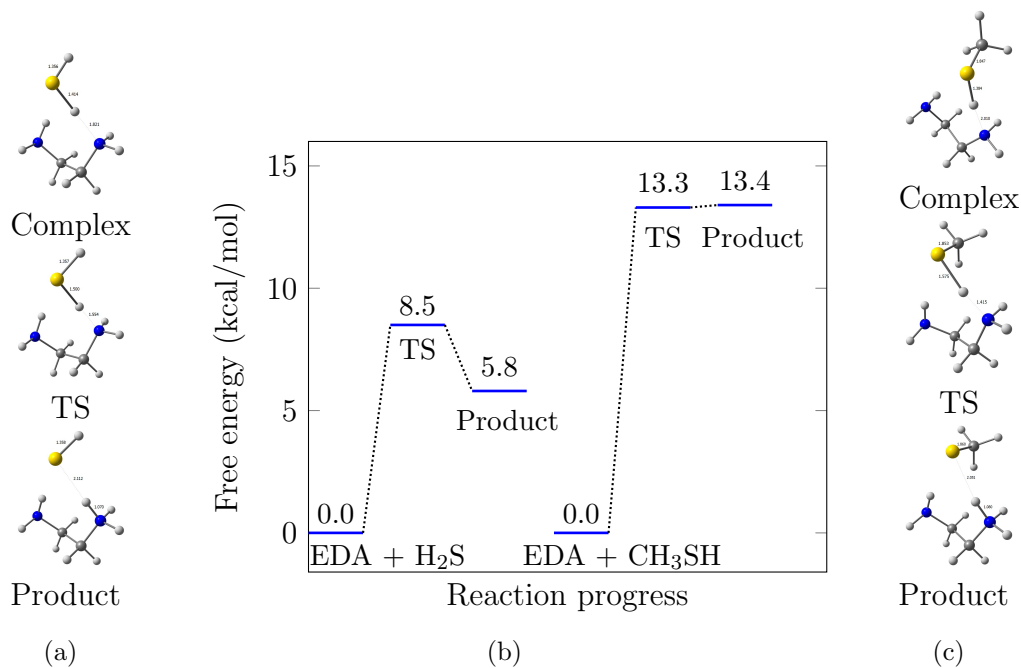


Figure 3-7: Structures of the g'Gt EDA-H₂S complex, TS and product (a) reaction profile of EDA with H₂S and CH₃SH (b) and structures of EDA-CH₃SH complex, TS and product (c)

Table 3.3: Summary of mercaptan absorption energetics (kcal/mol)

Mercaptan	$\Delta G_{B3LYP-D3}^\ddagger$	$\Delta G_{CCSD(T)}^\ddagger$	$\Delta G_{B3LYP-D3}^{Prod}$	$\Delta G_{CCSD(T)}^{Prod}$
H ₂ S	3.9	8.5	0.2	5.8
CH ₃ SH	7.9	13.3	8.1	13.4
	$\Delta G_{B3LYP-D3}^{Complex \rightarrow TS}$	$\Delta G_{CCSD(T)}^{Complex \rightarrow TS}$	$\Delta G_{B3LYP-D3}^{Complex \rightarrow Prod}$	$\Delta G_{CCSD(T)}^{Complex \rightarrow Prod}$
H ₂ S	-0.7	0.9	-4.4	-1.8
CH ₃ SH	5.8	4.7	-2.8	4.8

absorption onto EDA - this is further explored in Section 3.2.3.

3.2.2.3 pK_a estimation

The pK_a of the zwitterionic species of CO_2 , COS and CS_2 and carbamate derivatives are estimated and presented in Table 3.4. All species are labeled with the acid site in red. The conformers used in pK_a estimates are included in the same table, with similar notation to that previously. No orientation symbol is given to fully protonated quaternary amines, but in the zwitterions formed with CO_2 , COS and CS_2 the position of addition is labeled in blue. The pK_a of solution species indicates the propensity to absorb H_2S , where recent experimental studies specifically correlate increases in amine pK_a with H_2S capacity.¹⁶⁸

There are several factors that influence the estimation of pK_a by quantum chemical methods, covered in a recent case study by Haworth et al.¹⁷⁰. Here the lowest energy conformers found in the SCRF are used, and where possible without an intramolecular hydrogen bond (iHB) as that may over-stabilise the acid or its conjugate base yielding inaccurate pK_a s.¹⁷⁰ The estimation of pK_{a1} for EDA by the direct method is remarkably accurate though it does not extend to the second dissociation constant for $EDAH_2^{2+}$, where the solvent model is unable to account for strong solute-solvent interactions.¹⁷¹ In the case of $EDAH_2^{2+}$ where both reactant and product are the lowest energy conformers found ($T \rightarrow g'G$) the pK_a is underestimated by over 3 units. In contrast, when the reactant is the lowest energy conformer and the product is the closest low energy conformer to the reactant as in $T \rightarrow gT$, the estimate is not as poor c.a. 1.9 units, where the difference for the $T \rightarrow g'G$ path is due to the internal rotation and over-stabilisation of the gauche conformer. The same effect is seen in the estimate for $EDAH^+COO^-$ where if the conformer which contains strong intramolecular bonding, gG , is used the pK_a is 3 units higher than with the trans gT conformer, where the relative energy of the gG (0) and gT (4.2) conformers accounts for the difference in pK_a . Given the relative energy difference, the gauche form of $EDAH^+COO^-$ is more likely to be found in solution (at $\sim 1000:1$) and as such closely resembles the experimental value of 10.11.¹⁵⁷ Intramolecular hydrogen bonds do not always cause large deviations in pK_a estimates, as with $EDAH^+COOH$, where the relative dif-

Table 3.4: pK_a of EDA and carbamate derivatives. Direct and PEX refer to the pK_a 's calculated via the direct and proton exchange methods, respectively, which are described in Section 3.1.

Species		Direct	PEX	Exp.
	EDAH ⁺ g'G → g'Gg	9.98	11.78	9.92 ¹⁶⁹
	EDAH ₂ ²⁺ T → g'G T → g'T	3.47 4.96	5.26 6.76	6.86 ¹⁶⁹
	EDA ⁺ CO ₂ ⁻ g'Gt → tGt gTt → tTg'	2.75 2.28	4.54 4.07	N/A
	EDA ⁺ COS ⁻ g'Gt → g'Gg	2.10	3.90	N/A
	EDA ⁺ CS ₂ ⁻ g'Gt → g'Gg	1.65	3.44	N/A
	EDAH ⁺ COO ⁻ gG → tGt gT → tTg'	9.22 6.25	11.01 8.05	10.11 ¹⁵⁷
	EDACOOH tGt → tGt gTt → tTg'	5.41 5.16	7.20 6.96	N/A
	EDAH ⁺ COOH g'G → tGt tT → tTg'	7.46 7.48	9.26 9.27	N/A
	g'G → tGt tT → tTg'	3.65 6.38	5.45 8.18	N/A

ference between the conformer with (0) and without one (1.2) does not cause a significant difference. Generally zwitterionic species stabilised by an iHB make a poor choice of conformer for pK_a estimates though it is not universal and depends on the relative energy of the stabilised conformer to that without.

Estimation of pK_a by the PEX method with methylamine as a reference acid shifted each value according to the aqueous free energy of protonation and the experimental pK_a . Though chemically similar to at least EDA, the PEX method overestimated the pK_a for the first dissociation constant by nearly as much as the correction it applies. The potential issue, as with the direct calculation of pK_{a2} of EDA, is the treatment of strong solute-solvent interactions which can not be accounted for with the SMD solvation model alone.

The zwitterions following CO_2 , COS and CS_2 absorption are highly acidic and increase in strength as sulfur replaces oxygen. The pK_a of free amine sites are consistently higher (or less acidic) than carbamic acid sites and are the likely interaction sites for zwitterion or mercaptan deprotonation. pK_a estimates by the direct method of H_2S and CH_3SH yield 13.1 and 18.3, respectively, which although correctly identifies the trend in acidity, significant overestimates the difference, where experimental values are 7 and 10.4, respectively.^{172,173} The large deviation from experiment is due to the the poor treatment of sulfur by the solvation model, SMD.¹³⁶ The pK_a of species in Table 3.4 relative to mercaptans (H_2S and CH_3SH) suggest that neutral EDA may participate in proton exchange, though the energetics presented in Figure 3-7 suggests it is thermodynamically unfavourable. The main method for mercaptan absorption is more likely to be direct hydrolysis as in Eqn. 3.16, given the pK_a of water is 14.0.¹⁶⁹ The interaction of H_2S , SH^- and CO_2 with EDA and its derivatives may still however be favourable, such that total solution capacity is not dictated by water hydrolysis or carbamate formation only. This is explored in the following section.

3.2.3 Interaction of product derivatives

As the expected quantity of H_2S and other mercaptans in well gas is generally low (ca. 2-3%),^{7,174} the combinatorial interactions of COS , CS_2 and CH_3SH with possible derivatives have not been considered, limiting the scope to the major

contaminants: CO_2 and H_2S , and products generated due to absorption thereof; EDAH^+ , $\text{EDA}\text{H}_2^{2+}$, EDACOO^- and SH^- . According to the pK_a s determined, EDAH^+ may form by protonation by H_2S or CO_2 , COS or CS_2 zwitterions while $\text{EDA}\text{H}_2^{2+}$ may only be generated by zwitterions deprotonation.

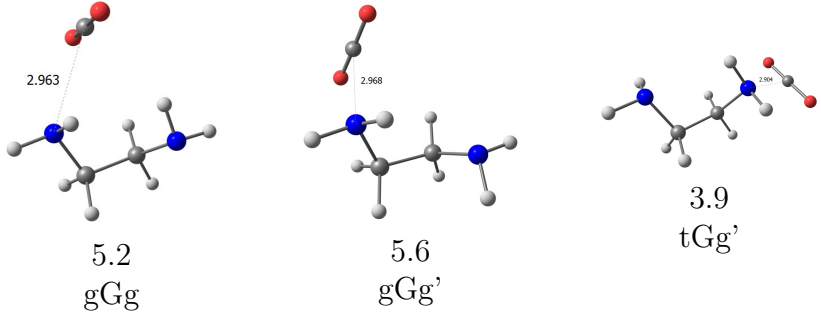
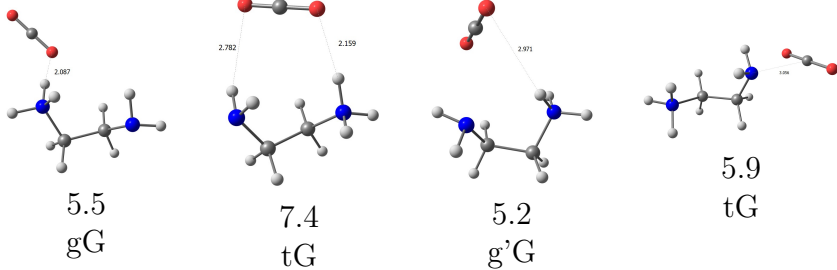
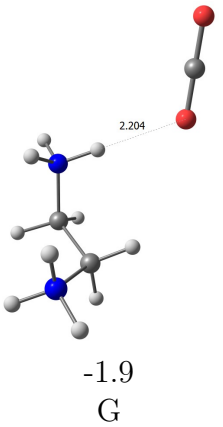
3.2.3.1 EDA and derivatives with CO_2

When the ratio of H_2S to CO_2 is high, the proportion of protonated amines increases which is anticipated to reduce not just direct carbamate formation by blocking active sites but by additionally acidifying the solution. The structure and free energy of complex formation of EDA, EDAH^+ and $\text{EDA}\text{H}_2^{2+}$ with neutral CO_2 is presented in Table 3.5 to assess blocking of the carbamate pathway. (Note: With each protonation of the amine group, the conformer notation drops the character that identifies the position of the nitrogen lone pair.)

The complexes formed between neutral EDA and CO_2 were largely aligned with the reaction coordinate for nucleophilic addition into the nitrogen lone pair, where the distance between nitrogen and carbon ranges from 2.9 to 3 Å. The energetics of complex formation are not significantly affected by method and basis set, where at the CCSD(T)/aug-cc-pvdz//SMD/B3LYP-D3/aug-cc-pvdz level complex formation of the g'Tt conformer (see Figure 3-5(c)) is comparable at 5.1 kcal/mol. Complexes of EDAH^+ and CO_2 were investigated to check for favourable electrostatic interaction of the CO_2 quadrupole with the quaternary amine, and the formation of complexes along the reaction coordinate of the free amine. Though CO_2 will orient towards the quaternary amine in gG and tG conformers, there is no thermodynamically favourable interaction. The formation of complexes along the reaction coordinate with the free amine is unlikely because in its lowest energy conformer, g'G, the N lone pair is engaged in an iHB, blocking reaction with CO_2 . As with neutral EDA, the N lone pair in EDAH^+ was oriented so as to facilitate CO_2 reaction in the tG conformer. Since the binding free energy is corrected for the initial conformer, and isolated tG EDAH^+ is 1.6 kcal/mol above g'G, the complex formation represents 7.5 kcal/mol, nearly double that seen for neutral EDA in the tGg' case.

The reaction profile of CO_2 addition to tG EDAH^+ was examined at the

Table 3.5: Structures (distances in Angstroms) and free energies (in kcal/mol) of complex formation between protonated EDA derivatives and CO₂.

Species	CO ₂
EDA	 <p>2.963 5.2 gGg</p> <p>2.968 5.6 gGg'</p> <p>2.904 3.9 tGg'</p>
EDAH ⁺	 <p>2.087 5.5 gG</p> <p>2.782 2.159 7.4 tG</p> <p>2.971 5.2 g'G</p> <p>2.904 5.9 tG</p>
EDAH ₂ ²⁺	 <p>2.204 -1.9 G</p>

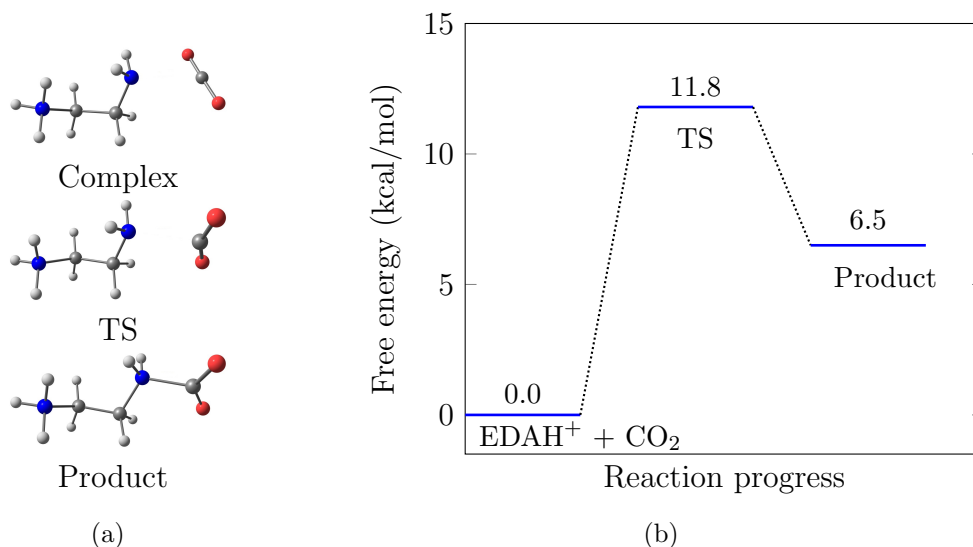


Figure 3-8: Structures of g'Gt EDAH⁺-CO₂ complex, TS and product (a) reaction profile of EDAH⁺ with CO₂ (b).

previous level of theory and presented in Figure 3-8(a). Though the activation barrier is not significantly different to that of the neutral gauche EDA, 11.8 vs 8.8 kcal/mol, and actually the same as in neutral trans EDA, the relative energy of the zwitterion intermediate is much higher (>6 kcal/mol) owing to faster reverse reactions and fewer carbamates forming via this pathway. The only favourable interaction with CO₂ is for doubly protonated EDAH₂²⁺, where carbamate formation is blocked and electrostatics dominate, however EDAH₂²⁺ is likely to be strongly solvated, and CO₂ displaced by water around the hydrogen bonding quaternary amine donors (See Section 3.2.4). Protonation of EDA reduces absorption of CO₂, as the path to carbamate formation is blocked, while the second protonation blocks carbamate formation entirely, where only minor electrostatic interactions are present. Given the pK_a of carbonic acid and bicarbonate (5.36 and 10.33 respectively),¹⁶⁹ the interactions of EDA, EDAH⁺ and EDAH₂²⁺ with CO₃²⁻, HCO₃⁻ and H₂CO₃ were not considered as the majority of dissolved carbon exists as carbamate.¹⁵⁷ Additionally, the formation of bicarbonate is anticipated to be slower than the direct formation of EDA carbamate (unless EDA is at capacity).

3.2.3.2 EDA and derivatives with H₂S

As the solution becomes more acidic, through CO₂ or H₂S absorption, the capacity for H₂S is expected to reduce as the active sites for absorption are occupied. The interactions of EDA, EDAH⁺ and EDAH₂²⁺ with H₂S and SH⁻ are presented in Table 3.6. Interactions with the bare S²⁻ anion were not considered as it is not expected to exist in aqueous solution.¹⁷²

The majority of interactions between protonated variants of EDA and H₂S and SH⁻ are unfavourable with the exception of between EDAH₂²⁺ and SH⁻, similar to that previously with CO₂ where electrostatic interactions dominate due to the charge difference and favourable complexes may arise. This interaction is predicated on the second protonation of EDA, which may only occur through reaction with a zwitterion intermediate, and is unable to be generated by mercaptans alone. In this way, the capacity for H₂S is increased if CO₂ is present. It is noted that the formation of the H₂S and EDA complex at each amine site is effectively equivalent, being marginally higher in the tGg' case as the iHB is disturbed. As complex formation is similar, it's expected that the barrier for proton transfer to EDA by H₂S to either amine site is equivalent.

Where simultaneous absorption of CO₂ and H₂S occurs, both H₂S and SH⁻ may interact with carbamate derivatives and the pK_a of the free amine will be sufficient to strip a proton from H₂S. The interactions of a gauche monocarbamate, the primary carbamate product, with H₂S and SH⁻ are presented in Table 3.7.

As per the pK_a estimation, H₂S and EDACOO⁻ forms a protonated carbamate with weak residual binding of products; more-so than between SH⁻ and EDAH⁺ where the iHB due to the carbamate is weaker than that in g'G EDAH⁺. The converged structure of EDACOO⁻ with SH⁻ settled at > 20 Å separation due to significant electrostatic repulsion, where carbamate is not stabilised by intramolecular charge transfer and cannot accommodate additional anion interaction. EDAHCOO⁻ with SH⁻ forms effectively the same conformer as EDACOO⁻ H₂S with slight changes in energetics while EDAHCOO with H₂S forms with similar energetics to EDAH⁺ with H₂S where there is no favourable interaction. These results are consistent with experiments where the capacity for

Table 3.6: Structures and free energies of complex formation between protonated EDA derivatives and H₂S (kcal/mol). Distances in Angstroms.

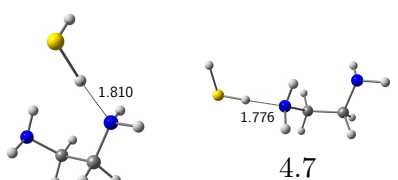
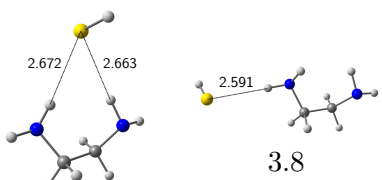
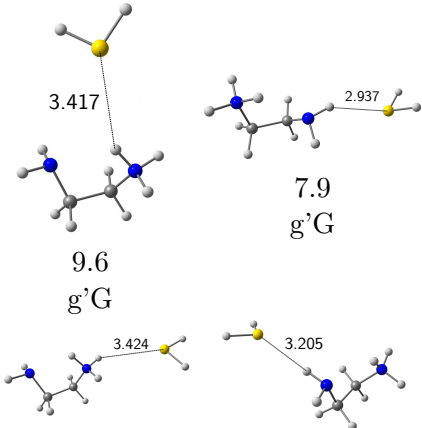
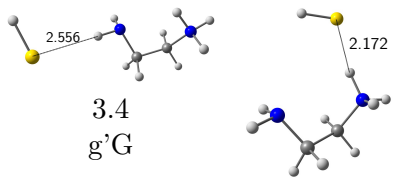
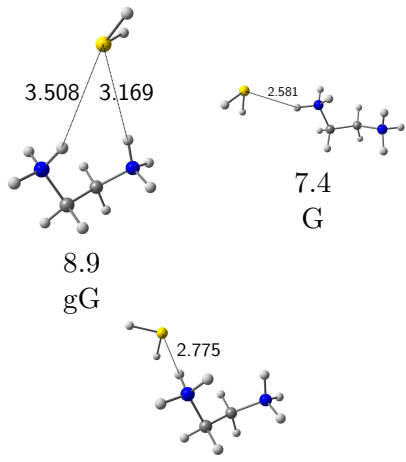
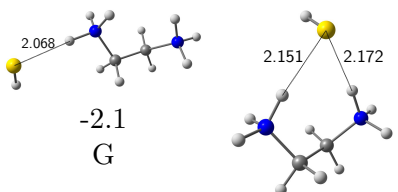
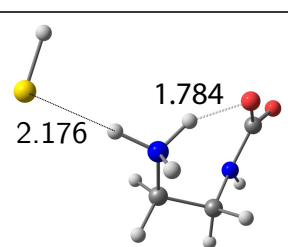
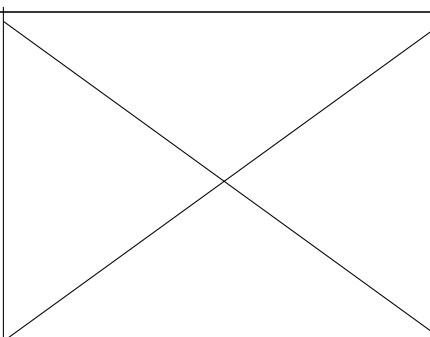
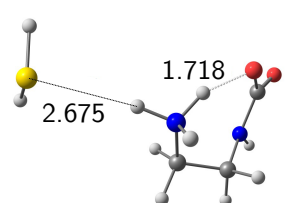
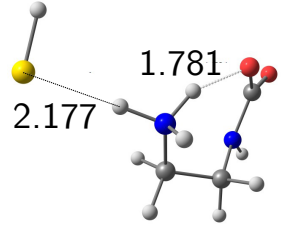
Species	H ₂ S	SH ⁻
EDA	 <p>5.0 tGg'</p> <p>4.7 tGg'</p>	 <p>3.9 gGg</p> <p>3.8 gGg</p>
EDAH ⁺	 <p>9.6 g'G</p> <p>7.9 g'G</p> <p>8.6 g'G</p> <p>8.1 g'G</p>	 <p>3.4 g'G</p> <p>2.0 g'G</p>
EDAH ₂ ²⁺	 <p>8.9 gG</p> <p>7.4 G</p> <p>8.4 G</p>	 <p>-2.1 G</p> <p>-6.0 G</p>

Table 3.7: Free energy changes for H₂S derivatives interacting with EDA derivatives (kcal/mol). Distances in Angstroms.

Species	H ₂ S	SH ⁻
EDACOO ⁻	 <p>2.176</p> <p>1.784</p> <p>-0.02 gG</p>	
EDAHCOO ⁻	 <p>2.675</p> <p>1.718</p> <p>8.9 gG</p>	 <p>2.177</p> <p>1.781</p> <p>-0.8 gG</p>

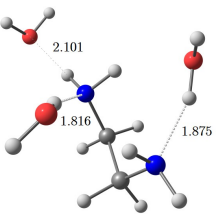
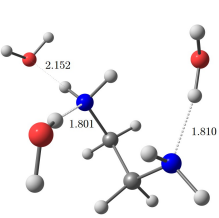
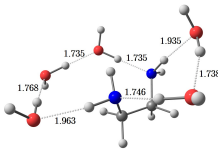
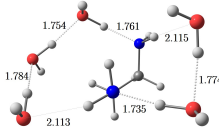
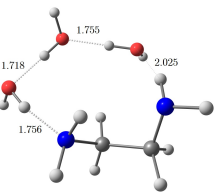
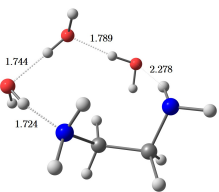
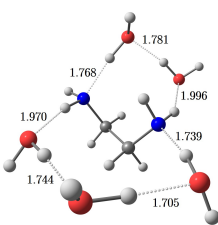
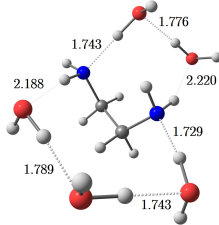
H₂S in EDA decreases as the aqueous carbon dioxide concentration is increased.¹⁷⁵ The weakly bound bisulfide is easily displaced from EDA and its derivatives, and protonated by newly forming CO₂ zwitterions (pK_a ~2.5) or carbonic acid (pK_a ~5.35).

3.2.4 Effect of explicit solvent on CO₂ zwitterion energetics

Given the implicit treatment of the solvent by SMD, the effect of explicit microsolvation was applied to neutral gauche conformers to examine differences in conformer energy, formation of the CO₂ EDA pair and relative energy of the CO₂ zwitterion. Including explicit water molecules has been shown to reduce activation energy barriers for primary amines,¹⁷⁶ and shift the interaction energy between CO₂ and amines towards being more negative.¹² The addition of explicit water increases computational cost and the configuration space, where ideally only a single water would be necessary to provide an adequate description of solute-solvent interactions to reduce complexity, though it is often insufficient.¹⁷⁷ Unfortunately, the number of explicit molecules necessary to achieve an accurate representation of the solvent is beyond quantum chemical methods alone, though with just five explicit waters good estimates of solvation free energies can be obtained (within 2 kcal/mol).^{75,178} Structures of neutral EDA in gauche gGg and g'Gt conformers were optimised with three and five explicit waters at the B3LYP/6-31G* level of theory in gas phase and solvent model SCRF to examine the difference in absolute free energy. Water molecules were initially placed where strong solute-solvent interactions are anticipated, at hydrogen bonding acceptor and donor locations around amine sites. The differences between gas phase and SCRF structures and their relative free energies are presented in Figure 3-9, where the column GP or SMD indicates the optimisation environment and G_{aq} is the free energy in solvent. In the GP column ΔG_{solv}^* is added for comparison to the SCRF optimised value.

Structures optimised in the presence of the solvent SCRF model demonstrate larger interatomic distances where the an amine acts as a hydrogen bond donor and shorter when it is a donor, when compared to structures generated in the gas

Figure 3-9: Relative free energies of neutral EDA with water clusters with respect to original gas phase conformer (kcal/mol). Distances in Angstroms.

EDA	3 H ₂ O		5 H ₂ O	
	GP	SMD	GP	SMD
gGg				
G_{solv}	-21.8	-17.8	-25.1	-22.6
g'Gt				
G_{solv}	-15.1	-17.3	-21.7	-23.8

phase. The hydrogen bonding donor ability of EDA is observed to be less significant than its acceptor behaviour, reflected in the average h-bond distances for each, ~ 2.20 Å and ~ 1.75 Å for donor and acceptor, respectively, consistent with molecular dynamics simulations.¹⁵⁹ As the surrounding water is free to respond to the dielectric constant of the solvent, rather than the solute in isolation, the stronger solute-solvent effects dominate. The changes in structure cause shifts of a few kcal/mol between single point solvation of gas phase structures and full optimised structures in the solvent SCRF. With three and five explicit waters, the gas phase structures with solvent corrections do not agree with the relative difference between gGg and g'Gt conformers determined at the CCSD(T)/aug-cc-pvdz//SMD/B3LYP-D3/aug-cc-pvdz level (~ 1 kcal/mol); in fact the reverse is seen for both. With 3 H₂O the SCRF optimised structure yields the same trend though overestimates the difference in stability, since in the g'Gt 3 H₂O structure only one amine is solvated with a hydrogen bonding donor. With 5 H₂O in the SCRF, the same relative energy difference is found as determined with the implicit solvent, where both amines are solvated and both conformers show similar water chains circling the hydrophilic region of EDA. Given the expense of optimising in the solvent SCRF, the energetics of CO₂ addition into neutral EDA was determined with the following thermodynamic cycle (Figure 3-10), where gas phase optimisation and single point solvation calculations were used to approximate solution phase energies as calculated in Eqn 3.8.

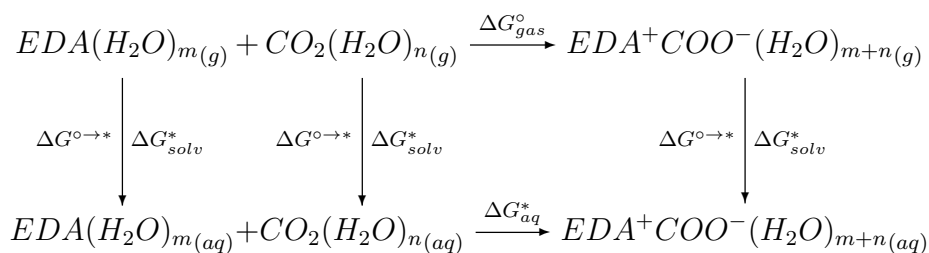


Figure 3-10: Thermodynamic cycle to determine the aqueous free energy of EDA⁺COO⁻ zwitterion formation.

The results obtained are summarised in Table 3.8. Firstly, it is noted that the zwitterion intermediate is stable in the gas phase and when under microsolvation conditions, as also reported by Hall and Smith¹⁷⁹. There is no clear trend

Table 3.8: Relative free energies of EDA \cdots CO₂ solvent-separated structures and zwitterions (kcal/mol). Number of explicit water molecules in the reactant geometries represented by m and n for EDA and CO₂, respectively, corresponding to the thermodynamic cycle shown in Figure 3-10.

EDA(H ₂ O) _{m}	CO ₂ (H ₂ O) _{n}	Solvent Sep.			Zwitterion		
		Conf.	ΔG_{gas}	ΔG_{aq}	Conf.	ΔG_{gas}	ΔG_{aq}
3 tGg'	1	gGt	3.9	3.0	g'Gt	8.1	3.8
3 g'Gt	2	g'Gt	6.4	17.2	g'Gt	7.0	0.9
5 gGg	1	gGg	5.1	8.5	g'Gt	18.1	13.2
5 g'Gt	2	g'Gt	-2.9	-6.9	g'Gt	9.5	2.0

in the aqueous free energy of the solvent separated states or of the zwitterion intermediate as the number of explicit waters is increased. This is largely due to the preferential interaction of EDA with explicit water and ejection of CO₂ such that no consistent local minimum is retained as explicit water is increased. In an attempt to achieve some consistency, initial geometries for optimisation were set such that CO₂ was aligned with the reaction coordinate for addition, where more often than not the resulting structure was the zwitterion intermediate - the example of the five water solvent-separated states and zwitterions are shown in Figure 3-11.

The structure in Figure 3-11(a) resembles the transition state for formation of EDAH⁺ and HCO₃⁻ by the base-catalysed hydration mechanism, though this has been previously estimated to be an unlikely reaction pathway for EDA.⁶¹ The more energetically favourable pathway is by the zwitterion intermediate, in the same Figure (b). The barrier formation of the g'Gt zwitterion (addition at g' site) was not evaluated previously though is anticipated to sit closer to addition to g'Gt than g'Tt, given the propensity for gauche EDA derivatives to form intramolecular bonds thereby stabilising the transition state. The anomalously high free energy of the 6 H₂O zwitterion is explained by the sporadic water clustering and minimal solvation around the carbamate moiety, especially in comparison to the 7 H₂O zwitterion structure - both present in Figure 3-12.

The isolated clusters in Figure 3-12(a) raise the energy of the structure by a few kcal/mol. In addition, the COO⁻ carbamate site and quaternary amine are

Figure 3-11: Structures and relative free energies of (a) solvent-separated and (b) zwitterionic $\text{EDA} \cdots \text{CO}_2$ with 5 H_2O . Gas phase free energies of product with aqueous relative free energies in parenthesis. Distances in Angstroms, energies in kcal/mol.

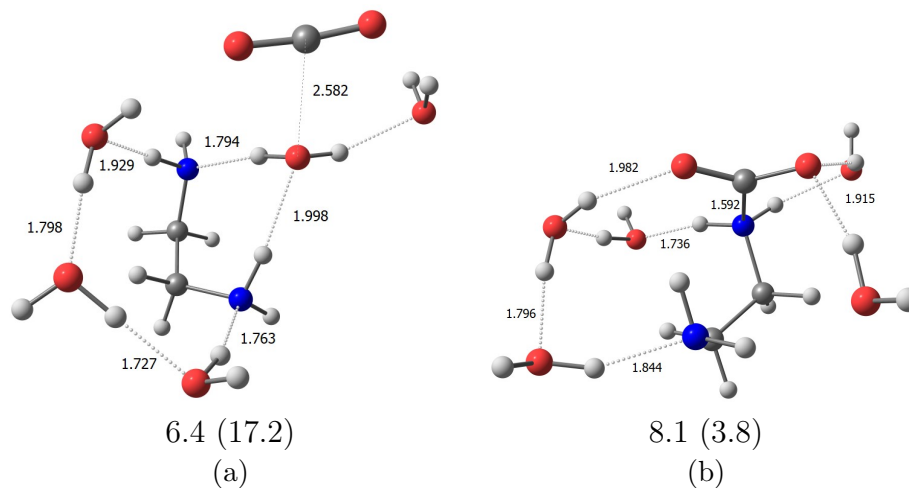
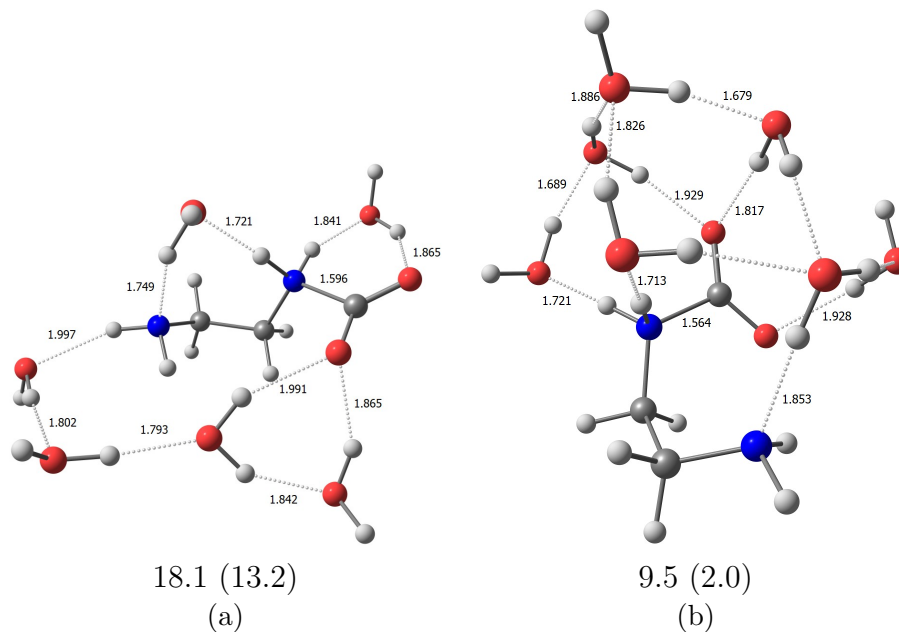


Figure 3-12: Structures and relative free energies of (a) 6 H_2O and (b) 7 H_2O zwitterionic $\text{EDA} \cdots \text{CO}_2$. Gas phase free energies of products with aqueous relative free energies in parenthesis. Distances in Angstroms(\AA), energy in kcal/mol.



minimally solvated explicitly and therefore rely on the solvent model to approximate strong short range contributions to the free energy. The hydrated zwitterion in Figure 3-12(b) represents a lower energy structure because the water cluster is in a more favourable arrangement,¹⁴³ since the more significant solute-solvent interactions are treated explicitly. The hydrogen bonding character of zwitterions is sufficiently different to the solvent separated structures, where their behaviour is similar to neutral EDA. Due to the high acidity of the zwitterion amine, estimated previously, the hydrogen bond distance decreases to 1.79 Å across all hydrated structures and to just 1.72 Å in that of Figure 3-12(b). The negative carboxylate group does not interact as strongly with explicit solvent, where its averaged hydrogen bonding acceptor distance across hydrated zwitterions is 1.90 Å.

Unfortunately, increasing the number of explicitly defined solvent molecules does not lead to any systematic improvement of the relative energy of the zwitterion. The free energy of the zwitterion and solvent-separated states are very sensitive to water number, position, orientation and clustering. A similar examination of the interaction between H₂S and EDA proved difficult for the same reasons. More rigorous sampling methods would be necessary to obtain reasonable estimates, such as Monte Carlo or QM/MM.¹⁸⁰

3.3 Summary

Computational results determined herein and surveyed literature support the absorption of CO₂, COS and CS₂ in aqueous EDA by a zwitterion intermediate mechanism where reactivity follows the same order. Estimates of the formation rate of the CO₂ zwitterion agree well with experimental observations, where minimal experimental rate data exists for COS and CS₂ zwitterion formation, though the results here fit the trend in expected reactivity. Mercaptan absorption onto EDA is found to be less thermodynamically favourable than zwitterion formation of electrophiles, where H₂S uptake may initially be faster than CO₂ but its capacity is lower in competitive absorption, which agrees well with experimental observations. The pK_a of EDA and derivatives thereof were estimated, and, where available, compare reasonably with experimental values. These estimates suggest

where potential secondary interaction between EDA derivatives and natural gas contaminants could take place. By examining the products of absorption and acid gases, it was found that there is no significant interaction between absorption products except where significant differences in species charge are present. Lastly, the effect of explicit water on the energetics of CO₂ zwitterion formation was examined, where no convergence of the energetics was observed due to a lack of conformational sampling of the solvation environment.

Chapter 4

Solvation and complexation of copper(II)

The second step in the EMAR cycle is the complexation of EDA with aqueous copper, where reducing EDA concentration also reduces the CO₂ solubility. The complexation energetics of copper and EDA are thus investigated with a number of density functionals. The drawback common to all functionals used is the solvation environment, and so explicit definition of at least the first solvation shell around copper is included in the majority of simulations. Given the pKa of aqueous metal cations, variation in the first solvation shell on complexation energetics is examined.

4.1 Methods

Initial conformers of copper(II) complexes were generated with the MMFF94 forcefield implemented in Avogadro as octahedral complexes (six-fold coordination) around the metal centre.¹³⁷ Given the difficulty of including charge transfer effects and the ability to predict the Jahn-Teller distortion of copper(II) complexes (discussed herein), quantum mechanical methods were used to examine the structure and energetics of ligand substitution. All quantum chemical calculations were performed in NWChem.¹³⁸ A number of density functionals were used in the optimisation of water and ethylenediamine copper(II) complexes, with initial conformers optimised in gas phase, with subsequent solvent corrections by the COSMO and SMD solvent models^{135,136}. To reduce computational cost, structures were first optimised with a double-zeta quality mixed basis set, 6-31+G*/LANL2DZ, employing the Los Alamos basis set for copper and 6-31+G* on remaining atoms (herein denoted as BS1).¹²⁷⁻¹²⁹ Further optimisation was performed with triple-zeta mixed basis sets, with LANL2TZ+ on copper and 6-311++G** on remaining atoms (herein denoted as BS2),¹⁸¹ where it is recommended diffuse functions are necessary to yield accurate energies of solvated copper(II) complexes.¹⁸²

All structures were confirmed to be a minimum on the PES by examining hessian eigenvalues in the relevant environment i.e. gas phase or solvent SCRF. In some cases, optimisation with the BS2 basis set yielded negative hessian eigenvalues, in which case single point energies at the previously BS1 optimised geometry were performed with the larger BS2 basis set, where zero-point energy corrections were included at the BS1 level (noted in text where applicable). Basis set superposition error was corrected for with the counterpoise method using the relevant basis set and density functional.

Species gas and aqueous phase free energies are calculated according to the equations described in the previous chapter; 3.6 and 3.7, respectively. The solvation free energy of a bare Cu^{2+} and the $[\text{Cu}(\text{EDA})]^{2+}$ complex is examined through the generic thermodynamic cycle for the solvation of ions in Figure 4-1, referred to in text as the cluster cycle.

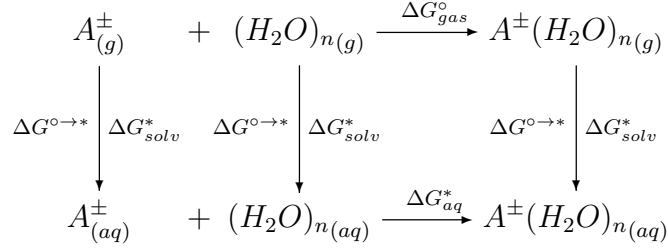


Figure 4-1: Thermodynamic cycle for the calculation of $\Delta G_{solv}^*(A^{\pm})$

Here the solvation free energy is then given by:

$$\begin{aligned}
\Delta G_{solv}^*(A^{\pm}) = \Delta G_{gas}^{\circ} + \Delta G_{solv}^*(A^{\pm}(H_2O)_n) - \Delta G_{solv}^*((H_2O)_n) \\
- \Delta G^{\circ \rightarrow *} - RT \ln([H_2O]/n) \quad (4.1)
\end{aligned}$$

Application of the above cycle requires the gas phase free energy and solvation free energy of water clusters. The optimal number of water molecules used in these clusters was determined by Bryantsev et al.¹⁴³, and subsequently employed here. They are treated with the same BS1 and BS2 basis sets and functional as copper complexes for consistency.

The aqueous complexation free energy of ethylenediamine to aqueous Cu(II) was then estimated with the thermodynamic cycle in Figure 4-2.

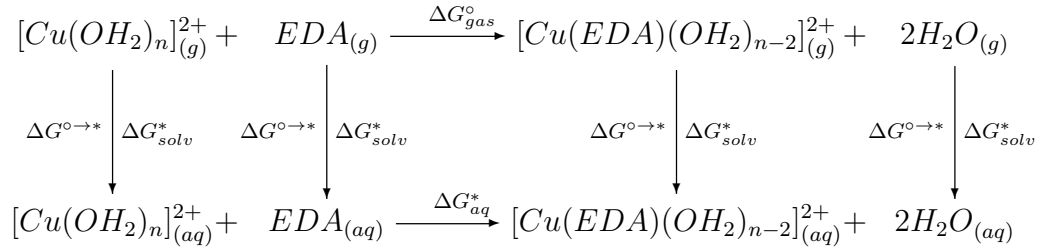


Figure 4-2: Thermodynamic cycle for calculation of the complexation free energy of Cu(II) with EDA in water

The aqueous free energy of complexation is then:

$$\Delta G_{aq}^* = \Delta G_{gas}^{\circ} + \Delta \Delta G_{solv}^* + \Delta G^{\circ \rightarrow *} + 2\Delta G^{l \rightarrow *} \quad (4.2)$$

As this cycle treats each water molecule as an individual reactant (in contrast to the cluster cycle) and since water is also the solvent, a correction term for the concentration change from bulk liquid to the standard state in solution, 1 M, is necessary i.e. $\Delta G^{l \rightarrow *}$ = RTln([H₂O]). Where neither of the two above thermodynamic cycles is employed, the reaction free energy is calculated simply as the difference between total product and reactant free energies (defined previously in Eqn. 3.4). Analysis of the electronic structure of some solvated copper(II) complexes was performed with the Natural Bonding Orbital¹⁸³ package, where the natural charge on the metal centre and surrounding ligands was tallied to assess charge transfer to the second solvation shell, if present.

The notation used to describe stereoisomers of metal chelate complexes follows that of Jensen¹⁸⁴. The helical system that results from polydentate ligand complexation is simplified and illustrated in Figure 4-4. A projection of those skew lines, AA and BB, are shown in Figure 4-3, where circles A identify the ligating atoms (which lie on the skew line AA), and B their neighbours (on skew line BB).^{*} This notation is used for all mono, bis and tris-ethylenediaminecopper(II) complexes.



Figure 4-3: Projection of skew lines, AA and BB, from Figure 4-3. Circles A signify ligating atoms, B the neighbouring atom and M the metal centre. Projection of right-handed helix (a) and left-handed helix (b). Notation used for mono, bis and tris metal-ligand complexes.

All images of molecular conformers were generated with Chemcraft,¹⁴⁷ using the Gaussview colour scheme: hydrogen - light grey; carbon - dark grey; nitrogen - blue; oxygen - red; copper - orange.

^{*}In the case of ethylenediamine, A would represent a nitrogen atom, and B a carbon atom.

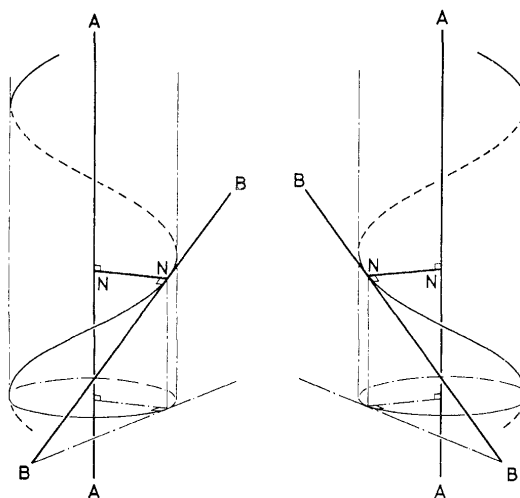


Figure 4-4: The two skew lines AA and BB (non-orthogonal) form a helical system. Line AA is taken as the axis of a cylinder, whose radius is formed by the common normal NN of the two skew lines. The line BB defines the helix upon this cylinder, tangent at the crossing point NN, forming a right-handed helix (**left**) and left-handed helix (**right**), denoted δ and λ , respectively.*

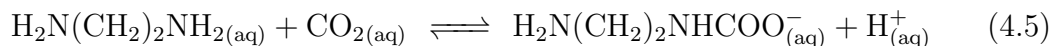
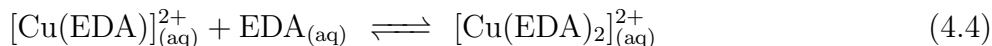
4.2 Results and Discussion

4.2.1 The copper(II) ethylenediamine complex in EMAR

The competing reactions of ethylenediamine with CO_2 and aqueous copper(II) are the means by which the EMAR process is able to moderate aqueous CO_2 content. When aqueous copper(II) is introduced into solution via the anode, the equilibrium is shifted to the right for Eqns. 4.3 and 4.4 and to the left for Eqn. 4.5.[†] While the previous chapter examined the energetics of reaction 4.5, this chapter focuses on the energetics of reactions 4.3 and 4.4.

*Reprinted (adapted) with permission from *Inorganic Chemistry*, Volume 9, Issue 1, 1 January 1970, Kai Arne Jensen, Tentative proposals for nomenclature of absolute configurations concerned with six-coordinated complexes based on the octahedron, 1-5. Copyright (2020) American Chemical Society. Copyright license in Appendix A.

[†]Where the ratio of $\text{Cu:EDA} \gg 3$, the trisethylenediamine copper(II) complex may form, though this it is not significantly observed in EMAR operation.



The complexation energetics for these reactions have been extensively studied experimentally, where the values from Barbucci et al.¹⁸⁵ are used in the derivation of EMAR thermodynamics by Stern et al.⁴⁴ (and in the process model presented in Chapter 6), and further summarised in a review by Paoletti¹⁸⁶. Few studies have examined these reactions computationally due to challenges in treating the solvation environment and the distortion in copper(II) complexes due to the Jahn-Teller effect, discussed herein.

4.2.2 Modelling copper(II) EDA complexation

4.2.2.1 Gas phase structures and solvent corrections

Initial investigations were performed in gas phase, at the B3LYP/BS2 level with single point solvation corrections applied with the COSMO model. The same initial MMFF94 structures were optimised in the COSMO SCRF to observe any structural changes. The free energy of complexation is calculated with the thermodynamic cycle shown below in Figure 4-5.*

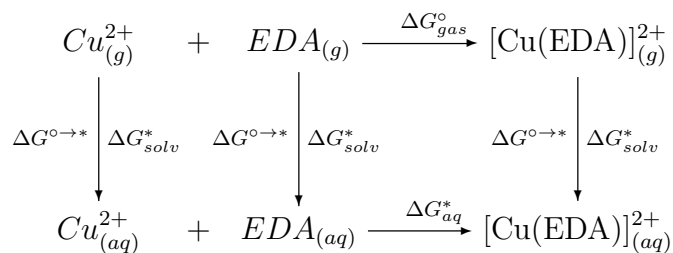


Figure 4-5: Thermodynamic cycle for calculation of the complexation free energy of Cu(II) with EDA

*The entropy of a gas phase copper(II) ion was estimated with the Sackur-Tetrode equation as there are no rotational or vibrational contributions to the partition function.¹⁸⁷ Enthalpy calculated with only electronic energy.

Where, ΔG_{aq}^* is given by:

$$\Delta G_{aq}^* = \Delta G_{gas}^{\circ} + \Delta G_{solv}^*([\text{Cu}(\text{EDA})]^{2+}) - \Delta G_{solv}^*(\text{EDA}) - \Delta G_{solv}^*(\text{Cu}^{2+}) - \Delta G^{\circ \rightarrow *}$$
 (4.6)

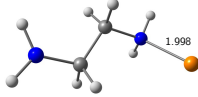
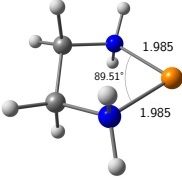
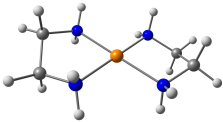
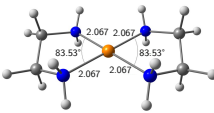
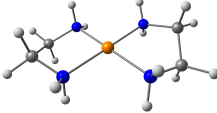
$[\text{Cu}(\text{EDA})]^{2+}$			
G_{rel}	2 (16)	0 (0)	
ΔG_{comp}^*	-236 (-139)	-238 (-155)	
$[\text{Cu}(\text{EDA})_2]^{2+}$			
G_{rel}	$\delta\delta$ 0 (0.04)	$\delta\lambda$ 0 (0)	$\lambda\lambda$ 0 (0.04)
ΔG_{comp}^*	-139 (-103)	-139 (-103)	-139 (-103)

Figure 4-6: Gas phase optimised structures of complexes of copper(II) with EDA and relative energy of conformers (kcal/mol). Relative gas phase free energies quoted below structures and relative aqueous free energies in parenthesis. Distances in Angstroms, angles in degrees.

The structures, relative energies of each conformer and free energies of complexation are presented in Figure 4-6. The difference in free energy between conformers of $[\text{Cu}(\text{EDA})]^{2+}$ in the gas phase accounts for the change in geometry of ethylenediamine (similar to differences in conformer energies Chapter 3), though when solvation contributions are included there is a reasonable change, where the 16 kcal/mol difference indicates stabilisation of the δ complex due to the chelate effect. The differences in stereoisomers of $[\text{Cu}(\text{EDA})_2]^{2+}$ are negligible in both gas phase and with COSMO solvent contributions. When solvation corrections are applied to the free energy of complexation, gas phase values are shifted by 86-97 kcal/mol more positive for the first complexation and 36 kcal/mol

for the second. The massive shift in energetics reveals the significant role of the solvent, though its effects cannot be adequately captured with implicit solvation models alone.* For quick comparison, the experimental value for complexation of a single EDA molecule with copper(II) is -14.44 kcal/mol[†].¹⁸⁵ The complexation of a single amino moiety with the copper(II) centre will be approximately half this value, ca. -7 kcal/mol, which is true for methylamine, CH₃NH₂, where the free energy of complexation determined experimentally is -5.61 kcal/mol,¹⁸⁸ and estimated with a good accuracy by a mixed implicit-explicit solvation method to be -5.58 kcal/mol.¹⁸⁹

In calculating ΔG_{solv}^* , the solvent model must account for the regions of high charge around the divalent metal cation before and after complexation. The solvation free energies of bare Cu(II) determined with the COSMO and SMD models with B3LYP/LANL2TZ+, are -299 and -353 kcal/mol, respectively, where the experimental value is -507 kcal/mol.^{189,190} The SMD[‡] model generally outperforms COSMO as more contributions of the solvation free energy are included, such as the solvent structural effects. The solvation free energy is generally expressed as the sum of $\Delta G_{ENP} + G_{CDS}$, where G_{ENP} encompasses electronic, nuclear and polarisation changes to the free energy and G_{CDS} includes contributions of solvent cavitation, dispersion and local structural changes.¹³⁶ The COSMO model does not account for local changes in the solvent structure while SMD does, which is reflected in the ~ 50 kcal/mol difference in estimates.[§] The accuracy of the total solvation free energy estimate can be improved by explicitly defining at least the first solvation shell around the solute. Metal ions in aqueous media form well-defined first solvation shells, which have long residence times around the central cation.¹⁹¹ Polarised by the metal ion, water molecules in the first solvation shell form strong hydrogen bonds with those in the second shell, which can potentially

*Structures optimised in the COSMO solvent model are not significantly different in geometry to the gas phase geometries shown, where the average equatorial distances in COSMO structures decrease by ~ 0.03 Å. Additionally, the effect of including dispersion corrections was examined in [Cu(EDA)₂]²⁺ complexes by optimising with B3LYP-D3. Here equatorial ligand distances were not significantly impacted, being reduced on average by approximately 0.001 Å.

[†]Extrapolated to -15 kcal/mol at zero ionic strength.

[‡] ΔG_{solv}^* via SMD is quite sensitive to numerical grid integration density, with 0.025 Ha (15.7 kcal/mol) difference between fine and xfine presets in NWChem.

[§]Additionally, COSMO and SMD models use different scaling of atomic Bondi radii in defining the solute cavity. Discussed briefly in Section 2.5

be captured in the G_{CDS} term, though generally the accuracy of a solvation free energy estimate improves as more water molecules are defined explicitly. The complication is that the second solvation shell is less well defined and as such only incremental improvements in the result may be observed at greater computational cost.

4.2.2.2 First solvation shell of Cu^{2+} and $\delta\text{-}[\text{Cu}(\text{EDA})]^{2+}$

A number of computational studies have examined the solvation behaviour of copper (II) with various methods.^{143,182,192–199} The most successful in reproducing experimentally observed structures and solvation dynamics are those that use quantum mechanics to describe at least the first solvation shell around the metal cation. This permits an accurate representation of the Jahn-Teller effect of solvated complexes and charge transfer from ligands to the metal centre.* Due to the d^9 electron configuration of copper(II), the partially filled degenerate e_g^* orbitals split, reducing the symmetry (from O_h to D_h) and the total energy. This manifests as elongation or compression of the octahedral structure, increasing and decreasing the axial bond lengths, respectively, splitting the e_g^* and t_{2g} frontier orbitals according to Figure 4-7. Beyond the first or second solvation shell, the remaining solvation environment can be treated with cheaper methods, either by classical mechanics or an implicit solvation model (e.g COSMO, SMD etc.).

Given the large number of explicitly defined water molecules, a low cost, reasonably accurate density functional or wavefunction method is necessary. Recent reviews have suggested a number of density functionals recommended for general transition metal thermochemistry,^{77,207} where the majority of studies on copper(II) are performed with B3LYP. The following functionals were used to optimise copper(II) with the first explicit solvation shell and its first complexation with EDA: MPWB1K and MPW1B95,²⁰⁸ B3LYP,^{115–118} PW6B95,²⁰⁹ PBE0,²¹⁰ SOGGA11-X,²¹¹ M06-L²¹². The tested functionals are mainly of the hybrid GGA or hybrid mGGA type, with the exception of M06-L which is a local mGGA.†

*The Jahn-Teller distortion of aqueous copper(II) and copper(II) chelate complexes has been extensively studied computationally,^{193,199–206} and is not the focus here.

†GGA - generalised gradient approximation. mGGA - Meta GGA. See Section 2.3 for more detail.

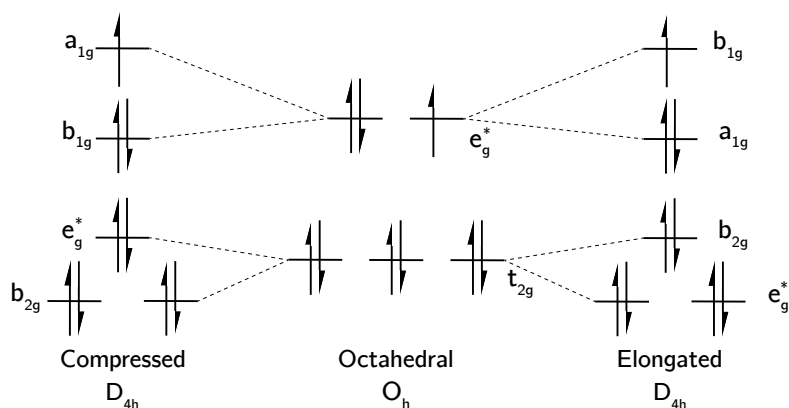


Figure 4-7: Splitting of 3d orbitals of a d^9 configuration due to the Jahn-Teller effect

M06-L has been reported to be reasonably accurate for transitional metal chemistry and at low computational cost due to the lack of exact exchange.²¹² The bond distances of optimised structures with each functional, obtained with the BS2 basis set, are presented in Table 4.1. Exchange-correlation functionals are sorted in order of ascending Hartree-Fock exchange in each functional category i.e. the local M06-L, B3LYP, PBE0, SOGGA11-X (global hybrids), and PW6B95, MPWB1K, MPW1B95 (meta global hybrids). The notation for bond lengths is shown in Figure 4-8(a) with the structures of the first coordination sphere around copper with 6 water ligands (b) and 4 water ligands with one ethylenediamine ligand (c).

All functionals used generate optimum geometries of a 4 + 2 coordination nature (equatorial + axial), where the axial ligand bond lengths are compressed or elongated compared to equatorial ones. Of the functionals tested, three display compressed geometries, M06-L, SOGGA11-X and MPWB1K, with 0, 40.15 and 44 % exact exchange, where excessively high proportions of exact exchange are not recommended for transition metal systems.^{78*} Though the compressed forms may appear as a dynamic Jahn-Teller distortion, they are not observed to be stable in solution. Functionals that generate structures with an elongated distortion

* Additionally, between 10 and 30% exact exchange is recommended for obtaining accurate metal-oxygen bond dissociation energies.²¹⁴

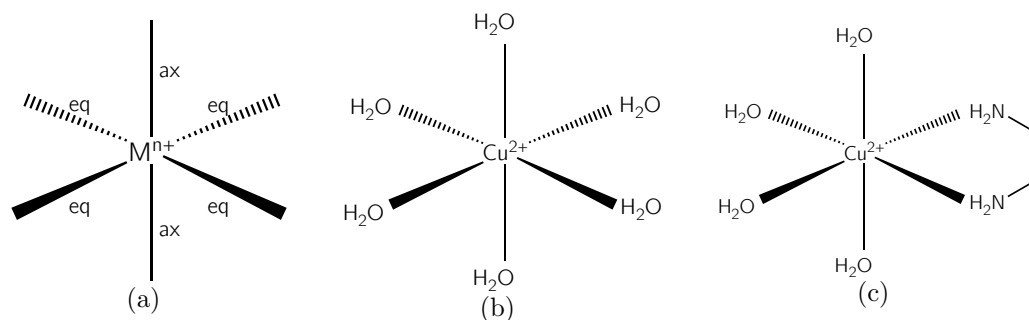


Figure 4-8: Notation for ligand bond locations in copper(II) complexes for the first solvation shell. Equatorial (eq) and axial (ax) ligands denoted around the metal centre (M^{n+}) (a), water occupying all ligand sites in $[\text{Cu}(\text{OH}_2)_6]^{2+}$ (b) and ethylenediamine occupying two equatorial ligand sites with water occupying remaining sites in $[\text{Cu}(\text{EDA})(\text{OH}_2)_4]^{2+}$.

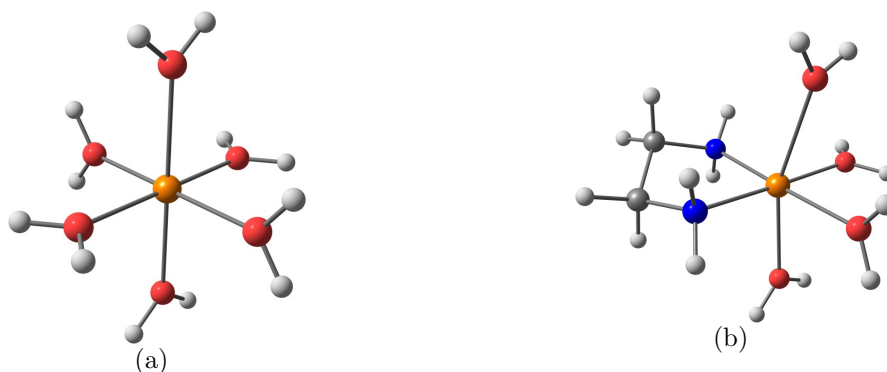


Figure 4-9: Structure of $[\text{Cu}(\text{OH}_2)_6]^{2+}$ (a) and $\delta\text{-}[\text{Cu}(\text{EDA})(\text{OH}_2)_4]^{2+}$ (b) optimised with B3LYP/LANL2TZ+/6-311++G**

provide reasonable geometries for $[\text{Cu}(\text{OH}_2)_6]^{2+*}$, though when two equatorial water ligands are replaced by EDA in the delta configuration, the axial water ligands are displaced further than is experimentally observed. Additionally, the $[\text{Cu}(\text{EDA})(\text{OH}_2)_4]^{2+}$ structure deviates from the regular tetragonally elongated octahedron, where axial water ligands are shifted off the principal axis, shown in Figure 4-9, as more electron density is donated to the metal orbitals via EDA.

The structures generated with B3LYP were further optimised with the disper-

*Where the majority of experiments find elongated octahedral geometries, depending on the ionic environment of the solution.^{200,215,216}

Table 4.1: Ligand bond distances (Å) at optimum geometries for the functionals examined.

Functional		Cu-O _{eq}		Cu-O _{ax}
<hr/>				
[Cu(OH ₂) ₆] ²⁺				
Local mGGA	M06-L	2.146 × 2, 2.154 × 2		1.984 × 2
	B3LYP	2.027 × 2, 2.032 × 2		2.281 × 2
Hybrid GGA	B3LYP ^a	2.017 × 2, 2.037 × 2		2.278 × 2
	B3LYP-D3 ^b	2.016 × 2, 2.034 × 2		2.243 × 2
	PBE0 ^c	2.015 × 2, 2.018 × 2		2.259 × 2
	SOGGA11-X	2.167 × 2, 2.152 × 2		2.079 × 2
Hybrid mGGA	PW6B95	2.018 × 4		2.252 × 2
	MPWB1K	2.143 × 2, 2.156 × 2		2.075 × 2
	MPW1B95	2.019 × 2, 2.008 × 2		2.243 × 2
Experiment ²¹³		1.97(1) × 4		2.26(2) × 2
<hr/>				
		Cu-O _{eq}	Cu-N _{eq}	Cu-O _{ax}
<hr/>				
[Cu(EDA)(OH ₂) ₄] ²⁺				
Local mGGA	M06-L	2.051, 2.070	2.034 × 2	2.371, 2.382
Hybrid GGA	B3LYP	2.058, 2.082	2.039, 2.048	2.417, 2.460
	B3LYP ^a	2.065, 2.057	2.033, 2.035	2.421, 2.355
	B3LYP-D3 ^b	2.058, 2.082	2.041, 2.051	2.356, 2.347
	PBE0 ^c	2.046, 2.069	2.022, 2.032	2.400, 2.382
	SOGGA11-X	2.043, 2.075	2.024, 2.033	2.372, 2.364
Hybrid mGGA	PW6B95	2.053, 2.075	2.032, 2.024	2.395, 2.377
	MPWB1K	2.038, 2.060	2.016, 2.025	2.343, 2.341
	MPW1B95	2.046, 2.067	2.017, 2.025	2.382, 2.366
Experiment ²¹³		1.98(3) × 2	2.00(3) × 2	2.31(2) × 2

^aOptimised in COSMO SCRF.

^bOptimised with B3LYP-D3/6-311(+,+)G(df,pd)/LANL2TZ+ with QChem 5.2

^cOptimised with PBE0/LANL2TZ+/6-311(+,+)G(df,pd) in QChem 5.2.

sion corrections of Grimme et al.¹²¹, and separately within the COSMO SCRF,

with results shown in Table 4.1. The bond distances are not significantly affected by optimising in the COSMO SCRF, though adding dispersion corrections contracts the equatorial and axial ligand distances slightly.

The energetics of the first complex formation were calculated with Eqn. 4.2, where both SMD and COSMO solvent models were used to determine ΔG_{sol}^* , with results presented in Table 4.2.

Table 4.2: Free energies of complexation with EDA (kcal/mol) to form δ -[Cu(EDA)(OH₂)₄]²⁺ with various XC functionals, and with the first solvation shell defined explicitly.

Functional	ΔG_{gas}^o	$\Delta G_{aq}^{* COSMO}$	$\Delta G_{aq}^{* SMD}$
M06-L	-40.6	-32.3	-29.3
B3LYP	-40.4	-32.7	-29.9
B3LYP-D3 ^a	-40.8	-33.5	-32.1
PBE0 ^b	-38.3	-31.1	-29.9
SOGGA11-X	-54.9	-49.1	-46.3
PW6B95	-38.7	-31.2	-28.3
MPWB1K	-55.0	-49.5	-46.7
MPW1B95	-51.7	-44.4	-31.0
Exp.		-14.4 ¹⁸⁵	

^aOptimised with B3LYP-D3/LANL2TZ+/6-311(+,+)G(df,pd) in QChem 5.2.

^bOptimised with PBE0/LANL2TZ+/6-311(+,+)G(df,pd) in QChem 5.2.

The bond lengths in Table 4.1 suggest M06-L yields the compressed conformer of [Cu(OH₂)₆]²⁺, though the calculated complexation free energy is similar to that determined with functionals that yield the elongated form of the same complex; B3LYP, PBE0 and PW6B95. Although SOGGA11-X and MPWB1K functionals display similar geometries to M06-L, they yield complexation energies 15 kcal more negative than M06-L and other functionals with half as much exact exchange. Excluding SOGGA11-X and MPWB1K, by defining the first solvation shell the free energy of complexation is closer to the experimental value by >100 kcal/mol due to an improvement in the description of the solvent. The difference due to the solvent model, often 3-4 kcal/mol, can be attributed to the DFT numerical grid sensitivity, a lack of short-range structural effects considered in the COSMO model, and extensive parameter fitting of the SMD model to reproduce

experimental data.

Given the still large discrepancy in the thermodynamics of EDA complexation to Cu(II) between the present calculated value and experiment, further solvation of each complex is necessary. Moving forward this will be performed with a single functional given the expense of explicitly defining greater than 25 atoms. B3LYP optimised structures show reasonable agreement with experimental data and have been used previously in the hydration of metal cations including copper(II),^{143,182,192,195,197,217} and evaluation of complexation thermochemistry.^{189,218}

Bryantsev et al.¹⁸⁹ demonstrated that as the number of explicitly defined solvent molecules is increased, the free energy of solvation for copper(II) and complexation between copper(II) and methylamine can be accurately estimated. Where they define only the first solvation shell, their results for the complexation of methylamine were approximately ~ 2.5 times more negative than the experimental value, which is also observed here.¹⁸⁹ Similarly, the thermodynamic cycle presented in Figure 4-2 was used to determine the free energy of complexation of copper(II) with ethylenediamine. The solvated structures of copper(II) necessary to calculate the complexation free energy were also used in the cluster cycle (Figure 4-1) to indicate how well the ion is solvated.

4.2.2.3 Beyond the first solvation shell

Bryantsev et al.¹⁴³ identified that specific numbers of explicit water molecules form low energy clusters, i.e. $(\text{H}_2\text{O})_n$ where $n = 6, 10, 14, 18$. These same water clusters were optimised at the level of theory identified above, with structures presented in Figure 4-10.

Solvated structures of copper(II) were then generated with the same number of water molecules as above, in gas phase and within the COSMO SCRF. While Bryantsev et al.¹⁴³ used COSMO optimised structures to estimate the free energy of solvation of copper(II), it is not uncommon in the literature to optimise in the gas phase and use single point solvation corrections. This is cheaper computationally but can yield erroneous results as optimisation in the gas phase can generate unfavourable water clustering, as seen in Chapter 3. For this reason, both gas phase and COSMO structures were optimised independently and their

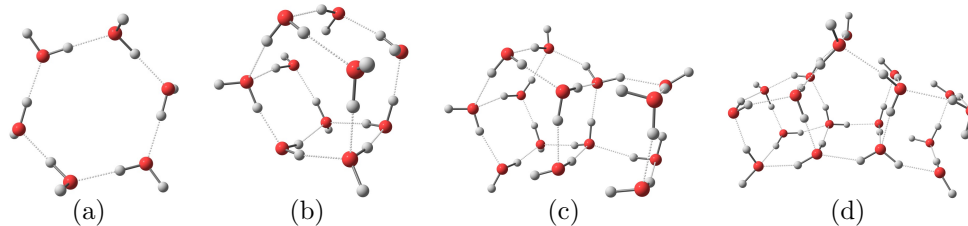


Figure 4-10: Low energy water clusters used in estimation of solvation free energy of copper(II) and its' complexes; $(\text{H}_2\text{O})_6$ (a), $(\text{H}_2\text{O})_{10}$ (b), $(\text{H}_2\text{O})_{14}$ (c), $(\text{H}_2\text{O})_{18}$ (d). Optimisation was performed in the gas phase with B3LYP/BS2.

structures and relative energies in gas phase and solvent are compared. Structural parameters for each are summarised and compared in Table 4.3, with gas phase and COSMO structures presented in Figure 4-11 and 4-12, respectively.

Table 4.3: Structural parameters in solvated Cu(II), $[\text{Cu}(\text{OH}_2)_n]^{2+}$. Comparison of average ligand distances between gas phase and COSMO optimised structures (\AA)

$(\text{H}_2\text{O})_n$	Gas phase		COSMO SCRF	
	Cu-O _{eq}	Cu-O _{ax}	Cu-O _{eq}	Cu-O _{ax}
6	2.030	2.281	2.027	2.278
10	2.011	2.364	2.015 ^a	2.414 ^a
14	2.026	2.319	2.068	2.355
18	2.025	2.374	2.045 ^a	2.309 ^a
Avg.	2.023	2.335	2.045	2.359
Exp. ²¹³	Cu-O _{eq}	1.97(1)	Cu-O _{ax}	2.26(2)

^aOptimised with B3LYP/BS1 with single point energy at B3LYP/BS2.

There is no clear trend in the equatorial and axial bond lengths as the number of explicit water molecules is increased for gas phase or COSMO SCRF optimised structures. Every structure obtained with B3LYP yields ligand bonds longer than the EXAFS[†] experimental data for an aqueous copper(II) nitrate solution.²¹³ Persson et al.²⁰⁰ showed that the variation of hydrated copper(II) bond lengths in the presence of various anions is minimal (0.005 - 0.01 \AA), although Schwenk and Rode¹⁹² state a “confidence area” exists for the available EXAFS data in the

[†]X-ray absorption fine structure

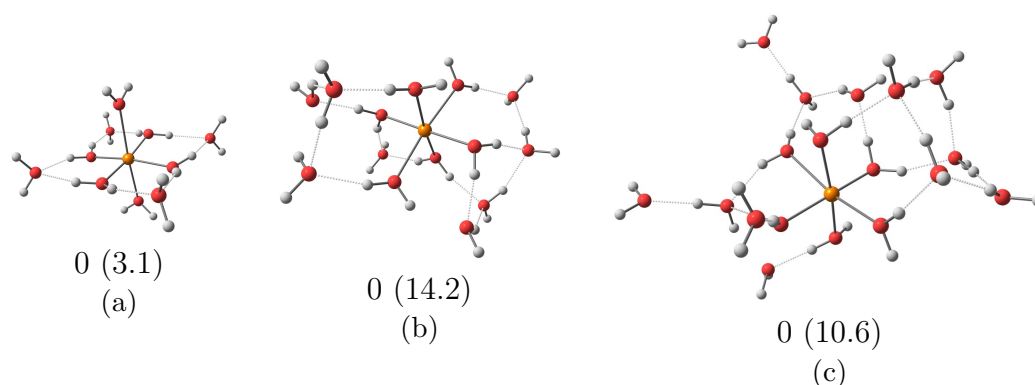


Figure 4-11: Gas phase structures of solvated Cu^{2+} . $[\text{Cu}(\text{OH}_2)_{10}]^{2+}$ (a), $[\text{Cu}(\text{OH}_2)_{14}]^{2+}$ (b), $[\text{Cu}(\text{OH}_2)_{18}]^{2+}$ (c). Relative gas phase free energy underneath structures (zero as they are the reference), relative aqueous free energy in parenthesis (w.r.t. COSMO optimised structures in Figure 4-12) (kcal/mol). Hydrogen bonds are represented by dashed lines.

literature for aqueous copper(II) of 1.88-2.02 Å for Cu-O_{eq} and 2.11-2.43 Å for Cu-O_{ax} .

As more water is added to the system, however, the gas phase and COSMO SCRF structures deviate more in the second solvation shell. In general, the average hydrogen bonded distance between water in the first and second shell decreases as more water is included; from 1.951 Å with 10 H_2O , 1.868 Å with 14 H_2O to 1.806 Å in the gas phase, and 1.874 Å to 1.816 Å with 10 and 14 H_2O , respectively, in the COSMO SCRF. The COSMO SCRF optimised structures form tighter hydrogen bonded networks between solvation shells, facilitating more significant through-space charge transfer. When COSMO solvent contributions are applied to gas phase structures, the resulting aqueous free energies are consistently higher than those directly optimised in the COSMO SCRF. With the above structures, the energetics of copper(II) solvation were determined by the cluster cycle (in Figure 4-1) with both gas phase and COSMO SCRF structures - results are presented in Table 4.4.

All methods used to determine the solvation free energy, whether with gas phase or COSMO SCRF optimised structures, trend (approximately) exponentially toward a bulk limit. Gas phase structures with solvation corrections converge around -501 kcal/mol, approximately 1% off the estimated experimen-

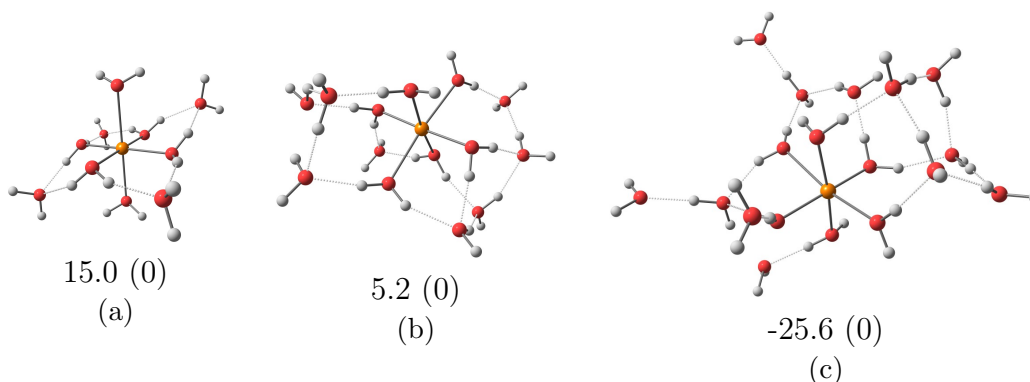


Figure 4-12: COSMO optimised structures of solvated Cu^{2+} . $[\text{Cu}(\text{OH}_2)_{10}]^{2+}$ (a), $[\text{Cu}(\text{OH}_2)_{14}]^{2+}$ (b), $[\text{Cu}(\text{OH}_2)_{18}]^{2+}$ (c). Relative gas phase free energy underneath structures (w.r.t. GP optimised structures in Figure 4-11) and relative aqueous free energy in parentheses (zero as they are the reference) (kcal/mol). Hydrogen bonds are represented by dashed lines.

tal value -507 ± 4 kcal/mol.^{146,190} Estimation of the solvation free energy from COSMO SCRF structures does not converge by $n = 18$, though is closer to the accepted experimental value than was determined from the gas phase structures, at $n = 18$. If fit to an exponential decay*, the projected solvation free energy of copper(II) determined with COSMO/B3LYP, $\Delta G_{\text{solv}}^*(n \rightarrow \infty)$, is -520.8 kcal/mol. This data is represented graphically in Figure 4-15 (left).

In order to estimate the first complexation energy, an accurate estimate of the solvation free energy of the $[\text{Cu}(\text{EDA})]^{2+}$ complex is necessary. The two stereoisomers of solvated $[\text{Cu}(\text{EDA})]^{2+}$ are δ and λ , as depicted in Figure 4-3. With a full first solvation shell i.e. $[\text{Cu}(\text{EDA})(\text{OH}_2)_4]^{2+}$ the δ and λ conformers differ by 0.7 kcal/mol at the COSMO-B3LYP/BS2 level in favour of the δ conformer. The cluster thermodynamic cycle was then applied to determine ΔG_{solv}^* for δ - $[\text{Cu}(\text{EDA})]^{2+}$, with structures optimised in the gas phase and in the COSMO SCRF, which are presented in Figure 4-13 and 4-14, respectively, and relevant structural parameters are summarised in Table 4.5. As with solvated copper(II) structures, the relative energy in gas phase and COSMO SCRF is positioned below the structure.

Given water is a stronger hydrogen bond donor than ethylenediamine, the

* $\Delta G_{\text{solv}}^*(n) = \Delta G_{\text{solv}}^*(n \rightarrow \infty) + ae^{bn}$, where $a = -70.73$ kcal/mol and $b = -0.1013$.

Table 4.4: Solvation free energy of Cu^{2+} ion calculated with the cluster cycle (kcal/mol)

Gas phase optimisation					
$(\text{H}_2\text{O})_n$	$\Delta G_{\text{gas bind}}^\circ$	$\Delta G_{\text{solv}}^*(\text{Cu}(\text{H}_2\text{O})_n)^{2+}$		$\Delta G_{\text{solv}}^*(\text{Cu}^{2+})$	
		SMD	COSMO	SMD	COSMO
0				-352.7	-299.3
6	-306.3	-195.5	-189.3	-483.9	-481.3
10	-352.3	-168.0	-161.4	-495.0	-493.2
14	-373.4	-157.3	-150.8	-501.1	-500.6
18	-383.3	-150.9	-143.3	-501.4	-500.9
COSMO SCRF optimisation					
$(\text{H}_2\text{O})_n$	$\Delta G_{\text{gas bind}}^\circ$	$\Delta G_{\text{solv}}^*(\text{Cu}(\text{H}_2\text{O})_n)^{2+}$		$\Delta G_{\text{solv}}^*(\text{Cu}^{2+})$	
6	-290.5		-205.7		-482.6
10	-334.2		-180.2		-493.7
14	-342.3		-187.1		-505.7
18 ^a	-357.7		-176.2		-508.2
$n \rightarrow \infty$					-520.8
Exp.					-507.0 \pm 4 ¹⁸⁹

^aOptimised with B3LYP/BS1, SP energy at B3LYP/BS2.

majority of water molecules within the second solvation shell form hydrogen bonds with those in the first. Only with 18 water molecules is the metal sufficiently solvated that water in the second solvation shell begins to form weak hydrogen bonds with ethylenediamine amino groups. Differences in the hydrogen bonding between solvation shells in gas phase and COSMO SCRF structures of $[\text{Cu}(\text{EDA})(\text{OH}_2)_n]^{2+}$ are not as significant as those in solvated copper(II). The average hydrogen bonding distance in gas phase structures increases as the number of water molecules is increased, from 1.738 Å, to 1.837 Å to 1.859 Å in moving from 6, to 10, to 14 H_2O , while there is no trend for COSMO SCRF structures, from 1.825 Å to 1.806 Å to 1.830 Å in 6, to 10, to 14 H_2O . The average hydrogen bonding distance correlates well with the natural charge on the metal centre and four equatorial ligands, where it reduces more slowly than for copper(II) alone as charge transfer is blocked through the hydrophobic backbone of ethylenedi-

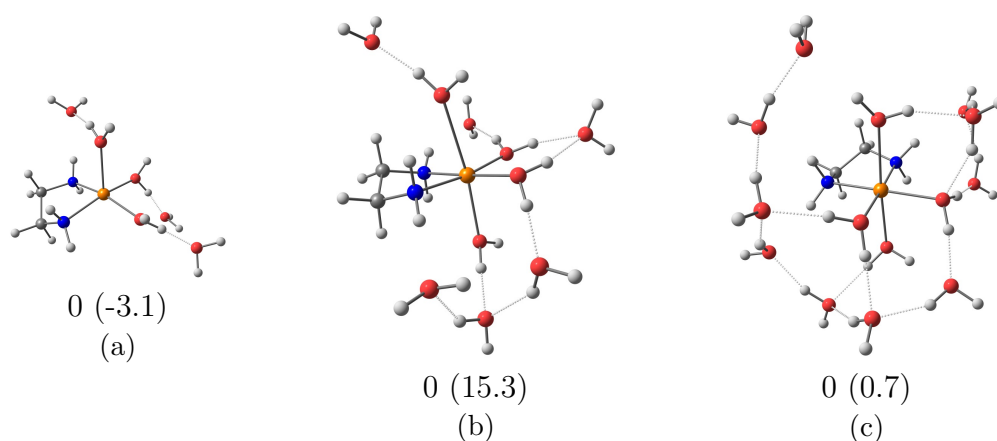


Figure 4-13: Gas phase structures of solvated $[\text{Cu}(\text{EDA})]^{2+}$. $\delta\text{-}[\text{Cu}(\text{EDA})(\text{OH}_2)_6]^{2+}$ (a), $\delta\text{-}[\text{Cu}(\text{EDA})(\text{OH}_2)_{10}]^{2+}$ (b), $\delta\text{-}[\text{Cu}(\text{EDA})(\text{OH}_2)_{14}]^{2+}$ (c). Relative gas phase free energy underneath structures (zero as they are the reference), with relative aqueous free energy in parenthesis (w.r.t. COSMO optimised structures in Figure 4-14) (kcal/mol). Hydrogen bonds are represented by dashed lines.

amine.* As EDA is a stronger σ donor than H_2O , there is an increase in the axial water ligand distance, though it is more significant in the structures observed here than from experiment.

The solvation free energy of $\delta\text{-}[\text{Cu}(\text{EDA})]^{2+}$ determined with the cluster cycle, calculated for both gas phase and COSMO SCRF structures, is presented in Table 4.6, and displayed in Figure 4-15 (right). Convergence in the solvation free energy requires fewer explicit water molecules here compared to bare copper(II) as the complexing ethylenediamine ligand donates reasonable charge to copper(II), i.e. the natural charge on copper in $[\text{Cu}(\text{OH}_2)_6]^{2+}$ is 1.55 versus 1.35 in $[\text{Cu}(\text{EDA})(\text{OH}_2)_4]^{2+}$.[†] The total charge on copper and coordinated equatorial ligands in the $[\text{Cu}(\text{EDA})(\text{OH}_2)_n]^{2+}$ complex compared to that of $[\text{Cu}(\text{OH}_2)_n]^{2+}$ is presented in Figure 4-16.

Evaluating solvation free energies with COSMO SCRF conformers tends to yield smoother and faster convergence behaviour, such that evaluation with 18 water molecules was not deemed necessary. The difference between gas phase

*Although the charge on the metal centre and equatorial ligands of $[\text{Cu}(\text{OH}_2)_{18}]$ is greater than $[\text{Cu}(\text{OH}_2)_{14}]$, slightly more charge has been donated to the metal centre as the natural charge on Cu shifts from 1.47 to 1.46 moving from 14 to 18 explicit water molecules.

[†]Natural atomic charges determined with NBO 6.0.

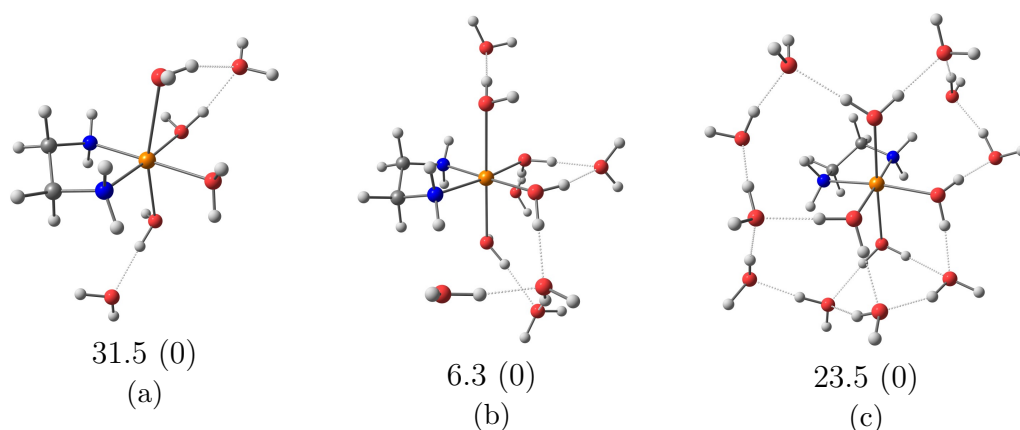


Figure 4-14: COSMO optimised structures of solvated δ -[Cu(EDA)]²⁺. δ -[Cu(EDA)(OH₂)₆]²⁺ (a), δ -[Cu(EDA)(OH₂)₁₀]²⁺ (b) δ -[Cu(EDA)(OH₂)₁₄]²⁺ (c). Relative gas phase free energy underneath structures (w.r.t. GP optimised structures in Figure 4-13), with relative aqueous free energy in parenthesis (zero as they are the reference) (kcal/mol). Hydrogen bonds are represented by dashed lines.

and COSMO SCRF evaluation of ΔG_{solv}^* for copper(II) is less significant than for [Cu(EDA)]²⁺ as the first solvation shell is more well defined for the bare ion. The inconsistent solvation behaviour of gas phase [Cu(EDA)]²⁺ on increasing explicit water, is in part due the asymmetric distribution of water molecules around the copper complex, which avoids interaction with the hydrophobic backbone of ethylenediamine. Shifts of >15 kcal in ΔG_{solv}^* , from $n = 6$ to 10, and from $n = 10$ to 14 (see Table 4.6 and Figure 4-15) would be carried through to estimates of complexation energies, preventing an accurate extrapolation to a bulk limit. In some cases, solvated structures with the BS2 basis set did not fully converge, marked in Table 4.5. Their energy was evaluated at the BS2 level for BS1 optimised structures. To check the difference in energy, the δ -[Cu(EDA)(OH₂)₆]²⁺ optimised with COSMO at the BS1 level, with single point energy evaluated at the BS2 basis set is approximately 1.4 kcal/mol higher in free energy than the COSMO structure fully optimised at the BS2 level. This limits the accuracy of the solvation free energy prediction at a specific number of water molecules, and will shift estimates of an extrapolated value. Extrapolating the solvation free energy with the COSMO SCRF structures (assuming exponential decay with increasing

Table 4.5: Structural parameters in solvated δ -[Cu(EDA)]²⁺. Comparison of average ligand distances between gas phase and COSMO optimised structures (Å)

$(\text{H}_2\text{O})_n$	Gas phase				COSMO SCRFF			
	Cu-N _{eq}	Cu-O _{eq}	Cu-O _{ax}	Cu-C	Cu-N _{eq}	Cu-O _{eq}	Cu-O _{ax}	Cu-C
6	2.044	2.070	2.439	2.895	2.034 ^a	2.061 ^a	2.388 ^a	2.862 ^a
10	2.042	2.037	2.523	2.894	2.038	2.057	2.429	2.876
14	2.046	2.052	2.444	2.888	2.047 ^a	2.054 ^a	2.487 ^a	2.887 ^a
Exp.					2.00(3)	1.98(3)	2.31(2)	2.88(1)

^aOptimised at the COSMO/B3LYP/BS1 level of theory with single point energies at COSMO/B3LYP/BS2.

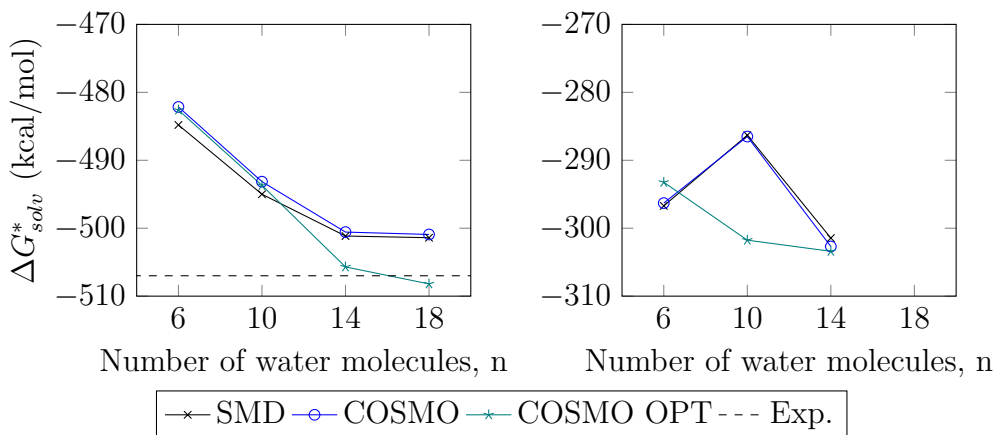


Figure 4-15: Trend in solvation free energy of Cu^{2+} (left) and Cu(EDA)^{2+} (right) as the number of explicit water molecules is increased.

water molecules as before) yields a best estimate of -306.2 kcal/mol.*

4.2.2.4 Complexation energetics

Given the solvation behaviour of both reactant and product can be reasonably well captured by the methods employed above, the first complexation free energy can be estimated in the bulk limit and compared to experimental results. The aqueous complexation free energy was determined for the λ conformer of Cu(EDA) with the thermodynamic cycle in Figure 4-2 and Eqn. 4.2. Structures

* $\Delta G_{solv}^*(n) = \Delta G_{solv}^*(n \rightarrow \infty) + ae^{bn}$, where $a = -95.97$ kcal/mol and $b = -0.3116$.

Table 4.6: Solvation free energy of δ -[Cu(EDA)]²⁺ complex calculated with the cluster cycle using gas phase optimised structures (kcal/mol)

		Gas phase optimisation			
(H ₂ O) _n	$\Delta G_{\text{gas bind}}^{\circ}$	$\Delta G_{\text{solv}}^*([\text{Cu}(\text{EDA})(\text{H}_2\text{O})_n]^{2+})$		$\Delta G_{\text{solv}}^*([\text{Cu}(\text{EDA})]^{2+})$	
		SMD	COSMO	SMD	COSMO
0				-235.9	-217.5
6	-145.8	-168.0	-164.0	-296.7	-296.3
10	-158.9	-152.7	-148.2	-286.3	-286.5
14	-183.4	-147.7	-142.9	-301.5	-302.7
		COSMO SCRF optimisation			
(H ₂ O) _n	$\Delta G_{\text{gas bind}}^{\circ}$	$\Delta G_{\text{solv}}^*([\text{Cu}(\text{EDA})(\text{H}_2\text{O})_n]^{2+})$		$\Delta G_{\text{solv}}^*([\text{Cu}(\text{EDA})]^{2+})$	
6	-290.0		-69.3		-293.2
10	-298.8		-71.4		-301.8
14	-300.7		-71.9		-303.4
$n \rightarrow \infty$					-306.2

of λ -[Cu(EDA)(OH₂)_{n-2}]²⁺, where $n = 6, 10, 14, 18$, were generated to determine the energetics, while the same structures used in the determination of ΔG_{solv}^* for copper(II) we used. Given the solvation free energy of δ -[Cu(EDA)]²⁺ was effectively converged with 14 explicit water molecules, estimates beyond $n - 2 = 14$ were not considered necessary.

As mentioned above, if gas phase structures are used in the estimate of the complexation free energy, the errors in estimating the free energy of solvation are carried through, resulting in no clear convergence behaviour of the estimate as the number of water molecules is increased. In contrast, when COSMO SCRF structures are used there is apparent convergent behaviour, where if the same decaying exponential behaviour is assumed in the complexation free energy, the bulk limit is -22.75 kcal/mol.* This extrapolated value is remarkably similar to that determined with gas phase structures where 6 or 10 water molecules are explicitly defined with solvation corrections by the SMD solvent model, the cause of which is likely a fortuitous cancellation in errors in solvation free energies. Al-

* $\Delta G_{\text{aq}}^*(n) = \Delta G_{\text{aq}}^*(n \rightarrow \infty) + ae^{bn}$, where $a = -47.45$ kcal/mol and $b = -0.2642$.

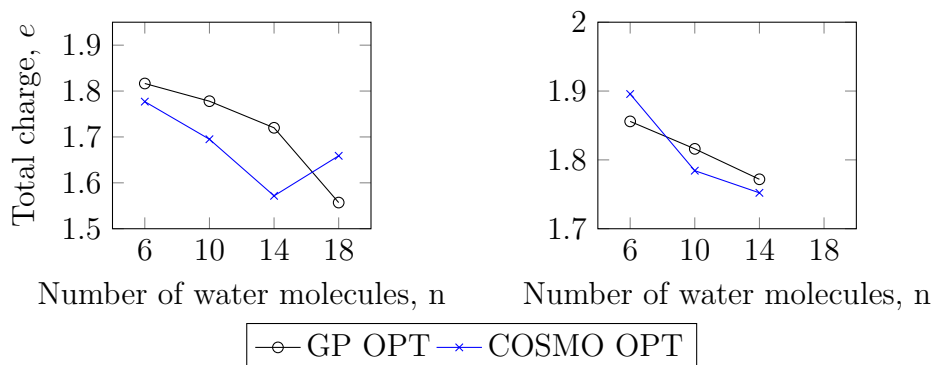


Figure 4-16: Natural charge on Cu(II) and four equatorial water ligands in $[\text{Cu}(\text{OH}_2)_n]^{2+}$ (left), and natural charge on Cu(II) and two equatorial water ligands and equatorial chelated EDA in $[\text{Cu}(\text{EDA})(\text{OH}_2)_n]^{2+}$ (right).

though the complexation free energy estimate is significantly lowered by explicitly defining at least the first solvation shell, it still more than 10 kcal lower than the accepted experimental value of -14.4 kcal/mol. This could suggest that the environment around aqueous copper(II) is not simply water but contains counter ions within the first or second solvation shell that are replaced or displaced on complexation with ethylenediamine. The majority of experiments determining the complexation energetics of Cu^{2+} with ethylenediamine (summarised by Paoletti¹⁸⁶) use a supporting electrolyte to facilitate potentiometric methods, typically a nitrate salt. Investigation of the solution structure of copper(II) nitrate suggests inner sphere ion pairing between Cu^{2+} and NO_3^- , with separation distances of $r_{\text{Cu}^{2+}-\text{N}}$ of 3.03 Å at 1.5 M $\text{Cu}(\text{NO}_3)_2$, placing nitrate ions in the second solvation shell.²¹⁹ The displacement of such an anion could explain some of the discrepancy observed here, though the density functional is most likely to blame. The inclusion of dispersion corrections improves complexation free energy estimates relative to CCSD(T)/CBS methods,²²⁰ which if used to calculate the pK_a of copper(II) complexes, are accurate to within one pK_a unit.¹⁹⁶ The deficiency of the computational method and neglect of counter ions in the second solvation shell result in the difference between the best estimate here of -22.75 and the experimental value of -14 kcal/mol for the first complexation free energy.

Table 4.7: Free energies of EDA complexation with $[\text{Cu}(\text{OH}_2)_n]^{2+}$, forming λ - $[\text{Cu}(\text{EDA})]^{2+}$ (kcal/mol). Complexation free energy, $\Delta G_{(aq)}^*$, is sum of gas phase binding free energy, $\Delta G_{\text{gas bind}}^\circ$, differential solvation free energy, $\Delta\Delta G_{\text{solv}}^*$, and concentration correction terms, $\Delta G^{\circ \rightarrow *}$ and $\Delta G^{* \rightarrow l}$.

		Gas phase optimisation			
		$\Delta\Delta G_{\text{solv}}^*$		ΔG_{aq}^*	
$(\text{H}_2\text{O})_n$	$\Delta G_{\text{gas bind}}^\circ$	SMD	COSMO	SMD	COSMO
0	-222.0	121.7	82.5	-102.2	-141.4
6	-41.3	12.1	1.0	-22.6	-33.7
10	-28.2	-0.6	-2.7	-22.1	-24.3
14	-40.2	0.5	-1.1	-33.0	-34.6
18	-31.0	-3.5	-5.4	-27.8	-29.7
		COSMO SCRF optimisation			
$(\text{H}_2\text{O})_n$	$\Delta G_{\text{gas bind}}^\circ$	$\Delta\Delta G_{\text{solv}}^*$		ΔG_{aq}^*	
6	-42.1	3.1		-32.4	
10	-28.1	-5.1		-26.5	
14	-13.3	-16.9		-23.6	
$n \rightarrow \infty$				-22.75	
Exp.		-14.4 ¹⁸⁵			

4.2.2.5 Effect of hydroxo ligands

Given the pK_a of aqueous copper(II) is 7.95,²²¹ and the majority of experiments are performed with excess ethylenediamine (pK_a 7 and 10), experimental values for the complexation free energy may conflate with contributions from $[\text{Cu}(\text{OH})]^+$ and hydroxo-bridged copper(II) complexes.¹⁸⁵ Given computational restrictions and the efficacy of defining only the first solvation shell in previous thermochemical estimates, the effect of substituting a hydroxo ligand for a single water ligand on the complexation free energy, was examined with only the first solvation shell defined, and using gas phase optimised structures with SMD solvent corrections. Ideally, the convergence behaviour as the number of water molecules is increased would be examined. The structures obtained, of $[\text{Cu}(\text{OH}_2)_4(\text{OH})]^+$ and $[\text{Cu}(\text{EDA})(\text{OH}_2)_2(\text{OH})]^+$, are presented in Figure 4-17.

The five-fold coordination structure of $[\text{Cu}(\text{OH})(\text{OH}_2)_5]^+$ agrees well with

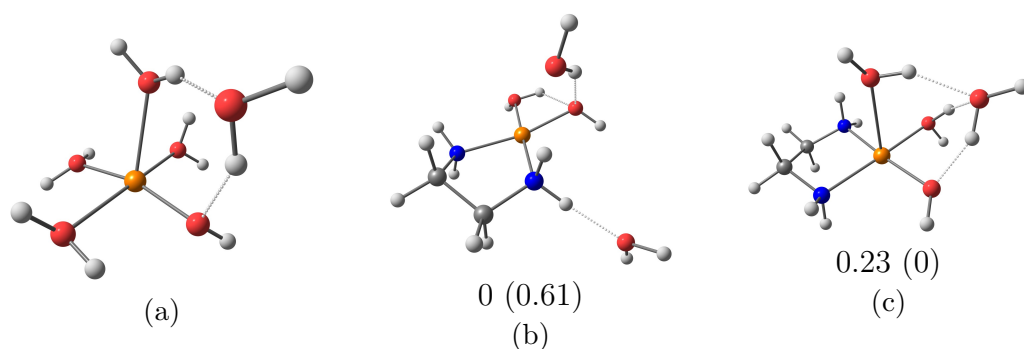


Figure 4-17: Gas phase structures showing complexation of EDA with $[\text{Cu}(\text{OH})]^+$. $[\text{Cu}(\text{OH})(\text{OH}_2)_5]^+$ (a), $4c \delta\text{-}[\text{Cu}(\text{OH})(\text{EDA})(\text{OH}_2)_3]^+$ (b), $5c \lambda\text{-}[\text{Cu}(\text{OH})(\text{EDA})(\text{OH}_2)_3]^+$ (c). Relative gas phase free energy underneath structures, with relative aqueous free energy with SMD contribution in parenthesis (kcal/mol). Hydrogen bonds are represented by dashed lines.

Table 4.8: Complexation energetics of ethylenediamine with $[\text{Cu}(\text{OH})(\text{OH}_2)_5]^+$ (kcal/mol).

Conformer	Gas phase optimisation		
	$\Delta G_{\text{gas bind}}^{\circ}$	$\Delta\Delta G_{\text{solv}}^*$	$\Delta G_{\text{complex}}^*$
$4c \delta\text{-}[\text{Cu}(\text{EDA})(\text{OH})(\text{OH}_2)_3]^+$	-27.2	-3.8	-24.3
$5c \delta\text{-}[\text{Cu}(\text{EDA})(\text{OH})(\text{OH}_2)_3]^+$	-30.0	-3.5	-26.9

previous computational studies into the hydrolysis behaviour of aqueous copper(II).¹⁸⁹ The difference between four- and five-fold coordination geometries of $[\text{Cu}(\text{OH})(\text{EDA})(\text{OH}_2)_3]^+$ in the gas phase and with SMD corrections applied is less than RT, and given the labile nature of axial ligands on copper(II) both forms are likely to coexist in solution. As the free energy of ethylenediamine complexation into $[\text{Cu}(\text{OH})(\text{OH}_2)_5]^+$ is more negative, and therefore more favourable than that calculated with only solvated copper, the deviation from experimental complexation energies cannot be attributed to hydroxo ligand substitution.

The free energy of hydrolysis, $\Delta G_{\text{hydr, aq}}^*$, or successive deprotonation free energy of $[\text{Cu}(\text{OH}_2)_6]^{2+}$ can be determined via the direct method outlined in Chapter 3 and Eqn. 3.10. With just the first solvation shell explicitly defined, and structures optimised in the COSMO SCRF, the first free energy of hydrolysis of $[\text{Cu}(\text{OH}_2)_6]^{2+}$ is 1.7 kcal/mol, and the experimental value, 10.85 ± 0.28 kcal/mol.²²¹

The poor estimate for the hydrolysis free energy translates to a low pK_a for the complex, 1.25, whereas the experimental value is 7.95.²²¹ This suggests an over-stabilisation of hydroxo complexes by B3LYP. In fact, Bryantsev et al.¹⁸⁹ demonstrated that even with 18 explicitly defined water molecules, accurate estimates of the successive free energies of Cu(II) hydrolysis cannot be determined with B3LYP. In contrast, with COSMO/CCSD(T)/aug-cc-pVDZ with 6 water molecules, Jackson et al.¹⁹⁶ determined the pK_a of $[\text{Cu}(\text{OH}_2)_6]^{2+}$ to within 1 unit.

4.2.2.6 Bisethylenediaminecopper(II) isomers

Given the ratio of EDA to Cu(II) in EMAR operation, the bisethylenediamine copper(II) complex, $[\text{Cu}(\text{EDA})_2]^{2+}$, will be a significant species in solution. The relative stability of its' isomers have been determined and presented in Table 4.9. Additionally, the four most stable isomers found are displayed in Figure 4-18.

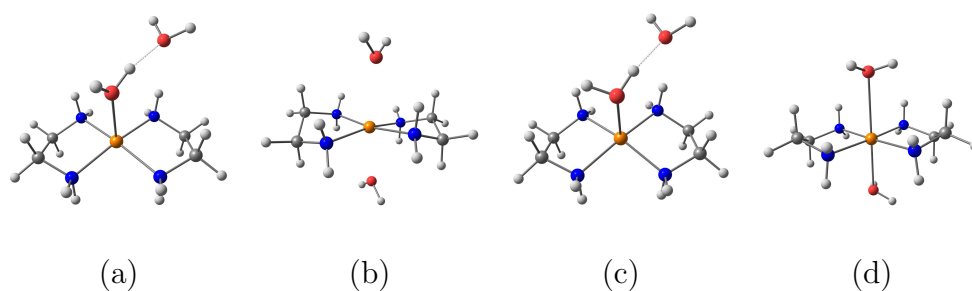


Figure 4-18: Lowest energy conformers of $[\text{Cu}(\text{EDA})_2(\text{OH}_2)_2]^{2+}$. Optimised in gas phase 5c- $\lambda\delta$ (a), 6c- $\lambda\delta$ (b) and in COSMO SCRF 5c- $\lambda\delta$ (c), 6c- $\lambda\delta$ (d). Hydrogen bonds are represented by dashed lines.

Five-fold coordinated structures are more favoured in the gas phase, while COSMO optimised structures show no preference. As two more water ligands are replaced by ethylenediamine, a stronger σ donating ligand, further elongation of remaining axial water ligands is observed. Though the quoted experimental reference suggests axial separation of 2.36Å,²¹³ additional studies find axial elongations as large as 2.92Å,²²² where the $[\text{Cu}(\text{EDA})_2]^{2+}$ complex can effectively be considered to be square planar, as seen in the structure represented in Figure 4-18(b). The effect of replacing a water ligand with a hydroxo ligand was also

Table 4.9: Relative free energy of bisethylenediamine copper(II) complexes (kcal/mol) with average ligand distances (Å). Here, #c indicates the number of coordinated ligands around the central Cu(II) ion, and δ and λ labels indicate EDA conformation (see Figure 4-3).

Conformer	Cu-N _{eq}	Cu-O _{ax}	Rel. Free Energy	
Gas phase				
6c $\delta\delta$	2.068	2.702	2.58	
6c $\lambda\delta$	2.067	2.779	2.08	
6c $\lambda\lambda$	2.068	2.702	2.55	
5c $\delta\delta$	2.081	2.332	0.64	
5c $\lambda\delta$	2.080	2.337	0	
5c $\lambda\lambda$	2.079	2.335	0.11	
Conformer	Cu-N _{eq}	Cu-O _{ax}	Cu-N _{ax}	Rel. Free Energy
COSMO SCRF				
6c $\delta\delta$	2.057	2.683	-	3.9
6c $\lambda\delta$	2.054	2.586	-	0.4
6c $\lambda\lambda$	2.057	2.602	-	4.6
5c $\delta\delta$	2.056	2.368	-	0.2
5c $\lambda\delta$	2.059	2.357	-	0
6c $\lambda\lambda^a$	2.174	2.407	2.023	10.5
Experiment ²¹³	2.02(1)	2.36(2)		

^aConformer 6c-cis- $\lambda\lambda$ -[Cu(EDA)₂(OH₂)₂]²⁺ has EDA in cis position. In all other conformers, EDA are trans to each other.

examined, though not with the same exhaustive isomer search. The structures and relative energies of two low energy [Cu(EDA)(OH)(OH₂)₃]⁺ conformers are shown in Figure 4-19.

The combined complexation energetics of EDA into δ -[Cu(EDA)(OH₂)₄]²⁺ and λ -[Cu(EDA)(OH)(OH₂)₃] complexes are summarised in Table 4.10. The second complexation is significantly more favourable to copper complexes with hydroxo ligands present, though the difference in free energy between the first and second complexation of EDA to only water and EDA surrounded metal centres raises the validity of the relative comparison. Experimental results suggest the first complexation of EDA into copper(II) is 2 kcal more favourable than the subsequent complexation reaction, though results generated with just the first

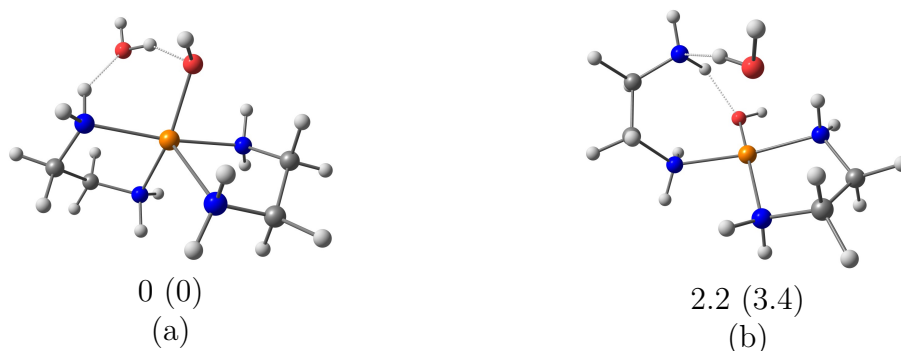


Figure 4-19: Lowest energy conformers of $[\text{Cu}(\text{EDA})_2(\text{OH})(\text{OH}_2)]^{2+}$. Optimised in gas phase with SMD solvent corrections added. Relative gas phase free energy below structure and relative aqueous free energy in parenthesis. 5c (a), 4c (b). Hydrogen bonds are represented by dashed lines.

Table 4.10: Complexation energetics of ethylenediamine into $\delta\text{-}[\text{Cu}(\text{EDA})(\text{OH}_2)_4]^{2+}$ and $\lambda\text{-}[\text{Cu}(\text{EDA})(\text{OH})(\text{OH}_2)_3]$ (kcal/mol).

Conformer	Gas phase optimisation		
	$\Delta G_{\text{gas bind}}^{\circ}$	$\Delta\Delta G_{\text{solv}}^*$	$\Delta G_{\text{complex}}^*$
$[\text{Cu}(\text{EDA})_2(\text{OH}_2)_2]^{2+}$ 6c- $\delta\lambda$	-35.2	-0.1	-27.6
$[\text{Cu}(\text{EDA})_2(\text{OH})(\text{OH}_2)]^+$ 4c	-12.4	-4.6	-10.3
5c	-10.2	-4.1	-7.6

solvation shell here see a reversal in that trend, with the second complexation more favourable than the first by 6 kcal/mol. Imbalances in estimates of the solvation free energy of reactant and product complexes can cause such discrepancies. Irregular coordination geometries and hydrophobic ligands prevent charge transfer beyond the first solvation shell, reducing the accuracy of the solvation free energy estimate.

4.2.3 Ethylenediamine carbamate dissociation

To bring the focus back to the EMAR process, the reaction free energy between the carbamates of ethylenediamine, formed by absorbing natural gas contami-

nants (CO₂, COS and CS₂), and aqueous copper(II), were evaluated with the the cluster-continuum cycle. In forming the ethylenediamine carbamates, one of the amino group loses a proton (the pK_a of which was estimated in Section 3.2.2.3). To account for this in an overall reaction free energy estimate, the copper(II) ethylenediamine complex formed will be deprotonated also. The overall reaction is represented by the thermodynamic cycle shown in Figure 4-20, where X represents one of CO₂, COS or CS₂.

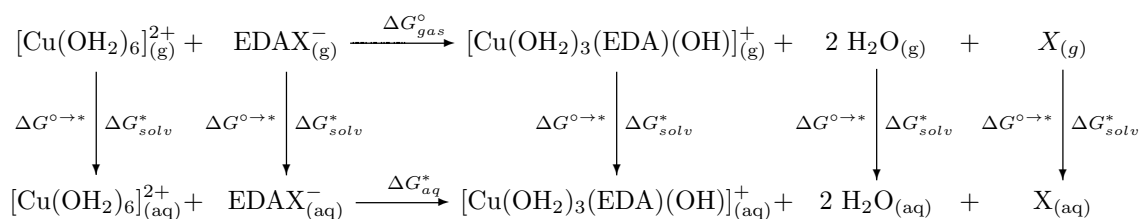


Figure 4-20: Thermodynamic cycle for calculation of the complexation free energy of Cu(II) with EDAX⁻ in water.

The aqueous complexation free energy is then calculated as per Eqn. 4.7 below.

$$\Delta G_{aq}^* = \Delta G_{gas}^{\circ} + \Delta \Delta G_{solv}^* + 2\Delta G^{\circ \rightarrow *} + 2\Delta G^{l \rightarrow *} \quad (4.7)$$

The carbamate structures presented in Chapter 3 were optimised with B3LYP-D3/aug-cc-pvdz, and therefore for consistency the copper(II) reactant, [Cu(OH₂)₆]²⁺, and product, [Cu(OH)(OH₂)₃(EDA)]⁺, were optimised at the same level of theory, and with the LANL2DZ basis set on copper.* The resulting free energy of reaction for species X, determined with B3LYP-D3 structures and energies and CCSD(T) energies, is presented in Table 4.11.

Table 4.11 also includes the first free energy of complexation between neutral EDA and copper(II) at the same level of theory for reference (where the experimental value is -14.4 kcal/mol).¹⁸⁵ As there is a proton transfer in reaction 4-20, the neutral complexation between [Cu(OH₂)₆]²⁺ and EDA cannot be used as a reference for the carbamates of species X in the Table, though it does indicate the

*Initial structures taken from Sections 4.2.2.2 and 4.2.2.5.

Table 4.11: Formation free energy of $[\text{Cu}(\text{OH}_2)_3(\text{OH})(\text{EDA})]^+$ with EDAX^- (kcal/mol).

X	-	CO_2	COS	CS_2
B3LYP-D3				
ΔG_{aq}^*	-31.70 ^a	-31.66	-35.33	-33.51
$\Delta G_{aq,rel}^*$	-	0	-3.67	-1.85
CCSD(T) ^b				
ΔG_{aq}^*	-27.79	-26.37	-29.39	-26.24
$\Delta G_{aq,rel}^*$	-	0	-3.02	0.13

^aStructures used for results shown in Table 4.2 were further optimised at B3LYP-D3/aug-cc-pvdz/LANL2DZ for direct comparison.

^bStructures optimised with SMD/B3LYP-D3/LANL2DZ/aug-cc-pvdz. SP energy at CCSD(T)/LANL2DZ/aug-cc-pvdz with UHF reference wavefunction and frozen core electrons.

hindrance of the carbamate in the dissociation and ligand exchange reaction. As was shown in Section 4.2.2.3 and 4.2.2.4, definition of just the first solvation shell is insufficient for determining an accurate solvation free energy or complexation free energy, respectively. For this reason, the $\Delta G_{aq,rel}^*$ is calculated with reference to ΔG_{aq}^* where $\text{X}=\text{CO}_2$, which is observed experimentally.³⁷

Results obtained with B3LYP-D3 overestimate the formation of $[\text{Cu}(\text{OH}_2)_4(\text{EDA})]^{2+}$ and the dissociation of all EDAX^- species when compared to CCSD(T) results. As seen in Chapter 3, B3LYP-D3 underestimated the stability of EDA^+X^- zwitterion intermediates, which translated to an over-estimation of their acidity. The pK_a estimate for $[\text{Cu}(\text{OH}_2)_6]^{2+}$ by B3LYP-D3 is worse, with a calculated value of 1.25 vs the experimental value 7.95²²¹ (Section 4.2.2.5). This combination results in more negative results for the aqueous free energy for EDAX^- dissociation.

CCSD(T) results suggest that the dissociation of EDACO_2^- and EDACS_2^- by copper(II) are marginally more favourable than the formation of the monoethylenediamine copper(II) complex. This is surprising given the difference between the pK_a of EDA, 6.86 and 9.92, and of $\text{EDA}^+\text{CO}_2^-$, EDA^+COS^- and $\text{EDA}^+\text{CS}_2^-$ are 2.75, 2.10 and 1.65, respectively. The comparable aqueous free energy estimate is likely due to an inaccurate differential solvation free energy

($\Delta\Delta G_{solv}^*$) due to the changing charge on the copper(II) complex. Regardless, the results suggest that the dissociation of sulfur substituted ethylenediamine carbamates is comparable to that of EDACOO⁻, which is observed experimentally. Additionally, they reinforce the finding that more of the solvation environment must be captured explicitly to determine accurate thermochemistry, given the more negative estimate of [Cu(OH₂)₄(EDA)]²⁺ by CCSD(T) compared to the experimental value.

4.3 Summary

The energetics of complexation between ethylenediamine and aqueous copper(II) were determined with the B3LYP functional, where reactants and products were optimised in the gas phase and subsequent solvation contributions added in an implicit manner. This method produced poor results when compared with experimental values. The effect of the DFT functional on the structural parameters of hydrated complexes and the reaction free energy was examined, with the first solvation shell defined explicitly. On the basis of the structures generated and comparison of the calculated and experimental complexation free energy, the B3LYP functional was applied with more of the solvation environment defined explicitly. Through increasing the number of explicitly defined solvent molecules, the solvation free energies of copper(II) and the δ -[Cu(EDA)]²⁺ complex were extrapolated to the bulk limit, approaching the experimental value. A comparison of gas phase and COSMO SCRF optimised structures was presented for copper(II) and δ -[Cu(EDA)]²⁺. COSMO SCRF structures form tighter hydrogen bonded networks around copper(II) than their gas phase counterparts, facilitating additional charge transfer which hastens convergence on the bulk limit for the solvation free energy. This effect was not observed for the δ -[Cu(EDA)]²⁺ complexes, where no trend in the hydrogen bonding distance was seen between gas phase and COSMO SCRF optimised structures. The free energy of complexation was estimated using solvated structures of reactant and products to arrive at the best estimate for the first complexation of EDA with copper(II) at -22.7 kcal/mol. Given the discrepancy with the experimental value of -14.4 kcal/mol, it was suggested counterions in the vicinity of solvated copper(II) ions impact the free energy of complexation.

As gas phase optimised structures with only the first solvation shell present reproduce the bulk limit for the free energy of complexation, the same technique was used to examine the effect of hydroxo ligands on complexation energetics when present in the first solvation shell. Results suggest that hydroxo ligands improve the stability of the first complexation product, though hinder the second. The results are called into question, however, as the relative difference between the first and second complexation calculated here does not match that observed experimentally. The relative free energy of bisethylenediaminecopper(II) complexes with the first solvation shell defined were examined in the gas phase based on the COSMO optimised structures, where isomers exhibit five and six-fold coordinate geometries with strong elongation of axial water ligands. Lastly, the overall reaction free energy for the dissociation of ethylenediamine carbamates by copper(II) was estimated with the B3LYP-D3 and CCSD(T) methods, where B3LYP-D3 yields a more negative dissociation free energy due to a poor estimation of reactant and product pK_a s. CCSD(T) results suggest that the sulfur substituted carbamates of ethylenediamine are similarly dissociated on reaction with copper(II).

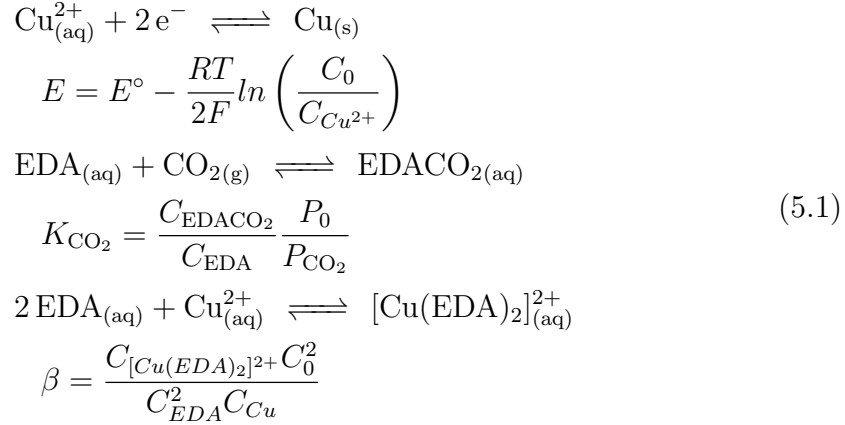
Chapter 5

Electrochemistry of EMAR with natural gas

The electrochemical behaviour of the original isolated system is presented, where the nature of the electrolyte impacts the kinetic behaviour and efficiency of the system. The addition of hydrogen sulfide to the electrochemical system consumes the active blocking species, copper(II), where the effects are quantified and means of mitigation proposed. The system is then examined at high pressures, to simulate the effect of operating at the conditions most favourable to natural gas treating. A representative mixture of natural gas is tested on the system, where results show little deviation from regular behaviour at atmospheric conditions. The reliability of EMAR depends on the reversible plating and dissolution of copper, and so factors effecting the deposits are investigated.

5.1 Electrochemistry of EMAR

The electrochemical description of EMAR, initially formulated by Stern³⁷ and refined by Shaw⁴⁹, is predicated on the electrochemical behaviour of the bisethylenediamine copper(II) complex. EMAR is classed as an Electrochemically Mediated Competitive Complexation Separation process, where the copper(II) species acts as a solid inactive blocker. Once electrochemically activated it competes with CO₂ for complexation with ethylenediamine, the active absorbent, and in so doing moderates the aqueous CO₂ concentration. The cell potential for such a system can be described in terms of a few key variables, namely the aqueous concentration of copper(II) and amine, the partial pressure of CO₂ and the operating conditions of the system. The equilibrium relationships and key variables are collected in Eqn 5.1, where the Nernst equation describes the half-cell potential and equilibrium expressions are presented for the absorption of CO₂ into EDA and the complexation of EDA with Cu(II).



The total cell potential, as a function of the above equilibrium constants and process variables may be written as:

$$E = E^\circ + \frac{RT}{2F} \left[\ln(x_{\text{Cu}}) + \ln \left(\frac{C_{\text{EDA}_0}}{2} \right) - \ln \left(1 + \beta \left[\frac{C_{\text{EDA}_0}(1 - x_{\text{Cu}})}{1 + K_{\text{CO}_2} P_{\text{CO}_2}} \right]^2 \right) \right] \tag{5.2}$$

Where x_{Cu} is defined as the copper loading:

$$x_{\text{Cu}} = \frac{2C_{[\text{Cu}(\text{EDA})_2]^{2+}}}{C_{\text{EDA}_0}} \simeq \frac{2C_{\text{Cu}_0}}{C_{\text{EDA}_0}} \tag{5.3}$$

for an initial amine and copper(II) concentration (C_{EDA_0} and C_{Cu_0}) respectively. A thermodynamic analysis of the electrochemical system describing key process variables, and the path traversed on the relevant thermodynamic cycle is covered by Shaw⁴⁹, which will be further addressed in Chapter 6. The focus here is how the chemical system behaviour is different when exposed to the contaminants present in natural gas. The largest contaminant besides CO₂ required to be removed from natural gas is H₂S, though before presenting the effect of sulfides on the EMAR electrochemistry, a review of the behaviour in absence of H₂S will be presented. CVs were used herein to present the kinetics of the electrochemical system. The response of the system under N₂ (effectively inert) and CO₂ provided the baseline for comparison when the behaviour with a simulated natural gas is tested.

5.2 Methods

Cyclic Voltammograms. CVs of the EMAR electrolyte were performed in a three electrode cell where glassy carbon was the working electrode and platinum wire was the counter electrode. Glassy carbon electrodes were rinsed with deionised water and polished with 0.05 μ m alumina powder, and the platinum counter was rinsed with HNO₃ and deionised water to remove any copper deposits. The reference electrode employed depended on total pressure and composition of the headspace. The standard Ag/AgCl reference electrode was used with nitrogen across all pressures, and with CO₂ and natural gas (NG) up to a total pressure of 1 bar.* At very high partial pressures of CO₂, dissolution and speciation of CO₂ shifts the pH and reference potential of the Ag/AgCl reference due to the formation of Ag₂CO_{3(s)}.²²⁴ Additionally, CO₂ dissolution from high pressures generated CO₂ bubbles within the reference electrode and the frit, altering the potential measured or applied to the cell. For these reasons, when charging with CO₂ containing gas above 1 bar total pressure, the non-aqueous AgNO₃ reference electrode[†] was used. Although the solubility of CO₂ in acetonitrile

*Standard Ag/AgCl reference from BASi modified to allow equilibration of electrolyte and common headspace. 0.205 V vs SHE.²²³

†0.01M AgNO₃, 0.1 M TBAPF₆ in CH₃CN. 0.503 V vs SHE.²²⁵

trile is high, as it is aprotic, dissolved CO_2 will not speciate and excessively shift the reference potential. Furthermore, the AgNO_3 reference couple in acetonitrile is not significantly affected by water, though to prevent excessive reference drift, the internal solution was refreshed after 2-3 uses.²²⁵ Reference electrodes were also cleared of $[\text{Cu}(\text{EDA})_2]^{2+}$ present in the glass frit with the relevant acid (HCl or HNO_3) and re-equilibrated with the appropriate electrolyte solution.

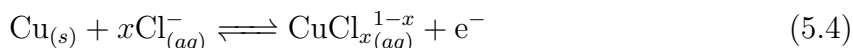
Solution preparation. The concentration the copper(II) in aqueous media was varied throughout the investigation to discern the behaviour in the presence of excess supporting electrolyte and at the conditions of the engineering implementation of EMAR, the EMAR stack. Solutions that were tested under a specific atmosphere had the relevant gas (N_2 , CO_2 or simulated NG) bubbled into the solution for 24 hours prior, and then during the CVs the gas flow was ceased. The solutions that were examined at elevated pressure with CVs were further bubbled for one additional hour at the target pressure prior to scanning. Bulk electrolysis solutions saturated in the same manner, though gas flow was maintained during the experiments to provide solution agitation as no other form was available.

Bulk electrolysis. A two electrode cell (sandwich) was constructed with 1/16" copper sheet, separated by 1/8" EPDM rubber, also used in the EMAR stack. The surface area of the electrode differs throughout, with specific geometry and size in-text. Stainless steel wire was soldered on the back of each copper electrode, and EPDM rubber was glued on top (with superglue) to insulate the reverse of the electrode. The space in-between electrodes resembled a flow channel as in the EMAR stack, though oriented vertically to prevent bubble trapping. A schematic representation and photo of experimental setup is shown in Figure 5-18. All electrodeposition tests were performed at ambient temperature ($23 \pm 2^\circ\text{C}$). EIS was performed before and after each electrodeposition experiment at the open circuit voltage, with 10 mV applied voltage perturbation over the frequency range 1Hz to 200kHz.

5.3 Results and Discussion

5.3.1 Electrolyte effect

As Eqn 5.2 shows, the potential of an EMAR half-cell depends on the temperature (T), copper loading (x_{Cu}), amine concentration (C_{EDA}), relative stability of the copper-amine complex (β) and the amine-CO₂ complex (K_{CO_2}) and lastly the partial pressure of CO₂ (P_{CO_2}). In analysing the system, Stern³⁷ performed CVs at the limits of the partial pressure CO₂, zero and the total operating pressure, 1 bar. The voltammograms were performed with CuSO₄, ethylenediamine and a NaNO₃ supporting electrolyte. Stern³⁷ also investigated the difference in kinetic response of the system under N₂ and CO₂ with both nitrate and chloride electrolytes. Although chloride salts improved the kinetics, powder formation in the system was observed, via the suggested pathway below:



Here the particle formation is due to the disproportionation of copper complexes, facilitated by a stabilised intermediate.* Though chlorides are used industrially to improve the quality of electrodeposited material,[†] chloride doping is typically in ppm concentrations and not significant enough to impact polarisation response.²²⁶ Shaw⁴⁹ employed a NaNO₃ electrolyte for EMAR stack operation on recommendation from previous work by Eltayeb⁴⁸. NaNO₃ is generally favourable as an electrolyte due to its low cost, high solubility, good conductivity and relatively stable behaviour across the electrochemical window of interest, though it was suspected to be electrochemically active and reducing the efficiency of the stack. This was confirmed, in part by examining the CVs of the background electrolyte, where Figure 5-1 (middle) shows a large cathodic current at approximately -1V vs Ag/AgCl for NaNO₃. The curve crossing below -0.9 V vs Ag/AgCl is indicative of a catalytic reduction at the electrode surface.

The cathodic current is due to nitrate reduction (shown in Eqn 5.6) and

*Copper powder was observed during EMAR stack and bulk electrolysis experiments.

[†]Stern³⁷ did note brighter electrodes in chloride salts.

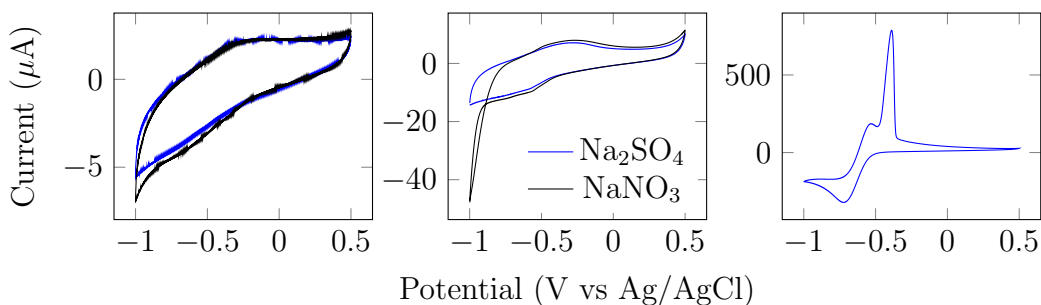
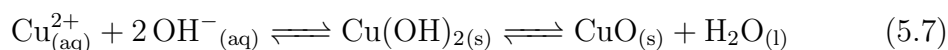


Figure 5-1: CVs of electrolyte at 1 molal Na (**left**), electrolyte with 1 molal EDA (**middle**), with copper(II) at 50 mM as analyte (**right**). All CVs performed with a glassy carbon working electrode, platinum counter, at 1 molal Na electrolyte solution, 25mVs^{-1} scan rate under N_2 .

though CVs were performed on glassy carbon electrodes, nitrate reduction is more significant on copper (and greater than other coinage metals).^{89,227} Adsorption and blocking of the electrode surface by nitrates occurs below -0.6 V vs Ag/AgCl and reduction below -0.9 V vs Ag/AgCl.²²⁸ The effect on the EMAR stack performance is addressed in Section 5.3.2. The reactions occurring at the cathode are then:



Given that reasonable currents for reduction of the bisethylenediamine copper(II) complex are not observed until potentials more negative than -0.5 V vs Ag/AgCl, nitrate salts block the electrode surface and consume current causing an imbalance in the cell performance for copper modulation. For this reason, sulfate electrolytes were used moving forward, though the trade off is slower kinetics in cathodic and anodic polarisation,* and its limited solubility.†

The right most panel of Figure 5-1 shows one reduction peak and two oxidation peaks. At 25mVs^{-1} the individual reduction peaks of Cu(I) and Cu(II) cannot be resolved. The anodic scan displays the first and second oxidation of

*Wang²²⁹ thesis unpublished

†Salts with higher solubility such as NaBF_4 were also tested for comparison, though electrode kinetics were similar at high salt loadings (up to 4M).

Cu_(s) into excess ethylenediamine, where larger currents are observed for the second oxidation due to the rapid formation of the bisethylenediamine copper(II) complex, compared with the mono or bisethylenediamine copper(I) complex²³⁰. By reducing the scan rate, the two reduction peaks are seen in Figure 5-2, representing reduction from copper(II) to copper(I) and the subsequent slow complexation with EDA. The kinetics of formation of copper(I) chelate complexes with EDA are slower and weaker than for copper(II), as demonstrated by the difference in stability constants β , $10^{19.6}$ and $10^{11.2}$ for copper(II) and copper(I), respectively.²³⁰ The diffusion coefficient of copper(II) was estimated with the peak anodic currents plotted against the square root of the scan rate, shown in Figure 5-2. The slope of this line follows the Randles-Sevick equation for a reversible electron transfer process, see Eqn 5.8, where i_P is the peak current (A), v is the scan rate (V/s), F is Faraday's constant, 96485 C/mol, n is the number of moles of electrons transferred, A the electrode surface area (m²), C_b the bulk concentration (mol/m³) and D the diffusion coefficient of the electroactive species (m²/s).

$$\frac{i_P}{v^{1/2}} = 0.4463 \left(\frac{F^3}{RT} \right)^{1/2} n^{1/2} A C_b D^{1/2} \quad (5.8)$$

The regression line in right of Figure 5-2 yields a diffusion coefficient of $8.39 \times 10^{-10} \text{ m}^2/\text{s}$ @ 295K for copper (II), in reasonable agreement with the literature.²³¹ The discrepancy is caused by the irreversible nature of the copper(II) ethylenediamine system. In a totally reversible electrochemical reaction, plots of normalised current $i/(Av^{1/2})$ against applied potential at different scan rates superimpose, whereas those of the copper ethylenediamine system deviate significantly (see Figure 5-3). As the scan rate is increased, anodic currents at ~ 330 mV vs Ag/AgCl reduce as freshly oxidised copper is reduced on the reverse scan prior to complexation with ethylenediamine.

Shaw⁴⁹ suggested that optimal EMAR stack performance would moderate the copper(II) concentration between 0.1 and 0.4M in a solution of 1M EDA - this represents a ratio of copper:EDA of 2:5 at the cathode and copper:EDA of 1:10 at the anode. The electrochemical response at these ratios was examined with CVs under N₂ and CO₂ to ensure there is no change in behaviour at different Cu:EDA ratios. Low analyte concentration and excess supporting electrolyte was

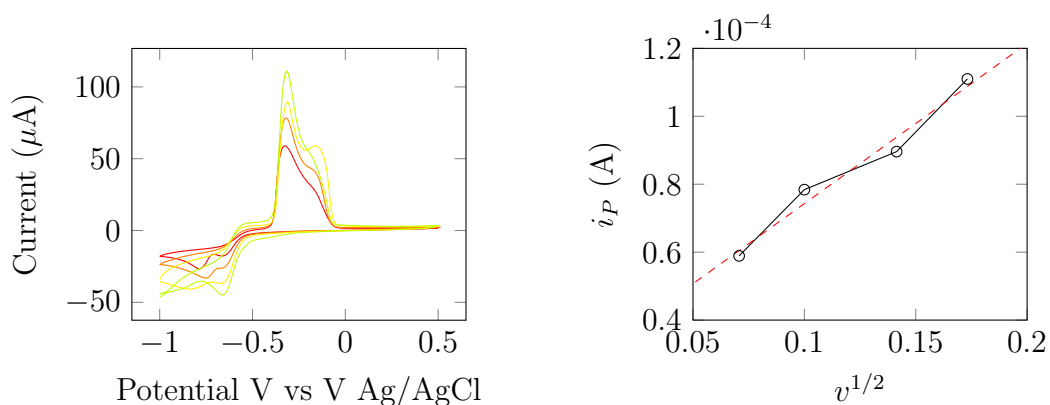


Figure 5-2: EMAR sulfate electrolyte at varying scan rates (**left**) with legend in Figure 5-3 and plot of peak anodic current against $v^{1/2}$ (**right**). Performed with glassy carbon working electrolyte, platinum counter, with Ag/AgCl reference electrode. All under N_2 headspace.

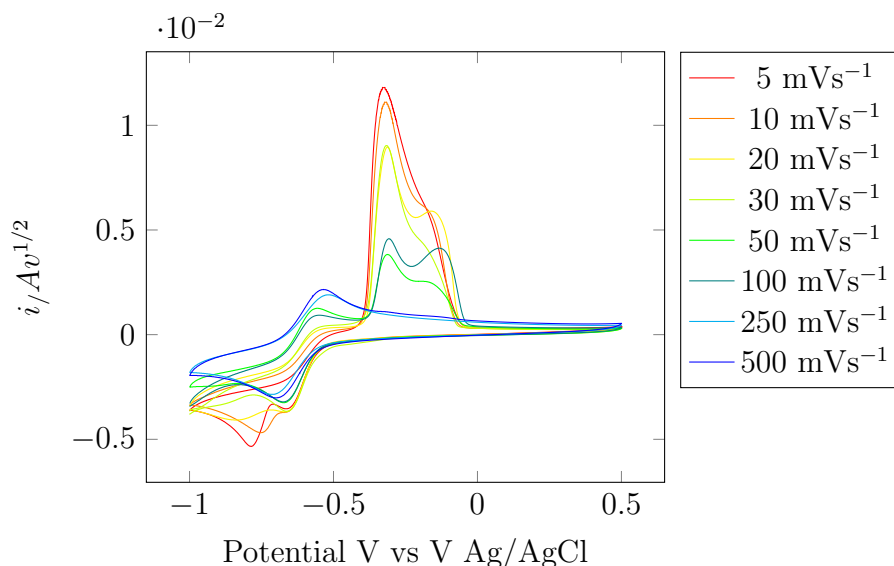


Figure 5-3: Normalised current density by $v^{1/2}$ at increasing scan rates with 5 mM CuSO_4 , 25 mM EDA, 0.5 M Na_2SO_4 under N_2 headspace. Performed with glassy carbon working electrolyte, platinum counter and Ag/AgCl reference electrode.

used to capture a clean electrochemical response, shown in Figure 5-4. Under N_2 and high ratios of EDA:Cu two oxidation peaks are observed corresponding to the formation of $\text{Cu}(\text{EDA})_2^+$ and $\text{Cu}(\text{EDA})_2^{2+}$. At lower concentrations of EDA (and pH as a result) the single Cu(I) cation complex is not stable enough to be

observed.²³⁰ There is a clear shift in the polarisation behaviour of the electrolyte system in CO₂ saturated conditions, captured by the last term in Eqn. 5.2. This is due to the dissociation of EDA carbamates as the free EDA is consumed in complexation reactions with copper(II).^{*} Furthermore, cathodic currents are much lower than anodic, due to asymmetry in activation barrier for reduction and oxidation, where the system follows Butler-Volmer kinetics with a transfer coefficient of $\alpha = 0.25$.³⁷

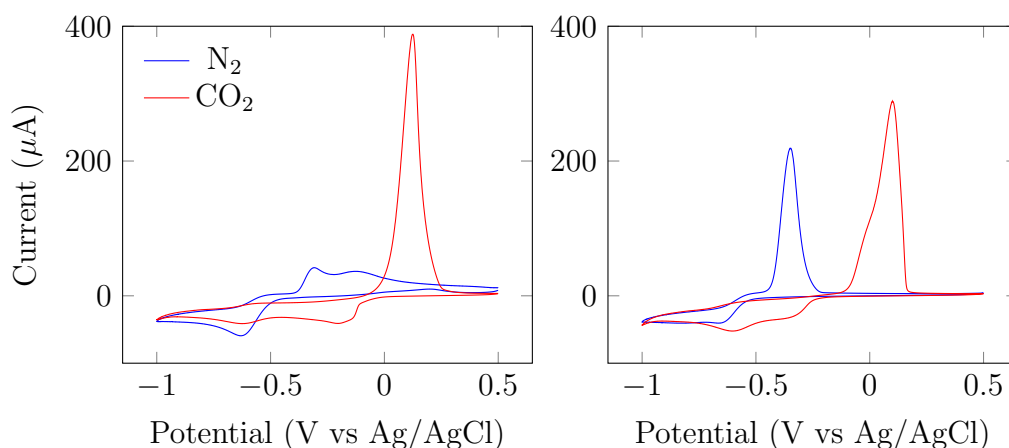


Figure 5-4: CVs of EMAR electrolyte with 5mM Cu(SO₄) at cathodic conditions where Cu:EDA=1:10 (**left**) and anodic conditions with Cu:EDA=2:5 (**right**). Glassy carbon working electrode, platinum counter, Ag/AgCl reference electrode. Scan rate 25 mVs⁻¹.

The effect of CO₂ loading at low analyte concentrations is clear, though this is not representative of the performance of electrodes in a real EMAR system because the ratio of analyte to salt is increased and pH effects are more significant due to the higher concentrations of amine present. The middle ground concentration of 0.25 M CuSO₄ with 1 M EDA and 0.5 M Na₂SO₄ was used to approximate the polarisation behaviour of EMAR, with N₂ and CO₂ headspaces, presented in Figure 5-5. At larger amine concentration, the pH under saturated nitrogen and CO₂ conditions differ by 5 units, 7.1 under CO₂ and 12.1 under N₂. As in Figure 5-4, Figure 5-5 demonstrates the impact of CO₂ loading on the shift in cell potential and current response. Both anodic and cathodic currents are

^{*}The kinetics of carbamate cleavage are covered in Ewing et al.²³² and Caplow¹⁵¹, where Stern³⁷ observed significantly hindered kinetics under CO₂.

lower when the concentration of copper is increased to the average stack value. Additionally the current response is less consistent under CO_2 where successive scans show a reduction in anodic and cathodic currents - not seen under N_2 .

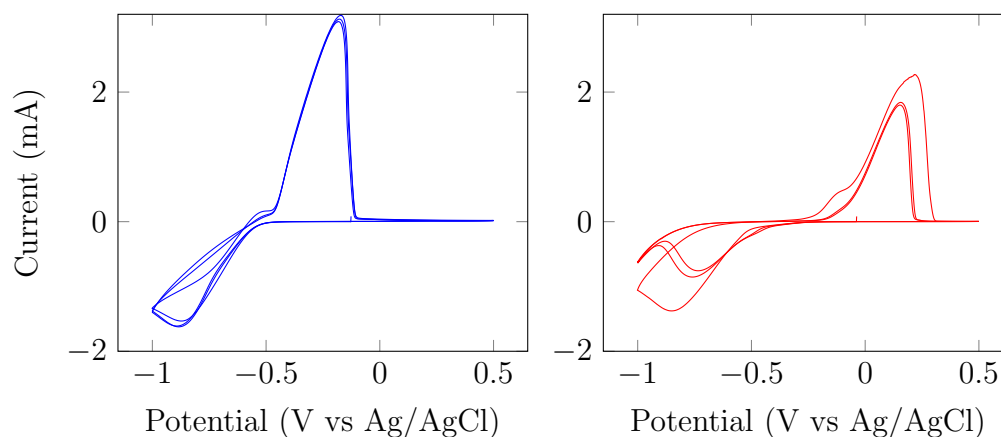


Figure 5-5: CVs of EMAR electrolyte at 0.25M CuSO_4 , 1 M EDA, 0.5 M Na_2SO_4 with N_2 headspace (**left**) and CO_2 headspace (**right**). Examined at 25 mVs^{-1} with a glassy carbon working electrode, platinum counter, and Ag/AgCl reference electrode.

The engineering implementation of this electrochemistry was developed by Stern³⁷ as a single flow cell, and expanded on by Eltayeb⁴⁸ and Shaw⁴⁹ in a stacked configuration to achieve the desired copper loading shift, covered next.

A simplified process level diagram and thermodynamic cycle of the EMAR process are shown in Figure 5-6. The CO_2 loaded amine is represented by point 1 at a CO_2 partial pressure of 0.15 bar (corresponding to flue gas output) where it enters the anode. The anode increases the copper loading of the solution, where the first curved section of the blue line represents the process where the physical solubility of the solution for CO_2 has not yet been exceeded, thus the aqueous CO_2 loading remains the same while the partial pressure increases. At a critical copper loading, where the partial pressure of CO_2 matches the desorber pressure, CO_2 leaves the solution as gas up to point 2, where the separation vessel separates gaseous CO_2 and the copper rich liquid phase. Starting at point 2, the cathode reduces the copper loading, where the aqueous CO_2 loading remains the same as the partial pressure of CO_2 reduces. The solution leaving the cathode, at point 3, returns to the absorber where the partial pressure is increased up to that of the entering gas composition.

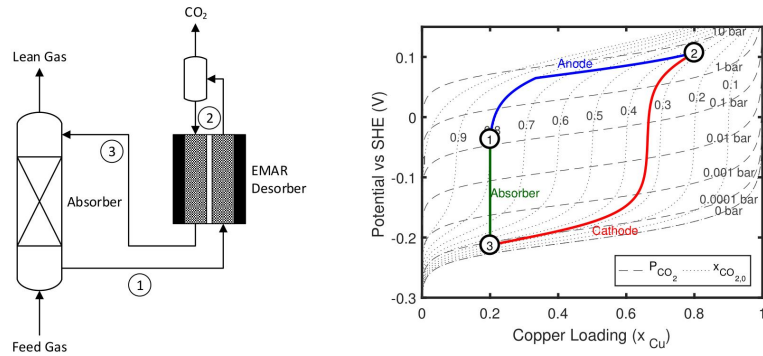


Figure 5-6: Simplified EMAR process diagram (**left**) and thermodynamic cycle (**right**) expressed as copper loading and open circuit potential. Reproduced from Shaw⁴⁹

5.3.2 The EMAR stack

There have been several designs of the cell used to implement the EMAR process: moving from a single flow cell, to a stacked design (neatly summarised in Shaw's thesis⁴⁹). The series version of the EMAR stack is presented in Figure 5-7, where each mid-plate has anodic and cathodic reactions occurring on each side, and the red line tracks the voltage profile through the stack. The potential is periodically switched to prevent total dissolution of the anode copper plate and buildup of deposited copper on the cathode.

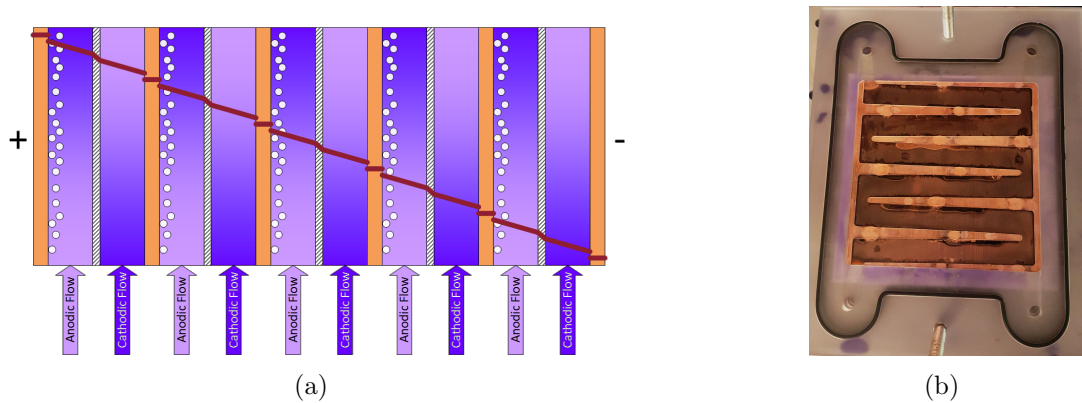


Figure 5-7: EMAR series configuration. Reproduced from Shaw's thesis.⁴⁹ (a). EMAR V8 series plate showing cathodic side after operation* (b)

To assess the applicability of the V8 EMAR stack to a natural gas treating application, first the performance with an absorber feed of 100% CO₂ was examined. Across a number of experiments the efficiency of the apparatus for CO₂ separation was low (< 10%).* This prompted a number of diagnostic experiments to evaluate the key reasons for its low efficiency. The major findings and means to mitigate some issues observed are below:†

- Temperature control across the system was lacking. Due to the exothermic nature of CO₂ absorption into ethylenediamine ($\Delta H_{CO_2} = -86.4\text{kJ/mol}^{37}$), the equilibrium constant K_{CO_2} is highly temperature dependent. The only source of heating (apart from Joule heating in the electrochemical cell) is the heating element at the absorber - a three neck flask. The multiple thermocouples indicated that the temperature only 7 cm downstream from the absorber had reached ambient conditions, and as such the cell was not operating at the assumed 50 °C but rather 23 °C. This prevented accurate estimation of the efficiency of the cell. Tubing in subsequent versions was made from stainless steel and insulated to prevent heat loss to the environment, and additional heating elements were located around the cell to maintain iso-thermal operation.
- The NaNO₃ supporting electrolyte. It was discussed in Section 5.3.1 that the reduction of nitrate on copper may reduce the efficiency of the system. This manifested as an upwards trend in the copper concentration as the cell continued to run, as the set of cathodes were either blocked by or reducing nitrate rather than decreasing the aqueous copper concentration. The left panel in Figure 5-8 shows the increase in aqueous copper concentration as the stack operates.‡ As a result, the solution capacity for CO₂ reduces with no means to cycle the capacity. Over the course of the latter 50

*EMAR series V8 plates and baffles were made from polycarbonate which was prone to cracks and leaks once assembled. Future plates were constructed from softer polypropylene while baffles were cut from EPDM rubber.

*Where efficiency here is defined as number of moles of CO₂ recovered at the flash tank for the charge delivered to the cell, assuming every mole of Cu(II) ions produced releases 2 moles of CO₂ from a presaturated solution.

†All of which have been implemented in version 9 of the EMAR system, and demonstrated by Wang et al.⁵⁰.

‡3V was applied to 5 series unit cells

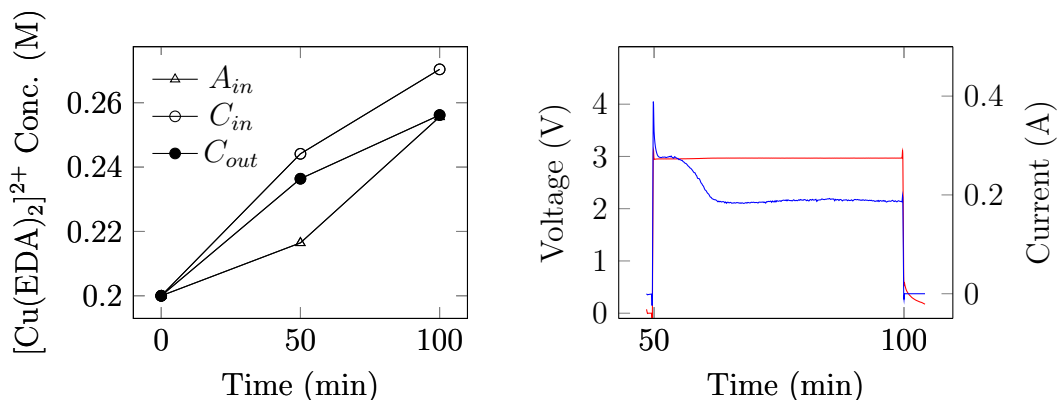


Figure 5-8: Aqueous $[\text{Cu}(\text{EDA})_2]^{2+}$ concentration over EMAR V8 operation at 3V (**left**) and current delivered at 3V across 5 unit cells in series (**right**).

minute run, 23.5 mL of CO_2 was released at the flash tank and $\sim 615\text{C}$ of charge was delivered to the stack (integrated current response in right panel of Figure 5-8), which due to the series configuration is multiplied by the number of unit cells (5) to determine efficiency. Assuming the below equation is driven completely to the right, 93C are necessary to evolve the captured CO_2 , yielding an efficiency of just 3%.*



The poor efficiency was caused in part by nitrate reduction which was later confirmed via bulk electrolysis experiments, see Figure 5-9 for the 1st generation apparatus. The quantitative efficiency of copper dissolution, subsequent CO_2 release and copper plating was examined in more detail by Miao Wang, with results presented in Wang et al.²³³ and Wang et al.⁵⁰. Of the electrolytes examined, Na_2SO_4 yielded efficiencies of near 100% for both plating and dissolution purposes.^{50,233}

- Ineffective cell membrane. As represented by the black shaded region in Figure 5-7, the cell membrane prevents bulk mixing of anodic and cathodic flows but allows migration of ions to balance charge. Filter paper was the membrane of choice for V8, due to its low cost and availability. By run-

*Solutions were pre-saturated with 100% CO_2 .



Figure 5-9: First generation bulk electrolysis experimental apparatus. The concentration of each half cell can be monitored individually, where a KNO_3 salt-bridge completes the circuit.

ning solutions of different copper loadings and CO_2 saturation on either side of the cell, it was discovered that significant cross-talk or exchange of copper and aqueous carbon (as carbonate or carbamate) was occurring. Internal mixing reduces the overall efficiency of the system because regenerated amine at the cathode may absorb CO_2 gas that has formed and wetted the membrane in the adjacent anode. An EMAR stack using hydrophilic membranes from Celgard (Celgard 3501) to reduce undesired ion migration and minimise CO_2 wetting, was then implemented.

- Bubble trapping in cell baffles. At the anode, where copper is dissolved, CO_2 bubbles form once the solubility of the solution is exceeded. Nucleated bubbles ideally pass through the cell to the flash tank for phase disengagement. The bright patches on the top bottom edges of the baffle shown in Figure 5-7(b) suggest a degree of bubble trapping. CO_2 bubbles are then re-absorbed into freshly regenerated amine on polarisation reversal. A number of different baffle designs were trialed which balance membrane scaffolding, minimising bubble trapping and maximising electrode surface area. Future stacked versions used a dot like baffle configuration as a compromise between these competing factors.

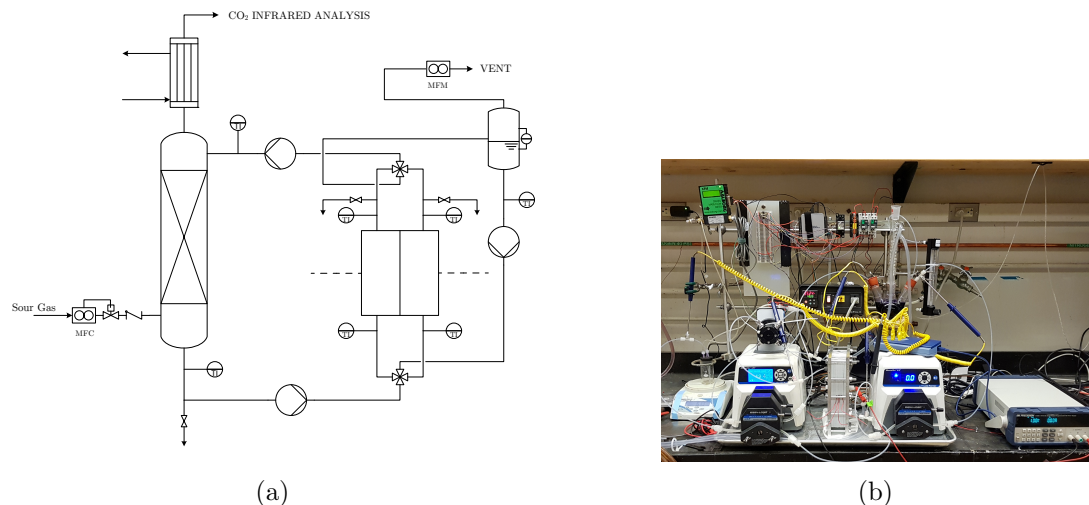


Figure 5-10: EMAR Stack V8 P&ID (a) and experimental apparatus (b)

Given the issues in attaining consistent high efficiency performance of the EMAR stack, investigation into the feasibility of the process for natural gas sweetening was established with more fundamental electrochemical techniques. Additionally, the experiments of Stern³⁷, Eltayeb⁴⁸ and Shaw⁴⁹ demonstrate the applicability of the process to separate CO₂ from flue gas*, though do not consider the additional components in natural gas. As discussed in Section 1.1, natural gas contains additional components; namely sulfur containing compounds and hydrocarbons which may impact EMAR performance. This is covered next.

5.3.3 Application to natural gas treating

CO₂ is common to both flue gas and natural gas, though the degree of removal depends on the application. The typical target for CO₂ removal from flue gas is 90% capture, while targets vary in natural gas treating from an outlet concentration from the absorber of 2 mole % to 50 ppmv, for domestic gas supply and LNG production respectively.²³⁴ Primary amines are capable of removing CO₂ to ppmv levels, often with faster reaction rates, though are generally more corrosive. The majority of remaining compounds in natural gas are saturated hydrocarbons,

* Assumed as a 15/85 mix of CO₂/N₂ where any SO_x and NO_x has been removed in earlier units, operating at 1 bar total pressure.

which have low solubility in aqueous media and do not exhibit an electrochemical response in the window for EMAR.* Hydrocarbon solubility becomes more relevant at high pressure operation, and can necessitate additional unit operations to remove coabsorbed hydrocarbons. The main species of concern is hydrogen sulfide. H₂S does exhibit electrochemical behaviour, bisulfide from dissolved H₂S due to the multiple oxidation states of sulfur. Although, CS₂ and COS may be present depending on the gas well, given their hydrolysis reactions (see Section 3.2.2), COS and CS₂ are not largely present and collapse via hydrolysis reactions to form H₂S and CO₂. The typical makeup (of a fairly lean gas) from a well in Western Australia is shown in Table 5.1.

Table 5.1: Composition of Natural Gas used in experiments probing behaviour of EMAR electrolyte.

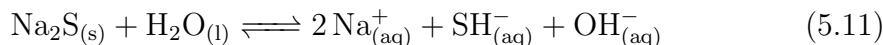
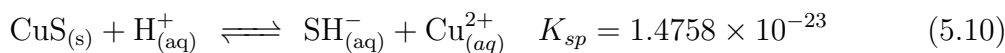
Component	Mole Fraction
Methane	0.8871
Ethane	0.0350
Propane	0.0100
i-Butane	0.0040
n-Butane	0.0040
i-Pentane	0.0015
n-Pentane	0.0015
neoPentane	0.0010
n-Hexane	0.0005
n-Heptane	0.0002
CO ₂	0.0300
H ₂ S	200 ppm
N ₂	0.0250

5.3.3.1 Effect of hydrogen sulfide

The most pressing concern when applying the EMAR process to natural gas treating is the presence of H₂S. H₂S hydrolyses to form bisulfide, SH⁻ and a proton where the spontaneous and near complete formation of metal sulfides occurs, represented by Eqn. 5.10. The solubility product for transition metal

*Redox behaviour of aliphatic hydrocarbons in aqueous media occurs at higher potentials, above approximately 0.4 V vs DHE,²³⁵ beyond those anticipated in EMAR operation.

sulfides is very low, typically $< 10^{-20}$, and as such little free copper remains.



To avoid the risk of handling H_2S , the addition of sulfide to the EMAR electrolyte was simulated with Na_2S as an aqueous source of sulfide. The addition of H_2S is worse as the solution continues to acidify, reducing the effectiveness of amine to absorb CO_2 , as seen in Chapter 3.

The formation of copper sulfide in acidic solutions,²³⁶ and in the presence of complexing agents such as ethylenediaminetetraacetic acid (EDTA),^{91,92,237,238} and EDA,²³⁹⁻²⁴¹ have been well studied. The effect of the complexing agent is two fold: the thermodynamic stability of the complex dictates the free copper ions in solution, while the nature of the complexing agent determines the sites available for bisulfide attack on the copper (II) complex. As computational results from Chapter 4 show, aqueous copper(II) adopts a distorted octahedron coordination geometry, while the bisethylenediamine copper(II) complex causes further distortion of the ligands in the axial direction. Although all equatorial sites are occupied by nitrogen from two ethylenediamine ligands, the axial sites are still open to water exchange and reaction with SH^- . This is the suspected point of attack in forming covellite, CuS . The stability of the bisethylenediamine copper(II) complex is not sufficient to prevent the formation of CuS , and increasing the aqueous sulfide concentration effectively produces a linear trend in the free copper(II) concentration, shown in Figure 5-11. Only with excess EDA is there residual copper as bisethylenediamine copper(II) present at equimolar Cu^{2+} and S^{2-} , though on further addition neither free copper nor the copper complex are detected.

The ratio of copper salt, complexing agent, and aqueous sulfide concentrations, and operating conditions affect the morphology and ratio of copper to sulfur in the solid formed. Here, the ratio appears to be 1:1 except at very high EDA loadings, though it is common to find ratios of 1.4:1 to 2:1 for $\text{Cu}:\text{S}$ formed in aqueous ethylenediamine solutions.²⁴⁰ As the cell potential (Eqn 5.2) is a function of operating conditions and the activity of Cu^{2+} , the behaviour of the EMAR

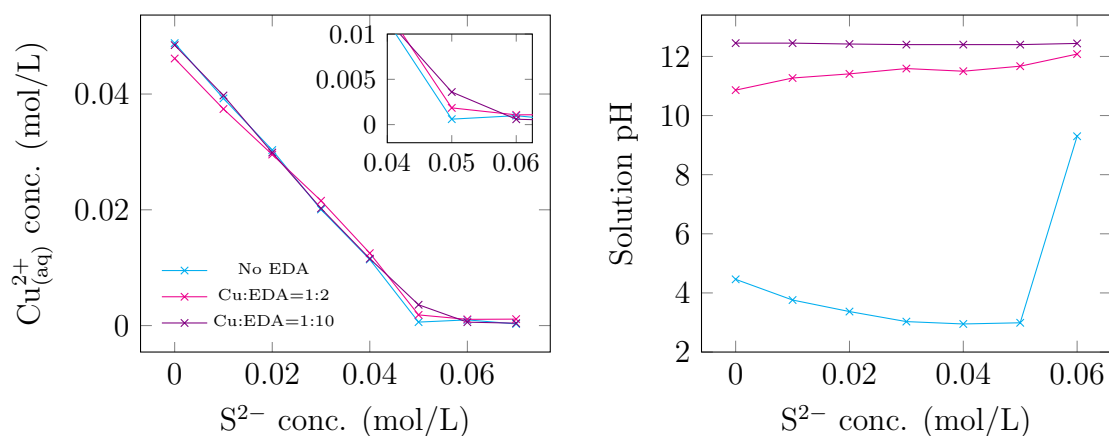


Figure 5-11: Free copper concentration following addition of Na₂S simulating H₂S absorption (**left**) and pH of final solutions (**right**). Total solution volume was 5 mL with 50 mM CuSO₄. Stock Na₂S solutions were bubbled with N₂ for >24 hours to remove dissolved oxygen and precipitation was performed under N₂.

electrolyte following Na₂S addition was examined. Cyclic voltammograms of the EMAR electrolyte at increasing sulfide concentration (from Na₂S) are shown in Figure 5-12

Though some metallic sulfides (depending on the morphology) display semiconductor properties, the electrochemical behaviour of interest for the operation of EMAR is effectively nullified as sulfides are introduced, such that the CV at greater than equimolar sulfide reduces to effectively a scan of the background electrolyte. Though H₂S concentrations in natural gas are relatively low, in the case where dissolved sulfides exceed the aqueous copper concentration and cell operation is maintained, mixed oxide and sulfide films will develop on the surface of each electrode blocking the effect of copper(II) in solution.^{242,243} In addition, the hydrolysis of H₂S acidifies the solution, reducing the working capacity for CO₂ over time.

Given the negative consequence of dissolved H₂S on the electrochemistry and therefore the larger process, it must be removed prior to the EMAR unit. Shaw⁴⁹ suggested the following calcination and dissolution steps to recover the copper lost

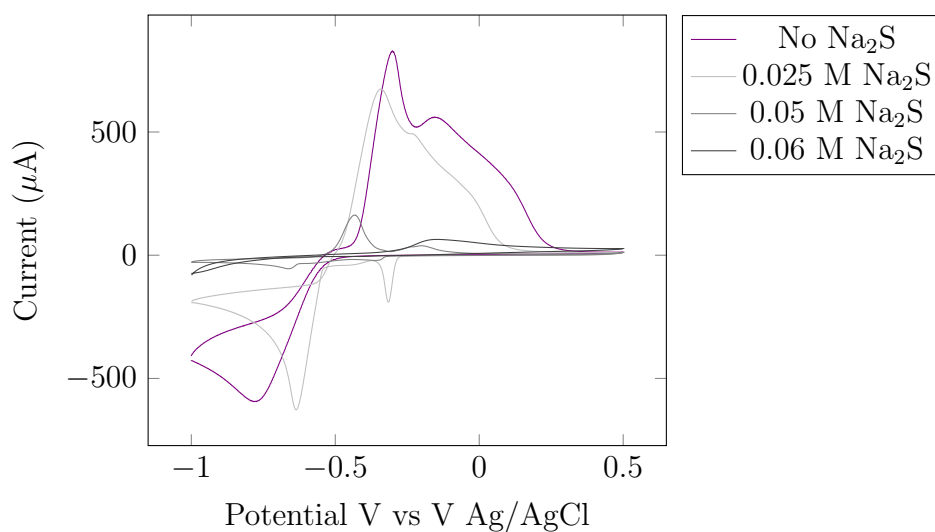
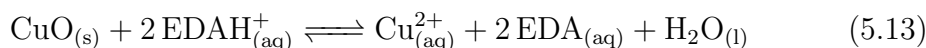
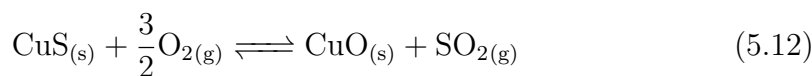
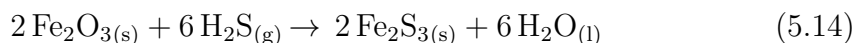


Figure 5-12: CVs of EMAR electrolyte at 0.05 M CuSO_4 , 0.5 M Na_2SO_4 and 0.1 M EDA where total Na_2S concentration is increased. Glassy carbon working electrode, platinum counter, Ag/AgCl reference electrode.

to CuS solid formation.



For process simplicity, the formation of particles, which necessitates additional equipment for their removal and intermittent process shutdowns can be avoided with adsorbent beds. These units, immediately upstream of the absorber, capture H_2S either irreversibly, by forming a solid metal sulfide (for example via an iron oxide sponge, reaction in Eqn 5.14), or reversibly via sorption into aluminosilicate zeolites.²⁴⁴



Iron sponge processes are cheap to operate though adsorption beds need replacing every 3-5 years, whereas zeolite adsorption beds can be regenerated through temperature swing utilising gas turbine exhaust on-site. Either solution is industrially available, and suitable for removal of the low to moderate levels of H_2S found in Australian well gas.^{174,245} In contrast, calcination requires temperatures of over

800 °C to ensure complete conversion of copper sulfide to oxide* and reintroduces solids to the flow system.²⁴⁶

On the assumption H₂S is removed by one of the above methods, the operation of an EMAR system with lean natural gas is examined.

5.3.3.2 Effect of hydrocarbons

To check the difference the presence of hydrocarbons makes to the behaviour of the EMAR system, the electrolyte was examined by CV once the the solution had been saturated with either N₂, 3 % CO₂ in N₂ and finally 3% CO₂ in the natural gas mixture presented in Table 5.1. The response of the electrolyte is shown for each case in Figure 5-13.

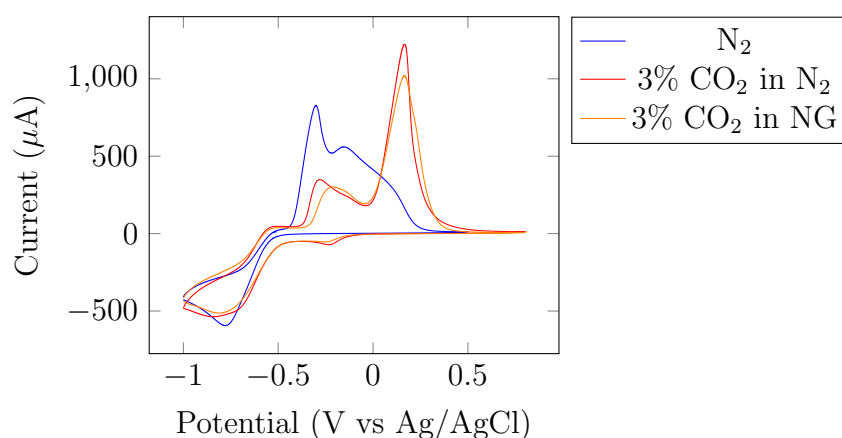


Figure 5-13: CV of EMAR electrolyte under various atmospheres. Glassy carbon working electrode, platinum counter electrode, Ag/AgCl reference electrode. All CVs performed with 0.05M CuSO₄, 0.1 M EDA, 0.5M Na₂SO₄

There is no qualitative difference between scans under different headspaces, especially at only 1 bar total pressure where hydrocarbon solubility is particularly low. The solubility of methane into an aqueous 1 molal solution of ethylenediamine is plotted in Figure 5-14 for reference.[†] At 1 bar methane, the solubility is just 0.0016 mol CH₄/kg water, which in a 15 mL CV vial will be swamped by the copper redox signal. As the EMAR cell may operate at elevated pressures

*Unavailable from the exhaust of gas turbines used for local power generation.

[†]Generated in Aspen HYSYS V8 with eNRTL/Peng-Robinson EoS.

hydrocarbons will be present in larger concentrations. The next section examines the electrochemical behaviour at high pressure and the effect of dissolved hydrocarbons on the response.

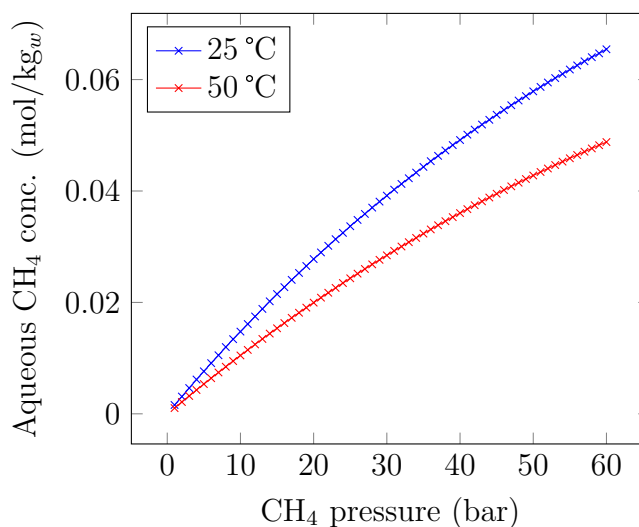


Figure 5-14: Methane solubility in 1 molal ethylenediamine at 25 °C and 50 °C.

5.3.4 Effect of cell pressure

In examining the performance of the EMAR stack, a number of improvements to the design for operation at 1 bar total pressure were identified. Even with many modifications implemented the stack (and ancillary equipment) was not suited to high pressure operation. Additionally, the behaviour of electrolyte had not been examined at elevated pressure. The same CV analysis was performed on the EMAR electrolyte, though at the elevated pressure to ensure the behaviour was consistent for pressurised operation.

An ideal thermodynamic equilibrium will exhibit weak pressure dependence as related to the standard volume of reaction ΔV° . This can be expressed in terms of the change in the standard cell potential, E° with pressure, shown in

Eqn. 5.17.⁹⁵

$$(\partial \ln K^\circ / \partial P)_T = -\Delta V^\circ / RT \quad (5.15)$$

$$\ln K^\circ = nF\Delta E^\circ / RT \quad (5.16)$$

$$\Delta V^\circ = -nF(\partial \Delta E^\circ / \partial P)_T \quad (5.17)$$

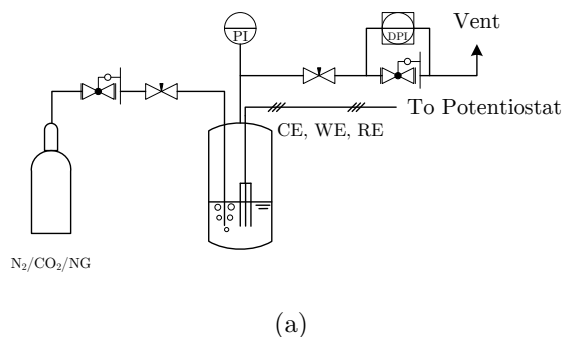
The standard volume change for aqueous copper deposition is $-20.7 \text{ cm}^3/\text{mol}$,^{247,248} which translates to $(\partial \Delta E^\circ / \partial P) = 1.07 \times 10^{-5} \text{ V}/\text{bar}$. This does not represent a significant change in potential over the 20 bar working range of the EMAR cell. The response of the electrolyte under high pressure was still examined to ensure it will perform with high pressure natural gas as it does at 1 bar total pressure.

CVs were performed on the same solutions as used in operation of the EMAR stack, 0.25 M CuSO₄, 1 M EDA and 0.5 M Na₂SO₄. A scan rate of 100 mVs⁻¹ produced reasonable repeatability for the experimental duration where at lower scan rates polarisation was less consistent as both cathodic and anodic currents consistently decreased. After approximately 10 cycles at 100 mVs⁻¹, the electrolyte system approached a pseudo steady state behaviour. To simulate a natural gas treating scenario, the solution was saturated with the natural gas (Table 5.1) first at 1 bar total pressure, then at 50 bar total pressure for one hour.* The total pressure was reduced (via the back pressure regulator) to 10 and 20 bar, where the same electrochemical technique was used to examine the system. The P&ID and picture of the experimental apparatus is shown in Figure 5-15. Open circuit voltage (OCV) and EIS measurements were performed before and after CVs. Peak anodic and cathodic potentials and currents are plotted and presented in Figure 5-16 and Table 5.2. As there is no peak cathodic current under CO₂, the cathodic current shown in Figure 5-16 is reported at -1.2 V vs the AgNO₃ reference (0.697 V vs SHE), and shown in Table 5.2.

The variations in the measured peak currents and potentials shown in Figure 5-16 are largely due to a lack of temperature control of the pressure cell (where the temperature dependence of the cell voltage is captured in Eqn. 5.2).[†] Under

*The operating pressure of the amine absorbed depends on many factors - often between 50 and 120 bar. The operating pressure here was limited by that available from the gas tank.

[†]Though the ambient temperature was maintained at 23±2 °C.



(a)



(b)

Figure 5-15: High pressure cell process and instrumentation diagram (a) and experimental apparatus (b). PI - Pressure Indicator. DPI - Differential Pressure Indicator.

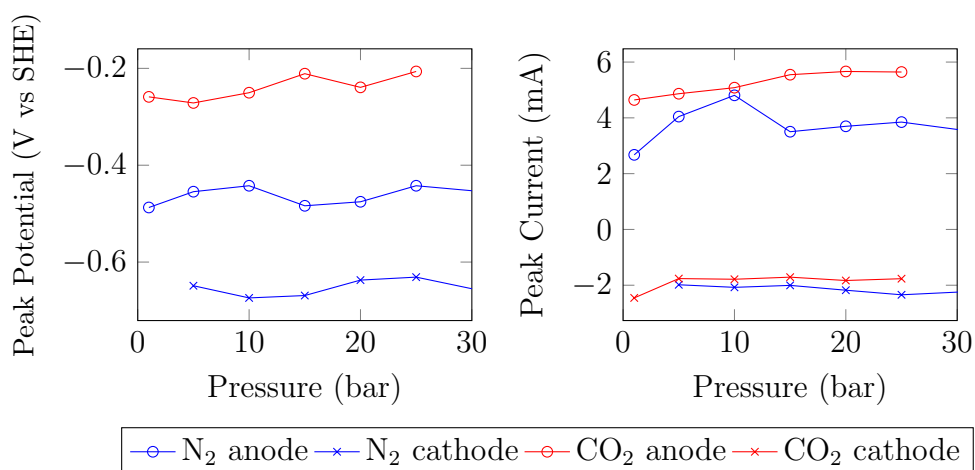


Figure 5-16: EMAR Electrolyte response at high pressure. Nitrogen headspace (left) and CO₂ headspace (right).

CO₂ the anodic currents are consistently higher than under N₂, though less of a difference is observed at the cathode. Given the fluctuations, little can be said about the response at elevated pressure, other than that there is no significant deviation from operation at one bar total pressure. OCVs before and after CVs

under N₂ are less consistent - the high pH of these solutions (~ 13) improves the stability of CuO which may be retained on the electrode surface.²³⁰ This is not the case under CO₂ saturated conditions where the OCV before and after CVs are far more consistent.

The response at pressure then serves to provide bounds for the response of the electrolyte under natural gas. Natural gas absorption at 50 bar total pressure represents 15 bar partial pressure of CO₂*, which once flashed to 10 or 20 bar produces liquid phases which are saturated or partially saturated with CO₂. The CV scans under natural gas are less stable than under N₂ or CO₂ in that the scans do not achieve a pseudo steady state condition - data from the 1st and 20th scans are presented in Table 5.2. For visual comparison, the CV scans of a CO₂ saturated solution at 10 and 20 bar are shown in Figure 5-17 with CVs from electrolyte saturated with natural gas at 50 bar and flashed down to the same pressure adjacent.

Table 5.2: Electrochemical response of EMAR electrolyte under pressure. Peak anodic and cathodic potentials, $E_{P,anode}$ and $E_{P,cathode}$, respectively, and OCVs in V vs SHE. Peak anodic and cathodic currents, $I_{P,anode}$ and $I_{P,cathode}$, respectively, in mA.

Pressure	Headspace	$E_{P,anode}$	$I_{P,anode}$	$E_{P,cathode}$	$I_{P,cathode}$	OCV
1	N ₂	-0.0773	2.674	-	-	-
	CO ₂	0.2441	4.462	-0.6970	-2.455	-0.0837 / -0.1026
5	N ₂	-0.04466	4.045	-0.64887	-1.984	0.1305 / -0.2983
	CO ₂	0.2316	4.865	-0.6970	-1.762	-0.0425 / -0.0638
10	N ₂	-0.03239	4.808	-0.6740	-2.076	0.1379 / -0.2685
	CO ₂	0.2527	5.082	-0.6970	-1.786	-0.0181 / -0.0346
15	N ₂	-0.0738	3.503	-0.6691	-2.006	-0.0206 / -0.2873
	CO ₂	0.2920	5.547	-0.6970	-1.711	-0.0107 / -0.0097
20	N ₂	-0.0655	3.967	-0.6372	-2.179	-0.0901 / -0.2811
	CO ₂	0.2638	5.663	-0.6970	-1.831	-0.0120 / -0.0325
25	N ₂	-0.0324	3.848	-0.6311	-2.343	-0.1038 / -0.2397
	CO ₂	0.2966	5.643	-0.6790	-1.766	0.0313 / 0.0117
10	3% CO ₂ in NG ^a	0.3159	4.104	-0.7080	-2.496	0.0751 / -0.0729
		0.3337	4.464	-0.7170	-2.863	
20	3% CO ₂ in NG ^a	0.2463	3.696	-0.7300	-2.222	0.0253 / 0.0291
		0.2576	3.860	-0.7210	-2.325	

^a1st and 20th scan results shown for comparison.

* Assuming ideal gas behaviour.

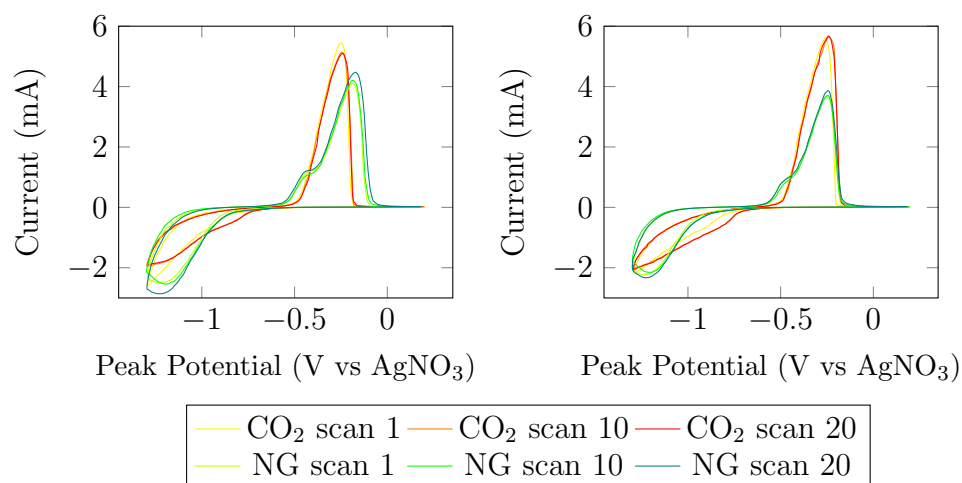


Figure 5-17: CVs of (top) 10 bar. (bottom) 20 bar. (left) CO₂ headspace. (right) NG headspace (3% CO₂)

The onset of reduction in the saturated natural gas solutions is more negative than under CO₂ alone, likely due to the pH difference of an undersaturated solution.* Additionally, the shoulder of the anodic scans indicate aqueous copper is released in a solution of unbound ethylenediamine (with respect to CO₂). Lastly, the NG saturated solutions achieve a peak cathodic current at approximately -1.22 V vs AgNO₃ (-0.72 V vs SHE) indicating a diffusion limitation that was not present under N₂ or CO₂. This may be caused by a reduction in the diffusion coefficient of copper due to dissolved hydrocarbons. These above effects necessitate additional polarisation of an EMAR cell to achieve the same current response as under pure CO₂. Though the total energy requirement will be greater due to dissolved hydrocarbons, there is no suggestion the system will not perform.

5.3.4.1 High pressure electrodeposition

The deposition of copper is integral to the operation of the EMAR cell, therefore factors that effect the nature of the deposit have been examined. Industrial copper electrodeposition is performed in acidic sulfate, cyanide, or pyrophosphate

*pH of fully CO₂ saturated solution at 10 and 20 bar is 6.56 and 6.29 respectively, while the pH of a 3% CO₂ saturated NG solution at 50 bar is 7.44. Determined from speciation model in Chapter 6

solutions, with few operating in the presence of complexing agents.²²⁶ Electrodeposition of copper(II) with ethylenediamine onto other metals (iron and zinc) was performed in the 1930s,²⁴⁹ though at a higher pH because of excess free ethylenediamine. The EMAR cathode is saturated with CO₂ where the ethylenediamine present is complexed with either copper(II) or CO₂ as carbamate, bringing the pH to approximately 6.5. As stable operation of the EMAR system depends on reversible plating and dissolution of copper electrodes, bulk electrolysis experiments under CO₂ saturated conditions were performed. A major benefit of the EMAR system is its pressurised operation, therefore electrodeposition was studied also at elevated pressures. The pressure vessel available could not be modified to include a stirrer. In order to provide solution mixing, CO₂ was bubbled through the solution at the desired operating pressure via the PEEK tube shown in Figure 5-18(b).

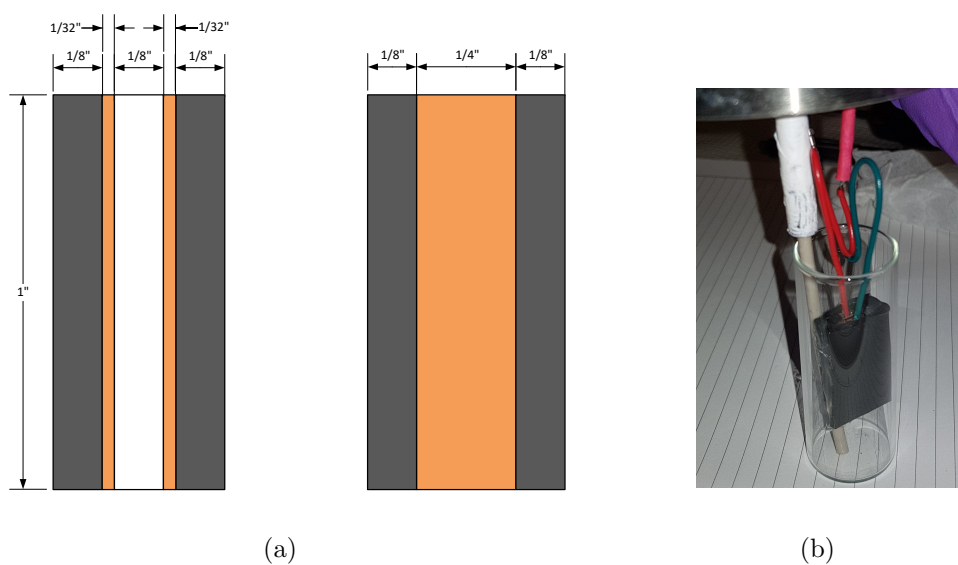


Figure 5-18: Depiction of bulk electrolysis setup. Side view (**left**) and front view (**middle**) of electrode sandwich (units in inches). Dark grey - EPDM rubber, pale orange - solid copper electrode, white - empty space/flow channel. Photo of apparatus with fresh electrodes (**right**).

Cyclic voltammograms of the sulfate system under CO₂ (Figure 5-5) demonstrate maximum cathodic and anodic currents at approximately 2 and 4 mA,

respectively, which for the 3 mm diameter working electrode translate to current densities of 28 and 56 mA/cm². Qualities, such as adhesion, appearance, mechanical properties etc., of electrodeposited material strongly depend on the applied potential and resulting current density, where for copper sulfate systems compact deposits are formed below 10 mA/cm² and those of powdery character are formed above this value.²⁵⁰ To avoid low quality deposits, electrodeposition was performed at a moderate 4 mA/cm² in CO₂ saturated solutions with the standard EMAR electrolyte. Separate deposition was performed at 1, 5, 10 and 15 bar total pressure CO₂, with at least 1 hour of equilibration at the total pressure prior to applying a potential. The resulting deposits on the cathode were imaged with an optical microscope at ~20× and SEM at 150× shown with the applied voltage over the 2 hour experiment duration in Figure 5-19.

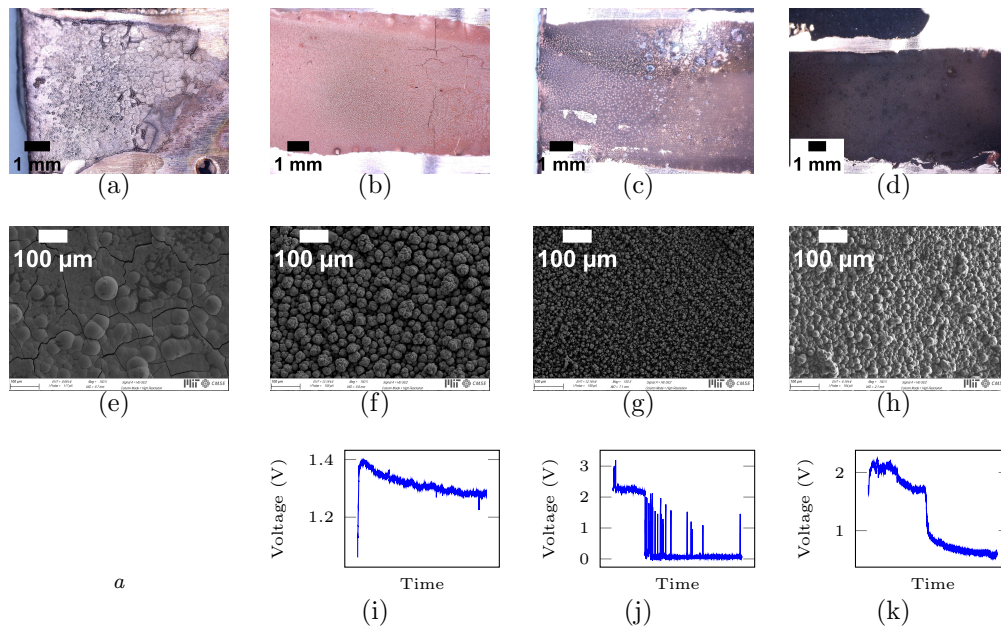


Figure 5-19: Photos of cathodes with optical microscope at 20× magnification (**top**), SEM at 150× magnification (**middle**) and graph of applied potential (V) over 2 hours experimental duration (**bottom**). Results from deposition under 100% CO₂ at 1 bar (a, e), 5 bar (b, f, i), 10 bar (c, g, j) and 15 bar (d, h, k) total pressure.

The dark and dull copper deposits are consistent with the observations of

[†]Data unavailable. ~1 V over duration.

Brockman and Mote²⁴⁹, and darken further with increased pressure, though the applied potential over the experiment duration is not consistent. Mass transfer limitations due to poor agitation by variable bubble propagation through the electrode sandwich prevented current being achieved by deposition and dissolution of copper(II) alone. Mass transfer limitations manifest as poor distribution of electrodeposited material shown in Figure 5-19(a), where only the left side of the electrode appears to have developed copper deposits. Above applied potentials of 1.23 V oxidation and reduction of water is expected to contribute to the current. Hydrogen evolution, due to the reduction of water, is proposed as the reason for the distributed ball-like structures seen on the cathode in Figure 5-19(f), (g) and (h).²⁵¹ The gas, which reduces in volume as the pressure increases, causing the same trend in the size of the ball-like structures, alters the hydrodynamic conditions near the electrode surface.²⁵¹ Pitting due to the formation of larger gas bubbles can be seen on the cathode surface in Figure 5-19(c) and (d). Anodes are not pictured as they are effectively featureless, even beyond $1-2K\times$ magnification. Fluctuation and reduction in the applied voltage over the course of experimental runs is due in part to the poor mass transfer, where once nearby electroactive species are consumed and not replenished, the potential rises to achieve the desired current density.

To prevent the breakdown of water, lower potentials were applied in a similar configuration in subsequent experiments. Rather than operating at constant currents, a constant potential was applied which is more in accordance with operation of the EMAR stack (0.5 - 1.0 V per unit cell). 0.6 V was applied across the cell, which achieves reasonable currents and is such that the Joule heating compensates for the enthalpy of desorption of the EDA-CO₂ complex.⁴⁹ The electrodeposits formed on the cathode under 1 and 5 bar CO₂ are shown in Figure 5-20.

The deposits formed at lower potentials are more uniformly spread than under chrono-potentiometric operation. Though the sulfate deposits in Figure 5-20 are more uniform and brighter, the flaky character indicates poor adhesion to electrode underneath, such that the deposited material has curled on itself. A more extreme case is under 5 bar deposition, shown in Figure 5-20(d), where the deposit has almost detached from the electrode such that the fresh electrode may

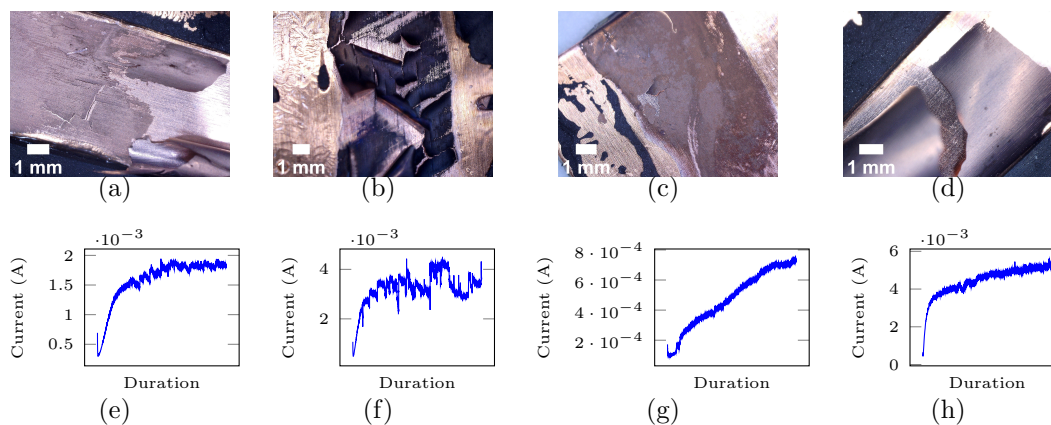


Figure 5-20: Bulk electrolysis experiments at constant applied potential 0.6V. Photo of cathode post deposition at $20\times$ magnification (**top**) and current response over the course of two hour electrodeposition (**bottom**). sulfate solution at 1 bar CO_2 (a), sulfate solution deposition at 1 bar CO_2 with Cl^- doping at 0.1 mg/L (b), Sodium tetrafluoroborate deposition (2M NaBF_4) under 1 bar CO_2 (c), sulfate solution deposition under 5 bar CO_2 (d).

be seen underneath. Poor deposit adhesion is a problem for EMAR operation as flaky deposits can be dislodged and short the cell or accumulate and block flow channels. Electrolyte solutions and common additives used in industrial copper electroplating were investigated for use in the EMAR electrolyte.

Chloride is a common additive in acid sulfate copper electroplating, used to improve mechanical properties and the throwing power of the electrolyte solution - which is the ability to plate a uniform cathode surface.²²⁶ The necessary chloride concentrations are in the order of 40-150 mg/L, enough to significantly alter the mechanical properties and appearance of the plate. 4mg of NaCl was added to the standard sulfate solution (160 mg Cl^- /L), with the resulting cathode shown in Figure 5-20(b) and current response below. Compared to the experiments without chloride, the colour of the plate is much darker but the same flaky deposits are formed. However, there is a doubling of the average current density over the experiment from 1 to 2 mA/cm².

Apart from sulfate electrolytes, acidic fluoroborate solutions are used industrially for copper electroplating.²²⁶ The deposit from a 2M NaBF_4 , with 0.25M $\text{Cu}(\text{BF}_4)_2$ and 1 M EDA saturated with CO_2 is shown in Figure 5-20(c) with

current response below. This deposit demonstrates similar adhesion to sulfate solutions though at much lower polarisation, averaging only 0.3 mA/cm² over the experiment. The majority of copper electrodeposition is performed at low pH (2-3), where soluble copper hydroxide and solid copper oxide are not stable. Unfortunately, the operating pH is limited by the presence of excess ethylenediamine, where fluoroborate deposition produces dark, dull and brittle deposits if the solution pH is above 1.7.²²⁶ Industrial plating in acid sulfate or fluoroborate solutions operates between 1 and 5 mA/cm², where deposition quality has been optimised with the use of additives over a century.²²⁶

Curiously the current response of the electrolyte under 5 bar CO₂ was significantly better, at nearly 3 times the current density (2.75 vs 1 mA/cm²). To investigate the difference in polarisation response of each electrolyte solution, EIS was performed before and after each deposition experiment. A Nyquist plot of the EIS response and the equivalent circuit used to fit the data are presented in Figure 5-21. As there is no diffusion-like resistance present in the Nyquist plot over the frequency range studied, a Randles circuit without the Warburg (diffusional) impedance, with a constant phase element (CPE) in place of the ideal capacitor was used to fit the results. The CPE can account for inhomogeneity in the double layer and electrode surface - its impedance is given by $Z_{CPE} = 1/C(j\omega)^n$, where C is traditional capacitance and n indicates deviation from ideal behaviour, where $n = 1$ is an ideal capacitor and $n = 0$ an ideal resistor. The parameters used in the model to fit the data, parameter error and total sum of squares error are presented in Table 5.3.

The addition of chloride is seen to significantly reduce the polarisation resistance, by nearly 7 times. Chloride ions form an ordered anion layer at each electrode, which at the cathode provides a lower energy path for deposition via inner sphere electron transfer and at the anode improves dissolution through a copper chloride intermediate.^{226,252,253} The change in the anion adlayer is reflected in the decrease of the capacitance value of C in the CPE. The fluoroborate electrolyte demonstrates a similar polarisation resistance to the sulfate system,* though the decrease in capacitance causes an increase in the total impedance of

*Grambow and Vielstich²⁵⁴ found exchange current densities for the copper system in BF₄ 85% of that in SO₄ electrolytes

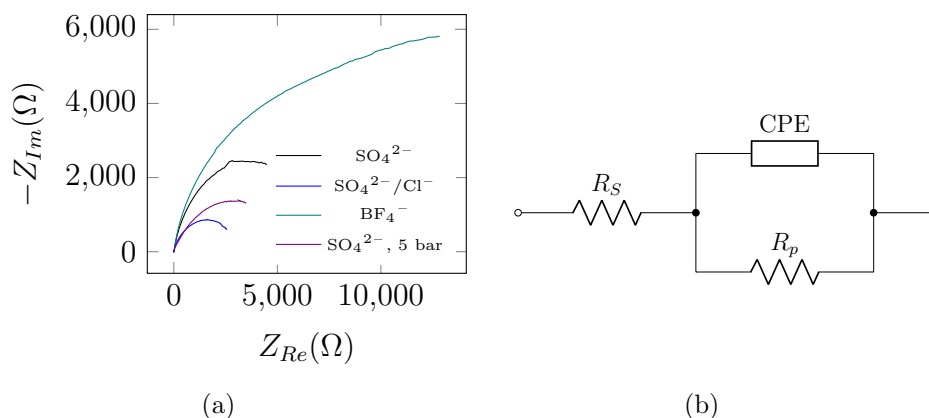


Figure 5-21: Nyquist plot of impedance for each electrolyte system (a) and the equivalent circuit use to analyse the response (b)

Table 5.3: Parameters extracted from impedance measurement fit to equivalent circuit. Resistance in Ω , capacitance in Farads. Percentage error quoted as beyond which change to the parameter reduces the goodness of fit.

Parameter	Electrolyte							
	SO_4^{2-}	% ϵ	$\text{SO}_4^{2-}/\text{Cl}^-$	% ϵ	BF_4^-	% ϵ	$\text{SO}_4^{2-}{}^a$	% ϵ
$R_s(\Omega)$	2.869	9.34	3.829	5.92	3.952	4.90	3.875	11.08
$R_p(\Omega)$	8858	11.90	1269	21.41	7938	13.99	1094	21.00
CPE, C (F)	7.25×10^{-6}	1.53	7.16×10^{-6}	15.61	2.28×10^{-6}	6.38	7.25×10^{-6}	25.52
CPE, n (-)	0.79295	61.35	0.82956	1.84	0.84044	0.77179	0.79472	3.13
Σe^2	0.265		0.215		0.066		0.606	

^aUnder 5 bar CO_2

the system in the parallel circuit, demonstrated by a large but not fully formed semicircle on the Nyquist plot. The total pressure of the system is seen to have the largest impact on the polarisation resistance, where in moving to 5 bar, R_p reduced by over 8 times, resulting in the near tripling of the current response in Figure 5-20. The improved polarisation response under moderate pressure, adds to the many benefits of operating the EMAR system above ambient pressure.

To examine the effect of polarity switching on the electrodes, a voltage of 0.6 V was applied and reversed each 15 minutes (900 seconds). One of the resulting electrodes and the current response is shown in Figure 5-22. The dull yellow

sections of the electrode are due to the predominately anodic reaction,* where darker flakes are indicative of electrodeposited copper. After approximately 45 minutes, the third polarity reversal, a section of the flaky electrodeposit bridged the gap and shorted the cell, allowing large currents to flow through the circuit ($>1\text{A}$). Prior to the short, each polarity reversal saw an increase in the average current density, from 0.41 to 0.83 to 1.23 mA/cm^2 due to an increase in surface roughness.

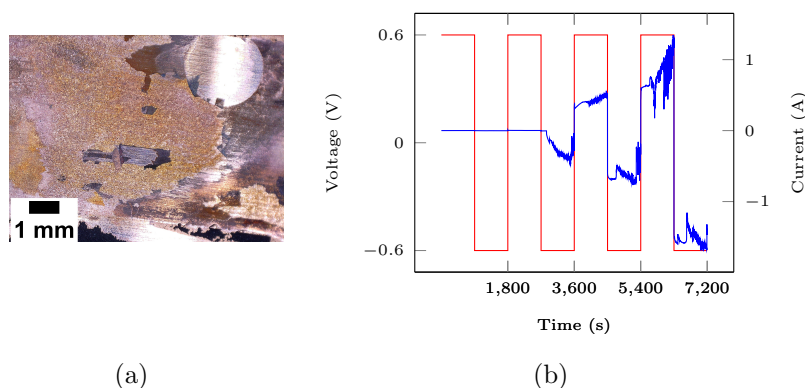


Figure 5-22: Photo of the electrode, post polarity switch (a) and potential and current response (b).

To avoid inconsistent agitation provided by CO_2 bubble propagation, electrodeposition was performed in a stirred solution with smaller electrodes. The cathodes resulting from electrodeposition at 0.5 mA over a $1/4$ inch square copper electrode are shown in Figure 5-23. It is clear from the applied potential shown in Figure 5-23(c) that the current in previous deposition experiments is mass transfer limited because the 1.24 mA/cm^2 applied here requires just 0.25 V on average compared to the 0.6 V applied previously. Deposits from the sulfate solution at lower overpotentials are more compact, though are confined to less than half the electrode surface area. Although the addition of chloride (at just 0.1 mg/L) affects the applied potential[†] and adhesion of the electrodeposit, the coverage is more uniform. Regions of the electrode in Figure 5-23(b) display an even flat distribution among sections of curled deposits. EIS measurements of

*Where the yellow colour may indicate the formation of a urea derivative or imine.

[†]Experiments were performed simultaneously with separate stirrers where the stirring speed could not be set explicitly.

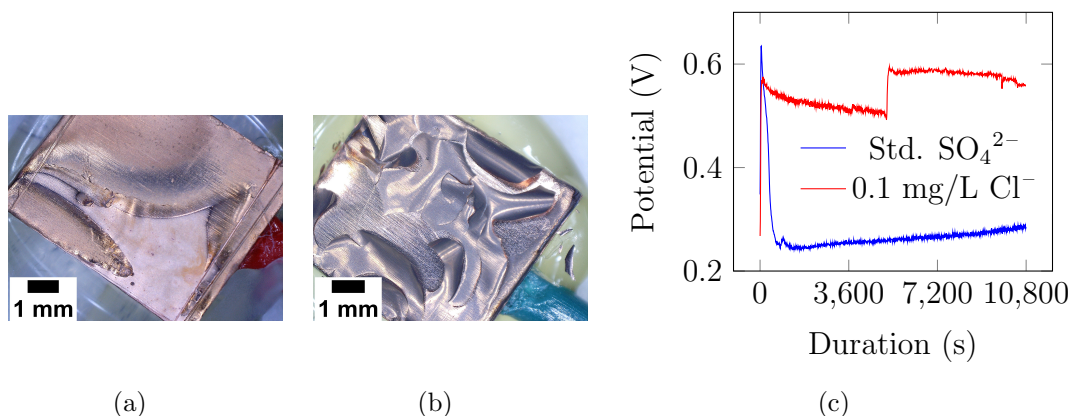


Figure 5-23: Photo of cathode post electrodeposition of standard sulfate solution (a) sulfate solution with 0.1 mg/L HCl (b) applied potential to maintain 0.5 mA (1.24 mA/cm²) over three (3) hour duration(c).

each electrode indicate that chloride again reduces the polarisation resistance, see Figure 5-24, and so the higher potentials in the chloride system are due to mass transfer limitations. The polarisation resistance (extracted when fit with the equivalent circuit) reduces from 7170 Ω to 1708 Ω with the addition of only 0.1mg/L Cl⁻. Given the large impact that the addition of chloride ions have on deposit quality and throwing power, further investigation into the ideal concentration is warranted.*

The majority of copper deposits examined were poorly adhered and flaky bar those obtained at low current densities and low overpotentials. Ambient temperature runs may have contributed to the poor deposits as Brockman and Mote²⁴⁹ noted brighter and adherent deposits can be obtained at above 50 °C. Their electrolyte did not contain carbonate (due to CO₂ saturation), which if present in excess yield grainy deposits in alkaline plating baths.²²⁶ Additionally, the products of sulfate reduction have a grain coarsening effect which can be mitigated by heating the electrolyte solution.²²⁶ Higher temperature operation and pre-treatment of the cathode via acid etch present good options for future improvement, before examining the many additives that have been used in industrial electroplating

*Eltayeb⁴⁸ noted bromide ions were co-deposited with copper, consuming the salt. This is likely due to its greater specific adsorption onto metal surfaces.²⁵² Adsorption energies for chloride is lower and so less will occur, though co-deposition of chloride can be beneficial to mechanical properties if the concentration is maintained.²²⁶

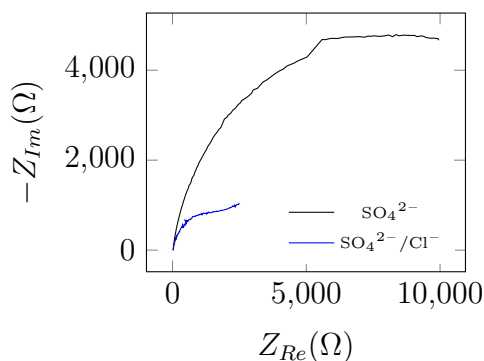


Figure 5-24: Nyquist plot comparing the impedance of the standard sulfate electrolyte and that with 0.1 mg/L HCl. Both solutions saturated with CO₂.

of copper. In order for EMAR to be competitive to traditional amine systems, high current densities (tied to the amine regeneration rate) and stability of the process are necessary. The addition of minimal chloride salts and operation at elevated pressure have the potential to significantly improve the current density and reliability of the system.

5.4 Summary

The ideal thermodynamic description of the EMAR process is presented and the effect of the electrolyte was examined. The previously employed nitrate electrolyte was investigated with CVs and displayed high cathodic currents - implying blocking and reaction at the cathode. sulfate electrolytes demonstrate more stable behaviour and were used in subsequent investigations. Cyclic voltammograms of a dilute EMAR electrolyte under CO₂ and N₂ are presented, where pH effects and the kinetics of carbamate dissociation shift the peak potentials and current response. Implementation of the electrochemistry in a stacked cell configuration suffered from low efficiency due to: poor temperature control, degradation of the nitrate electrolyte, mixing due to ineffective cell membranes and bubble trapping in the baffle system. All of these were addressed and improved in future stack versions though not sufficiently to perform experiments with natural gas. The effects of the contaminants in natural gas were then investigated. H₂S was found to suppress the electrochemical response of the EMAR electrolyte in 1:1 (H₂S:Cu)

ratio forming solid CuS in the process. CuS solids can be removed, treated by calcination and reintroduced as solid copper oxide to dissolve in the electrolyte returning to the EMAR circuit, or a simpler adsorbent bed may be employed upstream of the EMAR absorber unit to avoid solids handling. EMAR electrolyte behaviour was then examined at elevated pressure which served as a baseline comparison for when natural gas was applied to the system. The effect of natural gas on the electrochemical response was minimal, where dissolved hydrocarbons appear to adversely affect copper(II) diffusion. The effects of pressure and electrolyte on the quality of electrodeposited copper were investigated. Increasing the pressure to 5 bar and introducing minimal chloride ions to the electrolyte were found to significantly decrease the polarisation resistance of the electrode sandwich examined. Weak adhesion of electrodeposited copper was observed across all electrolyte systems, though chloride additives demonstrated superior leveling of the copper plate. Elevated temperature deposition and pretreatment of fresh copper electrodes are suggested to improve plate adhesion while operation with chloride additives at elevated pressure is recommended to reduce energy requirements and generate level copper deposits.

Chapter 6

Process model

As EMAR has been proven viable for natural gas treating by a combination of quantum chemical modelling and electrochemical experiments, the energy for CO₂ capture by an EMAR system is now compared against that for current state of the art thermal systems. An example natural gas, similar to that used in the experiments of Chapter 5, is simulated in an EMAR process model to determine the energetics of CO₂ capture. A number of case studies are presented, where key process variables such as the operating concentration of amine, absorption pressure and EMAR cell pressure are varied with results presented. A thermal amine system was modelled in Aspen Hysys V10 and the EMAR model used is an extension of the work published in Wang et al.¹⁰¹. The solubility of natural gas components and application of the Peng-Robinson equation of state to the gas phase have been added to address hydrocarbon losses in the system and the non-ideality of natural gas mixtures at high pressure.

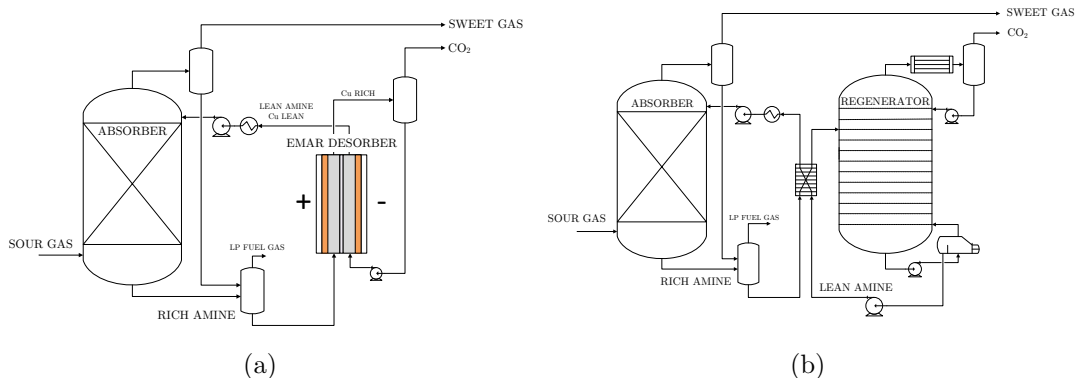


Figure 6-1: Simple process diagrams of the electrochemical (a) and thermal (b) regeneration cycles for aqueous amine solvents.

6.1 EMAR process model

Having examined specific EMAR reactions with quantum chemistry and confirmed the behaviour of a real EMAR electrolyte under a natural gas atmosphere and at elevated pressure, an overall thermodynamic model was built to understand the total energy requirements of the whole system for CO₂ capture. Results from the EMAR process model are benchmarked against those from a model of the current state of the art thermal regeneration systems. A simplified process scheme for electrochemical and thermal amine regeneration are shown in Figure 6-1 (a) and (b), respectively.

6.1.1 Model development

The EMAR model was built on the work of Wang et al.¹⁰¹ where components and relations specifically relevant to natural gas sweetening were added. The aqueous phase is treated similarly but the gas phase was modelled with the Peng-Robinson Equation of State (EoS), which is more applicable to the simulation of natural gas.^{255,256} This combination mirrors that used in commercial packages such as Aspen HYSYS V10, where the recommended property package for acid gas treating (Acid Gas - Chemical Solvents) simulations is a combination of Peng-Robinson EoS and symmetric eNRTL.^{257,258} In that specific combination of packages, ki-

netic and equilibrium relations are included for some reactive amines such as MEA, MDEA and DEA though does not include EDA because it has not been considered viable for thermal amine stripping.⁵¹ Since commercial packages cannot simulate the EMAR process, all model equations were written and solved in MATLAB. Equations that dictate the behaviour of the liquid and vapour phases, and the governing equations of each unit operation are described herein.

6.1.2 Liquid and vapour phase treatment

Liquid phase calculations are performed with the B-dot activity coefficient model according to standard procedures outlined in the geochemical speciation package EQ3/6 v8.0 manual.²⁵⁹ Temperature dependent equilibrium constants were extracted from the extensive database available in EQ3/6, where specific relations for copper(II) with EDA were obtained from Paoletti¹⁸⁶ and EDA with CO₂ from Stern³⁷. The speciation equations considered in this model are presented in Table 6.1.

The activity of species i is given by:

$$a_i = \gamma_i c_i \quad (6.14)$$

The activity coefficients of ionic species (e.g. carbonate and sulfate ions) were determined with equation 6.15, and converted to the National Bureau of Standards (NBS) scale using the B-dot activity coefficient of Cl⁻ and the relations 6.17 and 6.18 below.

$$\log \gamma_i = -\frac{A_{\gamma,10} z_i^2 \sqrt{I}}{1 + a_i B_{\gamma} \sqrt{I}} + B \bar{I} \quad (6.15)$$

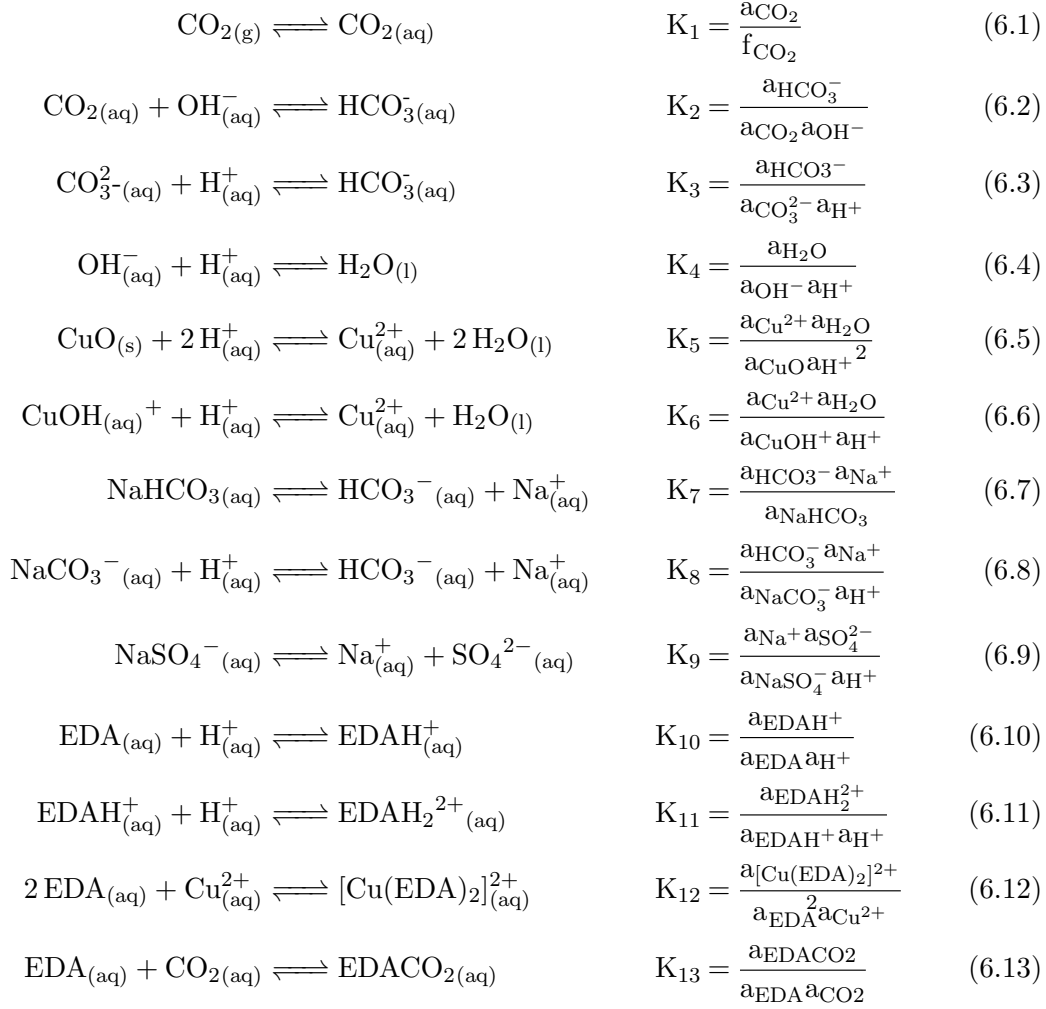
$$\bar{I} = \frac{1}{2} \sum_i c_i z_i^2 \quad (6.16)$$

$$\log \gamma_i|_{NBS} = \log \gamma_i|_{B-dot} + \frac{z_i}{z_{Cl^-}} (\log \gamma_{Cl^-}|_{NBS} - \log \gamma_{Cl^-}|_{B-dot}) \quad (6.17)$$

$$\log \gamma_{Cl^-}|_{NBS} = -\frac{A_{\gamma,10} \sqrt{I}}{1 + 1.5 \sqrt{I}} \quad (6.18)$$

The constants $A_{\gamma,10}$, B_{γ} are temperature dependent Debye-Hückel parameters, z

Table 6.1: Speciation equations considered in the EMAR process model.



the charge of the ion, a the hard sphere radius of the ion, \dot{B} the B-dot parameter and \bar{I} the ionic strength given by Eqn 6.16. The activity coefficients for all neutral polar species are set to unity, except H_2O and $\text{CO}_{2(\text{aq})}$. The activity coefficient for $\text{CO}_{2(\text{aq})}$ is calculated as per Eqn. 6.19, where T is the absolute temperature and the constants are defined as $C = -1.0312$, $F = 0.0012806$, $G = 255.9$, $E = 0.4445$ and $H = -0.001606$. The activity of H_2O is calculated in Eqn 6.20, where Ω is the concentration of water and σ and x are given by Eqn 6.21 and 6.22, respectively. The activity coefficient of dissolved neutral non-polar solutes is given by Eqn 6.23, where the coefficients a , b and c are a temperature dependent fit to 3rd order polynomials.²⁶⁰

$$\log\gamma_{\text{CO}_{2(\text{aq})}} = \left(C + FT + \frac{G}{T}\right)\bar{I} - (E + HT)\frac{\bar{I}}{1 + \bar{I}} \quad (6.19)$$

$$\log a_{\text{H}_2\text{O}} = \frac{1}{\Omega} \left(-\frac{\sum_i c_i}{2.303} + \frac{2}{3}A_{\gamma,10}\bar{I}^{1.5}\sigma - \dot{B}\bar{I}^2\right) \quad (6.20)$$

$$\sigma = \frac{3}{x^3} \left(1 + x - \frac{1}{1 - x} - 2\ln(1 + x)\right) \quad (6.21)$$

$$x = 4B_\gamma\sqrt{\bar{I}} \quad (6.22)$$

$$\log\gamma_{\text{NNP}} = a\bar{I} + b\bar{I}^2 + c\bar{I}^3 \quad (6.23)$$

Molar balances around each species yields Eqns. 6.24 through 6.28, which in concert with the charge balance (Eqn 6.29) and equilibrium relations in Eqns. 6.1 through 6.13 are solved to determine the aqueous concentration of each species.

$$c_{\text{Na}} = c_{\text{Na}^+} + c_{\text{NaHCO}_{3(\text{aq})}} + c_{\text{NaCO}_3^-} + c_{\text{NaSO}_4^-} \quad (6.24)$$

$$c_{\text{SO}_4} = c_{\text{SO}_4^{2-}} + c_{\text{NaSO}_4^-} \quad (6.25)$$

$$c_{\text{Cu}} = c_{\text{Cu}^{2+}} + c_{\text{CuOH}^+} + c_{\text{CuO}_{(\text{aq})}} + c_{[\text{Cu}(\text{EDA})_2]^{2+}} \quad (6.26)$$

$$c_{\text{EDA}} = c_{\text{EDA}_{(\text{aq})}} + c_{\text{EDAH}^+} + c_{\text{EDAH}_2^{2+}} + c_{\text{EDACO}_{2(\text{aq})}} + 2c_{[\text{Cu}(\text{EDA})_2]^{2+}} \quad (6.27)$$

$$c_{\text{C}} = c_{\text{CO}_{2(\text{aq})}} + c_{\text{HCO}_3^-} + c_{\text{CO}_3^{2-}} + c_{\text{NaHCO}_{3(\text{aq})}} + c_{\text{NaCO}_3^-} + c_{\text{EDACO}_{2(\text{aq})}} \quad (6.28)$$

$$\sum_i c_i z_i = 0 \quad (6.29)$$

The aqueous concentration of individual dissolved hydrocarbons (methane, ethane

and propane denoted as C1, C2 and C3, respectively) was approximated via solubility studies performed in HYSYS V10.²⁵⁵ Hydrocarbon solubility was determined in the flow sheet shown in Figure 6-2(a), in which the concentration of EDA in the liquid stream, temperature and total pressure were varied to extract a solubility relationship for each component, i.e. Eqn. 6.30.*

$$a_{C_1-C_3} = f(P, T, c_{EDA}) \quad (6.30)$$

The resulting relationship was fitted to a polynomial and included in the MATLAB model. The solubility of each component at 25 °C and 1 molal EDA is presented in Figure 6-2(b). At increased EDA concentration and low temperature the solubility of hydrocarbons is greater, and for CH₄ and C₂H₆ reaches a saturation limit, seen by the plateau in Figure 6-2(b). Propane exhibits erroneous behaviour with this combination of property packages, where aqueous solubility increases linearly up to a saturation limit where a separate liquid phase is formed. A detailed investigation into the appropriate treatment of hydrocarbon solubility is beyond the scope of this work. Since the propane content in natural gas is low (circa 1%), the exhibited partial pressure is also low, approx 0.5 - 1 bar and the differential solubility is not significant. As the treatment of a separate liquid phase in HYSYS V10 with the Acid Gas - Chemical Solvents package is not recommended, similarly the treatment of a hydrocarbon phase and partitioning of species between phases has not been considered here.

In the gas phase, the vapour pressure of water (P_{v,H_2O}) and EDA ($P_{v,EDA}$) are determined from equations 6.31 and 6.32 respectively.^{261,262} Where for P_{v,H_2O} : $T_c = 647.096 \text{ K}$, $P_c = 22.064 \text{ MPa}$ and $\sigma = \left(1 - \frac{T}{T_c}\right)$ and the a coefficients are $a_1 = -7.85951783$, $a_2 = 1.84408259$, $a_3 = -11.7866497$, $a_4 = 22.6807411$, $a_5 = -15.9618719$, $a_6 = 1.801220502$. With those for $P_{v,EDA}$: $A = 4.22368$,

*The activity coefficient of hydrocarbons in the water-EDA mixture was assumed to be unity, and when transferred to the present model, the activity coefficient is determined by Eqn 6.23.

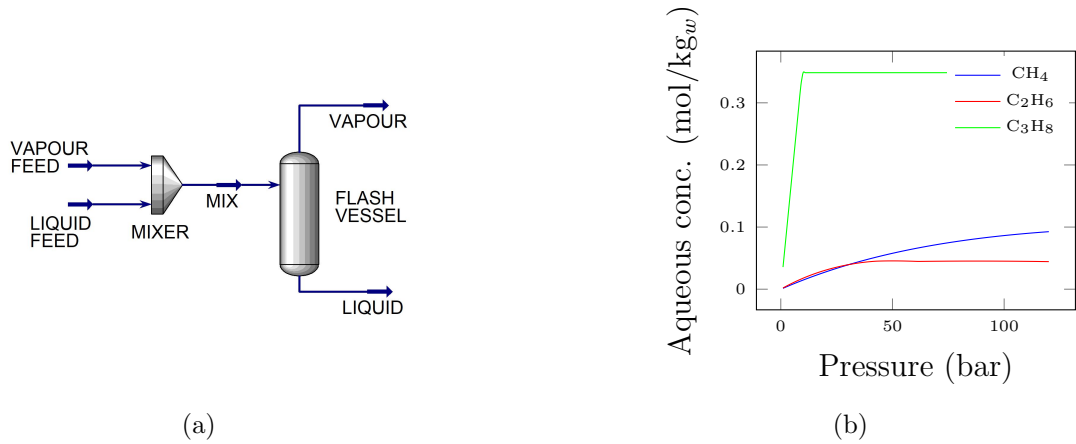


Figure 6-2: Flowsheet used to determined hydrocarbon solubility of C1 - C3 hydrocarbons in EDA-H₂O mixture (a), example hydrocarbon solubility in 1 molal EDA at 25 °C (b).

$B = 1302.256$ and $C = -81.788$.

$$\ln \frac{P_{v,H_2O}}{P_c} = \frac{T_c}{T} (a_1\sigma + a_2\sigma^{1.5} + a_3\sigma^3 + a_4\sigma^{3.5} + a_5\sigma^4 + a_6\sigma^{7.5}) \quad (6.31)$$

$$\ln P_{v,EDA} = A - \frac{B}{T + C} \quad (6.32)$$

The gas phase fugacity coefficients of each species are initially assumed to be unity and iteratively solved through application of the Peng-Robinson EoS.²⁵⁷ Fugacities of volatile components H₂O, EDA, CO₂ and hydrocarbons (C₁ - C₃) are determined with Raoult's law, Eqns 6.33 and 6.34.

$$f_i = y_i\phi_iP \quad (6.33)$$

$$y_i = \frac{a_iP_i^{sat}}{\phi_iP} \quad (6.34)$$

The P_i^{sat} term for H₂O and EDA which corresponds to their respective vapour pressures, P_v , for CO₂, is determined from Eqn. 6.1 and for hydrocarbons (C₁ - C₃) is determined by Eqn. 6.30. The Peng-Robinson binary mixing parameters ($k_{i,j}$) were extracted from the Aspen HYSYS V10 database where available.* Ta-

*If unavailable the relevant $k_{i,j}$ was set to zero.

Table 6.2: Dimensionless binary interaction parameters ($k_{i,j}$) extracted from Aspen HYSYS V10 used in Peng-Robinson Equation of State.

Species	CO ₂	N ₂	H ₂ O	H ₂ S	EDA	CH ₄	C ₂ H ₆	C ₃ H ₈
CO ₂	0	-0.02	$k_{\text{CO}_2,\text{H}_2\text{O}}$	0.1	0	0.1	0.12980	0.13500
N ₂	-0.02	0	$k_{\text{N}_2,\text{H}_2\text{O}}$	0.1676	0	0.036	0.05	0.08
H ₂ O	$k_{\text{H}_2\text{O},\text{CO}_2}$	$k_{\text{H}_2\text{O},\text{N}_2}$	0	$k_{\text{H}_2\text{O},\text{H}_2\text{S}}$	0	0.5	0.5	0.48
H ₂ S	0.1	0.1676	$k_{\text{H}_2\text{O},\text{H}_2\text{S}}$	0	0	0.085	0.084	0.075
EDA	0	0	0	0	0	0	0	0
CH ₄	0.1	0.036	0.5	0.085	0	0	0.00224	0.00683
C ₂ H ₆	0.12980	0.05	0.5	0.084	0	0.00224	0	0.00126
C ₃ H ₈	0.13500	0.08	0.48	0.075	0	0.00683	0.00126	0

Table 6.2 presents the binary interaction parameters used in this model. Though the original binary interaction parameters in the Peng-Robinson (PR) EoS model are independent of concentration, temperature and pressure, temperature dependence was included in Aspen HYSYS V10, and extracted to work within the model presented herein.²⁵⁵ The parameters that are acknowledged to be temperature dependent are $k_{\text{H}_2\text{O},\text{N}_2}$, $k_{\text{H}_2\text{O},\text{CO}_2}$, $k_{\text{H}_2\text{O},\text{H}_2\text{S}}$ and H₂O with any hydrocarbon, though over the temperature range examined (25 °C - 100 °C), only $k_{\text{H}_2\text{O},\text{N}_2}$, $k_{\text{H}_2\text{O},\text{CO}_2}$ and $k_{\text{H}_2\text{O},\text{H}_2\text{S}}$ expressed temperature dependence in a linear fashion. Variables describing the temperature dependence are in place of the constants in Table 6.2 below, with the dependence described in equations 6.35 to 6.37.*

$$k_{\text{H}_2\text{O},\text{N}_2} = 3.547281 \times 10^{-3}(T - 273.15) - 7.414581 \times 10^{-1} \quad (6.35)$$

$$k_{\text{H}_2\text{O},\text{CO}_2} = 1.021859 \times 10^{-3}(T - 273.15) - 1.346382 \times 10^{-1} \quad (6.36)$$

$$k_{\text{H}_2\text{O},\text{H}_2\text{S}} = 7.966677 \times 10^{-4}(T - 273.15) - 4.341113 \times 10^{-2} \quad (6.37)$$

The Peng-Robinson cubic equation of state, in the cubic form in Eqn. 6.45 may

*Note that $k_{i,j} = k_{j,i}$.

then be solved for the compressibility factor, Z , of each phase formed.

$$P = \frac{RT}{V_m - b} - \frac{a\alpha}{V_m^2 + 2bV_m - b^2} \quad (6.38)$$

$$T_r = \frac{T}{T_c} \quad P_r = \frac{P}{P_c} \quad (6.39)$$

$$\alpha = \left(1 + \kappa \left(1 - T_r^{\frac{1}{2}}\right)\right)^2 \quad (6.40)$$

$$\kappa \approx 0.37464 + 1.54226\omega - 0.26992\omega^2 \quad (6.41)$$

$$a \approx 0.45724\alpha \frac{R^2 T_c^2}{P_c} \quad b \approx 0.07780 \frac{RT_c}{P_c} \quad (6.42)$$

$$a_{i,j} = (1 - k_{i,j})\sqrt{a_i a_j} \quad a_{eff} = \sum_i y_i a_{i,j} y_j \quad b_{eff} = \sum_i b_i y_i \quad (6.43)$$

$$A = \frac{aP}{R^2 T^2} \quad B = \frac{bP}{RT} \quad Z = \frac{PV}{RT} \quad (6.44)$$

$$Z^3 - (1 - B)Z^2 + (A - 2B - 3B^2)Z - (AB - B^2 - B^3) = 0 \quad (6.45)$$

In Eqns 6.38 through 6.45, P is the absolute pressure, T the absolute temperature and P_r and T_r their reduced variants (that is divided by the critical pressure and temperature of the pure component, respectively), V_m is the specific molar volume and a and b are constants depending on the temperature, pressure and composition of the gas mixture. ω is defined as follows $\omega = -\log_{10}(p_r^{sat}) - 1$ at $T_r = 0.7$. When the equation is applied to pure components the coefficients to the cubic EoS (in Eqn. 6.45) are formed from a and b determined in Eqn 6.42. When the properties of a mixture are requested the coefficients to the cubic EoS are formed from the effective a and b that arise from a mixture of components and employ the binary interaction parameters in Eqn. 6.43.

The fugacity coefficient is then calculated by the following Eqn. 6.46.

$$\ln\phi_i = \frac{b_i}{b_{mix}}(Z_v - 1) - \ln(Z_v - B_{mix}) - \left(\frac{A_{mix}}{2\sqrt{2}B_{mix}}\right) \left(\frac{2\sum_j y_j a_{i,j}}{a_{mix}} - \frac{b_i}{b_{mix}}\right) \ln\left(\frac{Z_v + B_{mix}(1 + \sqrt{2})}{Z_v + B_{mix}(1 - \sqrt{2})}\right) \quad (6.46)$$

The lack of binary interaction parameters for EDA is not a significant issue due

Component	Mole Fraction
Methane	0.887
Ethane	0.035
Propane	0.010
CO ₂	0.030
N ₂	0.038

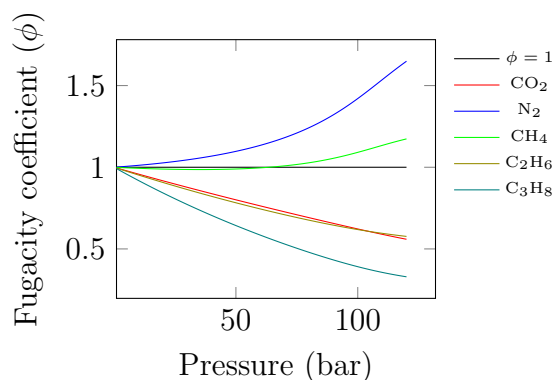


Figure 6-3: Composition of trial gas to determine fugacity coefficients (**left**) and fugacity coefficient (ϕ_i) of each component (by PR EoS) as total pressure is increased (**right**). Plotted with unity fugacity coefficient for comparison.

to its low vapour pressure and therefore concentration in the vapour phase. The change in the fugacity coefficient of a sample gas mixture as the pressure is increased is shown in Figure 6-3. There is significant deviation in all components (bar methane) at a common absorber operating pressure of 50 bar. At these conditions, were the ideal gas equation used, the equilibrium concentration of dissolved CO₂ would be over-represented leading to unrealistic values in the total amine circulation rate required.

Additional thermodynamic values, such as the enthalpy and entropy of the gas phase, are determined with the departure functions in Eqn 6.47 and Eqn 6.48, respectively. These combined with the ideal gas relations for a mixture (see Eqns 6.51 - 6.56) are used to determine the total gas enthalpy and entropy. Polynomial correlations for individual component specific heat capacity were obtained from Yaws²⁶³. Departure functions and total enthalpy and entropy were validated

against Aspen HYSYS V10.²⁵⁵

$$h_{mix}^{dep} = RT(Z_v - 1) + \frac{T \left(\frac{da_{mix}}{dT} \right) - a_{mix}}{2\sqrt{2}b_{mix}} \ln \left(\frac{Z_v + B_{mix}(1 + \sqrt{2})}{Z_v + B_{mix}(1 - \sqrt{2})} \right) \quad (6.47)$$

$$s_{mix}^{dep} = R \ln(Z_v - B_{mix}) + \frac{\left(\frac{da_{mix}}{dT} \right)}{2\sqrt{2}b_{mix}} \ln \left(\frac{Z_v + B_{mix}(1 + \sqrt{2})}{Z_v + B_{mix}(1 - \sqrt{2})} \right) \quad (6.48)$$

$$\left(\frac{da_{mix}}{dT} \right) = \frac{1}{2} \sum_{i=1}^N \sum_{j=1}^N y_i y_j (1 - k_{i,j}) \left(\sqrt{\frac{a_j}{a_i}} \left(\frac{da_i}{dT} \right) + \sqrt{\frac{a_i}{a_j}} \left(\frac{da_j}{dT} \right) \right) \quad (6.49)$$

$$\frac{da_i}{dT} = \frac{-\kappa_i a_i}{\sqrt{\alpha_i T T_{ci}}} \quad (6.50)$$

$$h_i^{IG} = \int_{T_{ref}}^T C_{P,i}^{IG} dT \quad (6.51)$$

$$h_{mix}^{IG} = \sum y_i h_i^{IG} \quad (6.52)$$

$$h_{mix} = h_{mix}^{IG} + h_{mix}^{dep} \quad (6.53)$$

$$s_i^{IG} = \int_{T_{ref}}^T \frac{C_{P,i}^{IG}}{T} dT - R \ln \frac{P}{P_0} \quad (6.54)$$

$$s_{mix}^{IG} = \sum y_i s_i^{IG} - R \sum y_i \ln y_i \quad (6.55)$$

$$s_{mix} = s_{mix}^{IG} + s_{mix}^{dep} \quad (6.56)$$

6.1.3 Process unit operations

The EMAR process model flow sheet is presented in Figure 6-4 where unit operations and streams have been labelled in capitals. The high pressure sour gas contacts the lean EDA (with respect to CO₂) in the absorption column (ABSORBER). The rich amine solution leaving the absorber bottoms is sent to a hydrocarbon flash tank (HC FLASH TANK), typically operated in thermal systems at around 8 bar to flash off dissolved hydrocarbons.* The liquid stream then enters the anode of the EMAR cell (EMAR DESORBER) where CO₂ is released. The two phase flow is separated (EMAR SEP. TANK) with the gas vented to atmosphere or compressed for utilisation or sequestration. The liquid

*The performance of this unit in the EMAR process and implications is explored in Section 6.3.3.

stream from the separation vessel is sent to the cathode and recycled back to the absorption column.

The wet gas streams leaving the ABSORBER, HC FLASH TANK and EMAR SEP. TANK all pass through partial condensers in which all water and amine are condensed and returned via a liquid stream. The sweet gas outlet of PC1 (saturated with water and amine vapour) is forwarded to the dehydration section of the facility, and is not considered here. The outlet of PC2 is sent to a low pressure fuel gas system, which forms part of the fuel gas utility within a LNG facility. The outlet of PC3 is sent to multistage compression to achieve sequestration pressures. There are three sections of the flow sheet that are assumed to operate isothermally, they are: 1. Absorber and PC1, 2. HC Flash Tank and PC2, 3. EMAR desorber, EMAR SEP TANK and PC3. In case studies where sections of the flowsheet are operated at different temperatures, the three utility heaters or coolers, UTIL 1 - 3, are used to adjust the process stream temperature.

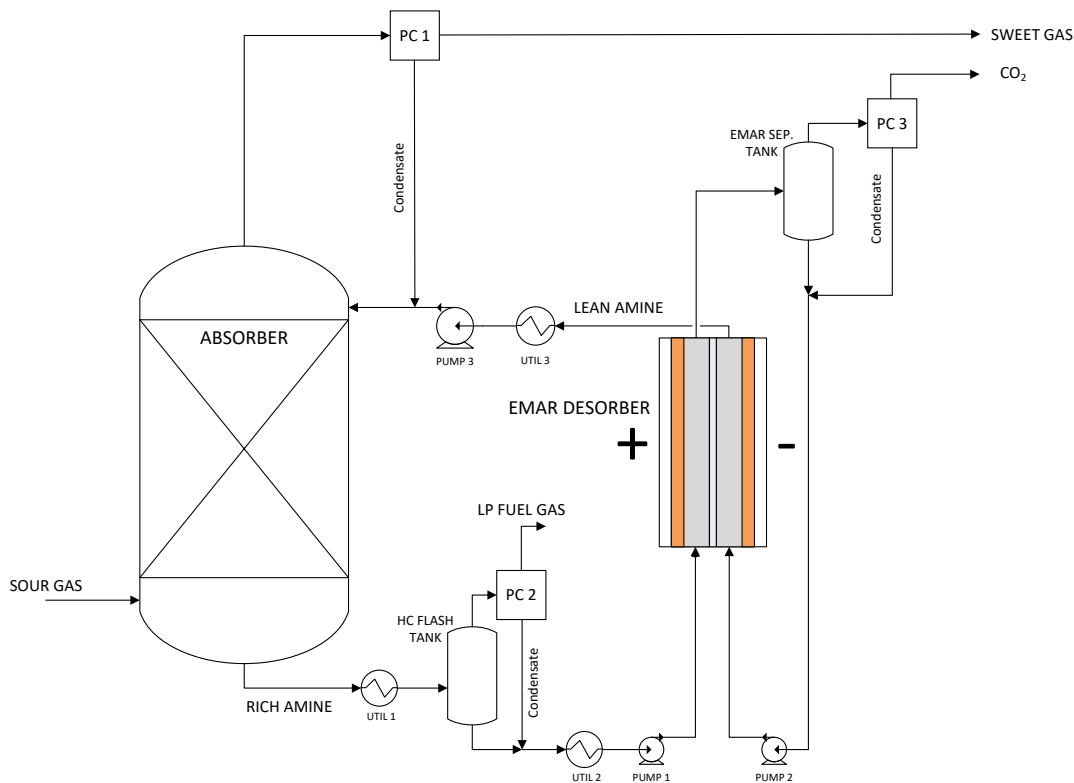


Figure 6-4: Flowsheet of the EMAR process modelled.

The governing equations, and any simplifying assumptions, for each class of unit operation follow.

6.1.3.1 Absorption column

A simple process diagram of the absorption column is shown in Figure 6-5. The following assumptions were made for the operation of the absorber:

- A1 Only CO_2 , N_2 , CH_4 , C_2H_6 and C_3H_8 enter the absorption column.
- A2 N_2 is an inert component that is not soluble in the liquid stream.
- A3 Perfect vapour-liquid equilibrium is present throughout the absorber and there are enough stages that the liquid leaving the bottom is in equilibrium with the inlet sour gas.
- A4 The absorber operates isothermally and all streams entering and leaving operate at this specified temperature.

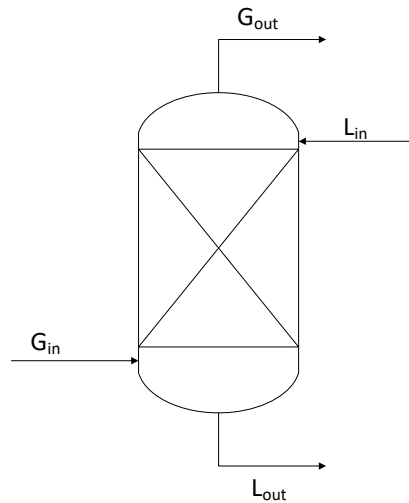


Figure 6-5: Diagram of absorption column. Flow rate of gaseous (G) and liquid streams (L). Stream L_{in} includes the makeup water and amine contribution accounting for evaporation.

The overall mass balance around the absorber:

$$G_{in} + L_{in} = G_{out} + L_{out} \quad (6.57)$$

The component molar balance for the inert, insoluble species N_2 is shown in

Eqn 6.58. For soluble and speciated CO₂ in Eqn 6.59, where c_C represents the total aqueous concentration of dissolved CO₂ as HCO₃⁻(aq), CO₃²⁻(aq), CO₂(aq) and EDA-CO₂(aq). The component balance for the soluble hydrocarbon species is shown in Eqn 6.60, where i represents one of CH₄, C₂H₆ or C₃H₈.

$$G_{m,in}y_{N_2,in} = G_{m,out}y_{N_2,out} \quad (6.58)$$

$$G_{m,in}y_{CO_2,in} + L_{in}x_{mw,in}c_{C,in} = G_{m,out}y_{CO_2,out} + L_{out}x_{mw,out}c_{C,out} \quad (6.59)$$

$$G_{m,in}y_{i,in} + L_{in}x_{mw,in}c_{i,in} = G_{m,out}y_{i,out} + L_{out}x_{mw,out}c_{i,out} \quad (6.60)$$

G_m refers to the molar flow rate of the gas stream according to Equation 6.61, where M is the molar mass of each gaseous species.

$$G_m = G / \sum_i y_i M_i \quad (6.61)$$

The mass balances for the non-volatile components $i \in [Na, SO_4, Cu]$ is given by:

$$L_{in}x_{mw,in}c_{i,in} = L_{out}x_{mw,out}c_{i,out} \quad (6.62)$$

Given a required (dry) outlet concentration of CO₂ downstream of acid gas removal, y_{CO_2} is set to $y_{CO_2,target}^*$ and the mole fraction constraint given by:

$$y_{CO_2,out} + y_{N_2,out} + y_{CH_4,out} + y_{C_2H_6,out} + y_{C_3H_8,out} + y_{H_2O,out} + y_{EDA,out} = 1 \quad (6.63)$$

where $y_{H_2O,out}$ and $y_{EDA,out}$ are determined from the vapour-liquid equilibrium condition at the top of the absorber. Given G_{in} , y_{in} , c_{in} and $y_{CO_2,target}$ are supplied, the above equations are used to calculate the remaining unknowns. The total energy balance around the isothermal absorber is:

$$\begin{aligned} \Delta H_{abs} = & -\Delta H_{EDA-CO_2}(G_{m,in}y_{CO_2,in} - G_{m,out}y_{CO_2,out}) + \lambda_{H_2O}(G_{m,out}y_{H_2O,out} \\ & - G_{m,in}y_{H_2O,in}) + \lambda_{EDA}(G_{m,out}y_{EDA,out} - G_{m,in}y_{EDA,in}) \end{aligned} \quad (6.64)$$

*Case studies herein examine system energy requirements at 50 ppm CO₂ and 2 mol % CO₂

Where the heat of reaction, $\Delta H_{\text{EDA}-\text{CO}_2} = 86 \text{ kJ}_{th}/\text{mol}_{\text{CO}_2}$,³⁷ and the heat of vaporisation for H₂O and EDA are $\lambda_{\text{H}_2\text{O}} = 42.91 \text{ kJ}_{th}/\text{mol}_{\text{H}_2\text{O}}$, and $\lambda_{\text{EDA}} = 43.9 \text{ kJ}_{th}/\text{mol}_{\text{H}_2\text{O}}$, respectively.^{262*} The enthalpy of reaction, $\Delta H_{\text{EDA}-\text{CO}_2}$, typically dominates the energy balance around the absorber and requires cooling to operate isothermally. The flow rate of cooling water required, the electrical equivalent energy required to regenerate the utility and the pump work are calculated for this absorber utility as described in Section 6.1.3.6.

6.1.3.2 Flash/Separation tank

Figure 6-6 shows the process diagram of the multicomponent flash tank. The following assumptions are made for the operation of the flash tank:

- A5 Gas and liquid streams leaving the flash tank are in equilibrium with each other.
- A6 Flash tank operates at isothermal conditions and all streams entering and leaving operate at the specified temperature.
- A7 Complete separation of vapour and liquid phases is achieved i.e. no liquid entrainment in vapour phase.

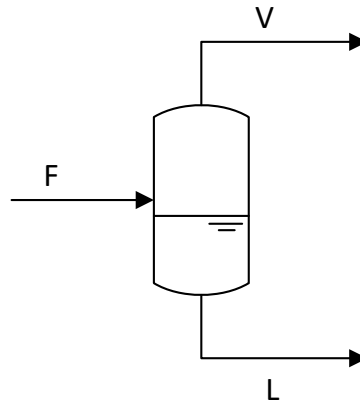


Figure 6-6: Diagram of the multicomponent flash tank. Mass flow rate of gaseous (V) and liquid streams (L) marked.

The overall mass balance of the flash tank is given by Eqn 6.65 and the component balances of volatile components ($i \in [\text{H}_2\text{O}, \text{EDA}, \text{CO}_2, \text{CH}_4, \text{C}_2\text{H}_6, \text{C}_3\text{H}_8]$)

* $\lambda_{\text{H}_2\text{O}}$ quoted at 50 °C where correlation from Linstrom and Mallard²⁶² was used to determine λ_{EDA} at a given temperature.

and non-volatile components ($i \in [\text{Na}, \text{SO}_4, \text{Cu}]$) are given by Eqn 6.66 and 6.67, respectively.

$$F = V + L \quad (6.65)$$

$$F_m x_{mx,in} c_i = V_m y_{i,out} + L x_{mw,out} c_{i,out} \quad (6.66)$$

$$F x_{mw,in} c_{i,in} = L x_{mw,out} c_{i,out} \quad (6.67)$$

The ratio of the vapour molar flow to feed molar flow (V_m/F_m) leaving the multicomponent flash tank is determined via an iterative method employing individual component K-values (K_i , see Eqn 6.68), the error function (ϵ , Eqn 6.69), its derivative (Eqn 6.70) and the Newton-Raphson method applied to the vapour feed split ratio (Eqn 6.71).²⁶⁴

$$K_i = \frac{y_i}{x_i} = \frac{\gamma_i P_i^{sat}}{\phi_i P} \quad (6.68)$$

$$\epsilon = \sum_i \frac{z_i (K_i - 1)}{1 + (V_m/F_m)(K_i - 1)} \quad (6.69)$$

$$\frac{d\epsilon}{d(V_m/F_m)} = - \sum_i \frac{z_i (K_i - 1)^2}{[1 + (V_m/F_m)(K_i - 1)]^2} \quad (6.70)$$

$$\epsilon + \frac{d\epsilon}{d(V_m/F_m)} \Delta(V_m/F_m) = 0 \quad (6.71)$$

$$x_i = \frac{z_i}{1 + (V_m/F_m)(K_i - 1)} \quad (6.72)$$

Where z_i is the mole fraction of volatile component i in the feed. Given the temperature, pressure and composition entering the flash tank, all unknowns above may be solved for. Additionally, the bubble point (P_{bub}) and dew point pressure (P_{dew}) are estimated for the mixture to ensure the flash tank is operating in a two phase region, as per the condition $P_{dew} < P_{FLASH\ TANK} < P_{bub}$. If the flash tank pressure is greater than the bubble point pressure, no vapour will leave the separation vessel and liquid composition leaving the flash tank is equal to that which entered. The flash tank code will not run (and will return an error) if its pressure is set to that below the dew point pressure calculated for the mixture.

The isothermal energy balance around the flash tank is then:

$$\Delta H_{FT} = \Delta H_{\text{EDA-CO}_2} V_m y_{\text{CO}_2, \text{out}} + \lambda_{\text{H}_2\text{O}} V_m y_{\text{H}_2\text{O}, \text{out}} + \lambda_{\text{EDA}} V_m y_{\text{EDA}, \text{out}} \quad (6.73)$$

There are two flash tanks in the flowsheet shown in Figure 6-4. The first flash vessel, HC Flash Tank, is operated nominally at 8-9 bar where it serves two main purposes: some acid gases are released due to the drop in partial pressure, and co-absorbed hydrocarbons are released and recovered in a low pressure fuel gas system. In thermal amine systems this reduces the load on the regenerator reboiler by removing some acid gases, and also reduces the amount of hydrocarbons lost to the environment at the regenerator gas outlet. The second flash tank, EMAR Sep Tank, serves to separate the gaseous stream generated in the anode and the liquid stream that is returned to the cathode. Depending on the operating conditions of this vessel additional hydrocarbons may be passed to staged compression for sequestration. Rigorous simulation of this unit was therefore necessary to assess its performance and utility in the EMAR process.

6.1.3.3 Electrochemical cell - anode and cathode

Governing equations. The mass and energy balances for the anodic chamber of the electrochemical cell are presented below. The balances around the cathodic chamber are simpler (requiring fewer terms) and have not been presented, rather the differences from the anodic chamber described. Figure 6-7 shows a schematic of the anodic chamber. Here the Cu^{2+} lean and CO_2 rich aqueous stream enters with mass flow rate L_{in} . A constant voltage is applied to the cell which results in the Faradaic reaction $\text{Cu}_{(s)} \rightarrow \text{Cu}_{(aq)}^{2+} + 2e^-$ (with mass flow of copper(II) ions \dot{m}_{el}) in the anode, reversed in the cathode, at the same total current, I . In the anode, aqueous copper(II) ions competitively bind with EDA, displacing CO_2 . Once sufficient copper(II) has been dissolved to increase the fugacity of CO_2 to the total cell pressure, gas is released with mass flow rate G_{out} . The remaining liquid leaves the cell chamber with mass flow L_{out} . The following assumptions have been made regarding the operation of the electrochemical cell:

- A8 If a gas phase is developed in the cell, perfect vapour-liquid equilibrium exists between phases.

- A9 Lateral gradients in concentration (between the electrode surface and membrane) are non-existent.
- A10 The ionic migration current through the membrane is only permitted by one or more of the following charged species: bicarbonate, carbonate, hydroxide, sulfate, protons or sodium.
- A11 The anodic and cathodic chambers operate isothermally and streams entering and leaving each compartment do so at this temperature.
- A12 Anodic and cathodic flows through the EMAR cell are co-current in nature, where the copper lean solution in the anode runs parallel to the copper rich stream in the cathode (as in Wang et al.¹⁰¹).

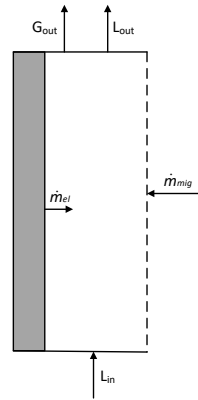


Figure 6-7: Diagram of the anode portion of the electrochemical cell. The grey region represents the solid copper electrode and the dashed line the membrane that connects that anode and cathodic chambers. \dot{m}_{el} is the mass flow of copper due to the Faradaic reaction and \dot{m}_{mig} the mass flow of ions that complete the electrical circuit.

The overall mass balance for the anodic compartment is given by Eqn 6.74. The molar balance for CO_2 around the chamber is given by Eqn 6.75, while those of other volatiles $i \in [\text{EDA}, \text{H}_2\text{O}, \text{CH}_4, \text{C}_2\text{H}_6, \text{C}_2\text{H}_8]$ are given by Eqn 6.76 and the balances of background electrolytes Na^+ and SO_4^{2-} are given by Eqn 6.77

and Eqn 6.78 respectively.

$$L_{in} + \dot{m}_{el} + \dot{m}_{mig} = G_{out} + L_{out} \quad (6.74)$$

$$L_{in}x_{mw,in}c_{C,in} + \dot{n}_{\text{HCO}_3^-,mig} + \dot{n}_{\text{CO}_3^{2-},mig} = G_{m,out}y_{\text{CO}_2,out} + L_{out}x_{mw,out}c_{C,out} \quad (6.75)$$

$$L_{in}x_{mw,in}c_{i,in} = G_{m,out}y_{i,out} + L_{out}x_{mw,out}c_{i,out} \quad (6.76)$$

$$L_{in}x_{mw,in}c_{\text{Na},in} + \dot{n}_{\text{Na},mig} = L_{out}x_{mw,out}c_{\text{Na},out} \quad (6.77)$$

$$L_{in}x_{mw,in}c_{\text{SO}_4,in} + \dot{n}_{\text{SO}_4,mig} = L_{out}x_{mw,out}c_{\text{SO}_4,out} \quad (6.78)$$

Where $\dot{n} = \dot{m}/M$. The balances for proton and hydroxide ions are not explicitly written because their concentrations are a result of solving the water dissociation reaction (Eqn 6.4) and charge balance (Eqn 6.29). Charge balance, on a molar flow basis, dictates that:

$$2\dot{n}_{\text{Cu}^{2+},el} + \dot{n}_{\text{Na}^+,mig} + \dot{n}_{\text{H}^+,mig} = \dot{n}_{\text{HCO}_3^-,mig} + 2\dot{n}_{\text{CO}_3^{2-},mig} + 2\dot{n}_{\text{SO}_4^{2-},mig} + \dot{n}_{\text{OH}^-,mig} \quad (6.79)$$

The molar flow rate of copper, $\dot{n}_{\text{Cu}^{2+},el}$ is based on the current through the electrochemical cell, I , and the Faradaic efficiency of the cell, η_{Cu} , by the following equation:

$$I = \frac{2\dot{n}_{\text{Cu}^{2+},el}F}{\eta_{Cu}} \quad (6.80)$$

where F is Faraday's constant. The migration of each ionic species depends on transport kinetics and concentration and electric field gradients. In this process model the migration of select species is specified as an input condition. The above equations can be used to solve for all of unknowns related to the anodic chamber. Similar relations are formed for the cathodic chamber with the following differences:

1. The direction of the migrating species is opposite to that in the anodic chamber.
2. The Faradaic reaction in the cathode is the deposition of copper ions, $\text{Cu}^{2+} + 2e^- \rightarrow \text{Cu}$.
3. No gaseous stream is present.

The energy balance over both chambers of the electrochemical cell can be

written as:

$$\Delta H_{cell} = \Delta H_{EDA-CO_2} G_m y_{CO_2, out} + \lambda_{H_2O} G_m y_{H_2O, out} + \lambda_{EDA} G_m y_{EDA, out} - W_{EMAR} \quad (6.81)$$

where W_{EMAR} is the electrical work supplied to the EMAR cell - defined in the next section. The temperature of the EMAR SEP. VESSEL is set to that of the desorber, and as such to maintain isothermal operation, cooling or heating may be required based on the balance of ΔH_{cell} and $\Delta H_{EMAR \text{ SEP VESSEL}}$. As with the Absorber, the heating or cooling utility requirements for the cell are provided by the CELL UTILITY, the specifics of which are determined by the relations in Section 6.1.3.6.

Thermodynamic cycle.

As shown in Section 5.1 of the previous chapter, an EMAR thermodynamic cycle can be described by key process variables, namely temperature, pressure, and the concentration of copper, amine and CO_2 . The aqueous copper(II) concentration is expressed as copper loading per two moles of amine i.e. x_{Cu} , where two indicates the stoichiometry of the copper ethylenediamine complex formed. Similarly, the total dissolved carbon concentration, which is the sum of HCO_3^- , CO_3^{2-} , $CO_{2(aq)}$ and $EDA-CO_2$ (not including any hydrocarbons), can be expressed as a loading with respect again to the amine concentration, x_C . These loading variables are summarised in Eqn 6.82.

$$x_{Cu} = \frac{2c_{Cu}}{c_{EDA}}, \quad x_C = \frac{c_C}{c_{EDA}} \quad (6.82)$$

$$E = E_0 + \frac{RT}{nF} \ln a_{Cu^{2+}} \quad (6.83)$$

The equilibrium potential of the half cell, with respect to aqueous copper(II), is given by 6.83. The half cell potential is a function of the above loading variables and operating conditions (shown previously in Eqn 5.2), and has been plotted at various copper loadings for increasing CO_2 fugacity and liquid phase concentration in 6-8(a). The red dotted lines are isolines of constant CO_2 fugacity (f_{CO_2}) and the dashed blue lines represent constant concentration of dissolved carbon

(x_C). A thermodynamic cycle for the EMAR process can be drawn by connecting isolines at constant CO_2 fugacity or liquid concentrations as in Figure 6-8(b). At the absorber inlet (Point 1) the concentration of dissolved carbon and partial pressure of CO_2 is low, as is the concentration of aqueous copper(II). The rich amine (Point 2), leaves the absorber (represented by the dashed green line) saturated with CO_2 at the fugacity of CO_2 in the absorber, here 1.67 bar.*The rich amine then enters the anodic chamber of the electrochemical cell where the aqueous copper(II) concentration is increased. Here an isoline of constant aqueous carbon loading ($x_C = 0.84$) is followed until sufficient Cu is dissolved such that the physical solubility for CO_2 has been reached (Point 3). Beyond this point, the anode further increases the aqueous copper(II) concentration and directly results in CO_2 gas release at the desorber pressure (20 bar) up to the end point x_{Cu} of the anode (Point 4). The gas liquid mixture is separated and the copper rich, carbon lean liquid is returned to the cathode. In the cathode, the copper(II) concentration is decreased while following the isoline of constant liquid carbon concentration, where it re-enters the absorber at point 1.

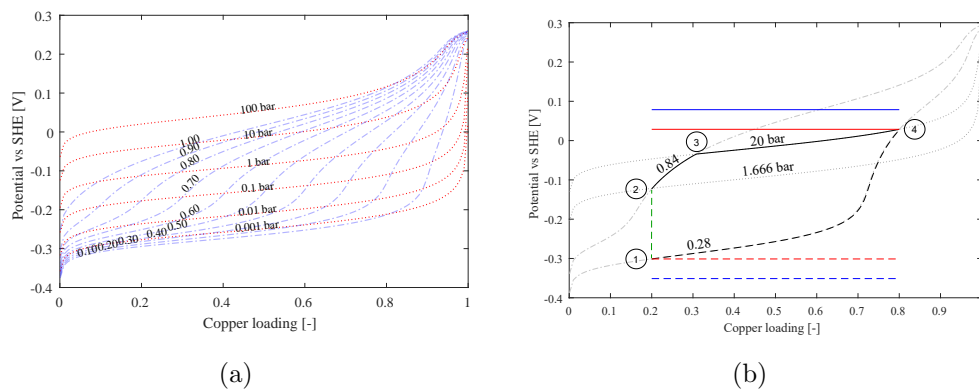


Figure 6-8: Half cell potential at increasing copper loading with isolines of CO_2 fugacity, f_{CO_2} (red dotted) and dissolved carbon, x_C (blue dashed)(a). Thermodynamic cycle of EMAR process applied to natural gas scenario (b). Black, red and blue lines are the half cell potential, maximum half cell potential and applied electrode potential respectively, where anodic lines are solid and cathodic are dashed. The dashed green line represents the absorption process, where the aqueous carbon loading (x_C) is increased.

*Simulation input conditions listed in Table 6.4, namely 4m EDA, 3% CO_2 in sour gas feed at 59.5 bar absorber pressure. 60% copper shift in electrochemical cell.

The current developed by the anodic and cathodic reactions is shown in Eqn 6.84, where the Q is the mass flow rate of liquid through the electrode section. The minimum work required by the electrochemical cell to perform the specific separation is given by Eqn 6.85, and is proportional to the area contained between the anodic and cathodic paths in Figure 6-8(b). In reality, the applied potential is provided by a single metallic electrode operating at a constant potential, and as a consequence develops a concentration overpotential as the copper and carbon concentrations change. The potential of a single metallic electrode is set at the maximum value for the anodic and cathodic paths, shown by the solid and dashed red lines in Figure 6-8(b) respectively. To achieve a desired current density, an additional surface and transport overpotential is applied above the maximum anode and cathode thermodynamic potential. This is indicated by the solid and dashed blue lines in Figure 6-8(b) for the anode and cathode respectively. Here a 100 mV overpotential is applied, which is assumed to be equally distributed between anode and cathode.* The total electrical work required by the cell is then a product of the potential difference applied and the current developed, shown in Eqn 6.86

$$dI = \frac{zF}{\eta_{Cu}} \left(Qx_{mw} \frac{x_{Cu}C_{EDA}}{2} \right) \quad (6.84)$$

$$W_{min} = \int_{x_{Cu}} E_{ox} dI - \int_{x_{Cu}} E_{red} dI \quad (6.85)$$

$$W_{EMAR} = \Delta V \int_{x_{Cu}} dI \quad (6.86)$$

Methods to reduce the EMAR cell work requirement have been investigated and presented by Wang et al.¹⁰¹ who proposed the use of multiple electrode segments, each operating at different potentials to reduce the required overpotential. Additionally Shaw and Hatton⁴⁷ proposed a simultaneous absorption and reduction process to reduce the area encapsulated between anodic and cathodic paths, thus reducing W_{min} . Neither of these modifications are considered in this process

*Overpotential partitioning depends on the transfer coefficient (α) of the system, which was determined by Stern³⁷ to be 0.25. This does not affect the work required at a specific applied overpotential.

model.

6.1.3.4 Partial condensers

The partial condensers are fictitious units, used to simplify the overall flow sheet mass and individual component mass balances - a schematic of the unit is shown in Figure 6-9. They serve to condense all water and EDA entering the unit and return the liquid stream to an appropriate location, while the dry gaseous components (CO_2 , N_2 , CH_4 , C_2H_6 , C_3H_8) leave the flow sheet from the location of the partial condenser. This avoids an explicit make-up water and amine stream because the flow sheet is closed with respect to these components. The following assumptions are made for the operation of the partial condensers:

A13 Partial condensers condense all water and EDA entering.

A14 The liquid condensate does not contain any dissolved CO_2 or hydrocarbons.

A15 The mass of condensate water that speciates is negligible.

The overall mass balance for the partial condenser is given by:

$$G_{in} = G_{out} + L_{out} \quad (6.87)$$

The component balances over a partial condenser for non-condensable components is given by Eqn 6.88, and for condensable components (H_2O and EDA) is given by Eqn 6.89

$$G_{m,in}y_{i,in} = G_{m,out}y_{i,out} \quad (6.88)$$

$$G_{m,in}y_{i,in} = L_{out}x_{mw}c_{i,out} \quad (6.89)$$

Depending on the configuration of a real facility, partial condensers may not be present where indicated in the EMAR flow sheet in Figure 6-4. In domestic gas and LNG production facilities, PC1 is simply a knockout drum prior to the dehydration section of the plant. Similarly, PC2 is replaced by a knockout drum and flashed gas is sent to the low pressure fuel gas system, and the real nature of PC3 depends on whether the facility performs CO_2 sequestration. Often acid gases leaving the desorber are vented directly to atmosphere and no additional units are required. Where carbon sequestration is desired a series of coolers,

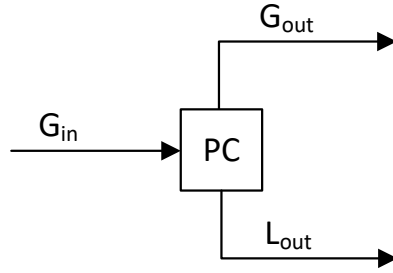


Figure 6-9: Diagram of simple (fictitious) partial condenser used in EMAR Process Model.

knockout drums and compressors are used to increase the pressure up to that required for sequestration (see Section 6.1.3.7).

6.1.3.5 Pumps

The work associated with pumping a fluid with mass flow rate Q , through a pressure change of ΔP is equal to:

$$W_{pump} = \frac{1}{\eta_{pump}} \left(\frac{\Delta P Q}{\rho} \right) \quad (6.90)$$

The pump efficiency has been assumed at 65% ($\eta_{pump} = 0.65$),³¹ and the fluid density 1000 kg/m³ throughout ($\rho = 1000 \text{ kg/m}^3$).

6.1.3.6 Heating and cooling utilities

Heating or cooling utilities are employed to maintain isothermal operation of individual unit operations or sections of the flow sheet and if units or sections are set to operate at different temperatures (handled by UTIL 1 through 3). The heating or cooling utility flow rate is then determined based on the following equations:

$$\Delta H_{util} = L_{util} C_p \Delta T_{util} \quad (6.91)$$

$$\Delta H_{util} = L_{unitop} C_p \Delta T_{unitop}. \quad (6.92)$$

Where H_{util} is the heating or cooling enthalpy required, L_{util} is the mass flow rate of the utility stream required (kg/s), $L_{unitop.}$ is the mass flow rate of the liquid stream between unit operations (kg/s), ΔT_{util} is the allowable temperature change in the utility stream (K), $\Delta T_{unitop.}$ is the difference between unit operating temperatures (K), and C_p is assumed to be that of water at 25 °C for all liquid streams ($C_p = 4.184 \text{ kJ}/(\text{kgK})$). The pump work associated with each utility may then be determined with Eqn. 6.90 and the equivalent electrical work for heating or cooling can be determined by the Carnot cycle as:

$$W_{util} = \eta_{turbine} \left(1 - \frac{T_C}{T_H} \right) \Delta H_{util} \quad (6.93)$$

Where T_H and T_C are the hot and cold sink temperatures for the Carnot cycle, $\eta_{turbine} = 0.9$ is the turbine efficiency,³¹ and ΔH_{util} is the utility thermal energy required (kJ_{th}). Where units are operated isothermally, the hot sink temperature is taken to be the operating temperature and the cold sink temperature is that of ambient air, 30 °C. Typically at LNG facilities cooling near ambient temperatures is often provided with fin-fan air coolers. Here cooling water at 30 °C has been used to approximate the utility heating and pumping requirements to avoid the complexity of sizing air coolers. For any utilities that do not operate isothermally, for instance interstage coolers in Figure 6-10 (similarly utility cooler UTIL 1 in Figure 6-11), the hot sink temperature is the log mean temperature the process stream experiences - more representative than the average temperature of the process stream in heat transfer applications.²⁶⁵ For example, the hot sink temperatures for an interstage cooler reducing the process temperature from 150 °C to 35 °C is determined by:

$$T_H = \frac{T_{H,out}/T_{H,in}}{\ln(T_{H,out}/T_{H,in})} \quad (6.94)$$

6.1.3.7 Compression

Figure 6-10 shows one stage of a multistage compression system used to deliver desorbed gases at the desired 300 bar pressure for sequestration.²⁶⁶ For simplicity, gas leaving the EMAR desorber is assumed to be dry with respect to water

and amine, as per the operation of PC 3, which negates the use of knockout drums and any further dehydration. The dry gas entering each compression stage is cooled to within 5 K of the cooling utility at 35 °C, and experiences a pressure drop of 50 kPa. As previously mentioned, though it is common to use air coolers in LNG facilities, and the interstage cooling in Figure 6-10 shown provided by an air cooler - for simplicity it has been estimated as cooling water at the same temperature as per Section 6.1.3.6. The cooled gas entering the compression stage is compressed such that the exhaust temperature does not exceed that recommended by API618²⁶⁷, 150 °C for reciprocating compressors in natural gas service to prevent evaporation or carbonisation of lubricating oils and auto-ignition of gaseous mixtures. To approximate the operation of real compressors an isentropic efficiency of $\eta_s = 0.85$ was used to determine the real gas enthalpy leaving the compressor. The process for a single stage is as follows: first the enthalpy of a gas leaving a reversible compression stage is determined assuming the following holds true $\Delta s = s_{in} - s_{out} = 0$, the enthalpy of the outlet gas from a real compressions stage is then calculated (with η_s) as per Eqn 6.95, and the outlet pressure is determined with Eqn 6.96, for a maximum exhaust gas temperature.

$$\eta_s = \frac{h_{out}^{real} - h_{in}}{h_{out}^{ideal} - h_{in}} \quad (6.95)$$

$$P_{out} = f(h_{out}^{real}, T_{max}) \quad (6.96)$$

Where h_{in} is the specific enthalpy of the gas entering the compressor, h_{out}^{ideal} is the enthalpy of the outlet gas following ideal isentropic compression, h_{out}^{real} is the enthalpy of the gas leaving a non-ideal compressor and T_{max} is the maximum allowable outlet temperature.

The work of compression is then the sum of the enthalpy differences required in each compression stage. Additionally, the work required for inter-stage cooling is estimated based on the necessary enthalpy change and Carnot cycle with appropriate hot and cold sink temperatures as per Section 6.1.3.6. As the number of compression stages varies depending on the desorber pressure, utility labels 6 and above are reserved for interstage cooling.

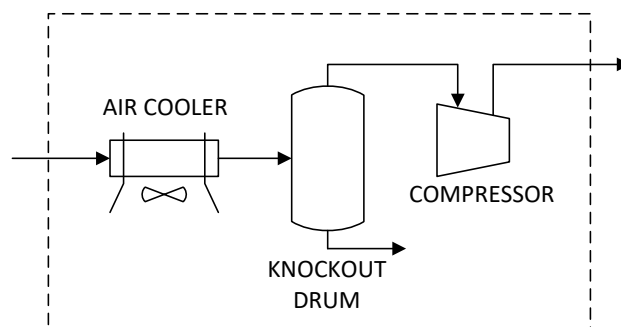


Figure 6-10: Diagram of a single stage of the a series multistage compression system with inter-stage air cooling.

6.2 Thermal amine model

Aspen Hysys V10 was used to develop and solve for key process variables and the total work of capture of a thermal amine flow sheet for comparison to various EMAR cases. The Acid Gas - Chemical Solvents property package* was used in the flow sheet shown in Figure 6-11.

A mixture of MDEA and PZ were used as the active absorbents in the circulating liquid. ‘OASE purple’, a BASF product specifically targeted at bulk removal of acid gases for LNG production,²⁶⁸ is a mixture of 75 wt% MDEA and 17 wt% PZ and balance water.²⁶⁹ Dr. McElroy²⁷⁰ suggested an approximate dilution of the stock ‘OASE purple’ product by a factor of two to achieve the composition of lean amine used in industry - this is consistent with the compositions reported in Petroleum Technology Quarterly²⁷¹. Analysis of the ideal ratio of these components is beyond the scope here, and so a composition of 38 wt% MDEA and 7 wt% PZ, balance water has been used in the following thermal amine flow sheet. The process is similar to that presented in Figure 6-4, where in place of the electrochemical cell, a distillation column performs the separation between acid gases and the aqueous solution, thereby regenerating the amine. Here the regenerator reboiler (REBOILER) provides the heat duty of the enthalpy of desorption of CO₂ from the amine mixture, the enthalpy to raise the

*As recommended by the property selection wizard and validated for various amine-CO₂ systems.⁹⁹

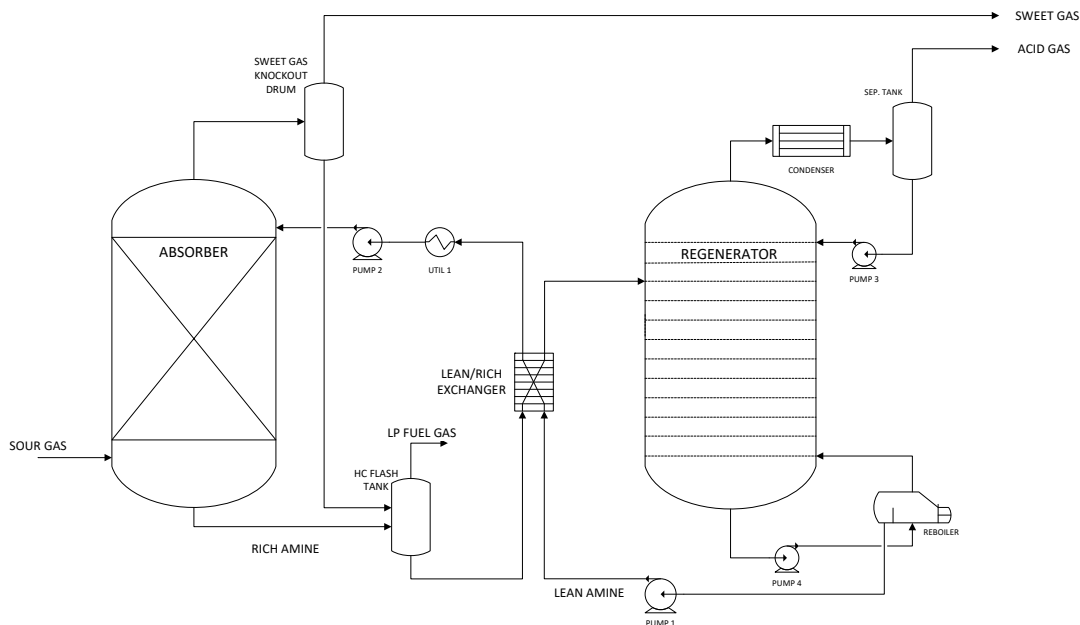


Figure 6-11: Flow sheet of thermal amine stripping system using MDEA/PZ blend. Modelled in Aspen Hysys V10.

incoming stream temperature to the column temperature and the enthalpy of generating steam within the column. This is the single largest energy requirement in the thermal amine sub-system. To reduce the reboiler duty, the lean amine leaving the reboiler is contacted with the rich amine from the absorber in the LEAN/RICH EXCHANGER. To account for the water and amine lost in the overheads of the ABSORBER, HC FLASH TANK and SEP. TANK, the MAKEUP WATER/AMINE stream is set to the sum total of these streams. For specific description of the governing equations of each process unit the reader is referred to the Aspen Technology Unit Operation Reference Guide.²⁵⁵ Acid gas compression, not shown in the above flowsheet (Figure 6-11), is performed by four stages of the compression sub-flowsheet shown in Figure 6-10 subject to the same constraints.

The total work of the thermal amine system is then the sum of the pump work (as calculated in Eqn 6.90), and the enthalpy changes required around the flow sheet once converted to an electrical power equivalent (as in 6.93). The total work of the thermal amine system is very sensitive to the lean amine loading, and

as such moderate process optimisation was performed for the sour gas conditions (Table 6.3 in the following section).

6.2.1 Process optimisation

The solvent circulation rate and reboiler duty of thermal amine systems is especially sensitive to the lean amine loading achieved at the reboiler of the regeneration column. When the lean amine loading is low (approx $x_{\text{CO}_2} = 0.01$) the circulation rate is also low as the cyclic capacity with respect to CO_2 is high. At these conditions, the reboiler duty necessary to achieve such a low x_C loading dominates the system work and negates the benefits of a lower circulation rate. At higher lean amine loadings, the reboiler duty is much lower, though the equilibrium partial pressure of CO_2 with the aqueous amine may exceed that required in the sweet gas leaving the absorber. At this condition, no increase in the amine circulation rate will reduce the sweet gas concentration to the target value. The optimal operating condition is then a compromise between the reboiler duty and circulation rate set by the lean amine loading. Full process optimisation is not within the scope of this study, though the effect of altering the lean amine loading on the performance of the absorption and regeneration column has been captured in Figure 6-12. The sour gas and solvent properties used in these simulations are presented in Table 6.3 and 6.4 respectively.*

Figure 6-12(a) demonstrates that as the dissolved CO_2 loading of the lean amine solution entering the absorber is increased the lean amine circulation rate ($\dot{m}_{\text{Soln.}}$) must be increased to achieve the 50 ppm CO_2 target up to a point. Above a lean loading of approximately $x_C = 0.07$, the rate-based (non-equilibrium) model predicts the absorption column can no longer achieve the desired CO_2 outlet target.⁹⁹ Here the lean loading is calculated as the moles of dissolved carbon over the total moles of amine i.e. PZ and MDEA, $x_C = c_C / (c_{\text{PZ}} + c_{\text{MDEA}})$. The resulting rich amine flow rate and loading was forwarded to the regenerator column where the duty requirement of the reboiler and condenser and necessary pump work are shown in Figure 6-12(b). The condenser and reboiler duties are

*For the 150 kg/s flow of natural gas through the absorber, approximately 10.9 kg/s of CO_2 (or 250 mol CO_2/s) are captured.

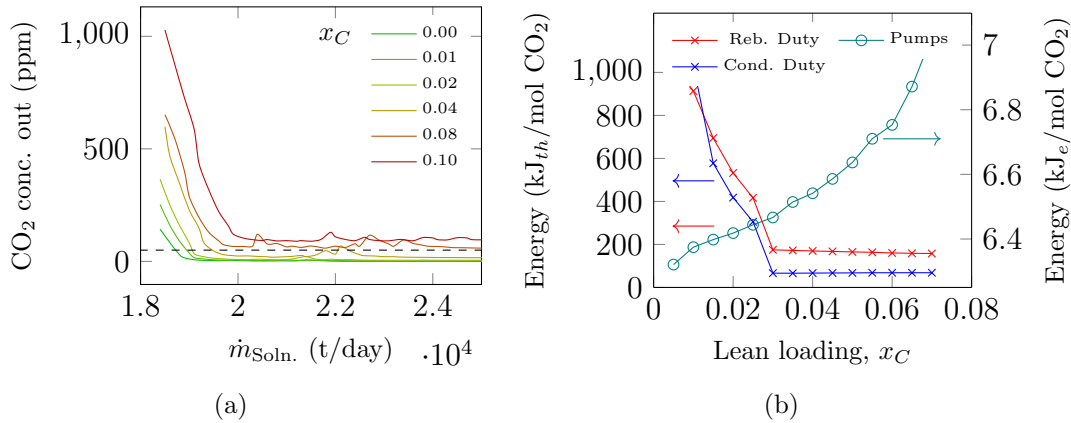


Figure 6-12: Resulting concentration of CO₂ in sweet gas leaving the absorber as the lean aqueous carbon loading (x_C mol C/mol amine) and lean amine flowrate ($\dot{m}_{Soln.}$ t/day) is increased. Dashed black horizontal line indicates target CO₂ concentration of 50 ppm (a). Reboiler and Condenser duties and associated pump work required in the regenerator column to achieve specific lean aqueous carbon loadings (x_C mol C/mol amine) (b). Inlet temperature to regenerator column is fixed at 105 °C. Reboiler and condenser duty on left axis (thermal energy), pump work on right axis (electrical energy).

strongly dependent on the lean amine loading, reducing from 1160 and 1040 kJ_{th}/mol CO₂ at $x_C = 0.01$ down to 70 and 160 kJ_{th}/mol CO₂ at $x_C = 0.07$, respectively. The increase in pump work is not as sensitive to the lean loading and so the higher the loading, the lower the work of regeneration becomes. A moderate loading of $x_C = 0.04$ was selected which balances the heating and cooling requirements in the regeneration column and pumping work required while still achieving the 50 ppm CO₂ outlet target in the sweet gas. The total equivalent electrical work of capture for this base case system is 18.57 MW_e or 74.8 kJ_e/mol CO₂.

6.3 EMAR: Sensitivity to process variables

A number of case studies were performed on key process variables in the EMAR flow sheet with comparisons made to the state of the art thermal system. Sensitivities to the following process variables were examined:

- Amine concentration

- Copper loading shift
- Desorption pressure
- Desorption temperature
- Surface and transport overpotential
- Absorber pressure and inlet CO₂ concentration
- Outlet CO₂ concentration target

The conditions of each the EMAR and thermal amine flow sheets are summarised in Table 6.4.

6.3.1 EDA concentration

The result of increasing the amine concentration on the total system work is presented in Figure 6-13. A moderate copper shift of 60% was selected for this case study, and the desorber was operated at the same pressure as in the thermal system, 2.1 bar. The total work is seen to steadily decrease from 90 kJ_e/mol CO₂ at 1 molal EDA down to 80.8 at 4 molal EDA. The reduction in overall work is mainly due to the reduced circulation rate of aqueous amine required, from 467 kg/s down to 145 kg/s, lower than the 245 kg/s circulation of the MDEA/PZ mixture required in the thermal system.

The cyclic capacity of the MDEA/PZ mixture in the thermal amine system shifts from 0.04 mol CO₂ per mol amine, or 0.291 mol CO₂/kg_w, to 0.325 mol CO₂/mol amine or 2.37 mol CO₂/kg_w. At 4 molal EDA (with a 60% copper shift)

Table 6.3: Natural gas conditions, common to both EMAR and thermal amine flow-sheets. Gas composition given as mole fraction.

Flue gas properties	
Flow rate, $G_{in,abs}$	150 kgs ⁻¹
CH ₄	0.887
C ₂ H ₆	0.035
C ₃ H ₈	0.01
CO ₂	0.03
N ₂	0.038
Temperature, $T_{G,in,abs}$	50 °C
Pressure, $P_{G,in,abs}$	50 bar

Table 6.4: Simulation conditions for EMAR simulation in MATLAB (**left**) and for thermal amine stripping simulation (**right**).

Solvent properties		Solvent properties	
EDA	1 - 4 mol kg ⁻¹	MDEA	37 wt %
Na ₂ SO ₄	0.5 mol kg ⁻¹	PZ	8 wt %
Absorption Column		H ₂ O	Balance
CO ₂ inlet conc., y_{CO_2}	0.01 - 0.3	Absorption Column	
Temperature, T_{abs}	50 °C	No. of stages, $N_{abs,s}$	20
Pressure, P_{abs}	1 - 120 bar	Temperature	50 °C
Intermediate Flash Tank		Pressure	50 bar
Temperature, T_{IFT}	50 °C	Regenerator Column	
Pressure, P_{IFT}	8.5 bar	No. of stages, $N_{reg,s}$	12
Electrochemical Cell		Feed stage	3
Temperature, T_{cell}	40 °C - 100 °C	Condenser Temperature, T_{cond}	35 °C
Pressure, P_{cell}	1 - 50 bar	CO ₂ loading in Reboiler outlet	0.04
Copper loading shift	2 - 98 %	Miscellaneous	
Overpotential	0 - 0.4 V	Minimum approach temperature	5 °C
$\eta_{op} = \eta_{anode} + \eta_{cathode}$			
Ion migration	SO ₄ ²⁻		
Miscellaneous			
Pressure drop in liquid piping, ΔP	1 bar		
Minimum approach temperature, $T_{minapproach}$	5 °C		
Heat capacity of aqueous streams, $C_{p,L}$	4.18 kJ/kg ⁻¹ K ⁻¹		

Table 6.5: Summary of miscellaneous process conditions common to EMAR and thermal amine flowsheets.

Utilities	
Cooling water inlet temperature, $T_{cw,in}$	35 °C
Cooling water outlet temperature, $T_{cw,out}$	40 °C
Compressors	
Max outlet temperature, $T_{max,comp}$	150 °C
Isentropic efficiency, $\eta_{Comp.}$	0.85

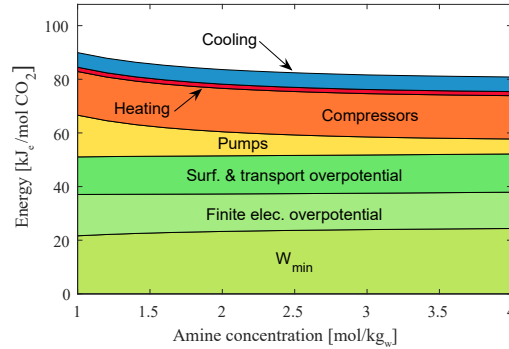


Figure 6-13: Total work as EDA concentration is increased. $\Delta x_{Cu} = 60\%$, $P_{cell} = 2.1$ bar, $P_{IFT} = 8.5$ bar.

the capacity is modulated between 0.91 - 3.34 mol CO_2/kg_w , a cyclic capacity increase of 17% over the thermal amine system. Additionally the work of desorption at high pressure significantly favours high EDA concentrations because less of a relative shift in the copper loading is necessary to exceed solution CO_2 capacity. As the amine concentration is increased, higher copper concentrations are necessary to achieve the same copper loading which raises potential salt solubility concerns, discussed in Section 6.3.3.

6.3.2 Copper loading shift

For an average copper loading in the system of $x_{Cu} = 0.5$, the copper loading shift defines the upper and lower operating points in the EMAR thermodynamic cycle, where the maximum copper loading is $x_{Cu,max} = x_{Cu,avg} + \Delta x_{Cu}$, and similarly the minimum copper loading $x_{Cu,min} = x_{Cu,avg} - \Delta x_{Cu}$. A 50% copper loading shift would then represent modulating the copper loading between 0.25 and 0.75; similarly a copper loading shift of 0.6 represents copper loading end points of 0.2 and 0.8. As shown previously in Figure 6-8(a), the half cell potential and therefore the work of separation depends on the copper loading, aqueous carbon concentration and fugacity of CO_2 . As LNG production includes the imposed constraint of no greater than 50 ppm CO_2 leaving in the sweet gas, there is a limit on the maximum aqueous carbon loading in the lean amine - that which is leaving the cathode and entering the absorber. The maximum

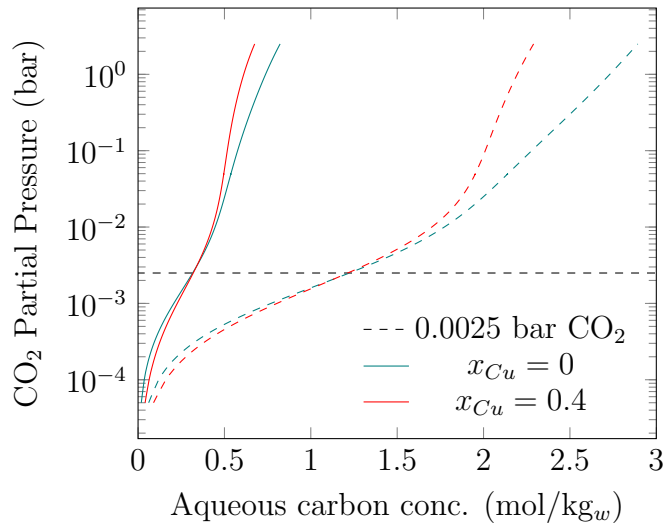


Figure 6-14: Equilibrium plots of CO₂ partial pressure vs aqueous carbon loading at increasing copper loading. Solution specification 1m Na₂SO₄, 50 bar and 50 °C, 1m EDA (solid) 4m EDA (dashed). 0.0025 bar at 50 bar total pressure corresponds to 50 ppm represented by a horizontal dashed black line.

allowable aqueous carbon loading is that which would be in equilibrium with the fugacity of CO₂ in the sweet gas leaving the absorber. The same data in Figure 6-8(a) can be represented in an equilibrium plot of f_{CO_2} vs x_C at varying copper loadings (x_{Cu}) and amine concentrations (c_A), shown in Figure 6-14. As the amine concentration is increased, the equilibrium lines shift to the right as higher molalities of aqueous carbon are achieved, though the loading of CO₂ per mole of amine does not significantly increase. Though there is not a significant difference in solution capacity at 2.5 mbar CO₂ at $x_{Cu} = 0$ and 0.4, the aqueous carbon loading effectively scales with the amine concentration i.e. four times greater at 4 molal EDA over 1 molal EDA. To attain the necessary CO₂ outlet target it is necessary that the copper shift in the anode is sufficiently high to reduce the aqueous carbon concentration to at most the value corresponding to the dashed line shown in the Figure 6-14

Figure 6-15 shows the variation in total work required as the copper loading shift is increased. At lower amine concentrations pump work dominates at low to moderate copper shifts, and the minimum copper shift necessary to achieve the CO₂ outlet target is 38%, corresponding to a total work of 94.5 kJ_e/mol CO₂,

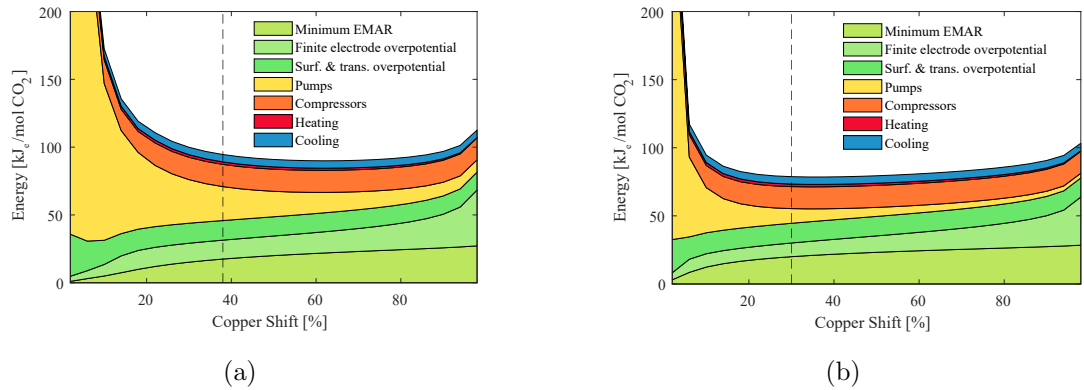


Figure 6-15: Total work as copper shift is increased. EDA concentration 1 molal (a) 4 molal (b). Desorber pressure 2.1 bar. Vertical dashed line represents minimum copper shift to achieve solution in equilibrium with 50 ppm CO₂ in sweet gas.

while the minimum total work is obtained at a copper shift of 62% and 89.9 kJ_e/mol CO₂. As the amine concentration is increased, the minimum copper shift required reduces to 30% with 78.7 kJ_e/mol CO₂, near that which attains the minimum system work of 78.5 kJ_e/mol CO₂ at 34% copper shift.

It is not recommended to operate the EMAR desorber at a copper shift that just yields the maximum allowable aqueous carbon loading in the lean amine. The reaction kinetics of CO₂ absorption begin to play a role, and as such the EMAR desorber should be operated at a higher copper shift to ensure the outlet CO₂ target is met. At 4 molal EDA there is a shallow minimum in the total system work up to a copper shift of approximately 45 %, where the total work is 79 kJ_e/mol CO₂. In further simulations, a moderate copper shift of 40% has been used, where the aqueous carbon concentration leaving the cathode (1.33 mol CO₂/kg_w) is 23 % below that of the maximum allowable lean concentration (1.72 mol CO₂/kg_w).

Across all amine concentrations, as the copper shift is increased beyond 80% the finite electrode overpotential dominates. This is further discussed in the next section and for a discussion on how this may be reduced see Wang et al.¹⁰¹ and Shaw and Hatton⁴⁷.

6.3.3 Desorption pressure

One potential benefit of an EMAR system is the ability to desorb CO₂ at elevated pressures. The maximum desorption pressure is limited by the physical solubility of CO₂ and the copper salt. Figure 6-16 displays the result of increasing the desorber pressure on the total work with the intermediate flash tank at its' standard value (8.5 bar) in (a) and without the flash tank in (b). The vertical red dashed line indicates where the 40% copper shift is no longer sufficient to reduce the aqueous carbon loading to below the equilibrium value of that required for the absorber outlet. Both sides of Figure 6-16 demonstrate a reduction in the total compression work required as the desorption pressure is increased. There is also a reduction in the number of compression stages required to increase the pressure from the desorber outlet to the sequestration target of 300 bar.* The number of compression stages is marked by the number above the total work area plot, where the transition from 4 to 3 and 3 to 2 stages occurs at a total desorption pressure of 6 and 21 bar, respectively. The reduction in compression work due to elevated desorption pressure does not reduce the overall work of capture as it is exceeded by the increase in the finite electrode overpotential. The change in finite electrode overpotential can be more clearly seen in the thermodynamic cycles for each process desorbing at 3 and 50 bar, shown in Figure 6-17 (a) and (b) respectively. At higher desorption pressures, higher copper shifts are necessary to reach the total desorber pressure, as shown in Figure 6-17(b) by the solid black operating line of the anode, where an isoline of x_C is followed. The consequence is a skewed area representing the minimum work required by the EMAR process, which increases the half cell potential at the anode end point (point 4). This increases the minimum EMAR work, from 23.2 to 31.4, and the finite electrode overpotential, 14.6 to 19.3 kJ_e/mol CO₂ in moving from 3 to 50 bar respectively.† Additionally, at elevated desorption pressures, increased copper shifts are necessary to reduce the aqueous copper loading to below a value

*The non-smooth nature of the compression and subsequent cooling areas is due to the staged nature of the compression calculations and shift in gas outlet composition as the pressure is increased.

†The applied overpotential is unaffected - its' area is constant at $\int \eta_{op} dI$, and is reflected by the area in Figure 6-16.

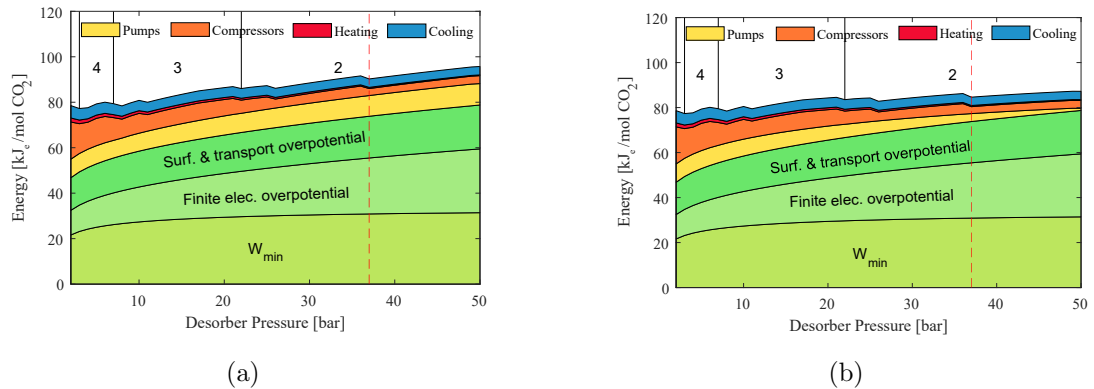


Figure 6-16: Total work as desorption pressure (P_{cell}) is increased. $c_A = 4$ molal EDA, $x_{Cu} = 40\%$, $\eta_{op} = 0.1V$, $P_{IFT} = 8.5$ bar (a), no intermediate flash tank (b).

that would be in equilibrium with the sweet gas leaving the absorber. Where previously a copper shift of 40 % at 2 bar desorption ensured the aqueous carbon concentration leaving the cathode was 20 % below the equilibrium value required at the absorber outlet, at 50 bar desorption 42 % copper shift is necessary just to meet the maximum allowable carbon loading. Increasing the copper shift to ensure a suitable buffer between the maximum allowable carbon loading and that leaving the absorber increases the total system work as demonstrated in Figure 6-15(b).

Since the intermediate flash tank is positioned between the absorber and the anode, the stream pressure must be increased following the flash vessel up to the desorber pressure. This results in the pump work in Figure 6-16(a) remaining consistent as the desorber pressure is increased. In the absence of this unit, the pump work reduces as desorber pressure is increased and the difference in total work between desorbing at 2 bar and 50 bar is 8.6 $\text{kJ}_e/\text{mol CO}_2$. The purpose of the intermediate flash vessel is to remove light hydrocarbon components from the system to avoid issues such as foaming back at the absorption column.¹⁷⁴ At the lower pressure in the intermediate flash tank (8-9 bar) it is possible liquid hydrocarbons may form a separate phase which are often skimmed off and recovered.¹⁷⁴ As the gas composition specified in this case study does not include heavier hydrocarbons, no liquid phase is predicted to exist at the conditions of the intermediate flash tank. Without the intermediate flash tank all dissolved

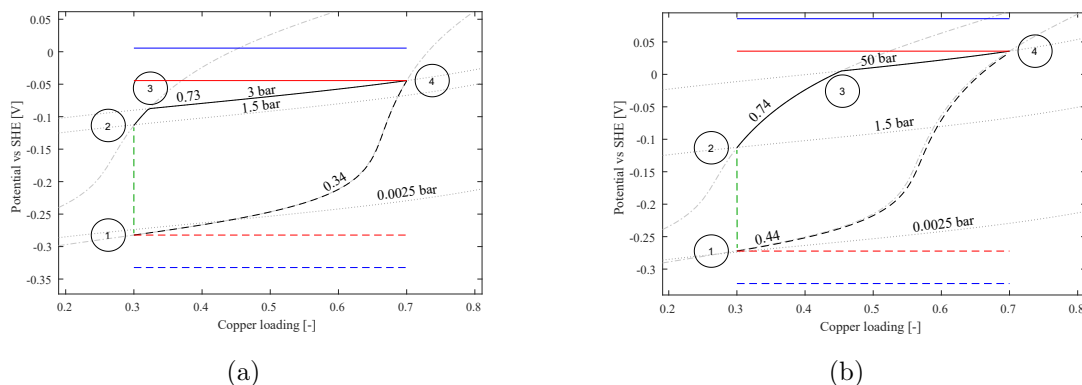


Figure 6-17: Thermodynamic cycle for EMAR process at desorption pressure 10 bar (a) and 50 bar (b). Black, red and blue lines are the half cell potential, maximum half cell potential and applied electrode potential, respectively, where anodic lines are solid and cathodic are dashed.

hydrocarbons will circulate to the anode where, depending on the operating pressure, may be released in the EMAR separation vessel. Figure 6-18 shows where hydrocarbons are leaving the flow sheet as a ratio of their molar flow into the absorber. The results with the intermediate flash tank are shown in (a) and the flowsheet without this unit in (b), both as the desorption pressure is increased.

In removing the intermediate flash tank from the flow sheet, the lighter methane and ethane that would otherwise be recovered to a LP fuel gas system is lost to the desorber outlet intended for sequestration.* In each case the ratio of hydrocarbons leaving the flowsheet increases as the total desorption pressure is raised. This is initially counter intuitive but can be reconciled when the ionic strength of the aqueous phase around the flow sheet is examined. The ionic strength is a function of the concentration and charge of the ionic species present (see Eqn. 6.16). In the anode the ionic strength is increased by three factors: the dissolution of copper(II) from the electrode surface, the migration of sulfate ions through the membrane (to maintain electroneutrality) and the equilibrium formation of carbonate and bicarbonate species as the desorber pressure (and partial pressure of CO_2) is increased. These factors serve to increase the ionic strength and decrease the solubility of neutral non-polar hydrocarbon solutes by

*Which only accounts for approximately 0.2% of the molar flow of hydrocarbons entering the absorber.

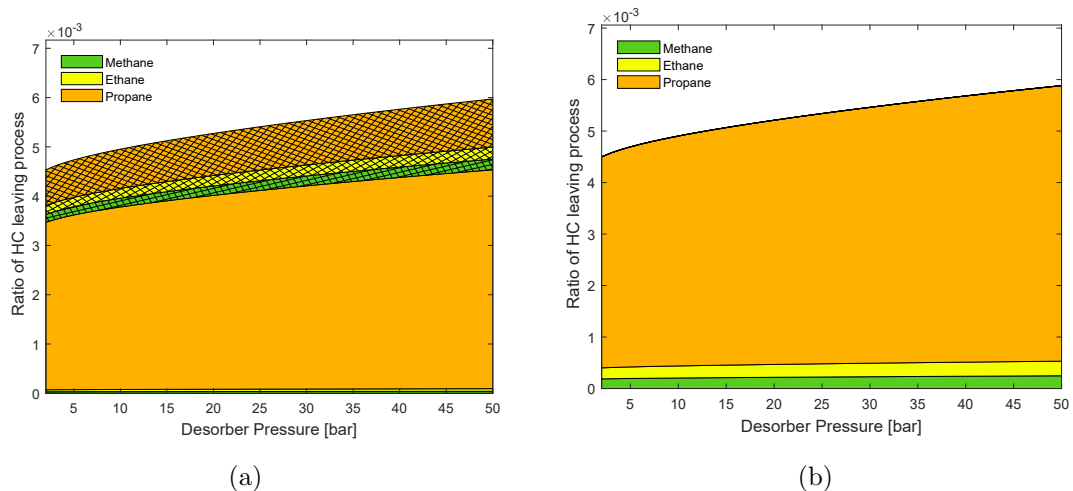


Figure 6-18: Molar flow rate of hydrocarbons leaving the EMAR flow sheet as desorption pressure increases, with an intermediate flash tank at 8.5 bar (a) without the intermediate flash tank (b). The cross-hatched section in (a) is that lost due to the intermediate flash tank, while the area without a pattern is lost from the EMAR separation vessel.

a salting out effect. The ionic strength of the aqueous phase in the intermediate flash tank and EMAR separation vessel for the flow sheet cases with and without the intermediate flash tank are shown in Figure 6-19(a) and the activity coefficient of neutral non-polar species and CO_2 as a function of ionic strength are plotted in Figure 6-19(b).

The solid blue and black lines in Figure 6-19(a), representing the ionic strength of the aqueous phase in the EMAR Separation Vessel (ESV) with and without the intermediate flash vessel, effectively overlap. The presence of the Intermediate Flash Tank (IFT) prior to the anodic chamber does not significantly reduce the CO_2 content or the ionic strength entering the anode.* The log of the activity coefficient for neutral non-polar (NNP) solutes has a cubic dependency on ionic strength, while that of CO_2 is much weaker (near linear dependence) shown again

*The mass flow rate of the vapour stream leaving the intermediate flash tank is approximately 0.01% of the incoming liquid stream.

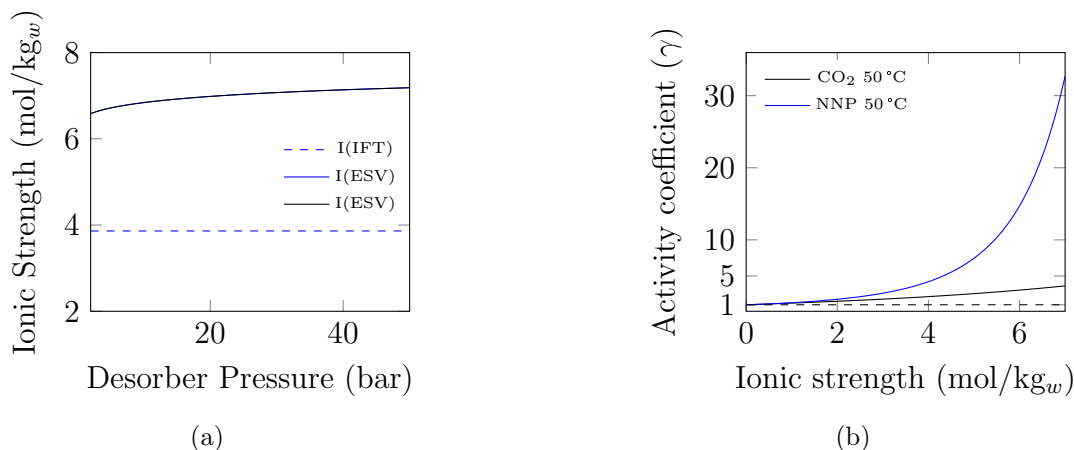


Figure 6-19: Ionic strength of aqueous phase in the intermediate flash tank and EMAR separation vessel as the desorber pressure is increased. Blue lines are of the flowsheet with the IFT and black without (a). Activity coefficient (γ) of neutral non-polar solutes and CO₂ as a function of ionic strength in the B-dot model, with constant γ of 1 as dashed black line (b).

in Eqn. 6.23 and 6.19 below:

$$\log \gamma_{\text{CO}_2(\text{aq})} = \left(C + FT + \frac{G}{T} \right) \bar{I} - (E + HT) \frac{\bar{I}}{1 + \bar{I}} \quad (6.19)$$

$$\log \gamma_{\text{NNP}} = a\bar{I} + b\bar{I}^2 + c\bar{I}^3 \quad (6.23)$$

Due to the presence of the Na₂SO₄ electrolyte in the EMAR circuit, the concentration of hydrocarbons leaving the absorber is lower than in a thermal amine system. In the thermal amine model, the loadings of hydrocarbons leaving in the rich amine are 0.071, 0.0054 and 0.0014 mol/kg_w for methane, ethane and propane, respectively.* In the EMAR flowsheet, the hydrocarbon loading leaving the absorber is 0.0092, 0.00042 and 0.0023 mol/kg_w for methane, ethane and propane, respectively. The loading of methane and ethane is approximately 10 times lower in an equivalent EMAR circuit because of the electrolyte present. The loading of aqueous propane is greater in an EMAR circuit, though this appears to be due to the anomalously high solubility extracted from the PR/eNRTL package shown in Figure 6-2. As a result, the loss of propane is over-represented

* Absorber operating at 50 bar and rich amine temperature 72.30 °C.

Table 6.6: Proportion of hydrocarbons lost from the intermediate flash tank and separation vessel at the regeneration unit. A value of 1 would indicate all hydrocarbons entering the flowsheet leaves at that specific location. Results compared for the distillation column in the thermal system and electrochemical cell in EMAR system. Where only a single number is quoted, no IFT is present in the flow sheet and hydrocarbons are lost only at the regeneration stage.

	Ratio of HC lost in unit (IFT + ESV).			
	Thermal MDEA/PZ	EMAR ^a	EMAR ^b	EMAR ^c
Methane	1.038e-3 + 1.898e-4	1.618e-4 + 3.055e-5	1.869e-4	2.290e-4
Ethane	1.713e-3 + 5.081e-4	1.805e-4 + 4.001e-5	2.145e-4	2.627e-4
Propane	1.563e-3 + 4.430e-4	7.241e-4 + 3.399e-3	4.098e-3	4.969e-3

^aWith IFT at 8.5 bar. Desorber at 2 bar.

^bNo IFT present. Desorber at 2 bar.

^cNo IFT present. Desorber at 30 bar.

in Figure 6-18. Table 6.6 compares the loss of hydrocarbon from the base thermal amine case and various EMAR cases.

Due the decreased solubility of hydrocarbons in the EMAR electrolyte the molar flow rates of hydrocarbons leaving the IFT are much lower, again by approximately 10 times. When the IFT is removed from the flow sheet the losses in the EMAR desorber, even at elevated pressure, are on par with those seen at the thermal amine regeneration stage. Thus there is no considerable loss of hydrocarbon product in operating without the intermediate flash tank. Since the EMAR electrochemistry was not significantly affected under a natural gas headspace (demonstrated in Chapter 5), removing the intermediate flash tank from the EMAR flow sheet will not impair performance of the system. There may still be, however, concerns over the foaming behaviour of the amine in the absorption column given dissolved hydrocarbons being present. The hydrocarbon loading (mol/kg_w) returning to the absorber from the base thermal amine flow sheet and of the same EMAR cases presented in Table 6.6 are shown in Table 6.7.

As the thermal amine regenerator operates at low pressure (2.1 bar) and elevated temperatures,[†] the hydrocarbon loading is reduced to zero, while the EMAR

[†]Regenerator reboiler temperature is 125.7 °C.

Table 6.7: Aqueous hydrocarbon concentration (mol/kg_w) returning to the absorber for thermal and EMAR flow sheet cases.

	Hydrocarbon loading entering Absorber.			
	Thermal MDEA/PZ	EMAR ^a	EMAR ^b	EMAR ^c
Methane	0	6.94e-8	4.22e-7	5.39e-6
Ethane	0	4.23e-9	2.25e-8	4.17e-4
Propane	0	2.21e-6	2.65e-6	2.66e-5

system retains a relatively low loading re-entering the absorber. The low loading of HCs in the absorber is not expected to exacerbate foaming within the absorber, though the presence of heavier hydrocarbons and the formation of a liquid phase has not been considered. Thus it is essential that the operating temperature of the absorber is maintained above the hydrocarbon dew point, consistent with the operation of thermal systems. As the HC solubility is heavily reduced by the increased ionic strength in the anode, and inclusion of the intermediate flash tank results in an increase in the pump work, further simulations are performed without the unit.

At a 40% copper shift the copper concentration at the anode inlet and outlet are 0.6 molal and 1.4 molal, respectively. Estimates for the solubility of CuSO₄ in aqueous solution at 35 °C are ca. 1.64 molal,²⁷² which would correspond to a maximum copper loading of 0.82, or 32% shift from the midpoint and 64% total copper shift. Assuming a 60% total copper shift, a similar case to that shown in Figure 6-16 was performed to determine the maximum desorber pressure achievable while still meeting the CO₂ outlet target. Though this significantly reduces the compressor energy requirement, there is an increase in the pump work to raise the pressure of rich amine to the EMAR desorber pressure, bringing the total system work to 93.5 kJ_e/mol CO₂. Additionally, operating an electrochemical cell at such pressures presents significant engineering challenges* thus for practical reasons and to reduce the system energy requirement, the EMAR desorber should be operated at low pressures and has been done so in further simulations.

*Though increasingly applied to CO₂ reduction.⁹³

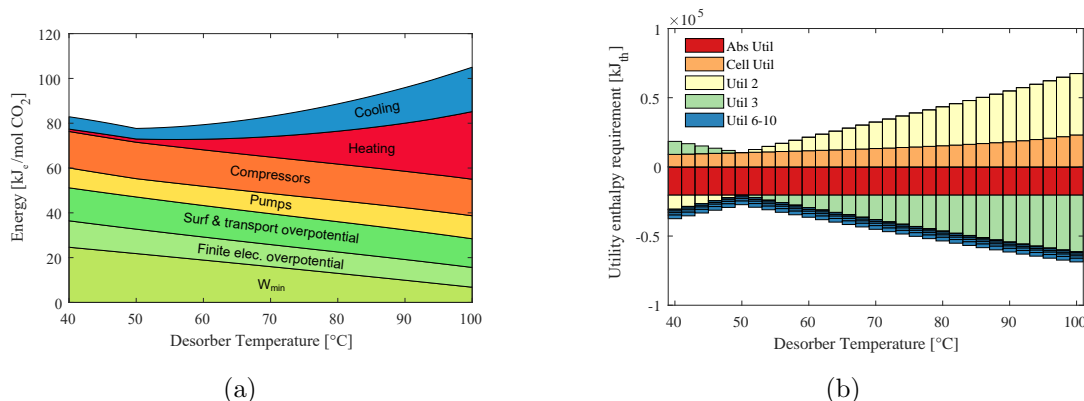


Figure 6-20: Total system work as desorber temperature is increased (a) and enthalpy required around the flowsheet to maintain isothermal operation or alter process temperatures (b). Negative enthalpy values indicate cooling is required, and positive values require heating.

6.3.4 Desorber temperature

Increasing the temperature of the EMAR cell has been demonstrated by Stern³⁷ to improve the kinetics of both anodic and cathodic processes. The kinetics of the electrode processes are not captured in this process model, rather the applied overpotential is included in an ad hoc manner to assess its impact on the total system energy requirement (see Section 6.3.5). The desorber temperature additionally impacts CO₂ solubility, anodic and cathodic half-cell potentials and enthalpy requirements around the system. The effect of increasing the desorption temperature on the total system work and the enthalpy required around the flow sheet is captured in Figure 6-20(a) and (b) respectively.

Starting at the minimum temperature (40 °C within 5K of the cooling utility available) the total system work decreases down to a minimum at 50 °C, where the desorption temperature is equal to the absorber temperature. Above this point the minimum EMAR work and associated finite electrode and surface and transport overpotentials reduce as the half-cell potentials for the anode and cathode approach each other. Additionally, above 58 °C the anode stream is now saturated with respect to CO₂ and the fugacity of CO₂ reaches the total pressure of the cell. Beyond 50 °C the heating and cooling enthalpy required to raise the stream temperature entering the anode and to cooling the stream leaving the

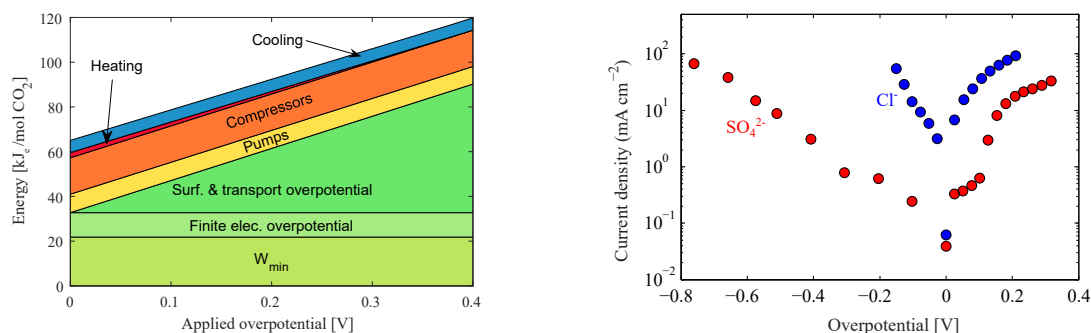
cathode to the absorber temperature begin to dominate the total system work. As the desorber temperature is increased, the flow sheet approaches that of the thermal amine system, where reboiler and condenser duties dominate the energy requirement. The utility requirement in red in Figure 6-20(b) represents the cooling necessary to maintain isothermal operation. If all the enthalpy of CO₂ absorption is assumed to result in a temperature increase of the rich amine, it would leave the absorber at approx 70 °C.* At the low overpotential specified (0.1 V) the Joule heating within the electrochemical cell is not sufficient to balance the enthalpy lost due to the desorption of CO₂ and as such the 'Cell Util' heating utility is necessary to maintain isothermal operation. As the desorber temperature is increased and the EMAR work reduces (and associated Joule heating) the Absorber utilities and Cell utilities become equal at 96 °C. This suggests the total system work can be reduced with staged energy balances around units rather than lumped isothermal operation.

The Cell utility is strongly dependent on the applied overpotential - as applied overpotential is increased, the enthalpy balance in the cell will shift to generating heat where cooling (either by contact with rich amine or utilities) is necessary to promote future absorption. Operation of the desorber at elevated temperature further reduces the hydrocarbon solubility, alleviating foaming concerns. As the minimum total system work is attained at 50 °C, further simulations were performed at this value.

6.3.5 Surface and transport overpotential

To drive a specific current density, a surface and transport overpotential is applied to the cell, above the cell potential determined by thermodynamics. The necessary overpotential depends on the electrolyte system and operating conditions of the cell. Results from Chapter 5 demonstrate that with small additions of chloride, or by operating at elevated pressure, the current density for the same applied voltage may be doubled. This effect is not quantitatively captured in this process model as further experimentation is necessary to capture the trend in system response under chloride doping or increasing pressure. The published

*Comparable to the outlet of the thermal amine system at 72.3 °C.



(a) $c_A = 4$ molal EDA, $x_{Cu} = 40\%$, $P_{cell}=2.1$ bar.

(b)

Figure 6-21: Total work as over-potential is increased (a) Tafel plot of the kinetics of the electrochemical reaction at 50 °C. 1 molal EDA + 0.5 molal Na_2SO_4 (red) and 4 molal EDA + 2 molal NaCl (blue). Positive overpotential refers to η_{anode} and negative to $\eta_{cathode}$. Reproduced from Wang et al.¹⁰¹ with permission.*

results of Wang et al.¹⁰¹ for the Cu-EDA system at atmospheric pressure with sulfate and chloride electrolytes will serve as bounds for what is expected of a system applied to natural gas treating. Figure 6-21(b) shows a Tafel plot with the current response of sulfate and chloride EMAR electrolytes. The sulfate system displays severely hindered kinetics in comparison to the chloride system, though the degree to which the chloride current can be attributed to the faradaic reaction of copper dissolution or plating is unknown.[†] The response of the sulfate electrolyte then serves as a lower bound given it can be increased as mentioned above. Figure 6-21(a) then shows the change in total system work required as the applied overpotential is increased.

To operate EMAR at the same energy consumption as the thermal amine system, the maximum overpotential must be limited to approx 0.07 V, at which the minimum current density (with a sulfate electrolyte) is 0.1 mA/cm^{-2} . Under these conditions, the required electrode surface area is $4.7 \times 10^6 \text{ m}^2$ for the nec-

[†]As addressed in Chapter 5 disproportionation in a chloride electrolyte reduces the efficiency of the EMAR process.

*Reprinted from International Journal of Greenhouse Gas Control, Volume 82, March 2019, Miao Wang, Subrahmaniam Hariharan, Ryan A. Shaw, T. Alan Hatton, Energetics of electrochemically mediated amine regeneration process for flue gas CO_2 capture, 48-58, Copyright (2018), with permission from Elsevier. Copyright license in Appendix A

essary current at 100% Faradaic efficiency. This is an impractically large area, though it can be reduced by dropping the total current required or increasing the current density. Figure 6-22(a) demonstrates how the total current required by the cell is affected by its operating temperature and pressure. The total current decreases moderately with increasing temperature and strongly increases at elevated pressures. As demonstrated in Chapter 5, the overpotential required to achieve the same current density can be reduced with the addition of chloride salts or increasing the pressure, though the effect may not be significant enough to counter the significant increase in current required.

As the overpotential is increased, heating of the electrochemical cell is no longer required because Joule heating outweighs the enthalpy lost through CO₂ desorption in the anode (W_{EMAR} in Eqn. 6.81). The utility requirements around the flow sheet as the overpotential is increased is shown in Figure 6-22(b). Though the heating utility requirement of the cell decreases to zero, and switches sign at 0.4 V applied overpotential (where cooling is now necessary to maintain isothermal operations), the energy cost of increasing overpotential is greater than the electrical equivalent saved due to the disappearing heating utility.

6.3.6 Absorber pressure and inlet CO₂ concentration

Given the variability in well gas operating conditions, the effect of total gas pressure and CO₂ inlet concentration on an EMAR flow sheet has been estimated. Onshore facilities typically operate at low to moderate pressures (ca. 60 bar) though bulk CO₂ removal can be performed nearer the well head at offshore facilities where the gas pressure may be up to 120 bar.¹⁷⁴ Gas wells around Western Australia are typically lean with respect to CO₂ though a range of compositions are seen i.e. from 3% at the Karratha Gas Plant to 15% at the Gorgon Gas Plant.^{270,273} The result of increasing the inlet CO₂ inlet concentration and the absorber pressure on the total system work are shown in Figure 6-23(a) and (b) respectively.

In examining the effect of CO₂ concentration on the total system work, the ratio of hydrocarbon components was maintained as the CO₂ concentration was increased up to 30% of the feed. Increasing the absorber pressure at the same

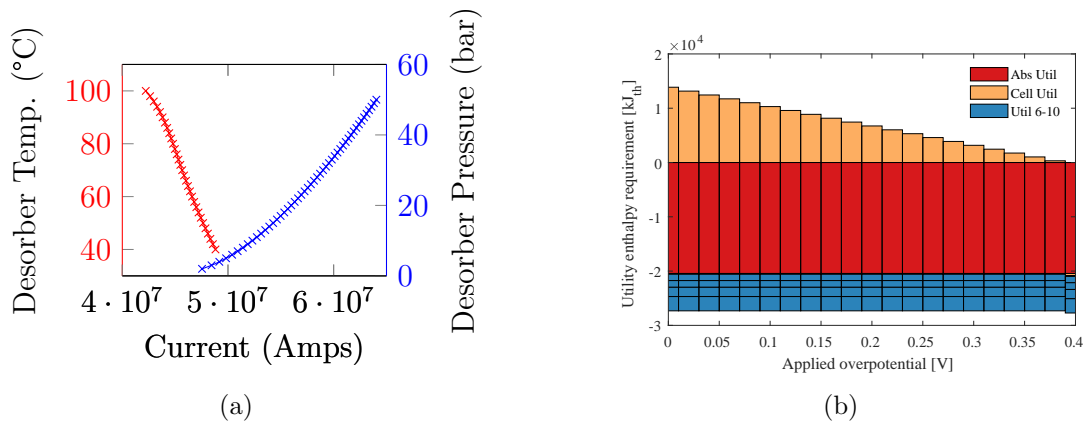


Figure 6-22: Total cell current at 40 % copper shift at increasing desorber temperature and pressure(a). Desorber temperature increased with desorber pressure set to 2 bar, total system work for this case shown in Figure 6-20(a). Desorber pressure increased with desorber temperature at 50 °C, total system work in Figure 6-16(b). Flow sheet utility requirement as EMAR cell overpotential is increased (b). Negative enthalpy indicates cooling is required to maintain isothermal operation and vice versa. $P_{cell} = 2.1 \text{ bar}$, $T_{cell} = 50 \text{ }^\circ\text{C}$.

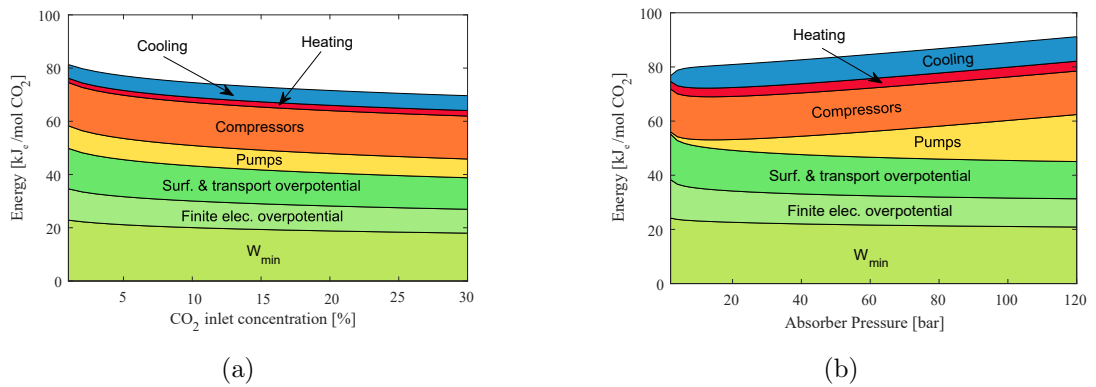


Figure 6-23: Total work as inlet CO_2 concentration is increased (a) and outlet target is increased (b). Desorber pressure 2.1 bar, copper shift 40%, $\eta_{op} = 0.1V$, $c_A = 4 \text{ molal}$.

CO₂ concentration and increasing the concentration of CO₂ at the same pressure has the same effect on the CO₂ fugacity, though the response in total system work is not consistent. As the CO₂ concentration is increased the EMAR system is able to achieve a higher shift in solution CO₂ capacity as at 1% CO₂ in the inlet an aqueous carbon loading of 2.85 mol/kg_w is reached and at 30%, a loading of 3.28 mol/kg_w is obtained, while the loading entering the absorber is consistent at 1.33 mol/kg_w. As the desorber in this set of simulations is 2.1 bar, when the CO₂ partial pressure exceeds 5% in the absorber rich amine solution is saturated at the conditions of the anode and flashing occurs at the anode inlet (as also with an increase in desorber temperature). Though increasing the pressure of the absorber results in a similar increase in the cyclic capacity of the amine, the system work is outweighed by the substantial pump work required to return the solvent to the absorber from the low pressure desorber. Though the pump work may be mitigated by increasing the desorber pressure, as shown in Section 6.3.3 an increase in the finite electrode overpotential results in a higher total system work.

6.3.7 Outlet CO₂ target concentration

The application of EMAR specifically to LNG production requires the strict outlet CO₂ target of 50 ppmv though many gas plants operate to provide domestic gas which is not subject to the same target since it is not liquefied and exported. Domestic gas must contain no more than 2 mol % CO₂ and is also subject to additional heating value specifications not addressed here. A summary of the total work of the MDEA/PZ thermal amine system and the EMAR system is shown in Figure 6-24 at both CO₂ outlet targets. Additionally, the work of capture for an EMAR system where the desorber operates at elevated pressure, 20 bar, is also presented for comparison.

The total energy requirement of EMAR systems are on par with current thermal amine systems when both are applied to LNG production, ca. 79 vs 74 kJ_e/mol CO₂, respectively. At a lower outlet target, the normalised work of capture for the thermal system drops significantly to 47.9 kJ_e/mol CO₂ while the work of the EMAR system remains approximately constant - where there is a

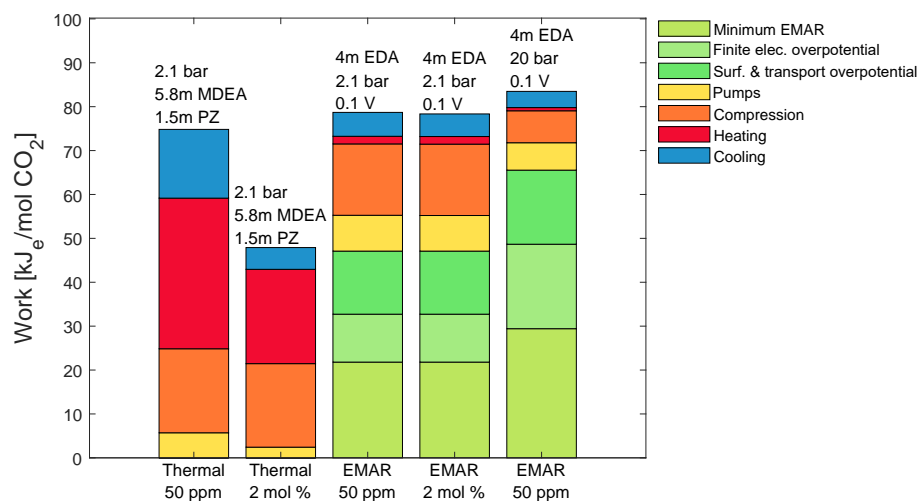


Figure 6-24: Summary of total system energy requirement for thermal and EMAR cases at various CO₂ outlet targets and operating conditions. All cases export compressed CO₂ at 300 bar. The concentration of the aqueous amine(s) and regeneration pressure are labeled on each case - in addition to the applied overpotential for the EMAR cases.

reduction in the heating and cooling required as it is linked to the amount of CO₂ absorbed and desorbed. Though the operating cost may be currently be greater than for the thermal amine system, the EMAR system presents a means to reduce the total capital cost. Though the effect of heavier hydrocarbons (C₃₊) on the system needs to be considered, removing the intermediate flash tank from the flowsheet due to the decreased solubility of neutral non-polar species presents an operational advantage. Additionally, operating the desorber at elevated pressure reduces the investment in compressors where CO₂ sequestration is required. In reality, process units will not operate isothermally and the heating due to exothermic absorption of CO₂ will serve to reduce the work in the desorber and eliminate the utility requirement (depending on the balance of absorber and desorber enthalpies). This has the potential to reduce the work requirement to below that of current state of the art thermal amine systems.

6.4 Powering EMAR

At the nominal 3% inlet operation the EMAR cell consumes 47 kJ_e/mol CO₂ (of the 78 kJ_e/mol CO₂ total) - at a 50 ppm CO₂ outlet target and 150 kg/s of sour gas processed (capture of ca. 250 mol CO₂/s) the total electrical energy required by the cell is 11.7 MW_e. Though the work of capture decreases as the CO₂ inlet concentration increases, the electrical power requirement of an EMAR cell at the Gorgon Gas Plant with 15% CO₂ in the feed gas and the same CO₂ outlet target is far greater at 82 MW_e because the CO₂ capture rates is approx. 1750 mol CO₂/s per train.* Such electrical power requirements are non-trivial given the total power supplied to the plant is of the order of 585 MW.⁹ Onshore and offshore facilities are typically equipped with gas turbines to provide power for the site or if power is available locally may still use gas turbines to run the compressors in the liquefaction circuit.^{7,273} Waste heat from gas turbine exhausts is used to generate the heating utilities for the plant, of which the largest consumer are the regenerator reboilers for amine regeneration at 80% of the heating medium.^{9,273} If EMAR is used in place of a thermal amine system, the waste heat from the gas turbines may be used for additional electricity generation via an Organic Rankine Cycle (ORC) to provide the additional power required by the cell. The ORC generates electricity via compression and expansion of the cyclopentane working fluid, where the total power delivery depends on the specific gas turbines used and associated exhaust conditions.²⁷⁴ At the Gorgon Gas Plant, for example, five Frame 9 turbines are used for power generation across the plant and two Frame 7 gas turbines are used in each liquefaction train to drive compression of the mixed refrigerant.⁹ With commercially available ORegen™ applied to the Frame 7 gas turbines used in compression, an additional 31 MW_e can be extracted, yielding 62 MW_e per train.²⁷⁵ To obtain the full 82 MW_e, the additional 20 MW_e per train may be extracted with a similar ORC from remaining gas turbines used for power generation.[†] Without the utilisation of waste heat recovery, powering an EMAR cell would require the addition of dedicated gas turbine generators or extensive

*Back calculated from 15.6 MTPA LNG production across 3 trains with 95:5 methane:ethane LNG ratio assuming no other components in the feed.

[†]Figures for the power generated from an ORC applied to Frame 9 gas turbines is unavailable.

solar panel arrays, increasing the capital cost and providing a disincentive for application of the process.

6.5 Summary

The process model of Wang et al.¹⁰¹, built in MATLAB, was modified and expanded to examine the energy requirements of an EMAR system applied to natural gas treating. The Peng-Robinson equation of state was added to the model to ensure accurate treatment of gas phase thermodynamics, similar to what is used in commercial process simulation packages such as Aspen Hysys. Binary interaction parameters for the Peng-Robinson model and solubility data generated in Aspen Hysys were extracted and transferred to the EMAR process model. A thermal amine model, using an industrially recommended MDEA/PZ composition, was built in Aspen Hysys to provide an appropriate comparison for the EMAR system. The total work requirement of the EMAR system was studied across a number of process variables, they were: amine concentration, copper loading shift, desorption pressure, desorption temperature, applied overpotential, absorber pressure, inlet CO₂ concentration and outlet CO₂ target concentration. The work of an EMAR system can be reduced by operating at high EDA concentrations and moderate copper shifts. Copper shifts above 40% are seen to be sufficient to ensure the CO₂ outlet target in the sweet gas is met at moderate total system work. Though one of the proposed benefits of an EMAR system is the capability to regenerate the amine solution and release acid gases at pressure, as the desorption pressure is increased the system work is also increased due to the contribution of the finite electrode overpotential. Means to reduce this portion of the total work are present in the literature, which may aid EMAR in becoming an alternative to present thermal systems. The overpotential strongly affects the total work of capture and to obtain the same total system work as current thermal amine systems it should be limited to no more than 0.07 V. The Tafel plot of a sulfate electrolyte provides a lower bound on the current density in an EMAR cell, which was previously shown to increase as desorber pressure is increased and electrolyte composition altered, though these traits are not explicitly considered in the process model presented. An increasing absorber pressure sees

the total system work rise due to the increasing difference in pressure between the absorber and desorber unit. Increasing the desorption pressure reduces this differential though still results in an increase in total system work as the finite electrode overpotential increases. Unlike thermal amine systems, the EMAR system is relatively insensitive to a decrease in the CO₂ outlet target - as at 2 mol % and 50 ppm the system work is similar. EMAR may then be more suited to LNG applications (over providing domestic gas) where the availability of waste heat from onsite gas turbines can be used to generate the necessary electrical power for the EMAR cell.

Chapter 7

Conclusions and Recommendations

7.1 Summary

This thesis examined the application of Electrochemically Mediated Amine Regeneration to natural gas treating. The introduction outlines the deficiencies of thermal swing methods currently used for acid gas capture, and though improvements are being made, the fundamental mechanism of separation prevents moderate temperature and high pressure operation of the desorber unit. New electrochemical separation techniques pose a number of advantages, though the effect of the contaminants found in natural gas on these systems was previously untested. The EMAR cycle (an EMCCS variant), aimed at Post-Combustion Carbon Capture, is among the most developed electrochemical separation methods available and uses amine solvents familiar to natural gas treating. It was therefore posited for the removal of acid gases, required for natural gas production. The EMAR cycle has three main stages: the absorption of acid gases into aqueous ethylenediamine, the dissolution of copper and subsequent release of acid gases, and the plating of copper(II) from the copper ethylenediamine complex. The chapters of this thesis present the reactions involved at each stage, the influence of natural gas contaminants on the cycle and lastly the overall process energetics.

Following a brief introduction to relevant methods in quantum chemistry used in this thesis, Chapter 3 examined the details of reactions between the active absorbent, ethylenediamine, and acid gas contaminants found in natural gas (CO_2 , COS , CS_2 , H_2S and CH_3SH), which constitutes the first stage of the EMAR cycle. Computational results suggest that CO_2 , COS and CS_2 will be absorbed into aqueous ethylenediamine by a zwitterion intermediate, as opposed to a direct hydrolysis mechanism. The theoretical activation free energy of CO_2 reaction with ethylenediamine determined is in excellent agreement with the experimental literature. The reactions of COS or CS_2 with ethylenediamine require much larger activation energies (8 kcal/mol or more), and follow the empirical observations in literature, where limited reaction rate data is available. Theoretical calculations of acid dissociation constants find that as oxygen is replaced by sulfur in ethylenediamine zwitterions, they become more acidic, resulting in more stable deprotonated products. The remaining contaminants, H_2S and CH_3SH , are absorbed by proton transfer to ethylenediamine and water, respectively, where only H_2S is sufficiently basic enough to protonate neutral ethylenediamine. No favourable interaction between the products of H_2S or CO_2 reaction with ethylenediamine are observed, consistent with experimental observations of a decrease in H_2S capacity as the aqueous CO_2 concentration is increased.

The next stage in the EMAR cycle is the dissolution of copper(II) and reaction with ethylenediamine to displace CO_2 . In Chapter 4, the complexation of ethylenediamine was examined with quantum chemical methods. Of the various DFT functionals trialed, B3LYP most accurately reproduced the geometries of copper(II) complexes (with the first solvation shell present), and the experimental free energy of complexation with ethylenediamine, though significantly different from the accepted value (107% off). The discrepancy between the experimental and theoretical result was reduced through the addition of up to 18 water molecules around the central copper(II) ion. In the extrapolated limit (of infinite surrounding water), the free energy of complexation between copper(II) and ethylenediamine with B3LYP is still 58% off from the experimental value of 14.4 kcal/mol. The effect of hydroxo ligands around copper(II) on the free energy of complexation was examined, though this did not materially impact the results. This suggests that the discrepancy is primarily due to the computational method

employed. The overall reaction free energy between solvated copper(II) and the products of ethylenediamine absorption of CO₂, COS, CS₂ were estimated. Computational results suggest that all ethylenediamine products will be dissociated when exposed to aqueous copper(II), and in so doing release CO₂, COS, or CS₂. This suggests that the EMAR process is not limited to capture and release of CO₂ alone, but can also be extended to COS and CS₂.

The behaviour of real EMAR electrolyte systems was investigated in Chapter 5, which covers stages 2 and 3 of the EMAR cycle. Nitrate electrolytes were found to be a poor choice for the system, as blocking and reduction of nitrate species at the cathode reduced the Faradaic current, and the overall efficiency. A sulfate electrolyte, though limited in solubility, demonstrated greater efficiency and was used in further experiments comparing the response under N₂, CO₂, and later, natural gas atmospheres. The irreversibility of the Faradaic process was highlighted and the diffusion coefficient of Cu(II) was calculated according to the Randles-Sevick equation, which was in reasonable agreement with literature. The performance of the engineering implementation of the EMAR cycle, the EMAR stack, was examined and subsequently improved by using a sulfate electrolyte, control of the temperature throughout the process and by improving the cell membrane and baffles. Though improved, the EMAR stack was not suitable for direct trials with natural gas, therefore, the effect of natural gas contaminants on the electrolyte were examined at a more fundamental level. H₂S in natural gas severely impacted the EMAR electrochemistry by consuming the active blocker species, copper(II), in forming insoluble copper sulfide. The effect of a natural gas headspace (without H₂S) on the electrochemical system was minimal, and only required slightly higher polarisation (voltages) to achieve the same current density as in their absence. Moderate pressure (5-10 bar) operation, and the addition of ppm levels of aqueous chloride, were seen to decrease the charge transfer resistance by 3-4 times in a sandwich electrode setup - a promising outcome for operation of the desorber at higher pressure. Lastly, the quality of electrodeposited copper was examined under moderate pressure CO₂ and with various additives. Aqueous chloride was again of benefit to the system by improving the leveling and quality of the deposited copper - ultimately necessary for long term operational stability of an EMAR cycle.

In Chapter 6, a process model was built to determine the energetics of the entire EMAR cycle applied to a hypothetical natural gas treating facility. An existing EMAR thermodynamic model was expanded on and modified with the Peng-Robinson Equation of State to accommodate natural gas components. This model was used to examine the sensitivity of the EMAR cycle to the following process variables: amine concentration, copper loading shift, desorption pressure and temperature, applied overpotential, absorber pressure, and inlet and outlet CO₂ concentration. The total system work can be reduced by using a high amine concentrations (4M) and moderate copper shift (> 40%), both of which improve the cyclic capacity and reduce pump work, while still achieving the required 50 ppm outlet CO₂ target. Though an EMAR system can desorb CO₂ at high pressure, it was found to be energetically unfavourable, due to the high associated finite electrode and surface and transport overpotentials. These overpotentials can be minimised by intensification of the absorption and electrochemical processes, increasing the cell operating pressure or by adding chloride to the electrolyte. If total overpotentials are limited to 0.07 V, an EMAR system can operate at the same equivalent energy consumption of current state of the art thermal systems (74 kJ_e/mol CO₂), confirmed through simulation of a thermal MDEA/PZ system in Aspen Hysys. The EMAR system is more suited to LNG production facilities over those that only supply domestic gas because the total system work is not sensitive to the required CO₂ outlet target. The electrical power required by the currently modeled EMAR system operating at an LNG facility can easily be supplied through application of Organic Rankine Cycles to onsite gas turbine generators. With further process intensification and modification, EMAR is a potential competitor to current thermal amine systems.

7.2 Directions for future research

This thesis has shown that an EMAR cycle, with suitable modifications, is applicable to natural gas treating, however, aspects of the system should be further explored before the process is ready for industrial implementation.

The long term stable operation of an EMAR system is essential, which dictates that copper plating and dissolution is reversible and that the solvent experiences

minimal degradation. The electrodeposited copper shown in Chapter 5 was, in areas, uneven and weakly adhered to the substrate. Over many polarisation switching cycles (which prevent complete dissolution of the anode), copper dendrites may form, bridging the electrodes, and negate the operation of the cell. Further investigation into the effect of temperature, pressure and additives on the quality and reversibility of the deposit should be performed based on the recommendations outlined in this thesis. Additives that may benefit electrodeposition could negatively impact the solvent stability and longevity. The long term stability of EDA at elevated temperature and at various CO₂ loadings has not been extensively studied. Additionally, it has also been reported that cupric ions catalyse the oxidative degradation of ethylenediamine, which has yet to be examined under the conditions in an EMAR cycle.

The construction and operation of a moderate to high pressure flow system will be integral to the evaluation of EMAR for an industrial implementation. In addition to providing experimental data to validate the thermodynamic analysis presented in Chapter 6, a high pressure flow system will be able to investigate the following: the effect of gas composition on electrode polarisation (concerning the coabsorption of heavy hydrocarbons into the aqueous amine solvent), the foaming behaviour of the electrolyte solution, the corrosion of, or plating of copper(II) onto common materials of construction (e.g. carbon steel), and mechanical design considerations of the high pressure electrochemical cell. The results from such investigation, coupled with computational results gathered in Chapter 3, can be used to develop a rate-based (kinetic) process model for the sizing and design of equipment in an EMAR flowsheet.

Alternative EMCCS schemes that replace copper (the solid blocker species) with a soluble alternative may be favourable. Such methods would avoid the issues associated with plating and dissolution of copper, as an active blocker would remain in solution. Additionally, the required overpotential for such a scheme would likely be lower, as no phase change of the blocker is required, resulting in faster reaction kinetics.

References

- [1] World Energy Outlook. Technical report, International Energy Agency, 2019. URL www.iea.org/weo.
- [2] Australian Government. Resources and Energy Quarterly: December 2019. Technical report, Department of Industry, Innovation and Science, 2019. URL www.industry.gov.au/REQ.
- [3] Nick Toscano. Australia tops Qatar as world's biggest LNG exporter. URL <https://www.smh.com.au/business/the-economy/australia-tops-qatar-as-world-s-biggest-lng-exporter-20200106-p53p5h.html>.
- [4] GPSA. *Engineering Data Book*. Gas Processors Suppliers Association, Tulsa, Oklahoma, 12th edition, 2004.
- [5] US Energy Information Administration. Australia is on track to become world's largest LNG exporter 2019. URL <https://www.eia.gov/todayinenergy/detail.php?id=40853>.
- [6] About *Today in Energy*. URL <https://www.eia.gov/todayinenergy/about.php>.
- [7] William Parrish and Arthur Kidnay. *Fundamentals of Natural Gas Processing*. Taylor & Francis, Boca Raton, FL, 2006. ISBN 0849334063. doi: 10.1201/9781420014044.
- [8] Douglas Aaron and Costas Tsouris. Separation of CO₂ from Flue Gas: A Review. *Separation Science and Technology*, 40(1-3):321–348, 2005. ISSN 0149-6395. doi: 10.1081/SS-200042244. URL <http://www.tandfonline.com/doi/abs/10.1081/SS-200042244>.
- [9] Chevron Australia. Gorgon Project: Application for a Licence to Operate LNG Trains 1 to 3 and their Associated Facilities. Technical report, 2017.
- [10] Sumedh S. Warudkar, Kenneth R. Cox, Michael S. Wong, and George J. Hirasaki. Influence of stripper operating parameters on the performance of amine absorption systems for post-combustion carbon capture: Part II. Vacuum strippers. *International Journal of Greenhouse Gas Control*, 16:351–360, 2013. ISSN 17505836. doi: 10.1016/j.ijggc.2013.01.049. URL <http://dx.doi.org/10.1016/j.ijggc.2013.01.049>.
- [11] Zhiwu Liang, Kaiyun Fu, Raphael Idem, and Paitoon Tontiwachwuthikul. Review on current advances, future challenges and consideration issues for post-combustion CO₂ capture using amine-based absorbents. *Chinese Journal of Chemical Engineering*, 24(2): 278–288, 2016. ISSN 10049541. doi: 10.1016/j.cjche.2015.06.013. URL <http://dx.doi.org/10.1016/j.cjche.2015.06.013>.
- [12] Kameron R. Jorgensen, Thomas R. Cundari, and Angela K. Wilson. Interaction energies of CO₂-amine complexes: Effects of amine substituents. *Journal of Physical Chemistry A*, 116(42):10403–10411, 2012. ISSN 10895639. doi: 10.1021/jp305347b.
- [13] Mohammadreza Momeni and Siavash Riahi. Prediction of amines capacity for carbon dioxide absorption in gas sweetening processes. *Journal of Natural Gas Science and*

- Engineering*, 21:442–450, 2014. ISSN 18755100. doi: 10.1016/j.jngse.2014.09.002. URL <http://dx.doi.org/10.1016/j.jngse.2014.09.002>.
- [14] Firoz Alam Chowdhury, Hidetaka Yamada, Takayuki Higashii, Yoichi Matsuzaki, and Shingo Kazama. Synthesis and characterization of new absorbents for CO₂ capture. *Energy Procedia*, 37:265–272, 2013. ISSN 18766102. doi: 10.1016/j.egypro.2013.05.111. URL <http://dx.doi.org/10.1016/j.egypro.2013.05.111>.
- [15] Sholeh Ma'mun, Hallvard F. Svendsen, Karl A. Hoff, and Olav Juliussen. Selection of new absorbents for carbon dioxide capture. *Energy Conversion and Management*, 48(1):251–258, jan 2007. ISSN 01968904. doi: 10.1016/j.enconman.2006.04.007. URL <https://linkinghub.elsevier.com/retrieve/pii/S0196890406001440>.
- [16] Shinji Murai, Yasuhiro Kato, Yukishige Maezawa, Takehiko Muramatsu, and Satoshi Saito. Novel hindered amine absorbent for CO₂ capture. *Energy Procedia*, 37:417–422, 2013. ISSN 18766102. doi: 10.1016/j.egypro.2013.05.126. URL <http://dx.doi.org/10.1016/j.egypro.2013.05.126><https://linkinghub.elsevier.com/retrieve/pii/S1876610213001367>.
- [17] Ugochukwu E. Aronu, Karl A. Hoff, and Hallvard F. Svendsen. CO₂ capture solvent selection by combined absorption–desorption analysis. *Chemical Engineering Research and Design*, 89(8):1197–1203, aug 2011. ISSN 02638762. doi: 10.1016/j.cherd.2011.01.007. URL <http://dx.doi.org/10.1016/j.cherd.2011.01.007><https://linkinghub.elsevier.com/retrieve/pii/S0263876211000335>.
- [18] Firoz Alam Chowdhury, Hidetaka Yamada, Takayuki Higashii, Kazuya Goto, and Masami Onoda. CO₂ capture by tertiary amine absorbents: A performance comparison study. *Industrial and Engineering Chemistry Research*, 52(24):8323–8331, 2013. ISSN 08885885. doi: 10.1021/ie400825u. URL <http://dx.doi.org/10.1021/ie400825u>.
- [19] Xiao Luo, Kaiyun Fu, Zhen Yang, Hongxia Gao, Wichitpan Rongwong, Zhiwu Liang, and Paitoon Tontiwachwuthikul. Experimental Studies of Reboiler Heat Duty for CO₂ Desorption from Triethylenetetramine (TETA) and Triethylenetetramine (TETA) + N-Methyldiethanolamine (MDEA). *Industrial and Engineering Chemistry Research*, 54(34):8554–8560, 2015. ISSN 15205045. doi: 10.1021/acs.iecr.5b00158.
- [20] Adewale Adeosun and Mohammad R.M. Abu-Zahra. Evaluation of amine-blend solvent systems for CO₂ post-combustion capture applications. *Energy Procedia*, 37:211–218, 2013. ISSN 18766102. doi: 10.1016/j.egypro.2013.05.104. URL <http://dx.doi.org/10.1016/j.egypro.2013.05.104>.
- [21] Lionel Dubois, Patrick Kahasha Mbasha, and Diane Thomas. CO₂ absorption into aqueous solutions of a polyamine, a sterically hindered amine, and their blends. *Chemical Engineering and Technology*, 33(3):461–467, 2010. ISSN 09307516. doi: 10.1002/ceat.200900489.
- [22] Helena Svensson, Christian Hulteberg, and Hans T. Karlsson. Heat of absorption of CO₂ in aqueous solutions of N-methyldiethanolamine and piperazine. *International Journal of Greenhouse Gas Control*, 17:89–98, 2013. ISSN 17505836. doi: 10.1016/j.ijggc.2013.04.021. URL <http://dx.doi.org/10.1016/j.ijggc.2013.04.021>.
- [23] Hanna Kierzkowska-Pawlak. Enthalpies of absorption and solubility of CO₂ in aqueous solutions of methyldiethanolamine. *Separation Science and Technology*, 42(12):2723–2737, 2007. ISSN 01496395. doi: 10.1080/01496390701513032.
- [24] C. Mathonat, V. Majer, A. E. Mather, and J. P.E. Grolier. Enthalpies of absorption and solubility of CO₂ in aqueous solutions of methyldiethanolamine. *Fluid Phase Equilibria*, 140(1-2):171–182, 1997. ISSN 03783812. doi: 10.1016/s0378-3812(97)00182-9.
- [25] Laila Jaafari, Bander Jaffary, and Raphael Idem. Screening study for selecting new activators for activating MDEA for natural gas sweetening. *Separation and Purification*

- Technology*, 199(February):320–330, 2018. ISSN 18733794. doi: 10.1016/j.seppur.2018.02.007.
- [26] Fred Closmann, Thu Nguyen, and Gary T. Rochelle. MDEA/Piperazine as a solvent for CO₂ capture. *Energy Procedia*, 1(1):1351–1357, 2009. ISSN 18766102. doi: 10.1016/j.egypro.2009.01.177. URL <http://dx.doi.org/10.1016/j.egypro.2009.01.177>.
- [27] Sanjay Bishnoi and Gary T. Rochelle. Absorption of carbon dioxide in aqueous piperazine/methyldiethanolamine. *AIChE Journal*, 48(12):2788–2799, dec 2002. ISSN 00011541. doi: 10.1002/aic.690481208. URL <http://doi.wiley.com/10.1002/aic.690481208>.
- [28] Tsukasa Kumagai, Koji Tanaka, Yasushi Fujimura, Takuya Ono, Fumihito Ito, Torsten Katz, Oliver Spuhl, and Aik Meam Tan. HiPACT- Advanced CO₂ capture technology for green natural gas exploration. *Energy Procedia*, 4(0):125–132, 2011. ISSN 18766102. doi: 10.1016/j.egypro.2011.01.032. URL <http://www.sciencedirect.com/science/article/pii/S1876610211000336>.
- [29] Koji Tanaka, Yasushi Fujimura, Takehiro Komi, Torsten Katz, Oliver Spuhl, and Erick Contreras. Demonstration test result of High Pressure Acid gas Capture Technology (HiPACT). *Energy Procedia*, 37:461–476, 2013. ISSN 18766102. doi: 10.1016/j.egypro.2013.05.132. URL <http://dx.doi.org/10.1016/j.egypro.2013.05.132>.
- [30] Junya Okazaki, Aiko Horikawa, Koji Tanaka, Graham Orr, Gatot Joyowardoyo, and Torsten Katz. Operational Experience of HiPACT[®] Process. In *14th International Conference on Greenhouse Gas Control Technologies*, number 14, 2018. ISBN 8145682800.
- [31] Yu Jeng Lin and Gary T. Rochelle. Approaching a reversible stripping process for CO₂ capture. *Chemical Engineering Journal*, 283:1033–1043, 2016. ISSN 13858947. doi: 10.1016/j.cej.2015.08.086. URL <http://dx.doi.org/10.1016/j.cej.2015.08.086>.
- [32] Ye Yuan and Gary T. Rochelle. Lost work: A comparison of water-lean solvent to a second generation aqueous amine process for CO₂ capture. *International Journal of Greenhouse Gas Control*, 84(October 2018):82–90, 2019. ISSN 17505836. doi: 10.1016/j.ijggc.2019.03.013. URL <https://doi.org/10.1016/j.ijggc.2019.03.013>.
- [33] Tianyu Gao, Joseph L. Selinger, and Gary T. Rochelle. Demonstration of 99% CO₂ removal from coal flue gas by amine scrubbing. *International Journal of Greenhouse Gas Control*, 83(January):236–244, 2019. ISSN 17505836. doi: 10.1016/j.ijggc.2019.02.013. URL <https://doi.org/10.1016/j.ijggc.2019.02.013>.
- [34] Gary T. Rochelle, Yuying Wu, Eric Chen, Korede Akinpelumi, Kent B. Fischer, Tianyu Gao, Ching Ting Liu, and Joseph L. Selinger. Pilot plant demonstration of piperazine with the advanced flash stripper. *International Journal of Greenhouse Gas Control*, 84(October 2018):72–81, 2019. ISSN 17505836. doi: 10.1016/j.ijggc.2019.03.014. URL <https://doi.org/10.1016/j.ijggc.2019.03.014>.
- [35] Le Li. *Carbon Dioxide Solubility and Mass Transfer in Aqueous Amines for Carbon Capture*. PhD thesis, The University of Texas at Austin, 2015.
- [36] Stephanie Anne Freeman and Gary Thomas Rochelle. Thermal degradation of aqueous piperazine for CO₂ capture: 2. product types and generation rates. *Industrial and Engineering Chemistry Research*, 51(22):7726–7735, 2012. ISSN 08885885. doi: 10.1021/ie201917c.
- [37] MC Stern. *Electrochemically-mediated amine regeneration for carbon dioxide separations*. PhD thesis, Massachusetts Institute of Technology, 2013. URL <http://dspace.mit.edu/handle/1721.1/87130>.
- [38] Sahag Voskian and T. Alan Hatton. Faradaic electro-swing reactive adsorption for CO₂ capture. *Energy and Environmental Science*, 12(12):3530–3547, 2019. ISSN 17545706. doi: 10.1039/c9ee02412c.

- [39] Burcu Gurkan, Fritz Simeon, and T. Alan Hatton. Quinone Reduction in Ionic Liquids for Electrochemical CO₂ Separation. *ACS Sustainable Chemistry and Engineering*, 3(7):1394–1405, 2015. ISSN 21680485. doi: 10.1021/acssuschemeng.5b00116.
- [40] Paul Scovazzo, Joe Poshusta, Dan DuBois, Carl Koval, and Richard Noble. Electrochemical Separation and Concentration of < 1% Carbon Dioxide from Nitrogen. *Journal of The Electrochemical Society*, 150(5):D91, 2003. ISSN 00134651. doi: 10.1149/1.1566962. URL <https://iopscience.iop.org/article/10.1149/1.1566962>.
- [41] Rajeev Ranjan, Jarred Olson, Poonam Singh, Edward D. Lorance, Daniel A. Buttry, and Ian R. Gould. Reversible Electrochemical Trapping of Carbon Dioxide Using 4,4'-Bipyridine That Does Not Require Thermal Activation. *Journal of Physical Chemistry Letters*, 6(24):4943–4946, 2015. ISSN 19487185. doi: 10.1021/acs.jpcclett.5b02220.
- [42] Poonam Singh, Joseph H. Rheinhardt, Jarred Z. Olson, Pilarisetty Tarakeshwar, Vladimiro Mujica, and Daniel A. Buttry. Electrochemical capture and release of carbon dioxide using a disulfide-thiocarbonate redox cycle. *Journal of the American Chemical Society*, 139(3):1033–1036, 2017. ISSN 15205126. doi: 10.1021/jacs.6b10806.
- [43] Joseph H. Rheinhardt, Poonam Singh, Pilarisetty Tarakeshwar, and Daniel A. Buttry. Electrochemical capture and release of carbon dioxide. *ACS Energy Letters*, 2(2):454–461, 2017. ISSN 23808195. doi: 10.1021/acsenerylett.6b00608.
- [44] Michael C. Stern, Fritz Simeon, Howard Herzog, and T. Alan Hatton. An electrochemically-mediated gas separation process for carbon abatement. *Energy Procedia*, 37:1172–1179, 2013. ISSN 18766102. doi: 10.1016/j.egypro.2013.05.214. URL <http://www.sciencedirect.com/science/article/pii/S1876610213002245>.
- [45] Michael C. Stern, Fritz Simeon, Howard Herzog, and T. Alan Hatton. Post-combustion carbon dioxide capture using electrochemically mediated amine regeneration. *Energy and Environmental Science*, 6(8):2505–2517, 2013. ISSN 17545692. doi: 10.1039/c3ee41165f. URL <http://pubs.rsc.org/en/content/articlehtml/2013/ee/c3ee41165f>.
- [46] Michael C. Stern and T. Alan Hatton. Bench-scale demonstration of CO₂ capture with electrochemically-mediated amine regeneration. *RSC Advances*, 4(12):5906–5914, 2014. ISSN 20462069. doi: 10.1039/c3ra46774k. URL <http://xlink.rsc.org/?DOI=c3ra46774k>.
- [47] Ryan A. Shaw and T. Alan Hatton. Electrochemical CO₂ capture thermodynamics. *International Journal of Greenhouse Gas Control*, 95(October 2019):102878, 2020. ISSN 17505836. doi: 10.1016/j.ijggc.2019.102878. URL <https://doi.org/10.1016/j.ijggc.2019.102878>.
- [48] Aly Eldeen O. Eltayeb. *Analysis and Design of Electrochemically-Mediated Carbon Dioxide Separation*. PhD thesis, Massachusetts Institute of Technology, 2015.
- [49] Ryan Alex Shaw. *Modeling and Design for Electrochemical Carbon Dioxide Capture Systems*. PhD thesis, Massachusetts Institute of Technology, 2019.
- [50] Miao Wang, Mohammad Rahimi, Amit Kumar, Subrahmaniam Hariharan, Wonyoung Choi, and T Alan Hatton. Flue gas CO₂ capture via electrochemically mediated amine regeneration: System design and performance. *Applied Energy*, 255(September):113879, dec 2019. ISSN 03062619. doi: 10.1016/j.apenergy.2019.113879. URL <https://doi.org/10.1016/j.apenergy.2019.113879><https://linkinghub.elsevier.com/retrieve/pii/S0306261919315661>.
- [51] Olev Trass and R. H. Weiland. Absorption of carbon dioxide in ethylenediamine solutions ii. pilot plant study of absorption and regeneration. *The Canadian Journal of Chemical Engineering*, 49(6):773–781, 1971. ISSN 00084034. doi: 10.1002/cjce.5450490611. URL <http://onlinelibrary.wiley.com/doi/10.1002/cjce.5450490611/abstract>.

- [52] Shan Zhou, Xi Chen, Thu Nguyen, Alexander K. Voice, and Gary T. Rochelle. Aqueous ethylenediamine for CO₂ capture. *ChemSusChem*, 3(8):913–918, 2010. ISSN 1864564X. doi: 10.1002/cssc.200900293.
- [53] Hari Prasad Mangalapally and Hans Hasse. Pilot plant experiments for post combustion carbon dioxide capture by reactive absorption with novel solvents. *Energy Procedia*, 4: 1–8, 2011. ISSN 18766102. doi: 10.1016/j.egypro.2011.01.015. URL <http://dx.doi.org/10.1016/j.egypro.2011.01.015>.
- [54] Markus Rabensteiner, Gerald Kinger, Martin Koller, Günter Gronald, and Christoph Hochenauer. Pilot plant study of ethylenediamine as a solvent for post combustion carbon dioxide capture and comparison to monoethanolamine. *International Journal of Greenhouse Gas Control*, 27:1–14, 2014. ISSN 17505836. doi: 10.1016/j.ijggc.2014.05.002. URL <http://dx.doi.org/10.1016/j.ijggc.2014.05.002>.
- [55] Valentín Vassilev-Galindo, Myrna H. Matus, and Miguel A. Morales-Cabrera. Analysis of the CO₂ absorption through a series of amines within the integration of a computational chemistry and process simulation scheme. *International Journal of Greenhouse Gas Control*, 50:198–205, 2016. ISSN 17505836. doi: 10.1016/j.ijggc.2016.04.029. URL <http://dx.doi.org/10.1016/j.ijggc.2016.04.029>.
- [56] Mayuri Gupta, Eirik F. Da Silva, Ardi Hartono, and Hallvard F. Svendsen. Theoretical study of differential enthalpy of absorption of CO₂ with MEA and MDEA as a function of temperature. *Journal of Physical Chemistry B*, 117(32):9457–9468, 2013. ISSN 15206106. doi: 10.1021/jp404356e.
- [57] Tingting Zhang, Yunsong Yu, Guoxiong Wang, and Zaoxiao Zhang. Ab Initio Calculations on Reaction Process of Piperazine Absorbing CO₂. *Energy Procedia*, 114(November 2016): 2121–2127, 2017. ISSN 18766102. doi: 10.1016/j.egypro.2017.03.1346. URL <http://dx.doi.org/10.1016/j.egypro.2017.03.1346>.
- [58] Kazi Z. Sumon, Amr Henni, and Allan L L East. Molecular dynamics simulations of proposed intermediates in the CO₂ + aqueous amine reaction. *Journal of Physical Chemistry Letters*, 5(7):1151–1156, 2014. ISSN 19487185. doi: 10.1021/jz500237v.
- [59] A. Maiti, W. L. Bourcier, and R. D. Aines. Atomistic modeling of CO₂ capture in primary and tertiary amines - Heat of absorption and density changes. *Chemical Physics Letters*, 509(1-3):25–28, 2011. ISSN 00092614. doi: 10.1016/j.cplett.2011.04.080. URL <http://dx.doi.org/10.1016/j.cplett.2011.04.080>.
- [60] Girma Gonfa, Mohamad Azmi Bustam, and Azmi M. Shariff. Quantum-chemical-based quantitative structure-activity relationships for estimation of CO₂ absorption/desorption capacities of amine-based absorbents. *International Journal of Greenhouse Gas Control*, 49:372–378, 2016. ISSN 17505836. doi: 10.1016/j.ijggc.2016.03.022. URL <http://dx.doi.org/10.1016/j.ijggc.2016.03.022>.
- [61] Tugba Davran-Candan. DFT modeling of CO₂ interaction with various aqueous amine structures. *Journal of Physical Chemistry A*, 118(25):4582–4590, 2014. ISSN 15205215. doi: 10.1021/jp503929g.
- [62] Hong Bin Xie, Yanzi Zhou, Yingkai Zhang, and J. Karl Johnson. Reaction mechanism of monoethanolamine with CO₂ in aqueous solution from molecular modeling. *Journal of Physical Chemistry A*, 114(43):11844–11852, 2010. ISSN 15205215. doi: 10.1021/jp107516k.
- [63] Milad Narimani, Sepideh Amjad-Iranagh, and Hamid Modarress. CO₂ absorption into aqueous solutions of monoethanolamine, piperazine and their blends: Quantum mechanics and molecular dynamics studies. *Journal of Molecular Liquids*, 233:173–183, 2017. ISSN 01677322. doi: 10.1016/j.molliq.2017.03.015. URL <http://dx.doi.org/10.1016/j.molliq.2017.03.015>.

- [64] Hong Bin Xie, Ning He, Zhiquan Song, Jingwen Chen, and Xuehua Li. Theoretical investigation on the different reaction mechanisms of aqueous 2-amino-2-methyl-1-propanol and monoethanolamine with CO₂. *Industrial and Engineering Chemistry Research*, 53(8):3363–3372, 2014. ISSN 08885885. doi: 10.1021/ie403280h.
- [65] Jae Goo Shim, Jun Han Kim, Young H. Jhon, Jaheon Kim, and Kwang Hwi Cho. DFT calculations on the role of base in the reaction between CO₂ and monoethanolamine. *Industrial and Engineering Chemistry Research*, 48(4):2172–2178, 2009. ISSN 08885885. doi: 10.1021/ie800684a.
- [66] Yoichi Matsuzaki, Hidetaka Yamada, Firoz A. Chowdhury, Takayuki Higashii, Shingo Kazama, and Masami Onoda. Ab initio study of CO₂ capture mechanisms in monoethanolamine aqueous solution: Reaction pathways from carbamate to bicarbonate. *Energy Procedia*, 37:400–406, 2013. ISSN 18766102. doi: 10.1016/j.egypro.2013.05.124. URL <http://dx.doi.org/10.1016/j.egypro.2013.05.124>.
- [67] Hsueh Chien Li and Ming Kang Tsai. A first-principle study of CO₂ binding by monoethanolamine and mono-n-propanolamine solutions. *Chemical Physics*, 452:9–16, 2015. ISSN 03010104. doi: 10.1016/j.chemphys.2015.02.012. URL <http://dx.doi.org/10.1016/j.chemphys.2015.02.012>.
- [68] Hongbin Xie, Pan Wang, Ning He, Xianhai Yang, and Jingwen Chen. Toward rational design of amines for CO₂ capture: Substituent effect on kinetic process for the reaction of monoethanolamine with CO₂. *Journal of Environmental Sciences (China)*, 37:75–82, 2015. ISSN 10010742. doi: 10.1016/j.jes.2015.03.033. URL <http://dx.doi.org/10.1016/j.jes.2015.03.033>.
- [69] Eirik F. Da Silva and Hallvard F. Svendsen. Study of the carbamate stability of amines using ab initio methods and free-energy perturbations. *Industrial and Engineering Chemistry Research*, 45(8):2497–2504, 2006. ISSN 08885885. doi: 10.1021/ie050501z.
- [70] Anita S. Lee and John R. Kitchin. Chemical and molecular descriptors for the reactivity of amines with CO₂. *Industrial and Engineering Chemistry Research*, 51(42):13609–13618, 2012. ISSN 08885885. doi: 10.1021/ie301419q.
- [71] Hong Bin Xie, J. Karl Johnson, Robert J. Perry, Sarah Genovese, and Benjamin R. Wood. A computational study of the heats of reaction of substituted monoethanolamine with CO₂. *Journal of Physical Chemistry A*, 115(3):342–350, 2011. ISSN 15205215. doi: 10.1021/jp1081627.
- [72] Phil Jackson, Ariana Beste, and Moetaz Attalla. Insights into amine-based CO₂ capture: An ab initio self-consistent reaction field investigation. *Structural Chemistry*, 22(3):537–549, 2011. ISSN 10400400. doi: 10.1007/s11224-010-9719-2.
- [73] Kazi Z. Sumon, Amr Henni, and Allan L.L. East. Predicting pK_a of amines for CO₂ capture: Computer versus pencil-and-paper. *Industrial and Engineering Chemistry Research*, 51(37):11924–11930, 2012. ISSN 08885885. doi: 10.1021/ie301033p.
- [74] Eirik F. da Silva and Hallvard F. Svendsen. Computational chemistry study of reactions, equilibrium and kinetics of chemical CO₂ absorption. *International Journal of Greenhouse Gas Control*, 1(2):151–157, 2007. ISSN 17505836. doi: 10.1016/S1750-5836(07)00022-9.
- [75] Mayuri Gupta, Eirik F. da Silva, and Hallvard F. Svendsen. Postcombustion CO₂ Capture Solvent Characterization Employing the Explicit Solvation Shell Model and Continuum Solvation Models. *The Journal of Physical Chemistry B*, 120(34):9034–9050, sep 2016. ISSN 1520-6106. doi: 10.1021/acs.jpcc.6b04049. URL <http://pubs.acs.org/doi/abs/10.1021/acs.jpcc.6b04049><https://pubs.acs.org/doi/10.1021/acs.jpcc.6b04049>.
- [76] Mayuri Gupta and Hallvard F. Svendsen. Understanding Carbamate Formation Reaction Thermochemistry of Amino Acids as Solvents for Postcombustion CO₂ Capture. *The Journal of Physical Chemistry B*, 123(40):8433–8447, oct 2019. ISSN 1520-6106.

- doi: 10.1021/acs.jpcc.9b06447. URL <https://pubs.acs.org/doi/10.1021/acs.jpcc.9b06447>.
- [77] Athanassios C. Tsipis. DFT flavor of coordination chemistry. *Coordination Chemistry Reviews*, 272:1–29, 2014. ISSN 00108545. doi: 10.1016/j.ccr.2014.02.023. URL <http://dx.doi.org/10.1016/j.ccr.2014.02.023>.
- [78] Christopher J. Cramer and Donald G. Truhlar. Density functional theory for transition metals and transition metal chemistry. *Physical Chemistry Chemical Physics*, 11(46):10757–10816, 2009. ISSN 14639076. doi: 10.1039/b907148b. URL <http://www.ncbi.nlm.nih.gov/pubmed/19924312>.
- [79] Malcolm A. Halcrow. Jahn-Teller distortions in transition metal compounds, and their importance in functional molecular and inorganic materials. *Chemical Society Reviews*, 42(4):1784–1795, 2013. ISSN 03060012. doi: 10.1039/c2cs35253b.
- [80] Sheida Esmailzadeh, Leila Azimian, Khadijeh Shekoohi, and Khosro Mohammadi. Coordination chemistry, thermodynamics and DFT calculations of copper(II) NNOS Schiff base complexes. *Spectrochimica Acta - Part A: Molecular and Biomolecular Spectroscopy*, 133:579–590, 2014. ISSN 13861425. doi: 10.1016/j.saa.2014.05.095. URL <http://dx.doi.org/10.1016/j.saa.2014.05.095>.
- [81] Hamid Golchoubian, Golasa Moayyedi, Ehsan Rezaee, and Giuseppe Bruno. Synthesis, characterization and solvatochromism study of mixed-chelate copper(II) complexes: A combined experimental and density functional theoretical study. *Polyhedron*, 96:71–78, 2015. ISSN 02775387. doi: 10.1016/j.poly.2015.04.029. URL <http://dx.doi.org/10.1016/j.poly.2015.04.029>.
- [82] María del Carmen Ramírez Avi, Ana África Márquez García, and Francisco Partal Ureña. Electronic structure of kaempferol–Cu²⁺ coordination compounds: a DFT, QTAIM and NBO study in the gas phase. *Theoretical Chemistry Accounts*, 134(4), 2015. ISSN 1432881X. doi: 10.1007/s00214-015-1655-1.
- [83] Liuming Yan, Yi Lu, and Xuejiao Li. A density functional theory protocol for the calculation of redox potentials of copper complexes. *Physical Chemistry Chemical Physics*, 18(7):5529–5536, 2016. ISSN 14639076. doi: 10.1039/c5cp06638g. URL <http://pubs.rsc.org/en/content/articlehtml/2016/cp/c5cp06638g>.
- [84] Matěj Pavelka and Jaroslav V. Burda. Computational study of redox active centres of blue copper proteins: A computational DFT study. *Molecular Physics*, 106(24):2733–2748, 2008. ISSN 00268976. doi: 10.1080/00268970802672684.
- [85] Haochen Zhang, Xiaoxia Chang, Jingguang G. Chen, William A. Goddard, Bingjun Xu, Mu Jeng Cheng, and Qi Lu. Computational and experimental demonstrations of one-pot tandem catalysis for electrochemical carbon dioxide reduction to methane. *Nature Communications*, 10(1):1–9, 2019. ISSN 20411723. doi: 10.1038/s41467-019-11292-9.
- [86] James W. Vickers, Dominic Alfonso, and Douglas R. Kauffman. Electrochemical Carbon Dioxide Reduction at Nanostructured Gold, Copper, and Alloy Materials. *Energy Technology*, 5(6):775–795, 2017. ISSN 21944296. doi: 10.1002/ente.201600580.
- [87] Javed Hussain, Egill Skúlason, and Hannes Jónsson. Computational study of electrochemical CO₂ reduction at transition metal electrodes. *Procedia Computer Science*, 51(1):1865–1871, 2015. ISSN 18770509. doi: 10.1016/j.procs.2015.05.419. URL <http://dx.doi.org/10.1016/j.procs.2015.05.419>.
- [88] Gabriela Elena Badea. Electrocatalytic reduction of nitrate on copper electrode in alkaline solution. *Electrochimica Acta*, 54(3):996–1001, 2009. ISSN 00134686. doi: 10.1016/j.electacta.2008.08.003.
- [89] K. Bouzek, M. Paidar, A. Sadílková, and H. Bergmann. Electrochemical reduction of

- nitrate in weakly alkaline solutions. *Journal of Applied Electrochemistry*, 31(11):1185–1193, 2001. ISSN 0021891X. doi: 10.1023/A:1012755222981.
- [90] Elena Pérez-Gallent, Marta C. Figueiredo, Ioannis Katsounaros, and Marc T.M. Koper. Electrocatalytic reduction of Nitrate on Copper single crystals in acidic and alkaline solutions. *Electrochimica Acta*, 227:77–84, 2017. ISSN 00134686. doi: 10.1016/j.electacta.2016.12.147. URL <http://dx.doi.org/10.1016/j.electacta.2016.12.147>.
- [91] Young Ku and Robert W. Peters. The effect of complexing agents on the precipitation and removal of copper and nickel from solution. *Particulate Science and Technology*, 6(4):441–446, 1988. ISSN 15480046. doi: 10.1080/02726358808906516.
- [92] George R Helz and Lewis M Horzempa. EDTA as a kinetic inhibitor of copper(II) sulfide precipitation. *Water Research*, 17(2):167–172, jan 1983. ISSN 00431354. doi: 10.1016/0043-1354(83)90097-0. URL <https://linkinghub.elsevier.com/retrieve/pii/0043135483900970>.
- [93] Sofia Messias, Miguel M. Sousa, Manuel Nunes Da Ponte, Carmen M. Rangel, Tiago Pardal, and Ana S.Reis MacHado. Electrochemical production of syngas from CO₂ at pressures up to 30 bar in electrolytes containing ionic liquid. *Reaction Chemistry and Engineering*, 4(11):1982–1990, 2019. ISSN 20589883. doi: 10.1039/c9re00271e.
- [94] Mahinder Ramdin, Andrew R.T. Morrison, Mariette De Groen, Rien Van Haperen, Robert De Kler, Leo J.P. Van Den Broeke, J. P. Martin Trusler, Wiebren De Jong, and Thijs J.H. Vlught. High Pressure Electrochemical Reduction of CO₂ to Formic Acid/Formate: A Comparison between Bipolar Membranes and Cation Exchange Membranes. *Industrial and Engineering Chemistry Research*, 58(5):1834–1847, 2019. ISSN 15205045. doi: 10.1021/acs.iecr.8b04944.
- [95] Debora Giovanelli, Nathan S. Lawrence, and Richard G. Compton. Electrochemistry at high pressures: A review. *Electroanalysis*, 16(10):789–810, 2004. ISSN 10400397. doi: 10.1002/elan.200302958.
- [96] Ying Zhang, Hern Chen, Chau Chyun Chen, Jorge M. Plaza, Ross Dugas, and Gary T. Rochelle. Rate-based process modeling study of CO₂ Capture with aqueous monoethanolamine solution. *Industrial and Engineering Chemistry Research*, 48(20):9233–9246, 2009. ISSN 08885885. doi: 10.1021/ie900068k.
- [97] Ying Zhang, Huiling Que, and Chau Chyun Chen. Thermodynamic modeling for CO₂ absorption in aqueous MEA solution with electrolyte NRTL model. *Fluid Phase Equilibria*, 311(1):67–75, 2011. ISSN 03783812. doi: 10.1016/j.fluid.2011.08.025. URL <http://dx.doi.org/10.1016/j.fluid.2011.08.025>.
- [98] Ying Zhang and Chau-Chyun Chen. Thermodynamic Modeling for CO₂ Absorption in Aqueous MDEA Solution with Electrolyte NRTL Model. *Industrial & Engineering Chemistry Research*, 50(1):163–175, jan 2011. ISSN 0888-5885. doi: 10.1021/ie1006855. URL <http://linkinghub.elsevier.com/retrieve/pii/S0378381211004043><https://pubs.acs.org/doi/10.1021/ie1006855>.
- [99] Jennifer Dymont and Suphat Watanasiri. Acid Gas Cleaning Using Amine Solvents : Validation with Experimental and Plant Data, 2018.
- [100] Suphat Watanasiri, Ying Zhang, Chad Mondor, and Jennifer Dymont. Validation of Acid Gas Cleaning in Aspen HYSYS [®] for Liquid Hydrocarbons, 2016.
- [101] Miao Wang, Subrahmaniam Hariharan, Ryan A. Shaw, and T. Alan Hatton. Energetics of electrochemically mediated amine regeneration process for flue gas CO₂ capture. *International Journal of Greenhouse Gas Control*, 82(January):48–58, 2019. ISSN 17505836. doi: 10.1016/j.ijggc.2018.12.028. URL <https://doi.org/10.1016/j.ijggc.2018.12.028>.
- [102] Erwin Schrödinger. An undulatory theory of the mechanics of atoms and molecules. *Physical Review*, 28(6):1049–1070, 1926.

- [103] M. Born and R. Oppenheimer. Zur Quantentheorie der Molekeln. *Annalen Der Physik*, 389(20):457–484, 1927.
- [104] D. R. Hartree. The Wave Mechanics of an Atom with a Non-Coulomb Central Field. Part I. Theory and Methods. *Proceedings of the Cambridge Philosophical Society*, 24(1): 89–110, 1928. doi: 10.1017/S0305004100011919.
- [105] C.C.J. Roothaan. New developments in molecular orbital theory. *Reviews of Modern Physics*, 23(2):69–89, 1951. ISSN 00346861. doi: 10.1103/RevModPhys.23.69.
- [106] Jiří Čížek. On the Correlation Problem in Atomic and Molecular Systems. Calculation of Wavefunction Components in Ursell- Type Expansion Using Quantum-Field Theoretical Methods. *The Journal of Chemical Physics*, 45:4256–4266, 1966. doi: 10.1063/1.1727484.
- [107] G. W. Trucks, J. A. Pople, and M. Head-Gordon. A fifth-order perturbation comparison of electron correlation theories. *Chemical Physics Letters*, 157(6):479–483, 1989.
- [108] Frank Jensen. *Introduction to Computational Chemistry*. John Wiley & Sons, West Sussex, England, 2nd edition, 2007.
- [109] P. Hohenberg and W. Kohn. Inhomogeneous Electron Gas. *Physical Review*, 136(3B): B864–B871, 1964.
- [110] W. Kohn and L. J. Sham. Self-Consistent Equations Including Exchange and Correlation Effects. *Physical Review*, 140(4A):A1133–A1138, nov 1965. ISSN 0031-899X. doi: 10.1103/PhysRev.140.A1133. URL <https://link.aps.org/doi/10.1103/PhysRev.140.A1133>.
- [111] J. P. Perdew and Karla Schmidt. Jacob’s ladder of density functional approximations for the exchange-correlation energy Jacob’s Ladder of Density Functional Approximations for the Exchange-Correlation Energy. In *AIP Conf. Proc.*, volume 577, pages 1–20, 2001. ISBN 0735400164. doi: 10.1063/1.1390175.
- [112] Narbe Mardirossian and Martin Head-Gordon. Thirty years of density functional theory in computational chemistry: An overview and extensive assessment of 200 density functionals. *Molecular Physics*, 115(19):2315–2372, 2017. ISSN 13623028. doi: 10.1080/00268976.2017.1333644. URL <https://doi.org/10.1080/00268976.2017.1333644>.
- [113] Lars Goerigk, Andreas Hansen, Christoph Bauer, Stephan Ehrlich, Asim Najibi, and Stefan Grimme. A look at the density functional theory zoo with the advanced GMTKN55 database for general main group thermochemistry, kinetics and noncovalent interactions. *Physical Chemistry Chemical Physics*, 19(48):32184–32215, 2017. ISSN 14639076. doi: 10.1039/c7cp04913g.
- [114] Bun Chan, Peter M.W. Gill, and Masanari Kimura. Assessment of DFT Methods for Transition Metals with the TMC151 Compilation of Data Sets and Comparison with Accuracies for Main-Group Chemistry. *Journal of Chemical Theory and Computation*, 15:3610–3622, 2019. ISSN 15499626. doi: 10.1021/acs.jctc.9b00239.
- [115] Axel D. Becke. Density-functional thermochemistry. III. The role of exact exchange. *The Journal of Chemical Physics*, 98(7):5648–5652, 1993. ISSN 00219606. doi: 10.1063/1.464913.
- [116] Chengteh Lee, Weitao Yang, and Robert G. Parr. Development of the Colle-Salvetti Correlation-Energy Formula into a Functional of the Electron Density. *Physical Review B*, 37(2):785–789, 1988. ISSN 0163-1829. doi: 10/cwkrpd. URL <https://link.aps.org/doi/10.1103/PhysRevB.37.785>.
- [117] P. J. Stephens, F. J. Devlin, C. F. Chabalowski, and M. J. Frisch. Ab Initio calculation of vibrational absorption and circular dichroism spectra using density functional force fields. *Journal of Physical Chemistry®*, 98(45):11623–11627, 1994. ISSN 00223654. doi: 10.1021/j100096a001.

- [118] S. H. Vosko, L. Wilk, and M. Nusair. Accurate spin-dependent electron liquid correlation energies for local spin density calculations: a critical analysis. *Canadian Journal of Physics*, 58(8):1200–1211, 1980. ISSN 0008-4204. doi: 10.1139/p80-159.
- [119] Stefan Grimme. Accurate description of van der Waals complexes by density functional theory including empirical corrections. *Journal of Computational Chemistry*, 25(12):1463–1473, 2004. ISSN 01928651. doi: 10.1002/jcc.20078.
- [120] Stefan Grimme. Semiempirical GGA-type density functional constructed with a long-range dispersion correction. *Journal of Computational Chemistry*, 27(15):1787–1799, nov 2006. ISSN 0192-8651. doi: 10.1002/jcc.20495. URL <http://doi.wiley.com/10.1002/jcc.20495>.
- [121] Stefan Grimme, Jens Antony, Stephan Ehrlich, and Helge Krieg. A consistent and accurate ab initio parametrization of density functional dispersion correction (DFT-D) for the 94 elements H-Pu. *Journal of Chemical Physics*, 132(15), 2010. ISSN 00219606. doi: 10.1063/1.3382344.
- [122] Stefan Grimme, Stephan Ehrlich, and Lars Goerigk. Effect of the damping function in dispersion corrected density functional theory. *Journal of Computational Chemistry*, 32(7):1456–1465, may 2011. ISSN 01928651. doi: 10.1002/jcc.21759. URL <http://doi.wiley.com/10.1002/jcc.21759>.
- [123] J. C. Slater. Atomic shielding constants. *Physical Review*, 36:57–64, 1930. doi: 10.1103/PhysRev.36.57.
- [124] Clarence Zener. Analytic atomic wave functions. *Physical Review*, 36:51–56, 1930. doi: 10.1103/PhysRev.36.51.
- [125] S. F. Boys. Electronic wave functions I. A general method of calculation for the stationary states of any molecular system. *Proceedings of the Royal Society*, 200(1063):542–554, 1950. doi: 10.1098/rspa.1950.0036.
- [126] Christopher J Cramer. *Essentials of Computational Chemistry: Theories and Models*. John Wiley and Sons, 2nd edition, 2004. ISBN 0470091819.
- [127] P. Jeffrey Hay and Willard R. Wadt. Ab initio effective core potentials for molecular calculations. Potentials for K to Au including the outermost core orbitals. *The Journal of Chemical Physics*, 82(1):299–310, jan 1985. ISSN 0021-9606. doi: 10.1063/1.448975. URL <http://aip.scitation.org/doi/10.1063/1.448975>.
- [128] P. Jeffrey Hay and Willard R. Wadt. Ab initio effective core potentials for molecular calculations. Potentials for the transition metal atoms Sc to Hg. *The Journal of Chemical Physics*, 82(1):270–283, 1985. ISSN 00219606. doi: 10.1063/1.448799.
- [129] Willard R. Wadt and P. Jeffrey Hay. Ab initio effective core potentials for molecular calculations. Potentials for main group elements Na to Bi. *The Journal of Chemical Physics*, 82(1):284–298, 1985. ISSN 00219606. doi: 10.1063/1.448800.
- [130] W. J. Hehre, R. F. Stewart, and J. A. Pople. Self-consistent molecular-orbital methods. I. Use of gaussian expansions of slater-type atomic orbitals. *The Journal of Chemical Physics*, 51(6):2657–2664, 1969. ISSN 00219606. doi: 10.1063/1.1672392.
- [131] R. Ditchfield, W. J. Hehre, and J. A. Pople. Self-consistent molecular-orbital methods. IX. An extended gaussian-type basis for molecular-orbital studies of organic molecules. *The Journal of Chemical Physics*, 54(2):720–723, 1971. ISSN 00219606. doi: 10.1063/1.1674902.
- [132] P. C. Hariharan and J. A. Pople. The influence of polarization functions on molecular orbital hydrogenation energies. *Theoretica Chimica Acta*, 28(3):213–222, 1973. ISSN 00405744. doi: 10.1007/BF00533485.

- [133] P. C. Hariharan and J. A. Pople. Accuracy of AHn equilibrium geometries by single determinant molecular orbital theory. *Molecular Physics*, 27(1):209–214, 1974. ISSN 13623028. doi: 10.1080/00268977400100171.
- [134] Rick A. Kendall, Thom H. Dunning, and Robert J. Harrison. Electron affinities of the first-row atoms revisited. Systematic basis sets and wave functions. *The Journal of Chemical Physics*, 96(9):6796–6806, 1992. ISSN 00219606. doi: 10.1063/1.462569.
- [135] A. Klamt and G. Schüürmann. COSMO: a new approach to dielectric screening in solvents with explicit expressions for the screening energy and its gradient. *J. Chem. Soc., Perkin Trans. 2*, (5):799–805, 1993. ISSN 0300-9580. doi: 10.1039/P29930000799. URL <http://xlink.rsc.org/?DOI=P29930000799>.
- [136] Aleksandr V. Marenich, Christopher J. Cramer, and Donald G. Truhlar. Universal solvation model based on solute electron density and on a continuum model of the solvent defined by the bulk dielectric constant and atomic surface tensions. *Journal of Physical Chemistry B*, 113(18):6378–6396, 2009. ISSN 15206106. doi: 10.1021/jp810292n.
- [137] Donald E Curtis, Tim Vandermeersch, Geoffrey R Hutchison, David C Lonie, Eva Zurek, and Marcus D Hanwell. Avogadro: an advanced semantic chemical editor, visualization, and analysis platform. *Journal of Cheminformatics*, 4(1):17, 2012. ISSN 17582946. doi: 10.1186/1758-2946-4-17.
- [138] M. Valiev, E. J. Bylaska, N. Govind, K. Kowalski, T. P. Straatsma, H. J.J. Van Dam, D. Wang, J. Nieplocha, E. Apra, T. L. Windus, and W. A. De Jong. NWChem: A comprehensive and scalable open-source solution for large scale molecular simulations. *Computer Physics Communications*, 181:1477–1489, 2010. ISSN 00104655. doi: 10.1016/j.cpc.2010.04.018.
- [139] Dominic A. Sirianni, Asem Alenaizan, Daniel L. Cheney, and C. David Sherrill. Assessment of Density Functional Methods for Geometry Optimization of Bimolecular van der Waals Complexes. *Journal of Chemical Theory and Computation*, 14(6):3004–3013, 2018. ISSN 15499626. doi: 10.1021/acs.jctc.8b00114.
- [140] Yan Zhao, Nria Gonzlez-Garda, and Donald G. Truhlar. Benchmark database of barrier heights for heavy atom transfer, nucleophilic substitution, association, and unimolecular reactions and its use to test theoretical methods. *Journal of Physical Chemistry A*, 109(9):2012–2018, 2005. ISSN 10895639. doi: 10.1021/jp045141s.
- [141] Benjamin J. Lynch, Patton L. Fast, Maegan Harris, and Donald G. Truhlar. Adiabatic Connection for Kinetics. *The Journal of Physical Chemistry A*, 104(21):4811–4815, 2002. ISSN 1089-5639. doi: 10.1021/jp000497z.
- [142] Ednilsom Orestes, Clia Machado Ronconi, and Jos Walkimar de Mesquita Carneiro. Insights into the interactions of CO₂ with amines: A DFT benchmark study. *Physical Chemistry Chemical Physics*, 16(32):17213–17219, 2014. ISSN 14639076. doi: 10.1039/c4cp02254h.
- [143] Vyacheslav S. Bryantsev, Mamadou S. Diallo, and William A. Goddard. Calculation of solvation free energies of charged solutes using mixed cluster/continuum models. *Journal of Physical Chemistry B*, 112(32):9709–9719, 2008. ISSN 15206106. doi: 10.1021/jp802665d.
- [144] Leo Radom, William A. Lathan, Warren J. Hehre, and John A. Pople. Molecular Orbital Theory of the Electronic Structure of Organic Compounds. XVII. Internal Rotation in 1,2-Disubstituted Ethanes. *Journal of the American Chemical Society*, 95(3):693–698, 1973. ISSN 15205126. doi: 10.1021/ja00784a008.
- [145] M. D. Liptak and G. C. Shields. Accurate pKa calculations for carboxylic acids using Complete Basis Set and Gaussian-n models combined with CPCM continuum solvation

- methods. *Journal of the American Chemical Society*, 123(30):7314–7319, 2001. ISSN 00027863. doi: 10.1021/ja010534f.
- [146] Michael D. Tissandier, Kenneth A. Cowen, Wan Yong Feng, Ellen Gundlach, Michael H. Cohen, Alan D. Earhart, James V. Coe, and Thomas R. Tuttle. The proton’s absolute aqueous enthalpy and Gibbs free energy of solvation from cluster-ion solvation data. *Journal of Physical Chemistry A*, 102(40):7787–7794, 1998. ISSN 10895639. doi: 10.1021/jp982638r.
- [147] Chemcraft - graphical software for visualization of quantum chemistry computations. <https://www.chemcraftprog.com>.
- [148] Y. P. Chang, T. M. Su, T. W. Li, and Ito Chao. Intramolecular hydrogen bonding, Gauche interactions, and thermodynamic functions of 1,2-ethanediamine, 1,2-ethanediol, and 2-aminoethanol: A global conformational analysis. *Journal of Physical Chemistry A*, 101(34):6107–6117, 1997. ISSN 10895639. doi: 10.1021/jp971022j.
- [149] Akimichi Yokozeiki and Kozo Kuchitsu. Structure and Rotational Isomerism of Ethylenediamine as Studied by Gas Electron Diffraction. *Bulletin of the Chemical Society of Japan*, 44(11):2926–2930, nov 1971. ISSN 0009-2673. doi: 10.1246/bcsj.44.2926. URL <http://www.journal.csj.jp/doi/10.1246/bcsj.44.2926>.
- [150] K. M. Marstokk and Harald Mollendal. Microwave spectrum, conformational equilibrium, intramolecular hydrogen bonding, inversion tunneling, dipole moments and centrifugal distortion of ethylenediamine. *Journal of Molecular Structure*, 49:221–237, 1978.
- [151] Michael Caplow. Kinetics of Carbamate Formation and Breakdown. *Journal of the American Chemical Society*, 90(24):6795–6803, 1968. ISSN 15205126. doi: 10.1021/ja01026a041.
- [152] P. V. Danckwerts. The reaction of CO₂ with ethanolamines. *Chemical Engineering Science*, 34(4):443–446, 1979. ISSN 00092509. doi: 10.1016/0009-2509(79)85087-3.
- [153] Juelin Li, Amr Henni, and Paitoon Tontiwachwuthikul. Reaction kinetics of CO₂ in aqueous Ethylenediamine, Ethyl Ethanolamine, and Diethyl Monoethanolamine solutions in the temperature range of 298-313 K, using the stopped-flow technique. *Industrial and Engineering Chemistry Research*, 46(13):4426–4434, 2007. ISSN 08885885. doi: 10.1021/ie0614982.
- [154] E. Alper and W. Bouhamra. Reaction kinetics of carbonyl sulfide with aqueous ethylenediamine and diethylenetriamine. *Gas Separation and Purification*, 1994. ISSN 09504214. doi: 10.1016/0950-4214(94)80003-0.
- [155] Henry Eyring. The Activated Complex in Chemical Reactions. *The Journal of Chemical Physics*, 3(2):107–115, 1935. ISSN 0021-9606. doi: 10.1063/1.1749604.
- [156] Ephraim Katchalski, Chaja Berliner-Klibanski, and Arie Berger. The Chemical Structure of Some Diamine Carbamates. *Journal of the American Chemical Society*, 73(4):1829–1831, 1951. ISSN 15205126. doi: 10.1021/ja01148a124.
- [157] Arne Jensen, Ruth Christensen, Roger Bonnichsen, and Artturi I. Virtanen. Studies on Carbamates. XI. The Carbamate of Ethylenediamine. *Acta Chemica Scandinavica*, 9(3):486–492, 1955. ISSN 0904-213X. doi: 10.3891/acta.chem.scand.09-0486.
- [158] Arlinda F. Ciftja, Ardi Hartono, and Hallvard F. Svendsen. Carbamate formation in aqueous - Diamine - CO₂ systems. *Energy Procedia*, 37(1876):1605–1612, 2013. ISSN 18766102. doi: 10.1016/j.egypro.2013.06.036. URL <http://dx.doi.org/10.1016/j.egypro.2013.06.036>.
- [159] A. V. Gubskaya and P. G. Kusalik. Molecular dynamics simulation study of ethylene glycol, ethylenediamine, and 2-aminoethanol. 2. Structure in aqueous solutions. *Journal of Physical Chemistry A*, 108(35):7165–7178, 2004. ISSN 10895639. doi: 10.1021/jp048921.

- [160] Gábor Lente, István Fábián, and Anthony J. Poë. A common misconception about the Eyring equation. *New Journal of Chemistry*, 29(6):759–760, 2005. ISSN 11440546. doi: 10.1039/b501687h.
- [161] Flemming Y. Hansen Niels E. Henriksen. *Theories of Molecular Reaction Dynamics: The Microscopic Foundation of Chemical Kinetics*. Oxford University Press USA OSO, Oxford, 2008. ISBN 9780199652754.
- [162] Xiaoguang Wang, William Conway, Robert Burns, Nichola McCann, and Marcel Maeder. Comprehensive study of the hydration and dehydration reactions of carbon dioxide in aqueous solution. *Journal of Physical Chemistry A*, 114(4):1734–1740, 2010. ISSN 10895639. doi: 10.1021/jp909019u.
- [163] M. M. Sharma. Kinetics of reactions of carbonyl sulphide and carbon dioxide with amines and catalysis by Brønsted bases of the hydrolysis of COS. *Transactions of the Faraday Society*, 61(6):681–688, 1965. ISSN 00147672. doi: 10.1039/TF9656100681.
- [164] Chao Deng, Qiang-Gen Li, Yi Ren, Ning-Bew Wong, San-Yan Chu, and Hua-Jie Zhu. A comprehensive theoretical study on the hydrolysis of carbonyl sulfide in the neutral water. *Journal of Computational Chemistry*, 29(3):466–480, feb 2008. ISSN 01928651. doi: 10.1002/jcc.20806. URL <http://doi.wiley.com/10.1002/jcc.20806>.
- [165] Chao Deng, Xiao-Peng Wu, Xiao-Ming Sun, Yi Ren, and Ying-Hong Sheng. Neutral hydrolyses of carbon disulfide: An ab initio study of water catalysis. *Journal of Computational Chemistry*, 30(2):285–294, jan 2009. ISSN 01928651. doi: 10.1002/jcc.21058. URL <http://doi.wiley.com/10.1002/jcc.21058>.
- [166] A H Zare and S Mirzaei. Removal of CO₂ and H₂S using aqueous alkanolamine solutions. *International Journal of Chemical, Molecular, Nuclear, Materials and Metallurgical Engineering*, 37(1):194–203, 2009. ISSN 2010376X. URL waset.org/Publication/15675.
- [167] Arthur L. Kohl and Richard B. Nielsen. Alkanolamines for Hydrogen Sulfide and Carbon Dioxide Removal. In *Gas Purification*, chapter 2, pages 40–186. Gulf Publishing Company, Houston, Texas, 5th edition, 1997. doi: 10.1016/b978-088415220-0/50002-1.
- [168] Usman Shoukat, Diego Pinto, and Hanna Knuutila. Study of Various Aqueous and Non-Aqueous Amine Blends for Hydrogen Sulfide Removal from Natural Gas. *Processes*, 7(3):160, 2019. doi: 10.3390/pr7030160.
- [169] David R. Lide. *CRC handbook of chemistry and physics a ready-reference book of chemical and physical data*. Boca Raton, Fla CRC Press, 90th ed edition, 2009. ISBN 1420090844. URL <http://openlibrary.org/books/OL25554411M>. "2009-2010." Includes bibliographical references and index.
- [170] Naomi L. Haworth, Qinrui Wang, and Michelle L. Coote. Modeling Flexible Molecules in Solution: A pK_a Case Study. *Journal of Physical Chemistry A*, 121(27):5217–5225, 2017. ISSN 15205215. doi: 10.1021/acs.jpca.7b04133.
- [171] Casey P. Kelly, Christopher J. Cramer, and Donald G. Truhlar. Adding explicit solvent molecules to continuum solvent calculations for the calculation of aqueous acid dissociation constants. *Journal of Physical Chemistry A*, 110(7):2493–2499, 2006. ISSN 10895639. doi: 10.1021/jp055336f.
- [172] Rollie J. Myers. The new low value for the second dissociation constant for H₂S: Its history, its best value, and its impact on the teaching of sulfide equilibria. *Journal of Chemical Education*, 63(8):687, 2009. ISSN 0021-9584. doi: 10.1021/ed063p687.
- [173] Ana Mijušković, Zorana Orešćanin-Dušić, Aleksandra Nikolić-Kokić, Marija Slavić, Mihajlo B. Spasić, Ivan Spasojević, and Duško Blagojević. Comparison of the effects of methanethiol and sodium sulphide on uterine contractile activity. *Pharmacological Reports*, 66(3):373–379, 2014. ISSN 17341140. doi: 10.1016/j.pharep.2013.12.012.

- [174] Saeid Mokhtab, William A. Poe, and James G. Speoght. *Handbook of Natural Gas Transmission and Processing*. Gulf Professional Publishing, Burlington, MA, 2006.
- [175] L. F. Marakhovski, Yu. I. Rezunenkov, and A. A. Popov. On the use of ethylenediamine to remove H₂S from coke oven gas, 1983.
- [176] Bjørnar Arstad, Richard Blom, and Ole Swang. CO₂ absorption in aqueous solutions of alkanolamines: Mechanistic insight from quantum chemical calculations. *Journal of Physical Chemistry A*, 111(7):1222–1228, 2007. ISSN 10895639. doi: 10.1021/jp065301v. URL [papers2://publication/doi/10.1021/jp065301v](https://doi.org/10.1021/jp065301v).
- [177] Casey P. Kelly, Christopher J. Cramer, and Donald G. Truhlar. Aqueous solvation free energies of ions and ion-water clusters based on an accurate value for the absolute aqueous solvation free energy of the proton. *Journal of Physical Chemistry B*, 110(32):16066–16081, 2006. ISSN 15206106. doi: 10.1021/jp063552y.
- [178] Eirik F. Da Silva, Hallvard F. Svendsen, and Kenneth M. Merz. Explicitly representing the solvation shell in continuum solvent calculations. *Journal of Physical Chemistry A*, 113(22):6404–6409, 2009. ISSN 10895639. doi: 10.1021/jp809712y.
- [179] Nathan E. Hall and Brian J. Smith. Solvation effects on zwitterion formation. *Journal of Physical Chemistry A*, 102(22):3985–3990, 1998. ISSN 10895639. doi: 10.1021/jp980627s.
- [180] Sylvio Canuto, editor. *Solvation Effects on Molecules and Biomolecules*, volume 6. Springer, 2008. ISBN 9781402082696.
- [181] Lindsay E. Roy, P. Jeffrey Hay, and Richard L. Martin. Revised Basis Sets for the LANL Effective Core Potentials. *Journal of Chemical Theory and Computation*, 4(7):1029–1031, jul 2008. ISSN 1549-9618. doi: 10.1021/ct8000409. URL <https://pubs.acs.org/doi/10.1021/ct8000409>.
- [182] Vyacheslav S Bryantsev, Mamadou S Diallo, Adri C. T. van Duin, and William A. Goddard III. Hydration of Copper(II): New Insights from Density Functional Theory and the COSMO Solvation Model. *The Journal of Physical Chemistry A*, 112(38):9104–9112, sep 2008. ISSN 1089-5639. doi: 10.1021/jp804373p. URL <https://pubs.acs.org/doi/10.1021/jp804373p>.
- [183] E. D. Glendening, J. K. Badenhoop, A. E. Reed, J. E. Carpenter, J. A. Bohmann, C. M. Morales, C. R. Landis, and F. Weinhold. NBO 6.0. <http://nbo6.chem.wisc.edu/>, 2013.
- [184] Kai Arne Jensen. Tentative proposals for nomenclature of absolute configurations concerned with six-coordinated complexes based on the octahedron. *Inorganic Chemistry*, 9(1):1–5, jan 1970. ISSN 0020-1669. doi: 10.1021/ic50083a001. URL <https://pubs.acs.org/doi/abs/10.1021/ic50083a001>.
- [185] R. Barbucci, L. Fabbrizzi, P. Paoletti, and A. Vacca. Thermodynamics of complex formation in aqueous solution. Reactions of copper(II) with ethylenediamine, NN'-dimethylethylenediamine, and NN-dimethylethylenediamine: log K, ΔH, and ΔS values. *J. Chem. Soc., Dalton Trans.*, 44(6):740–745, 1972. ISSN 0300-9246. doi: 10.1039/DT9720000740. URL <http://xlink.rsc.org/?DOI=DT9720000740>.
- [186] Piero Paoletti. Formation of metal complexes with ethylenediamine: a critical survey of equilibrium constants, enthalpy and entropy values. *Pure and Applied Chemistry*, 56(4):491–522, jan 1984. ISSN 1365-3075. doi: 10.1351/pac198456040491. URL <http://www.degruyter.com/view/j/pac.1984.56.issue-4/pac198456040491/pac198456040491.xml>.
- [187] Julio de Paula Peter Atkins. *Physical Chemistry*. Oxford University Press: Oxford, UK, 9th edition, 2010.
- [188] Liliana Ilcheva and Jannik Bjerrum. Metal Ammine Formation in Solution. XVII. Stability Constants of Copper(II) Methylamine and Diethylamine Complexes Obtained from

- Solubility Measurements with Gerhardtite, $\text{Cu}(\text{OH})_{1.5}(\text{NO}_3)_{0.5}$. *Acta Chemica Scandinavica*, 30:343–350, 1976.
- [189] Vyacheslav S. Bryantsev, Mamadou S. Diallo, and William A. Goddard. Computational Study of Copper(II) Complexation and Hydrolysis in Aqueous Solutions Using Mixed Cluster/Continuum Models. *Journal of Physical Chemistry A*, 113(34):9559–9567, 2009. ISSN 10895639. doi: 10.1021/jp904816d.
- [190] Yizhak Marcus. *Ions in Solution and their Solvation*. John Wiley and Sons, 2015. ISBN 9781118892336. doi: 10.1002/9781118892336.
- [191] Peter Atkins, Tina Overton, Jonathan Rourke, Mark Weller, Fraser Armstrong, and Michael Hagerman. *Inorganic Chemistry*. Oxford University Press, Great Britain, 5th edition, 2010. ISBN 9780716748786.
- [192] Christian F. Schwenk and Bernd M. Rode. Extended ab initio quantum mechanical/molecular mechanical molecular dynamics simulations of hydrated Cu^{2+} . *Journal of Chemical Physics*, 119(18):9523–9531, 2003. ISSN 00219606. doi: 10.1063/1.1614224. URL <http://scitation.aip.org/content/aip/journal/jcp/119/18/10.1063/1.1614224>.
- [193] Christian F. Schwenk and Bernd M. Rode. New insights into the Jahn-Teller effect through ab initio quantum-mechanical/molecular-mechanical molecular dynamics simulations of Cu(II) in water. *ChemPhysChem*, 4(9):931–943, 2003. ISSN 14394235. doi: 10.1002/cphc.200300659.
- [194] Vyacheslav S. Bryantsev, Mamadou S. Diallo, Adri C.T. Van Duin, and William A. Goddard. Evaluation of B3LYP, X3LYP, and M06-Class density functionals for predicting the binding energies of neutral, protonated, and deprotonated water clusters. *Journal of Chemical Theory and Computation*, 5(4):1016–1026, 2009. ISSN 15499618. doi: 10.1021/ct800549f. URL <http://pubs.acs.org/doi/abs/10.1021/ct800549f>.
- [195] Demian Riccardi, Hao Bo Guo, Jerry M. Parks, Baohua Gu, Liyuan Liang, and Jeremy C. Smith. Cluster-continuum calculations of hydration free energies of anions and group 12 divalent cations. *Journal of Chemical Theory and Computation*, 9(1):555–569, 2013. ISSN 15499626. doi: 10.1021/ct300296k.
- [196] Virgil E. Jackson, Andrew R. Felmy, and David A. Dixon. Prediction of the pK_a 's of Aqueous Metal Ion +2 Complexes. *Journal of Physical Chemistry A*, 119(12):2926–2939, 2015. ISSN 15205215. doi: 10.1021/jp5118272.
- [197] Jaroslav V. Burda, Matěj Pavelka, and Milan Šimánek. Theoretical model of copper Cu(I)/Cu(II) hydration. DFT and ab initio quantum chemical study. *Journal of Molecular Structure: THEOCHEM*, 683(1-3):183–193, 2004. ISSN 01661280. doi: 10.1016/j.theochem.2004.06.013.
- [198] Kanjarat Sukrat and Vudhichai Parasuk. Importance of hydrogen bonds to stabilities of copper-water complexes. *Chemical Physics Letters*, 447(1-3):58–64, 2007. ISSN 00092614. doi: 10.1016/j.cplett.2007.09.004.
- [199] Gerhard W. Marini, Klaus R. Liedl, and Bernd M. Rode. Investigation of Cu^{2+} hydration and the Jahn-Teller effect in solution by QM/MM Monte Carlo simulations. *Journal of Physical Chemistry A*, 103(51):11387–11393, 1999. ISSN 10895639. doi: 10.1021/jp992015t.
- [200] Ingmar Persson, Per Persson, Magnus Sandström, and Ann-Sofi Ullström. Structure of Jahn–Teller distorted solvated copper(II) ions in solution, and in solids with apparently regular octahedral coordination geometry. *Journal of the Chemical Society, Dalton Transactions*, 45(7):1256, 2002. ISSN 1472-7773. doi: 10.1039/b200698g. URL <http://xlink.rsc.org/?DOI=C6DT01176D><http://xlink.rsc.org/?DOI=b200698g>.

- [201] Robert J. Deeth and Laura J. A. Hearnshaw. Molecular modelling of Jahn–Teller distortions in Cu(II)N₆ complexes: elongations, compressions and the pathways in between. *Dalton Trans.*, 6(8):1092–1100, 2006. ISSN 1477-9226. doi: 10.1039/B509274D. URL <http://xlink.rsc.org/?DOI=B509274D>.
- [202] Maja Gruden-Pavlović, Matija Zlatar, Carl Wilhelm Schläpfer, and Claude Daul. DFT study of the Jahn-Teller effect in Cu(II) chelate complexes. *Journal of Molecular Structure: THEOCHEM*, 954(1-3):80–85, 2010. ISSN 01661280. doi: 10.1016/j.theochem.2010.03.031.
- [203] Emma Carter, E. Louise Hazeland, Damien M. Murphy, and Benjamin D. Ward. Structure, EPR/ENDOR and DFT characterisation of a [Cu^{II}(en)₂](OTf)₂ complex. *Dalton Transactions*, 42(42):15088–15096, 2013. ISSN 14779226. doi: 10.1039/c3dt51694f.
- [204] B. Beagley, A. Eriksson, J. Lindgren, I. Persson, L G M Pettersson, M. Sandstrom, U. Wahlgren, and E. W. White. A computational and experimental study on the Jahn-Teller effect in the hydrated copper (II) ion. Comparisons with hydrated nickel (II) ions in aqueous solution and solid Tutton’s salts. *Journal of Physics: Condensed Matter*, 1(13):2395–2408, apr 1989. ISSN 0953-8984. doi: 10.1088/0953-8984/1/13/012. URL <http://stacks.iop.org/0953-8984/1/i=13/a=012?key=crossref.4efa523dead4adce6f4260ac898a01e1>.
- [205] Ralf Aakesson, Lars G. M. Pettersson, Magnus Sandstroem, and Ulf Wahlgren. Theoretical calculations of the Jahn-Teller effect in the hexahydrated Copper(II), chromium(II), and manganese(III) ions, hexaaquacopper(2+), hexaaquachromium(2+) and hexaaquamanganese(3+), and comparisons with the hexahydrated copper(I), chromium(III), a. *The Journal of Physical Chemistry*, 96(1):150–156, 2005. ISSN 0022-3654. doi: 10.1021/j100180a031. URL <http://pubs.acs.org/doi/abs/10.1021/j100180a031>.
- [206] Tapan Kumar Kundu, Raf Bruyndonckx, Claude Daul, and Periakaruppan T. Manoharan. A density functional approach to the jahn-teller effect of [Cu(en)₃]²⁺ as a model for a macrobicyclic cage complex of copper(II). *Inorganic Chemistry*, 38(17):3931–3934, 1999. ISSN 00201669. doi: 10.1021/ic981111q.
- [207] Sijie Luo, Boris Averkiev, Ke R. Yang, Xuefei Xu, and Donald G. Truhlar. Density functional theory of open-shell systems. The 3d-series transition-metal atoms and their cations. *Journal of Chemical Theory and Computation*, 10(1):102–121, 2014. ISSN 15499618. doi: 10.1021/ct400712k. URL <http://pubs.acs.org/doi/pdf/10.1021/ct400712k>.
- [208] Yan Zhao and Donald G. Truhlar. Hybrid Meta Density Functional Theory Methods for Thermochemistry, Thermochemical Kinetics, and Noncovalent Interactions: The MPW1B95 and MPWB1K Models and Comparative Assessments for Hydrogen Bonding and van der Waals Interactions. *The Journal of Physical Chemistry A*, 108(33):6908–6918, aug 2004. ISSN 1089-5639. doi: 10.1021/jp048147q. URL <https://pubs.acs.org/doi/10.1021/jp048147q>.
- [209] Yan Zhao and Donald G. Truhlar. Design of Density Functionals That Are Broadly Accurate for Thermochemistry, Thermochemical Kinetics, and Nonbonded Interactions. *The Journal of Physical Chemistry A*, 109(25):5656–5667, jun 2005. ISSN 1089-5639. doi: 10.1021/jp050536c. URL <https://pubs.acs.org/doi/10.1021/jp050536c>.
- [210] Carlo Adamo and Vincenzo Barone. Toward reliable density functional methods without adjustable parameters: The PBE0 model. *The Journal of Chemical Physics*, 110(13):6158–6170, apr 1999. ISSN 0021-9606. doi: 10.1063/1.478522. URL <http://aip.scitation.org/doi/10.1063/1.478522>.
- [211] Roberto Peverati and Donald G. Truhlar. Communication: A global hybrid generalized gradient approximation to the exchange-correlation functional that satisfies the second-

- order density-gradient constraint and has broad applicability in chemistry. *The Journal of Chemical Physics*, 135(19):191102, nov 2011. ISSN 0021-9606. doi: 10.1063/1.3663871. URL <http://aip.scitation.org/doi/10.1063/1.3663871>.
- [212] Yan Zhao and Donald G. Truhlar. Density Functionals with Broad Applicability in Chemistry. *Accounts of Chemical Research*, 41(2):157–167, feb 2008. ISSN 0001-4842. doi: 10.1021/ar700111a. URL <https://pubs.acs.org/doi/10.1021/ar700111a>.
- [213] Yasuhiro Inada, Kazuhiko Ozutsumi, Shigenobu Funahashi, Sayo Soyama, Takuji Kawashima, and Motoharu Tanaka. Structure of Copper(II) Ethylenediamine Complexes in Aqueous and Neat Ethylenediamine Solutions and Solvent-Exchange Kinetics of the Copper(II) Ion in Ethylenediamine As Studied by EXAFS and NMR Methods. *Inorganic Chemistry*, 32(14):3010–3014, 1993. ISSN 1520510X. doi: 10.1021/ic00066a009.
- [214] Klaus A. Moltved and Kasper P. Kepp. Performance of Density Functional Theory for Transition Metal Oxygen Bonds. *ChemPhysChem*, 20(23):3210–3220, dec 2019. ISSN 1439-4235. doi: 10.1002/cphc.201900862. URL <https://onlinelibrary.wiley.com/doi/abs/10.1002/cphc.201900862>.
- [215] I. M. Shapovalov and I V Radchenko. X-ray study of water and aqueous solutions of manganese, zinc, and copper sulfates. *Journal of Structural Chemistry*, 12(5):705–708, 1972. ISSN 0022-4766. doi: 10.1007/BF00743332. URL <http://link.springer.com/10.1007/BF00743332>.
- [216] P. S. Salmon and G. W. Neilson. The coordination of Cu(II) in a concentrated copper nitrate solution. *Journal of Physics: Condensed Matter*, 1(31):5291–5295, 1989. ISSN 09538984. doi: 10.1088/0953-8984/1/31/028. URL <http://stacks.iop.org/0953-8984/1/i=31/a=028?key=crossref.275887a756fe70b566adc5ca63b91c44>.
- [217] Matěj Pavelka and Jaroslav V. Burda. Theoretical description of copper Cu(I)/Cu(II) complexes in mixed ammine-aqua environment. DFT and ab initio quantum chemical study. *Chemical Physics*, 312(1-3):193–204, 2005. ISSN 03010104. doi: 10.1016/j.chemphys.2004.11.034.
- [218] M. Peschke, A. T. Blades, and P. Kebarle. Binding energies for doubly-charged ions $M^{2+} = Mg^{2+}, Ca^{2+}$ and Zn^{2+} with the ligands $L = H_2O$, acetone and N-methylacetamide complexes in ML_n^{2+} for $n = 1$ to 7 from gas phase equilibria determinations and theoretical calculations. *Journal of the American Chemical Society*, 122(42):10440–10449, 2000. ISSN 00027863. doi: 10.1021/ja002021z.
- [219] G. Licheri, A. Musinu, G. Paschina, G. Piccaluga, G. Pinna, and A. F. Sedda. Coordination of Cu(II) in $Cu(NO_3)_2$ aqueous solutions. *The Journal of Chemical Physics*, 80(10):5308–5311, 1984. ISSN 00219606. doi: 10.1063/1.446559. URL <http://aip.scitation.org/doi/10.1063/1.446559>.
- [220] Tamara Husch, Leon Freitag, and Markus Reiher. Calculation of Ligand Dissociation Energies in Large Transition-Metal Complexes. *Journal of Chemical Theory and Computation*, 14(5):2456–2468, 2018. ISSN 15499626. doi: 10.1021/acs.jctc.8b00061.
- [221] Kipton J. Powell, Paul L. Brown, Robert H. Byrne, Tamás Gajda, Glenn Hefter, Staffan Sjöberg, and Hans Wanner. Chemical speciation of environmentally significant metals with inorganic ligands Part 2: The Cu^{2+} - OH^- , Cl^- , CO_3^{2-} , SO_4^{2-} , and PO_4^{3-} systems (IUPAC Technical Report). *Pure and Applied Chemistry*, 79(5):895–950, jan 2007. ISSN 1365-3075. doi: 10.1351/pac200779050895. URL <http://www.degruyter.com/view/j/pac.2007.79.issue-5/pac200779050895/pac200779050895.xml>.
- [222] Tadao Fujita and Hitoshi Ohtaki. An X-Ray Diffraction Study on the Structures of Bis- and Tris(ethylenediamine)copper(II) Complexes in Solution. *Bulletin of the Chemical Society of Japan*, 56(11):3276–3283, nov 1983. ISSN 0009-2673. doi: 10.1246/bcsj.56.3276. URL <http://www.journal.csj.jp/doi/10.1246/bcsj.56.3276>.

- [223] Donald Sawyer T., Andrzej Sobkowiak, and Julian Roberts L. *Electrochemistry for Chemists*. John Wiley and Sons, 2nd edition, 1995.
- [224] Matěj Velický, Kin Y. Tam, and Robert A.W. Dryfe. On the stability of the silver/silver sulfate reference electrode. *Analytical Methods*, 4(5):1207–1211, 2012. ISSN 17599660. doi: 10.1039/c2ay00011c.
- [225] Byron Kratochvil, Esther Lorah, and Carl Garber. Silver-Silver Nitrate Couple as Reference Electrode in Acetonitrile. *Analytical Chemistry*, 41(13):1793–1796, 1969. ISSN 15206882. doi: 10.1021/ac60282a011.
- [226] Mordechai Schlesinger and Milan Paunovic, editors. *Modern Electroplating*. Wiley, fifth edition, 2010. ISBN 9780470167786. doi: 10.1002/9780470602638.
- [227] G. E. Dima, A. C.A. De Vooy, and M. T.M. Koper. Electrocatalytic reduction of nitrate at low concentration on coinage and transition-metal electrodes in acid solutions. *Journal of Electroanalytical Chemistry*, 554-555(1):15–23, 2003. ISSN 15726657. doi: 10.1016/S0022-0728(02)01443-2.
- [228] David Reyter, Daniel Bélanger, and Lionel Roué. Study of the electroreduction of nitrate on copper in alkaline solution. *Electrochimica Acta*, 53(20):5977–5984, 2008. ISSN 00134686. doi: 10.1016/j.electacta.2008.03.048.
- [229] Miao Wang. *Flue Gas CO₂ Capture using Electrochemically Mediated Amine Regeneration*. Phd, Massachusetts Institute of Technology, 2019.
- [230] Serdar Aksu and Fiona M. Doyle. Electrochemistry of Copper in Aqueous Ethylenediamine Solutions. *Journal of The Electrochemical Society*, 149(7):B340–B347, 2002. URL <http://jes.ecsdl.org/cgi/doi/10.1149/1.1481067>.
- [231] T. I. Quickenden and X. Jiang. The diffusion coefficient of copper sulphate in aqueous solution. *Electrochimica Acta*, 29(6):693–700, 1984. ISSN 00134686. doi: 10.1016/0013-4686(84)80002-X.
- [232] Sheila P. Ewing, Daniel Lockshon, and William P. Jencks. Mechanism of Cleavage of Carbamate Anions. *Journal of the American Chemical Society*, 102(9):3072–3084, 1980. ISSN 15205126. doi: 10.1021/ja00529a033.
- [233] Miao Wang, Subrahmaniam Bharadwaj Hariharan, Michael Edward Massen-Hane, Ryan Shaw, and T. Alan Hatton. Alkaline plating and stripping of metal-amine complexes for amine regeneration in gas scrubbing processes. *Meeting Abstracts*, MA2018-01(20):1296, 2018. URL <http://ma.ecsdl.org/content/MA2018-01/20/1296.abstract>.
- [234] Arthur L. Kohl and Richard B. Nielsen. *Gas Purification*. Gulf Publishing Company, Houston, Texas, 5th edition, 1997. ISBN 978-0-88-415220-0. doi: 10.1016/b978-088415220-0/50009-4. URL <http://linkinghub.elsevier.com/retrieve/pii/B9780884152200500094%5Cnhttp://www.ncbi.nlm.nih.gov/pubmed/13687142>.
- [235] Karl W. Frese. Partial electrochemical oxidation of methane under mild conditions. *Langmuir*, 7(1):13–15, jan 1991. ISSN 0743-7463. doi: 10.1021/la00049a004. URL <https://pubs.acs.org/doi/abs/10.1021/la00049a004>.
- [236] Cem Oktaybaş, Ercan Açma, Cüneyt Arslan, and Okan Addemir. Kinetics of copper precipitation by H₂S from sulfate solutions. *Hydrometallurgy*, 35(1):129–137, 1994. ISSN 0304386X. doi: 10.1016/0304-386X(94)90024-8.
- [237] D. Shea and G. R. Helz. Kinetics of inhibited crystal growth: Precipitation of CuS from solutions containing chelated copper(II). *Journal of Colloid And Interface Science*, 116(2):373–383, 1987. ISSN 00219797. doi: 10.1016/0021-9797(87)90133-0.
- [238] Jung Yoon Choi, Dong Su Kim, and Joong Yeon Lim. Fundamental features of copper ion precipitation using sulfide as a precipitant in a wastewater system. *Journal of Environmental Science and Health - Part A Toxic/Hazardous Substances and Environmental Engineering*, 41(6):1155–1172, 2006. ISSN 10934529. doi: 10.1080/10934520600623059.

- [239] Heriberto Grijalva, Motomichi Inoue, Sajiv Boggavarapu, and Paul Calvert. Amorphous and crystalline copper sulfides, CuS. *Journal of Materials Chemistry*, 6(7):1157–1160, 1996. ISSN 09599428. doi: 10.1039/jm9960601157. URL <http://xlink.rsc.org/?DOI=jm9960601157>.
- [240] S. Gorai, D. Ganguli, and S. Chaudhuri. Shape selective solvothermal synthesis of copper sulphides: Role of ethylenediamine-water solvent system. *Materials Science and Engineering B: Solid-State Materials for Advanced Technology*, 116(2):221–225, 2005. ISSN 09215107. doi: 10.1016/j.mseb.2004.10.003.
- [241] Zheng Kun Yang, Le Xin Song, Yue Teng, and Juan Xia. Ethylenediamine-modulated synthesis of highly monodisperse copper sulfide microflowers with excellent photocatalytic performance. *Journal of Materials Chemistry A*, 2(47):20004–20009, 2014. ISSN 20507496. doi: 10.1039/c4ta04232h. URL <http://dx.doi.org/10.1039/C4TA04232H>.
- [242] I. Zaafarany and H. Boller. Corrosion of copper electrode in sodium sulfide solution. *Journal of Saudi Chemical Society*, 14(2):183–189, apr 2010. ISSN 13196103. doi: 10.1016/j.jscs.2010.02.019. URL <http://dx.doi.org/10.1016/j.jscs.2010.02.019><https://linkinghub.elsevier.com/retrieve/pii/S1319610310000347>.
- [243] H. M. Hollmark, P. G. Keech, J. R. Vegelius, L. Werme, and L. C. Duda. X-ray absorption spectroscopy of electrochemically oxidized Cu exposed to Na₂S. *Corrosion Science*, 54(1):85–89, 2012. ISSN 0010938X. doi: 10.1016/j.corsci.2011.09.001. URL <http://dx.doi.org/10.1016/j.corsci.2011.09.001>.
- [244] Mansi S. Shah, Michael Tsapatsis, and J. Ilja Siepmann. Hydrogen Sulfide Capture: From Absorption in Polar Liquids to Oxide, Zeolite, and Metal-Organic Framework Adsorbents and Membranes. *Chemical Reviews*, 117(14):9755–9803, 2017. ISSN 15206890. doi: 10.1021/acs.chemrev.7b00095.
- [245] UOP. Proven gas treating solutions for offshore floating or fixed platforms. Technical report, UOP A Honeywell Company, 2011. URL www.uop.com.
- [246] M. Nafees, M. Ikram, and S. Ali. Thermal behavior and decomposition of copper sulfide nanomaterial synthesized by aqueous sol method. *Digest Journal of Nanomaterials and Biostructures*, 10(2):635–641, 2015. ISSN 18423582.
- [247] J. Sachinidis, R. D. Shalders, and P. A. Tregloan. The measurement of molar volume changes of redox reactions using high-pressure voltammetry. *Journal of Electroanalytical Chemistry*, 327(1-2):219–234, 1992. ISSN 00220728. doi: 10.1016/0022-0728(92)80149-X.
- [248] Ralph Albert Horne. *Water and aqueous solutions : structure, thermodynamics, and transport processes / edited by R.A. Horne*. Wiley-Interscience, New York, 1972.
- [249] C.J. Brockman and J.H. Mote. Alkaline Plating Baths Containing Organic Amines Part II. Copper Plating from Solutions Containing Ethylenediamine. *Transactions of The Electrochemical Society*, 61(1937):371–376, 1938. URL <http://jes.ecsd1.org/content/73/1/371.short>.
- [250] Mordechai Schlesinger and Milan Paunovic. *Fundamentals of Electrochemical Deposition*. Wiley-Interscience, 2nd edition, 2006. ISBN 9780471712213.
- [251] N. D. Nikolić, K. I. Popov, Lj J. Pavlović, and M. G. Pavlović. Morphologies of copper deposits obtained by the electrodeposition at high overpotentials. *Surface and Coatings Technology*, 201(3-4):560–566, 2006. ISSN 02578972. doi: 10.1016/j.surfcoat.2005.12.004.
- [252] O. M. Magnussen. Ordered Anion Adlayers on Metal Electrode Surfaces. *Chemical Reviews*, 102(3):679–726, 2002. ISSN 0009-2665. doi: 10.1021/cr000069p.
- [253] Z. Nagy, J. P. Blaudeau, L. A. Curtiss, D. J. Zurawski, and N. C. Hung. Chloride Ion Catalysis of the Copper Deposition Reaction. *Journal of the Electrochemical Society*, 142(6):87–89, 1995. ISSN 19457111. doi: 10.1149/1.2044254.

- [254] L. Grambow and W. Vielstich. Diffusion Coefficients and Kinetic Parameters in Copper Sulfate Electrolytes and in Copper Fluoroborate Electrolytes Containing Organic Addition Agents. *Journal of the Electrochemical Society*, 121(6):779, 1974. ISSN 19457111. doi: 10.1149/1.2401912.
- [255] Aspen Technology. Aspen HYSYS Unit Operations Reference Guide: V10, 2017. URL <http://www.aspentech.com>.
- [256] Zaman Ziabakhsh-Ganji and Henk Kooi. An Equation of State for thermodynamic equilibrium of gas mixtures and brines to allow simulation of the effects of impurities in subsurface CO₂ storage. *International Journal of Greenhouse Gas Control*, 11 (SUPPL):21–34, 2012. ISSN 17505836. doi: 10.1016/j.ijggc.2012.07.025. URL <http://dx.doi.org/10.1016/j.ijggc.2012.07.025>.
- [257] Ding Yu Peng and Donald B. Robinson. A New Two-Constant Equation of State. *Industrial and Engineering Chemistry Fundamentals*, 15(1):59–64, 1976. ISSN 01964313. doi: 10.1021/i160057a011.
- [258] Yuhua Song and Chau Chyun Chen. Symmetric electrolyte nonrandom two-liquid activity coefficient model. *Industrial and Engineering Chemistry Research*, 48(16):7788–7797, 2009. ISSN 08885885. doi: 10.1021/ie9004578.
- [259] TW Wolery. Eq3/6-software for geochemical modeling, version 8.0. Technical report, UCRL-CODE-2003-009, Lawrence Livermore National Laboratory, Livermore CA, 2002.
- [260] Craig M. Bethke. *Geochemical Reaction Modelling: Concepts and Applications*. Oxford University Press, Cary, USA, 1996.
- [261] W. Wagner and A. Pruß. The IAPWS formulation 1995 for the thermodynamic properties of ordinary water substance for general and scientific use. *Journal of Physical and Chemical Reference Data*, 31(2):387–535, 2002. ISSN 00472689. doi: 10.1063/1.1461829.
- [262] P.J. Linstrom and W.G. Mallard, editors. National Institute of Standards and Technology, Gaithersburg MD, 20899, retrieved June 17, 2018. doi: 10.18434/T4D303.
- [263] Carl L. Yaws. Gulf Publishing Company, Houston, Texas, 2006. ISBN 1933762071.
- [264] J. M. Smith, H. C. Van Ness, and M. M. Abbott. McGraw-Hill, Singapore, 5th edition, 1996.
- [265] Frank P. Incropera, David P. Dewitt, Theodore L. Bergman, and Andrienne S. Lavine. *Fundamentals of Heat and Mass Transfer*. John Wiley & Sons, Hoboken, NJ, 6th edition, 2007.
- [266] Technical Appendix E3: Public Risk Assessment. Technical report, Environmental Risk Solutions, Perth, 2004. URL https://www.chevronaustralia.com/docs/default-source/default-document-library/e3_public_risk_assessment.pdf?sfvrsn=0.
- [267] API618. Reciprocating Compressors for Petroleum, Chemical, and Gas Industry Services. Standard, American Petroleum Institute, Washington, DC, Jun 2007.
- [268] BASF. OASE Gas Treating Excellence, 2013.
- [269] Inger Marit Elvevoll. *Experimental study of foaming in alkanolamine system*. PhD thesis, Norwegian University of Science and Technology, 2013.
- [270] Luke McElroy. Personal communication, January 2020.
- [271] Refining Gas Processing Petrochemicals. *Petroleum Technology Quarterly*, page 156, 2013.
- [272] Alexander Apelblat. The vapour pressures of saturated aqueous solutions of potassium bromide, ammonium sulfate, copper(II) sulfate, iron(II) sulfate, and manganese(II) dichloride, at temperatures from 283 K to 308 K. *Journal of Chemical Thermodynamics*, 25(12):1513–1520, 1993. doi: 10.1006/jcht.1993.1151.

- [273] Chevron. Environmental Impact Statement and Environmental Review and Management Programme. pages 94–149, 2005.
- [274] *The ORegen™ Waste Heat Recovery Cycle: Reducing the CO₂ Footprint by Means of Overall Cycle Efficiency Improvement*, volume Volume 3: Controls, Diagnostics and Instrumentation; Education; Electric Power; Microturbines and Small Turbomachinery; Solar Brayton and Rankine Cycle of *Turbo Expo: Power for Land, Sea, and Air*, 06 2011. doi: 10.1115/GT2011-45051. URL <https://doi.org/10.1115/GT2011-45051>.
- [275] Andrea Burrato. ORegen Waste Heat Recovery: Development and Applications, 2013. URL <http://www.asme-orc2013.nl/uploads/File/PPT098.pdf>.

Every reasonable effort has been made to acknowledge the owners of copyright material. I would be pleased to hear from any copyright owner who has been omitted or incorrectly acknowledged.

Appendix A

Copyright agreements

ELSEVIER LICENSE TERMS AND CONDITIONS

May 11, 2020

This Agreement between Curtin University -- Michael Massen-Hane ("You") and Elsevier ("Elsevier") consists of your license details and the terms and conditions provided by Elsevier and Copyright Clearance Center.

License Number	4811150533609
License date	Apr 17, 2020
Licensed Content Publisher	Elsevier
Licensed Content Publication	International Journal of Greenhouse Gas Control
Licensed Content Title	Electrochemical CO2 capture thermodynamics
Licensed Content Author	Ryan A. Shaw,T. Alan Hatton
Licensed Content Date	Apr 1, 2020
Licensed Content Volume	95
Licensed Content Issue	n/a
Licensed Content Pages	1
Start Page	102878
End Page	0
Type of Use	reuse in a thesis/dissertation
Portion	figures/tables/illustrations
Number of figures/tables/illustrations	1
Format	both print and electronic
Are you the author of this Elsevier article?	No
Will you be translating?	No
Title	Natural Gas Sweetening via Electrochemically Mediated Amine Regeneration
Institution name	Curtin University
Expected presentation date	Apr 2020
Portions	Figure 1
Requestor Location	Curtin University Kent Street Bentley Perth, Western Australia 6102 Australia Attn: Curtin University
Publisher Tax ID	GB 494 6272 12
Total	0.00 AUD
Terms and Conditions	

INTRODUCTION

1. The publisher for this copyrighted material is Elsevier. By clicking "accept" in connection with completing this licensing transaction, you agree that the following terms and conditions apply to this transaction (along with the Billing and Payment terms and conditions established by Copyright Clearance Center, Inc. ("CCC"), at the time that you opened your Rightslink account and that are available at any time at <http://myaccount.copyright.com>).

GENERAL TERMS

2. Elsevier hereby grants you permission to reproduce the aforementioned material subject to the terms and conditions indicated.
3. Acknowledgement: If any part of the material to be used (for example, figures) has appeared in our publication with credit or acknowledgement to another source, permission must also be sought from that source. If such permission is not obtained then

that material may not be included in your publication/copies. Suitable acknowledgement to the source must be made, either as a footnote or in a reference list at the end of your publication, as follows:

"Reprinted from Publication title, Vol /edition number, Author(s), Title of article / title of chapter, Pages No., Copyright (Year), with permission from Elsevier [OR APPLICABLE SOCIETY COPYRIGHT OWNER]." Also Lancet special credit - "Reprinted from The Lancet, Vol. number, Author(s), Title of article, Pages No., Copyright (Year), with permission from Elsevier."

4. Reproduction of this material is confined to the purpose and/or media for which permission is hereby given.

5. Altering/Modifying Material: Not Permitted. However figures and illustrations may be altered/adapted minimally to serve your work. Any other abbreviations, additions, deletions and/or any other alterations shall be made only with prior written authorization of Elsevier Ltd. (Please contact Elsevier at permissions@elsevier.com). No modifications can be made to any Lancet figures/tables and they must be reproduced in full.

6. If the permission fee for the requested use of our material is waived in this instance, please be advised that your future requests for Elsevier materials may attract a fee.

7. Reservation of Rights: Publisher reserves all rights not specifically granted in the combination of (i) the license details provided by you and accepted in the course of this licensing transaction, (ii) these terms and conditions and (iii) CCC's Billing and Payment terms and conditions.

8. License Contingent Upon Payment: While you may exercise the rights licensed immediately upon issuance of the license at the end of the licensing process for the transaction, provided that you have disclosed complete and accurate details of your proposed use, no license is finally effective unless and until full payment is received from you (either by publisher or by CCC) as provided in CCC's Billing and Payment terms and conditions. If full payment is not received on a timely basis, then any license preliminarily granted shall be deemed automatically revoked and shall be void as if never granted. Further, in the event that you breach any of these terms and conditions or any of CCC's Billing and Payment terms and conditions, the license is automatically revoked and shall be void as if never granted. Use of materials as described in a revoked license, as well as any use of the materials beyond the scope of an unrevoked license, may constitute copyright infringement and publisher reserves the right to take any and all action to protect its copyright in the materials.

9. Warranties: Publisher makes no representations or warranties with respect to the licensed material.

10. Indemnity: You hereby indemnify and agree to hold harmless publisher and CCC, and their respective officers, directors, employees and agents, from and against any and all claims arising out of your use of the licensed material other than as specifically authorized pursuant to this license.

11. No Transfer of License: This license is personal to you and may not be sublicensed, assigned, or transferred by you to any other person without publisher's written permission.

12. No Amendment Except in Writing: This license may not be amended except in a writing signed by both parties (or, in the case of publisher, by CCC on publisher's behalf).

13. Objection to Contrary Terms: Publisher hereby objects to any terms contained in any purchase order, acknowledgment, check endorsement or other writing prepared by you, which terms are inconsistent with these terms and conditions or CCC's Billing and Payment terms and conditions. These terms and conditions, together with CCC's Billing and Payment terms and conditions (which are incorporated herein), comprise the entire agreement between you and publisher (and CCC) concerning this licensing transaction. In the event of any conflict between your obligations established by these terms and conditions and those established by CCC's Billing and Payment terms and conditions, these terms and conditions shall control.

14. Revocation: Elsevier or Copyright Clearance Center may deny the permissions described in this License at their sole discretion, for any reason or no reason, with a full refund payable to you. Notice of such denial will be made using the contact information provided by you. Failure to receive such notice will not alter or invalidate the denial. In no event will Elsevier or Copyright Clearance Center be responsible or liable for any costs, expenses or damage incurred by you as a result of a denial of your permission request, other than a refund of the amount(s) paid by you to Elsevier and/or Copyright Clearance Center for denied permissions.

LIMITED LICENSE

The following terms and conditions apply only to specific license types:

15. **Translation:** This permission is granted for non-exclusive world **English** rights only unless your license was granted for translation rights. If you licensed translation rights you may only translate this content into the languages you requested. A professional translator must perform all translations and reproduce the content word for word preserving the integrity of the article.

16. **Posting licensed content on any Website:** The following terms and conditions apply as follows: Licensing material from an Elsevier journal: All content posted to the web site must maintain the copyright information line on the bottom of each image; A hyper-text must be included to the Homepage of the journal from which you are licensing at <http://www.sciencedirect.com/science/journal/xxxxx> or the Elsevier homepage for books at <http://www.elsevier.com>; Central Storage: This license does not include permission for a scanned version of the material to be stored in a central repository such as that provided by Heron/XanEdu.

Licensing material from an Elsevier book: A hyper-text link must be included to the Elsevier homepage at <http://www.elsevier.com>. All content posted to the web site must maintain the copyright information line on the bottom of each image.

Posting licensed content on Electronic reserve: In addition to the above the following clauses are applicable: The web site must be password-protected and made available only to bona fide students registered on a relevant course. This permission is granted for 1 year only. You may obtain a new license for future website posting.

17. **For journal authors:** the following clauses are applicable in addition to the above:

Preprints:

A preprint is an author's own write-up of research results and analysis, it has not been peer-reviewed, nor has it had any other value added to it by a publisher (such as formatting, copyright, technical enhancement etc.).

Authors can share their preprints anywhere at any time. Preprints should not be added to or enhanced in any way in order to appear more like, or to substitute for, the final versions of articles however authors can update their preprints on arXiv or RePEc with their Accepted Author Manuscript (see below).

If accepted for publication, we encourage authors to link from the preprint to their formal publication via its DOI. Millions of researchers have access to the formal publications on ScienceDirect, and so links will help users to find, access, cite and use the best available version. Please note that Cell Press, The Lancet and some society-owned have different preprint policies. Information on these policies is available on the journal homepage.

Accepted Author Manuscripts: An accepted author manuscript is the manuscript of an article that has been accepted for publication and which typically includes author-incorporated changes suggested during submission, peer review and editor-author communications.

Authors can share their accepted author manuscript:

- immediately
 - via their non-commercial person homepage or blog
 - by updating a preprint in arXiv or RePEc with the accepted manuscript
 - via their research institute or institutional repository for internal institutional uses or as part of an invitation-only research collaboration work-group
 - directly by providing copies to their students or to research collaborators for their personal use
 - for private scholarly sharing as part of an invitation-only work group on commercial sites with which Elsevier has an agreement
- After the embargo period
 - via non-commercial hosting platforms such as their institutional repository
 - via commercial sites with which Elsevier has an agreement

In all cases accepted manuscripts should:

- link to the formal publication via its DOI
- bear a CC-BY-NC-ND license - this is easy to do
- if aggregated with other manuscripts, for example in a repository or other site, be shared in alignment with our hosting policy not be added to or enhanced in any way to appear more like, or to substitute for, the published journal article.

Published journal article (JPA): A published journal article (PJA) is the definitive final record of published research that appears or will appear in the journal and embodies all value-adding publishing activities including peer review co-ordination, copy-editing, formatting, (if relevant) pagination and online enrichment.

Policies for sharing publishing journal articles differ for subscription and gold open access articles:

Subscription Articles: If you are an author, please share a link to your article rather than the full-text. Millions of researchers have access to the formal publications on ScienceDirect, and so links will help your users to find, access, cite, and use the best available version.

Theses and dissertations which contain embedded PJAs as part of the formal submission can be posted publicly by the awarding institution with DOI links back to the formal publications on ScienceDirect.

If you are affiliated with a library that subscribes to ScienceDirect you have additional private sharing rights for others' research accessed under that agreement. This includes use for classroom teaching and internal training at the institution (including use in course packs and courseware programs), and inclusion of the article for grant funding purposes.

Gold Open Access Articles: May be shared according to the author-selected end-user license and should contain a [CrossMark logo](#), the end user license, and a DOI link to the formal publication on ScienceDirect.

Please refer to Elsevier's [posting policy](#) for further information.

18. **For book authors** the following clauses are applicable in addition to the above: Authors are permitted to place a brief summary of their work online only. You are not allowed to download and post the published electronic version of your chapter, nor may you scan the printed edition to create an electronic version. **Posting to a repository:** Authors are permitted to post a summary of their chapter only in their institution's repository.

19. **Thesis/Dissertation:** If your license is for use in a thesis/dissertation your thesis may be submitted to your institution in either print or electronic form. Should your thesis be published commercially, please reapply for permission. These requirements include permission for the Library and Archives of Canada to supply single copies, on demand, of the complete thesis and include permission for Proquest/UMI to supply single copies, on demand, of the complete thesis. Should your thesis be published commercially, please reapply for permission. Theses and dissertations which contain embedded PJAs as part of the formal submission can be posted publicly by the awarding institution with DOI links back to the formal publications on ScienceDirect.

Elsevier Open Access Terms and Conditions

You can publish open access with Elsevier in hundreds of open access journals or in nearly 2000 established subscription journals that support open access publishing. Permitted third party re-use of these open access articles is defined by the author's choice of Creative Commons user license. See our [open access license policy](#) for more information.

Terms & Conditions applicable to all Open Access articles published with Elsevier:

Any reuse of the article must not represent the author as endorsing the adaptation of the article nor should the article be modified in such a way as to damage the author's honour or reputation. If any changes have been made, such changes must be clearly indicated.

The author(s) must be appropriately credited and we ask that you include the end user license and a DOI link to the formal publication on ScienceDirect.

If any part of the material to be used (for example, figures) has appeared in our publication with credit or acknowledgement to another source it is the responsibility of the user to ensure their reuse complies with the terms and conditions determined by the rights holder.

Additional Terms & Conditions applicable to each Creative Commons user license:

CC BY: The CC-BY license allows users to copy, to create extracts, abstracts and new works from the Article, to alter and revise the Article and to make commercial use of the Article (including reuse and/or resale of the Article by commercial entities), provided the user gives appropriate credit (with a link to the formal publication through the relevant DOI), provides a link to the license, indicates if changes were made and the licensor is not represented as endorsing the use made of the work. The full details of the license are available at <http://creativecommons.org/licenses/by/4.0>.

CC BY NC SA: The CC BY-NC-SA license allows users to copy, to create extracts, abstracts and new works from the Article, to alter and revise the Article, provided this is not done for commercial purposes, and that the user gives appropriate credit (with a link to the formal publication through the relevant DOI), provides a link to the license, indicates if changes were made and the licensor is not represented as endorsing the use made of the work. Further, any new works must be made available on the same conditions. The full details of the license are available at <http://creativecommons.org/licenses/by-nc-sa/4.0>.

CC BY NC ND: The CC BY-NC-ND license allows users to copy and distribute the Article, provided this is not done for commercial purposes and further does not permit distribution of the Article if it is changed or edited in any way, and provided the user gives appropriate credit (with a link to the formal publication through the relevant DOI), provides a link to the license, and that the licensor is not represented as endorsing the use made of the work. The full details of the license are available at <http://creativecommons.org/licenses/by-nc-nd/4.0>. Any commercial reuse of Open Access articles published with a CC BY NC SA or CC BY NC ND license requires permission from Elsevier and will be subject to a fee.

Commercial reuse includes:

- Associating advertising with the full text of the Article
- Charging fees for document delivery or access
- Article aggregation
- Systematic distribution via e-mail lists or share buttons

Posting or linking by commercial companies for use by customers of those companies.

20. Other Conditions:

v1.9

Questions? customercare@copyright.com or +1-855-239-3415 (toll free in the US) or +1-978-646-2777.

ELSEVIER LICENSE TERMS AND CONDITIONS

May 11, 2020

This Agreement between Curtin University -- Michael Massen-Hane ("You") and Elsevier ("Elsevier") consists of your license details and the terms and conditions provided by Elsevier and Copyright Clearance Center.

License Number	4784600134022
License date	Mar 09, 2020
Licensed Content Publisher	Elsevier
Licensed Content Publication	International Journal of Greenhouse Gas Control
Licensed Content Title	Energetics of electrochemically mediated amine regeneration process for flue gas CO2 capture
Licensed Content Author	Miao Wang,Subrahmaniam Hariharan,Ryan A. Shaw,T. Alan Hatton
Licensed Content Date	Mar 1, 2019
Licensed Content Volume	82
Licensed Content Issue	n/a
Licensed Content Pages	11
Start Page	48
End Page	58
Type of Use	reuse in a thesis/dissertation
Portion	figures/tables/illustrations
Number of figures/tables/illustrations	1
Format	print
Are you the author of this Elsevier article?	No
Will you be translating?	No
Title	Natural Gas Sweetening via Electrochemically Mediated Amine Regeneration
Institution name	Curtin University
Expected presentation date	Apr 2020
Portions	Figure 7 on page 55.
Requestor Location	Curtin University Kent Street Bentley Perth, Western Australia 6102 Australia Attn: Curtin University
Publisher Tax ID	GB 494 6272 12
Total	0.00 USD
Terms and Conditions	

INTRODUCTION

1. The publisher for this copyrighted material is Elsevier. By clicking "accept" in connection with completing this licensing transaction, you agree that the following terms and conditions apply to this transaction (along with the Billing and Payment terms and conditions established by Copyright Clearance Center, Inc. ("CCC"), at the time that you opened your Rightslink account and that are available at any time at <http://myaccount.copyright.com>).

GENERAL TERMS

2. Elsevier hereby grants you permission to reproduce the aforementioned material subject to the terms and conditions indicated.
3. Acknowledgement: If any part of the material to be used (for example, figures) has appeared in our publication with credit or acknowledgement to another source, permission must also be sought from that source. If such permission is not obtained then

that material may not be included in your publication/copies. Suitable acknowledgement to the source must be made, either as a footnote or in a reference list at the end of your publication, as follows:

"Reprinted from Publication title, Vol /edition number, Author(s), Title of article / title of chapter, Pages No., Copyright (Year), with permission from Elsevier [OR APPLICABLE SOCIETY COPYRIGHT OWNER]." Also Lancet special credit - "Reprinted from The Lancet, Vol. number, Author(s), Title of article, Pages No., Copyright (Year), with permission from Elsevier."

4. Reproduction of this material is confined to the purpose and/or media for which permission is hereby given.

5. Altering/Modifying Material: Not Permitted. However figures and illustrations may be altered/adapted minimally to serve your work. Any other abbreviations, additions, deletions and/or any other alterations shall be made only with prior written authorization of Elsevier Ltd. (Please contact Elsevier at permissions@elsevier.com). No modifications can be made to any Lancet figures/tables and they must be reproduced in full.

6. If the permission fee for the requested use of our material is waived in this instance, please be advised that your future requests for Elsevier materials may attract a fee.

7. Reservation of Rights: Publisher reserves all rights not specifically granted in the combination of (i) the license details provided by you and accepted in the course of this licensing transaction, (ii) these terms and conditions and (iii) CCC's Billing and Payment terms and conditions.

8. License Contingent Upon Payment: While you may exercise the rights licensed immediately upon issuance of the license at the end of the licensing process for the transaction, provided that you have disclosed complete and accurate details of your proposed use, no license is finally effective unless and until full payment is received from you (either by publisher or by CCC) as provided in CCC's Billing and Payment terms and conditions. If full payment is not received on a timely basis, then any license preliminarily granted shall be deemed automatically revoked and shall be void as if never granted. Further, in the event that you breach any of these terms and conditions or any of CCC's Billing and Payment terms and conditions, the license is automatically revoked and shall be void as if never granted. Use of materials as described in a revoked license, as well as any use of the materials beyond the scope of an unrevoked license, may constitute copyright infringement and publisher reserves the right to take any and all action to protect its copyright in the materials.

9. Warranties: Publisher makes no representations or warranties with respect to the licensed material.

10. Indemnity: You hereby indemnify and agree to hold harmless publisher and CCC, and their respective officers, directors, employees and agents, from and against any and all claims arising out of your use of the licensed material other than as specifically authorized pursuant to this license.

11. No Transfer of License: This license is personal to you and may not be sublicensed, assigned, or transferred by you to any other person without publisher's written permission.

12. No Amendment Except in Writing: This license may not be amended except in a writing signed by both parties (or, in the case of publisher, by CCC on publisher's behalf).

13. Objection to Contrary Terms: Publisher hereby objects to any terms contained in any purchase order, acknowledgment, check endorsement or other writing prepared by you, which terms are inconsistent with these terms and conditions or CCC's Billing and Payment terms and conditions. These terms and conditions, together with CCC's Billing and Payment terms and conditions (which are incorporated herein), comprise the entire agreement between you and publisher (and CCC) concerning this licensing transaction. In the event of any conflict between your obligations established by these terms and conditions and those established by CCC's Billing and Payment terms and conditions, these terms and conditions shall control.

14. Revocation: Elsevier or Copyright Clearance Center may deny the permissions described in this License at their sole discretion, for any reason or no reason, with a full refund payable to you. Notice of such denial will be made using the contact information provided by you. Failure to receive such notice will not alter or invalidate the denial. In no event will Elsevier or Copyright Clearance Center be responsible or liable for any costs, expenses or damage incurred by you as a result of a denial of your permission request, other than a refund of the amount(s) paid by you to Elsevier and/or Copyright Clearance Center for denied permissions.

LIMITED LICENSE

The following terms and conditions apply only to specific license types:

15. **Translation:** This permission is granted for non-exclusive world **English** rights only unless your license was granted for translation rights. If you licensed translation rights you may only translate this content into the languages you requested. A professional translator must perform all translations and reproduce the content word for word preserving the integrity of the article.

16. **Posting licensed content on any Website:** The following terms and conditions apply as follows: Licensing material from an Elsevier journal: All content posted to the web site must maintain the copyright information line on the bottom of each image; A hyper-text must be included to the Homepage of the journal from which you are licensing at <http://www.sciencedirect.com/science/journal/xxxxx> or the Elsevier homepage for books at <http://www.elsevier.com>; Central Storage: This license does not include permission for a scanned version of the material to be stored in a central repository such as that provided by Heron/XanEdu.

Licensing material from an Elsevier book: A hyper-text link must be included to the Elsevier homepage at <http://www.elsevier.com>. All content posted to the web site must maintain the copyright information line on the bottom of each image.

Posting licensed content on Electronic reserve: In addition to the above the following clauses are applicable: The web site must be password-protected and made available only to bona fide students registered on a relevant course. This permission is granted for 1 year only. You may obtain a new license for future website posting.

17. **For journal authors:** the following clauses are applicable in addition to the above:

Preprints:

A preprint is an author's own write-up of research results and analysis, it has not been peer-reviewed, nor has it had any other value added to it by a publisher (such as formatting, copyright, technical enhancement etc.).

Authors can share their preprints anywhere at any time. Preprints should not be added to or enhanced in any way in order to appear more like, or to substitute for, the final versions of articles however authors can update their preprints on arXiv or RePEc with their Accepted Author Manuscript (see below).

If accepted for publication, we encourage authors to link from the preprint to their formal publication via its DOI. Millions of researchers have access to the formal publications on ScienceDirect, and so links will help users to find, access, cite and use the best available version. Please note that Cell Press, The Lancet and some society-owned have different preprint policies. Information on these policies is available on the journal homepage.

Accepted Author Manuscripts: An accepted author manuscript is the manuscript of an article that has been accepted for publication and which typically includes author-incorporated changes suggested during submission, peer review and editor-author communications.

Authors can share their accepted author manuscript:

- immediately
 - via their non-commercial person homepage or blog
 - by updating a preprint in arXiv or RePEc with the accepted manuscript
 - via their research institute or institutional repository for internal institutional uses or as part of an invitation-only research collaboration work-group
 - directly by providing copies to their students or to research collaborators for their personal use
 - for private scholarly sharing as part of an invitation-only work group on commercial sites with which Elsevier has an agreement
- After the embargo period
 - via non-commercial hosting platforms such as their institutional repository
 - via commercial sites with which Elsevier has an agreement

In all cases accepted manuscripts should:

- link to the formal publication via its DOI
- bear a CC-BY-NC-ND license - this is easy to do
- if aggregated with other manuscripts, for example in a repository or other site, be shared in alignment with our hosting policy not be added to or enhanced in any way to appear more like, or to substitute for, the published journal article.

Published journal article (JPA): A published journal article (PJA) is the definitive final record of published research that appears or will appear in the journal and embodies all value-adding publishing activities including peer review co-ordination, copy-editing, formatting, (if relevant) pagination and online enrichment.

Policies for sharing publishing journal articles differ for subscription and gold open access articles:

Subscription Articles: If you are an author, please share a link to your article rather than the full-text. Millions of researchers have access to the formal publications on ScienceDirect, and so links will help your users to find, access, cite, and use the best available version.

Theses and dissertations which contain embedded PJAs as part of the formal submission can be posted publicly by the awarding institution with DOI links back to the formal publications on ScienceDirect.

If you are affiliated with a library that subscribes to ScienceDirect you have additional private sharing rights for others' research accessed under that agreement. This includes use for classroom teaching and internal training at the institution (including use in course packs and courseware programs), and inclusion of the article for grant funding purposes.

Gold Open Access Articles: May be shared according to the author-selected end-user license and should contain a [CrossMark logo](#), the end user license, and a DOI link to the formal publication on ScienceDirect.

Please refer to Elsevier's [posting policy](#) for further information.

18. **For book authors** the following clauses are applicable in addition to the above: Authors are permitted to place a brief summary of their work online only. You are not allowed to download and post the published electronic version of your chapter, nor may you scan the printed edition to create an electronic version. **Posting to a repository:** Authors are permitted to post a summary of their chapter only in their institution's repository.

19. **Thesis/Dissertation:** If your license is for use in a thesis/dissertation your thesis may be submitted to your institution in either print or electronic form. Should your thesis be published commercially, please reapply for permission. These requirements include permission for the Library and Archives of Canada to supply single copies, on demand, of the complete thesis and include permission for Proquest/UMI to supply single copies, on demand, of the complete thesis. Should your thesis be published commercially, please reapply for permission. Theses and dissertations which contain embedded PJAs as part of the formal submission can be posted publicly by the awarding institution with DOI links back to the formal publications on ScienceDirect.

Elsevier Open Access Terms and Conditions

You can publish open access with Elsevier in hundreds of open access journals or in nearly 2000 established subscription journals that support open access publishing. Permitted third party re-use of these open access articles is defined by the author's choice of Creative Commons user license. See our [open access license policy](#) for more information.

Terms & Conditions applicable to all Open Access articles published with Elsevier:

Any reuse of the article must not represent the author as endorsing the adaptation of the article nor should the article be modified in such a way as to damage the author's honour or reputation. If any changes have been made, such changes must be clearly indicated.

The author(s) must be appropriately credited and we ask that you include the end user license and a DOI link to the formal publication on ScienceDirect.

If any part of the material to be used (for example, figures) has appeared in our publication with credit or acknowledgement to another source it is the responsibility of the user to ensure their reuse complies with the terms and conditions determined by the rights holder.

Additional Terms & Conditions applicable to each Creative Commons user license:

CC BY: The CC-BY license allows users to copy, to create extracts, abstracts and new works from the Article, to alter and revise the Article and to make commercial use of the Article (including reuse and/or resale of the Article by commercial entities), provided the user gives appropriate credit (with a link to the formal publication through the relevant DOI), provides a link to the license, indicates if changes were made and the licensor is not represented as endorsing the use made of the work. The full details of the license are available at <http://creativecommons.org/licenses/by/4.0>.

CC BY NC SA: The CC BY-NC-SA license allows users to copy, to create extracts, abstracts and new works from the Article, to alter and revise the Article, provided this is not done for commercial purposes, and that the user gives appropriate credit (with a link to the formal publication through the relevant DOI), provides a link to the license, indicates if changes were made and the licensor is not represented as endorsing the use made of the work. Further, any new works must be made available on the same conditions. The full details of the license are available at <http://creativecommons.org/licenses/by-nc-sa/4.0>.

CC BY NC ND: The CC BY-NC-ND license allows users to copy and distribute the Article, provided this is not done for commercial purposes and further does not permit distribution of the Article if it is changed or edited in any way, and provided the user gives appropriate credit (with a link to the formal publication through the relevant DOI), provides a link to the license, and that the licensor is not represented as endorsing the use made of the work. The full details of the license are available at <http://creativecommons.org/licenses/by-nc-nd/4.0>. Any commercial reuse of Open Access articles published with a CC BY NC SA or CC BY NC ND license requires permission from Elsevier and will be subject to a fee.

Commercial reuse includes:

- Associating advertising with the full text of the Article
- Charging fees for document delivery or access
- Article aggregation
- Systematic distribution via e-mail lists or share buttons

Posting or linking by commercial companies for use by customers of those companies.

20. Other Conditions:

v1.9

Questions? customercare@copyright.com or +1-855-239-3415 (toll free in the US) or +1-978-646-2777.



Taylor & Francis Group LLC - Books - License Terms and Conditions

This is a License Agreement between Michael Massen-Hane ("You") and Taylor & Francis Group LLC - Books ("Publisher") provided by Copyright Clearance Center ("CCC"). The license consists of your order details, the terms and conditions provided by Taylor & Francis Group LLC - Books, and the CCC terms and conditions.

All payments must be made in full to CCC.

Order Date	18-Jun-2020	Type of Use	Republish in a thesis/dissertation
Order license ID	1042624-1	Publisher	TAYLOR & FRANCIS GROUP LLC
ISBN-13	9780849334061	Portion	Image/photo/illustration

LICENSED CONTENT

Publication Title	Fundamentals of natural gas processing	Country	United States of America
Author/Editor	KIDNAY, ARTHUR J.	Rightholder	Taylor & Francis Group LLC - Books
Date	01/01/2006	Publication Type	Book
Language	English		

REQUEST DETAILS

Portion Type	Image/photo/illustration	Distribution	Worldwide
Number of images / photos / illustrations	1	Translation	Original language of publication
Format (select all that apply)	Electronic	Copies for the disabled?	No
Who will republish the content?	Academic institution	Minor editing privileges?	No
Duration of Use	Life of current edition	Incidental promotional use?	No
Lifetime Unit Quantity	Up to 999	Currency	USD
Rights Requested	Main product		

NEW WORK DETAILS

Title	Natural Gas Sweetening via Electrochemically Mediated Amine Regeneration	Institution name	Curtin University
Instructor name	Vishnu Pareek	Expected presentation date	2020-09-30

ADDITIONAL DETAILS

Order reference number	N/A	The requesting person / organization to appear on the license	Michael Massen-Hane
-------------------------------	-----	--	---------------------

REUSE CONTENT DETAILS

Title, description or numeric reference of the portion(s)	Figure 5.1	Title of the article/chapter the portion is from	Chapter 5 Gas Treating
Editor of portion(s)	N/A	Author of portion(s)	KIDNAY, ARTHUR J.
Volume of serial or monograph	N/A	Issue, if republishing an article from a serial	N/A
Page or page range of portion	97	Publication date of portion	2006-01-01

PUBLISHER TERMS AND CONDITIONS

Taylor and Francis Group and Informa healthcare are division of Informa plc. Permission will be void if material exceeds 10% of all the total pages in your publication and over 20% of the original publication. This includes permission granted by Informa plc and all of its subsidiaries.

CCC Republication Terms and Conditions

1. Description of Service; Defined Terms. This Republication License enables the User to obtain licenses for republication of one or more copyrighted works as described in detail on the relevant Order Confirmation (the "Work(s)"). Copyright Clearance Center, Inc. ("CCC") grants licenses through the Service on behalf of the rights holder identified on the Order Confirmation (the "Rights holder"). "Republishing", as used herein, generally means the inclusion of a Work, in whole or in part, in a new work or works, also as described on the Order Confirmation. "User", as used herein, means the person or entity making such republication.
2. The terms set forth in the relevant Order Confirmation, and any terms set by the Rights holder with respect to a particular Work, govern the terms of use of Works in connection with the Service. By using the Service, the person transacting for a republication license on behalf of the User represents and warrants that he/she/it (a) has been duly authorized by the User to accept, and hereby does accept, all such terms and conditions on behalf of User, and (b) shall inform User of all such terms and conditions. In the event such person is a "freelancer" or other third party independent of User and CCC, such party shall be deemed jointly a "User" for purposes of these terms and conditions. In any event, User shall be deemed to have accepted and agreed to all such terms and conditions if User republishes the Work in any fashion.
3. Scope of License; Limitations and Obligations.
 - 3.1. All Works and all rights therein, including copyright rights, remain the sole and exclusive property of the Rights holder. The license created by the exchange of an Order Confirmation (and/or any invoice) and payment by User of the full amount set forth on that document includes only those rights expressly set forth in the Order Confirmation and in these terms and conditions, and conveys no other rights in the Work(s) to User. All rights not expressly granted are hereby reserved.
 - 3.2. General Payment Terms: You may pay by credit card or through an account with us payable at the end of the month. If you and we agree that you may establish a standing account with CCC, then the following terms apply: Remit Payment to: Copyright Clearance Center, 29118 Network Place, Chicago, IL 60673-1291. Payments Due: Invoices are payable upon their delivery to you (or upon our notice to you that they are available to you for downloading). After 30 days, outstanding amounts will be subject to a service charge of 1-1/2% per month or, if less, the maximum rate allowed by applicable law. Unless otherwise specifically set forth in the Order Confirmation or in a separate written agreement signed by CCC, invoices are due and payable on "net 30" terms. While User may exercise the rights licensed immediately upon issuance of the Order Confirmation, the license is automatically revoked and is null and void, as if it had never been issued, if complete payment for the license is not received on a timely basis either from User directly or through a payment agent, such as a credit card company.
 - 3.3. Unless otherwise provided in the Order Confirmation, any grant of rights to User (i) is "one-time" (including the editions and product family specified in the license), (ii) is non-exclusive and non-transferable and (iii) is subject to any and all limitations and restrictions (such as, but not limited to, limitations on duration of use or circulation) included in the Order Confirmation or invoice and/or in these terms and conditions. Upon completion of the licensed use, User shall either secure a new permission for further use of the Work(s) or immediately cease any new use of the Work(s) and shall render inaccessible (such as by deleting or by removing or severing links or other locators) any further copies of the Work (except for copies printed on paper in accordance with this license and still in User's stock at the end of such period).

- 3.4. In the event that the material for which a republication license is sought includes third party materials (such as photographs, illustrations, graphs, inserts and similar materials) which are identified in such material as having been used by permission, User is responsible for identifying, and seeking separate licenses (under this Service or otherwise) for, any of such third party materials; without a separate license, such third party materials may not be used.
- 3.5. Use of proper copyright notice for a Work is required as a condition of any license granted under the Service. Unless otherwise provided in the Order Confirmation, a proper copyright notice will read substantially as follows: "Republished with permission of [Rightsholder's name], from [Work's title, author, volume, edition number and year of copyright]; permission conveyed through Copyright Clearance Center, Inc. " Such notice must be provided in a reasonably legible font size and must be placed either immediately adjacent to the Work as used (for example, as part of a by-line or footnote but not as a separate electronic link) or in the place where substantially all other credits or notices for the new work containing the republished Work are located. Failure to include the required notice results in loss to the Rightsholder and CCC, and the User shall be liable to pay liquidated damages for each such failure equal to twice the use fee specified in the Order Confirmation, in addition to the use fee itself and any other fees and charges specified.
- 3.6. User may only make alterations to the Work if and as expressly set forth in the Order Confirmation. No Work may be used in any way that is defamatory, violates the rights of third parties (including such third parties' rights of copyright, privacy, publicity, or other tangible or intangible property), or is otherwise illegal, sexually explicit or obscene. In addition, User may not conjoin a Work with any other material that may result in damage to the reputation of the Rightsholder. User agrees to inform CCC if it becomes aware of any infringement of any rights in a Work and to cooperate with any reasonable request of CCC or the Rightsholder in connection therewith.
4. Indemnity. User hereby indemnifies and agrees to defend the Rightsholder and CCC, and their respective employees and directors, against all claims, liability, damages, costs and expenses, including legal fees and expenses, arising out of any use of a Work beyond the scope of the rights granted herein, or any use of a Work which has been altered in any unauthorized way by User, including claims of defamation or infringement of rights of copyright, publicity, privacy or other tangible or intangible property.
5. Limitation of Liability. UNDER NO CIRCUMSTANCES WILL CCC OR THE RIGHTSHOLDER BE LIABLE FOR ANY DIRECT, INDIRECT, CONSEQUENTIAL OR INCIDENTAL DAMAGES (INCLUDING WITHOUT LIMITATION DAMAGES FOR LOSS OF BUSINESS PROFITS OR INFORMATION, OR FOR BUSINESS INTERRUPTION) ARISING OUT OF THE USE OR INABILITY TO USE A WORK, EVEN IF ONE OF THEM HAS BEEN ADVISED OF THE POSSIBILITY OF SUCH DAMAGES. In any event, the total liability of the Rightsholder and CCC (including their respective employees and directors) shall not exceed the total amount actually paid by User for this license. User assumes full liability for the actions and omissions of its principals, employees, agents, affiliates, successors and assigns.
6. Limited Warranties. THE WORK(S) AND RIGHT(S) ARE PROVIDED "AS IS". CCC HAS THE RIGHT TO GRANT TO USER THE RIGHTS GRANTED IN THE ORDER CONFIRMATION DOCUMENT. CCC AND THE RIGHTSHOLDER DISCLAIM ALL OTHER WARRANTIES RELATING TO THE WORK(S) AND RIGHT(S), EITHER EXPRESS OR IMPLIED, INCLUDING WITHOUT LIMITATION IMPLIED WARRANTIES OF MERCHANTABILITY OR FITNESS FOR A PARTICULAR PURPOSE. ADDITIONAL RIGHTS MAY BE REQUIRED TO USE ILLUSTRATIONS, GRAPHS, PHOTOGRAPHS, ABSTRACTS, INSERTS OR OTHER PORTIONS OF THE WORK (AS OPPOSED TO THE ENTIRE WORK) IN A MANNER CONTEMPLATED BY USER; USER UNDERSTANDS AND AGREES THAT NEITHER CCC NOR THE RIGHTSHOLDER MAY HAVE SUCH ADDITIONAL RIGHTS TO GRANT.
7. Effect of Breach. Any failure by User to pay any amount when due, or any use by User of a Work beyond the scope of the license set forth in the Order Confirmation and/or these terms and conditions, shall be a material breach of the license created by the Order Confirmation and these terms and conditions. Any breach not cured within 30 days of written notice thereof shall result in immediate termination of such license without further notice. Any unauthorized (but licensable) use of a Work that is terminated immediately upon notice thereof may be liquidated by payment of the Rightsholder's ordinary license price therefor; any unauthorized (and unlicensable) use that is not terminated immediately for any reason (including, for example, because materials containing the Work cannot reasonably be recalled) will be subject to all remedies available at law or in equity, but in no event to a payment of less than three times the Rightsholder's ordinary license price for the most closely analogous licensable use plus Rightsholder's and/or CCC's costs and expenses incurred in collecting such payment.
8. Miscellaneous.

6/18/2020 <https://marketplace.copyright.com/rs-ui-web/mp/license/c565cfa7-5a39-48ef-900b-60d2f5d5a574/45f20b57-aec1-49c0-aa03-2cfad8...>

- 8.1. User acknowledges that CCC may, from time to time, make changes or additions to the Service or to these terms and conditions, and CCC reserves the right to send notice to the User by electronic mail or otherwise for the purposes of notifying User of such changes or additions; provided that any such changes or additions shall not apply to permissions already secured and paid for.
- 8.2. Use of User-related information collected through the Service is governed by CCC's privacy policy, available online here: <https://marketplace.copyright.com/rs-ui-web/mp/privacy-policy>
- 8.3. The licensing transaction described in the Order Confirmation is personal to User. Therefore, User may not assign or transfer to any other person (whether a natural person or an organization of any kind) the license created by the Order Confirmation and these terms and conditions or any rights granted hereunder; provided, however, that User may assign such license in its entirety on written notice to CCC in the event of a transfer of all or substantially all of User's rights in the new material which includes the Work(s) licensed under this Service.
- 8.4. No amendment or waiver of any terms is binding unless set forth in writing and signed by the parties. The Rightsholder and CCC hereby object to any terms contained in any writing prepared by the User or its principals, employees, agents or affiliates and purporting to govern or otherwise relate to the licensing transaction described in the Order Confirmation, which terms are in any way inconsistent with any terms set forth in the Order Confirmation and/or in these terms and conditions or CCC's standard operating procedures, whether such writing is prepared prior to, simultaneously with or subsequent to the Order Confirmation, and whether such writing appears on a copy of the Order Confirmation or in a separate instrument.
- 8.5. The licensing transaction described in the Order Confirmation document shall be governed by and construed under the law of the State of New York, USA, without regard to the principles thereof of conflicts of law. Any case, controversy, suit, action, or proceeding arising out of, in connection with, or related to such licensing transaction shall be brought, at CCC's sole discretion, in any federal or state court located in the County of New York, State of New York, USA, or in any federal or state court whose geographical jurisdiction covers the location of the Rightsholder set forth in the Order Confirmation. The parties expressly submit to the personal jurisdiction and venue of each such federal or state court. If you have any comments or questions about the Service or Copyright Clearance Center, please contact us at 978-750-8400 or send an e-mail to support@copyright.com.

v 1.1



Home

Help

Email Support

Michael Massen-Hane ▾

Tentative proposals for nomenclature of absolute configurations concerned with six-coordinated complexes based on the octahedron



Author: Kai Arne Jensen

Publication: Inorganic Chemistry

Publisher: American Chemical Society

Date: Jan 1, 1970

Copyright © 1970, American Chemical Society

PERMISSION/LICENSE IS GRANTED FOR YOUR ORDER AT NO CHARGE

This type of permission/license, instead of the standard Terms & Conditions, is sent to you because no fee is being charged for your order. Please note the following:

- Permission is granted for your request in both print and electronic formats, and translations.
 - If figures and/or tables were requested, they may be adapted or used in part.
 - Please print this page for your records and send a copy of it to your publisher/graduate school.
 - Appropriate credit for the requested material should be given as follows: "Reprinted (adapted) with permission from (COMPLETE REFERENCE CITATION). Copyright (YEAR) American Chemical Society." Insert appropriate information in place of the capitalized words.
 - One-time permission is granted only for the use specified in your request. No additional uses are granted (such as derivative works or other editions). For any other uses, please submit a new request.
- If credit is given to another source for the material you requested, permission must be obtained from that source.

[BACK](#)[CLOSE WINDOW](#)